Adv. Catal. 51 (2007) 133–263

Sum Frequency Generation and Polarization–Modulation Infrared Reflection Absorption Spectroscopy of Functioning Model Catalysts from Ultrahigh Vacuum to Ambient Pressure

GÜNTHER RUPPRECHTER
Institute of Materials Chemistry, Vienna University of Technology, Veterinärplatz 1, A-1210 Vienna, Austria; E-mail: grupp@imc.tuwien.ac.at

It has long been debated whether the results of classical surface science investigations carried out under ultrahigh vacuum (UHV) can be truly transferred to heterogeneous catalysis, which is normally carried out at ambient or even higher pressures. In an effort to answer this question, several surface-sensitive methods have been developed that can operate in a pressure range from UHV to 1 bar. By the application of characterization methods to single-crystal surfaces as well as supported nanoparticles while they are functioning as catalysts, the pressure and materials gaps between surface science and heterogeneous catalysis can be simultaneously bridged.

Vibrational spectroscopy techniques, like infrared-visible (IR-vis) sum frequency generation (SFG), and polarization–modulation IR reflection absorption spectroscopy (PM-IRAS) have been applied to characterize the adsorption, coadsorption, and reaction of small molecules on transition metal surfaces (palladium, platinum, rhodium, gold, ruthenium, etc.) at pressures ranging from UHV to 1 bar. The goal of these investigations at mbar pressures is to elucidate the elementary steps of heterogeneous catalytic reactions. The investigations considered here include CO adsorption and dissociation, CO oxidation and hydrogenation, ethene adsorption and hydrogenation, and methanol decomposition and partial oxidation taking place on low-index single-crystal surfaces, defect-rich (stepped or ion-bombarded) single-crystal surfaces, and oxide-supported metal nanoparticles. When available, complementary structural information determined by high-pressure scanning tunneling microscopy (HP-STM) and compositional analysis by high-pressure photoelectron spectroscopy (HP-XPS) is included. The implications of the high pressure results on the mechanisms of catalytic reactions are discussed, and potential future research directions are suggested.

Abbreviations: AAS, atomic absorption spectroscopy; AES, Auger electron spectroscopy; AFM, atomic force microscopy; BE, binding energy; DFG, difference frequency generation; DFT, density functional theory; EBL, electron beam lithography; EELS, electron energy loss spectroscopy; ETEM, environmental transmission electron microscopy; fcc, face-centered cubic; FEM/FIM, field emission

ISSN: 0360-0564
DOI: 10.1016/S0360-0564(06)51004-1

microscopy/field ionization microscopy; FFT, fast Fourier transform; GC, gas chromatography; hcp, hexagonal close-packed; HREELS, high-resolution electron energy loss spectroscopy; HRTEM, high-resolution transmission electron microscopy; IETS, inelastic tunneling spectroscopy; IRAS, IR reflection absorption spectroscopy; LEED, low-energy electron diffraction; MCT, mercury cadmium telluride; MEP, minimum energy path; ML, monolayer; MS, mass spectrometry; Nd:YAG, neodymium yttrium–aluminum–garnet; NEXAFS, near-edge X-ray absorption fine structure; OPA, optical parametric amplification; PED, photoelectron diffraction; PEM, photoelastic modulator; PES, potential energy surface; PMMA, polymethylmethacrylate; RAIRS, reflection absorption IR spectroscopy; SFG, sum frequency generation; SHG, second-harmonic generation; STM, scanning tunneling microscopy; TDS, thermal desorption spectroscopy; TED, transmission electron diffraction; TEM, transmission electron microscopy; THG, third-harmonic generation; Ti:Sa, titanium sapphire; TOF, turnover frequency; TPD, temperature-programmed desorption; UHV, ultrahigh vacuum; UPS, ultraviolet photoelectron spectroscopy; XAS, X-ray absorption spectroscopy; XPS, X-ray photoelectron spectroscopy.

I. Introduction

Catalysis is of tremendous importance in many fields of applied chemistry, including the more traditional bulk/fine chemical synthesis and petrochemistry, as well as the more recent and still developing areas of environmental technology and energy generation/storage (*1–6*). Heterogeneous catalysis has reached a mature state, with the most industrial catalytic processes having been optimized long ago. Nevertheless, one can still ask critically how well we understand catalysis on a molecular level. Although substantial efforts have been devoted to the elucidation of elementary steps of heterogeneous catalytic reactions (such as gas adsorption, surface diffusion, adsorbate–adsorbate interactions, bond breaking, bond formation, desorption, etc.), it is still very difficult to predict the catalytic properties of a new material (*1,3–5*). One reason for the difficulty is that real catalysts are often too complex to allow atomic-scale characterization, and many fundamental investigations deal with model catalysts that may be too simple (e.g., single crystals) and are carried out under conditions that are too far different from those applied in technological catalysis (e.g., ultrahigh vacuum (UHV)/cryogenic temperatures vs. high-pressure/high temperature). Details are presented below.

A strategy to develop new catalysts or to improve existing ones must encompass at least three aspects: (i) an analysis of the catalyst structure and composition, (ii) an analysis of the interactions of reactants and products with the catalyst surface, and (iii) characterizations that should be performed under conditions as close as possible to those of the technological process, ideally as the catalyst is working and rates are measured simultaneously.[1] It is difficult to meet all of these requirements in a single experiment, but the necessary information can be obtained in parallel investigations, and spectroscopy of the working catalytic surfaces and molecules adsorbed on them is thus the focus of much current research (*7*).

---

[1] In describing the characterization of working catalysts, we avoid the term *in situ*, which is sometimes also used for experiments that simply avoid air exposure of the catalyst between preparation and specific measurements.

Provided that the species adsorbed on a well-characterized surface can be related to the activity of a catalyst and distinguished from unreactive spectator species (e.g., by isotope exchange experiments), spectra of the working catalysts allow one to deduce reaction mechanisms rather straightforwardly. As discussed next, this goal can be attained by combining complementary characterization techniques. Although some of the methods provide information about the catalyst and adsorbed and gas-phase species (e.g., IR and photoelectron spectroscopy), the following strategy is typically applied.

(i) The main techniques to examine the *structure and composition* of the technological catalysts (particle size and shape, support morphology, crystallographic phases, etc.) are transmission electron microscopy and diffraction (TEM/TED), X-ray diffraction (XRD), X-ray absorption spectroscopy (XAS), X-ray photoelectron spectroscopy (XPS), atomic absorption spectroscopy (AAS), Raman spectroscopy, and (indirectly) chemisorption measurements. Significant advances have been made in all of these techniques—even TEM and XPS can now be carried out with catalysts under reaction conditions (*8,9*)—but technological catalysts are often too complex to allow unambiguous atomic level characterization, for example, in the case of mixed-metal oxides, combined metal/oxide systems, bimetallics, etc. A noble metal typically comprises at most only a few percent of the catalyst mass and may be difficult to characterize. The situation is more complex when promoters are present, which may comprise only a few percent of the metal loading but still drastically change the catalyst performance. Furthermore, for structural features on a nanometer scale (metal or oxide nanoparticles), bulk crystallographic structures may not be appropriate.

For example, Fig. 1a shows a high-resolution TEM image of a complex catalyst, Pt/CeTbO$_x$, a metal supported on a mixed-metal oxide with a structure and composition the determination of which require elaborate image contrast simulations using various model structures (*10*). Furthermore, the platinum particles are partly embedded in the oxide support, creating sites with activities

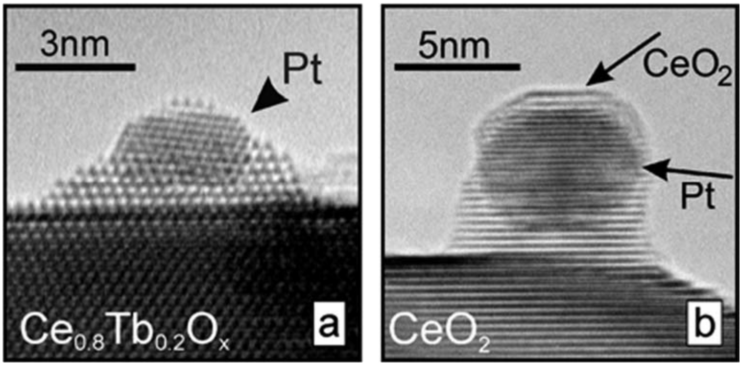

Fig. 1. High-resolution transmission electron micrograph of a mixed-metal oxide catalyst (a) and metal–support interaction (b) illustrating the complexity of technological catalysts; adapted from (*11,12*) with permission from Elsevier.

that are difficult to predict (*11*). The situation is more complicated if the structure and composition of the catalyst change with the changes in operating conditions or over the course of operation, for example, by metal sintering, coking, poisoning, etc. Figure 1b represents a catalyst that was initially relatively simple in composition and structure, platinum/CeO_2 (*12*). After high-temperature hydrogen reduction, the platinum particles were covered with cerium (sub-?) oxide, leading to a strong metal-support interaction (SMSI) effect, (*13–15*) again adding complexity to the characterization challenge (initial stages of SMSI can also be observed in Fig. 1a).

(ii) The interaction of gas molecules with catalyst surfaces is frequently investigated by vibrational spectroscopy (IR, Raman) and by chemisorption and temperature-programmed (TP) techniques (TP-reduction, -oxidation, -desorption, etc.). Vibrational spectroscopy may provide information indicating whether gas molecules adsorb intact or dissociate on the surface, the binding strength between reactants/products and the catalyst, the surface binding site (which may be a catalytically active site), and adsorbate–adsorbate interactions (*16–19*). In favorable cases, the geometry of an adsorbed molecule may be deduced as well, and a comparison of unpromoted and promoted and of fresh and aged catalysts may elucidate effects of promoters and poisons. Vibrational spectra of probe molecules (such as CO or NH_3) adsorbed on the catalyst before and after catalysis may allow one to "titrate" the available surface sites and hence to monitor structural alterations or catalyst deactivation.

Chemisorption and TP techniques provide similar information, but if various coadsorbed species are involved, the interpretation may be complex (with vibrational spectroscopy, one is typically able to distinguish various species).

Vibrational spectroscopy has been used to characterize a wide variety of technological catalysts, as is reviewed elsewhere (*16–19*). Interpretation of vibrational data generally relies on the quality of a prior structure characterization. Consequently, characterizations of gas–solid interactions may be as challenging as those of catalyst structure. If the structure and composition of a catalyst change with operating conditions (cf. Fig. 1b), pronounced alterations of the adsorption properties typically also occur.

(iii) All characterizations (of structure, composition, and adsorption properties) should be performed under catalytic reaction (working) conditions. Neglecting technical limitations for the moment (not all techniques may be available in a single laboratory), the analysis and interpretation of the information is involved for complex technological catalysts. For example, if the catalyst support is porous, there are contributions from both external and internal surfaces, and some surface-sensitive techniques can thus access only a small part of the active catalyst surface. Furthermore, the catalyst performance is influenced by gradients in composition and temperature, as influenced, for example, by the reactor design and details of catalyst synthesis and loading in the reactor.

Thus, complex high-area catalysts are typically not the best for fundamental investigations at the atomic or molecular level. Although many broadly important characteristics of heterogeneous catalysis, such as metal particle size effects, support effects, metal–support interaction, and the influence of the promoters and poisons were discovered by systematic investigations of technological catalysts (e.g., References *13,20–24*)), the explanations deduced from these investigations were often based on indirect evidence.

Model catalysts that are grown in a UHV environment offer several advantages over conventional catalysts, but to be a good model, a (model) catalyst must still mimic the essential properties of a technological catalyst. The advantages of the model approach include the following:

(i) Model catalysts are typically planar and nonporous,[2] and often only a few nanometers in thickness. These properties circumvent the problems discussed above, because the entire catalytically active surface is accessible to the reactants and to the characterization methods.

(ii) The preparation under UHV guarantees that unwanted residues (which may be a serious problem in conventional catalysts prepared by wet-chemical methods (*26,27*)) are absent and that the catalyst composition is well defined.

(iii) Surface analysis can be performed on the clean catalyst (without intermediate exposure to air or other environments), either by techniques that are inherently surface specific or by application of bulk (volume) methods under glancing angles (thereby increasing the surface sensitivity). This is true both for the investigations under UHV and at elevated pressures, provided that UHV-high-pressure reaction cells are used. Using high-pressure cells, catalytic activity of model catalysts can be examined by gas chromatographic analysis of products.

(iv) There are also more specific advantages of model catalysts (for details, see Section II). Model systems are typically grown on conducting substrates, and charging problems that limit electron spectroscopy on technological catalysts are avoided. Electrical conduction is also vital for scanning tunneling microscopy (STM) (and, furthermore, technological catalysts are too rough for STM). Planar substrates that reflect well also facilitate the application of laser spectroscopy and other optical reflection methods, whereas real catalysts scatter too much light. The defined orientation between a model catalyst surface and its underlying metallic substrate also allows the separation of surface and gas-phase contributions (e.g., via polarization of incident IR light). Model catalysts should also exhibit a sufficient thermal conductivity to allow the unrestricted use of TP techniques.

A variety of model catalysts have been employed; we start with the simplest. Single-crystal surfaces of noble metals (platinum, rhodium, palladium, etc.) or oxides are structurally the best defined and the most homogeneous substrates, and the structural definition is beneficial both to experimentalists and theorists. Low-energy electron diffraction (LEED) facilitated the discovery of the relaxation and reconstruction of clean surfaces and the formation of ordered overlayers of adsorbed molecules (*3,28–32*). The combined application of LEED, Auger electron spectroscopy (AES), temperature-programmed desorption (TPD), field emission microscopy (FEM), X-ray and UV-photoelectron spectroscopy (XPS, UPS), IR reflection

---

[2] Porosity may sometimes be vital to the control of reaction selectivity, and there have been attempts to create thin porous model systems (*25*).

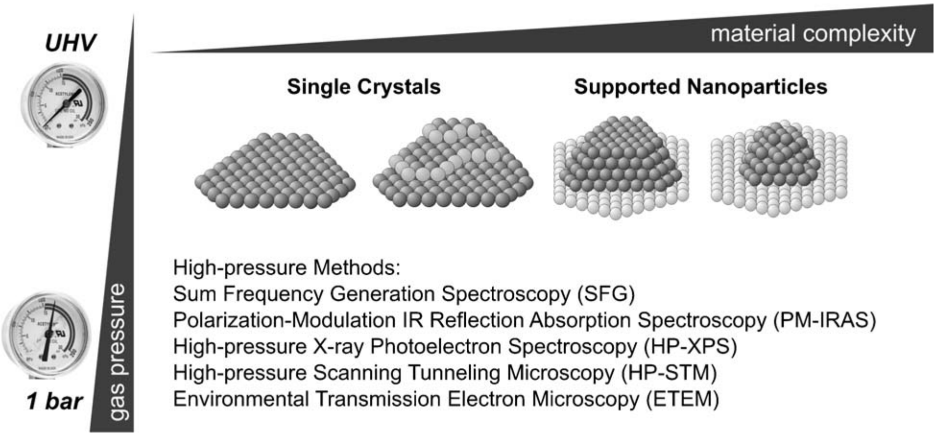

FIG. 2. Illustration of the "pressure and materials gap" between surface science and heterogeneous catalysis. The largest gap exists between UHV investigations of single crystals and atmospheric-pressure processes on supported metal nanoparticles. The gaps can be bridged by using different model catalysts (including smooth and stepped single crystal surfaces as well as supported nanoparticles of various surface roughness) and surface-sensitive techniques capable of operating over wide pressure ranges (ideally, from UHV to $\geq$ 1 bar).

absorption spectroscopy (IRAS), high-resolution electron energy loss spectroscopy (HREELS), etc. permits atomic-scale characterization of a given adsorbate/substrate system in terms of its geometric and electronic structure, composition, metal oxidation state, bond strengths, lateral interactions, etc. (*3,33–42*). A huge database of surface properties has been acquired in the past 40 years, which is of enormous importance for a molecular understanding of heterogeneous catalysis and surface chemistry in general.

Notwithstanding the wealth of information and the improved understanding of catalytic processes gained from these experiments, the relevance of surface-sensitive investigations under UHV for technological catalysis is often questioned (*43–45*). The questions are justified, because there is at least a 10 order-of-magnitude pressure difference between typical surface science UHV investigations[3] and applied catalysis, corresponding to the so-called *pressure gap* (Fig. 2). It has been speculated that at high pressure (>1 bar), saturation coverages observed in UHV may be exceeded and that new adsorbate structures with different geometries and binding energies may occur (*45*). Especially at elevated temperatures, the UHV investigations are generally limited to low coverages, in contrast to technological catalysis. If an active species is weakly bound it will only appear at high pressure (high coverage), after all the strongly adsorbing sites on the surface are occupied by more strongly bonded species (*46*). Furthermore, surfaces may undergo restructuring at elevated pressures and temperatures (e.g., step formation, surface roughening)

---

[3] Attributed to the mean free path required for the involved electrons, ions, atoms, etc. to reach the detector, surface analysis is typically restricted to a UHV environment ($<10^{-8}$ mbar), whereas practical heterogeneous catalysis is carried out at pressures ≥ 1 bar.

(*15,47–54*). The composition of the surface may also depend on gas pressure, for example, a surface may change from that of a metal with adsorbed oxygen to a surface metal oxide (*55–59*) or to a metastable (subsurface) oxide that cannot be identified in UHV or by other analysis (*60,61*). It is apparent that such "pressure effects" have a strong impact on the catalytic properties and that measurements under elevated pressure are desirable.

A second point of criticism of single-crystal investigations is that they are oversimplified. The structural difference between a single-crystal surface and metal nanoparticles in a supported catalyst (typically $\sim 1-10$ nm in diameter) is typically referred to as a "materials gap" (*34,62,63*). Figure 2 shows a ball model of a palladium nanoparticle approximately 3 nm in diameter) on a planar Al_2O_3 support. The palladium nanoparticle has a cuboctahedral shape, similar to the particle in Fig. 1a. Considering that the nanoparticle exhibits only low Miller index facets, and assuming that the support material is inert and does not contribute to the reaction, the catalytic properties of a low-index plane on a metal nanoparticle and those of the corresponding single-crystal surface could be similar.

However, this assumption is not necessarily justified. Even for a well-faceted nanoparticle there are a number of nonequivalent adsorption sites. For example, in addition to the low-index facets, the palladium nanoparticle exhibits edges and interface sites as well as defects (steps, kinks) that are not present on a Pd(1 1 1) or Pd(1 0 0) surface. The overall catalytic performance will depend on the contributions of the various sites, and the activities of these sites may differ strongly from each other. Of course, one can argue that stepped/kinked high-index single-crystal surfaces (Fig. 2) would be better models (*64,65*), but this approach still does not mimic the complex situation on a metal nanoparticle. For example, the diffusion-coupled interplay of molecules adsorbed on different facets of a nanoparticle (*66*) or the size-dependent electronic structure of a metal nanoparticle cannot be represented by a single crystal with dimensions of centimeters (*67*). It is also shown below that some properties are merely determined by the finite size or volume of nanoparticles (*68*). Consequently, the properties of a metal nanoparticle are not simply a superposition of the properties of its individual surface facets.

Furthermore, the lack of a support material in single-crystal investigations does not allow for spillover or phase-boundary effects (*14*). This limitation may be partly overcome by depositing thin oxide films on single-crystal surfaces ("inverse catalysts" (*14,47,69*)), but the geometric and electronic structure of the oxide and of the exposed metal may still be quite different from that of a dispersed catalyst with nominally identical composition.

An attempt to close both gaps must integrate several approaches (as illustrated schematically in Fig. 2).

First, surface-sensitive techniques that can operate under technologically relevant conditions, i.e., at least in the $1-1000$ mbar pressure range, are required. In this respect, photon-based techniques such as sum frequency generation (SFG) and polarization–modulation IR reflection absorption spectroscopy (PM-IRAS) provide surface vibrational spectra of adsorbates from UHV up to atmospheric pressure. Although electron spectroscopies are typically limited to pressures $<10^{-4}$ mbar, recent developments in XPS allow the determination of complementary chemical information at pressures up to ~1 mbar. Direct structural information under mbar pressure can be provided by high-pressure STM.

Second, apart from single crystals, nanoparticle model catalysts should be employed to better mimic the complex properties of supported metals. Nevertheless, the metal nanoparticles should still exhibit well-defined surface facets to allow more reliable data interpretation and a comparison with single-crystal results.

In this chapter, this approach and recent advances are illustrated with case studies. The focus is on vibrational spectroscopic investigations carried out with well-defined noble metal surfaces under catalytic reaction conditions, at gas pressures of 1–1000 mbar. After an introduction presenting the model catalysts and experimental techniques, results of investigations of adsorption on noble metal single crystals and nanoparticles at pressures far in excess of those used in ultrahigh-vacuum experiments are presented, followed by results of investigations of catalysts functioning for various reactions (CO oxidation, CO hydrogenation, ethene hydrogenation, methanol decomposition, and methanol partial oxidation). Related investigations carried out at similar pressures with complementary techniques (XPS and STM) are also briefly discussed, including time-dependent and polarization-dependent characterizations, and electron microscopic investigations of metal nanoparticles.

II. Model Catalysts for Investigations of Elementary Steps of Catalytic Reactions

Figure 3 presents an overview of the most frequently used model catalysts (*14,34,37,62,63,70–84*). Details of their preparation and properties are discussed below in connection with the corresponding spectroscopic investigations, and only a brief introductory description is given here. Single-crystal surfaces of transition metals are the simplest and structurally the best-defined model catalysts, exhibiting specific crystallographic planes. These can be characterized exactly by a variety of techniques (e.g., LEED, STM, AES, XPS). Figure 3a shows an STM image of a Pd(1 1 1) surface (*85,86*). By using low Miller index single-crystal surfaces of various orientations (*64,65,87*) as well as stepped and kinked surfaces (*3,35*), researchers demonstrated the origin of structure sensitivity and the importance of surface defects (low-coordinated sites) in catalysis. Support effects and metal–support interactions were mimicked by growing thin oxide overlayers on metal surfaces (*14,47,69,88*) (Fig. 3b). The effects of promoters and poisons on adsorption and catalytic activity were elucidated by depositing atoms such as K, Na, S, Cl, C, etc., which may either directly influence the surface structure or modify the bonding of reactants or products (*87,89–95*).

Recognition of the differences between single-crystal model catalysts and supported nanoparticles, mentioned above, stimulated the development of *nanoparticle model catalysts* (*14,34,37,62,63,70–83,99*). The most straightforward approach to their preparation is to grow metal nanoparticles on a single crystal of the support material. Figure 3c shows a HRTEM image of a Au/MgO model catalyst prepared

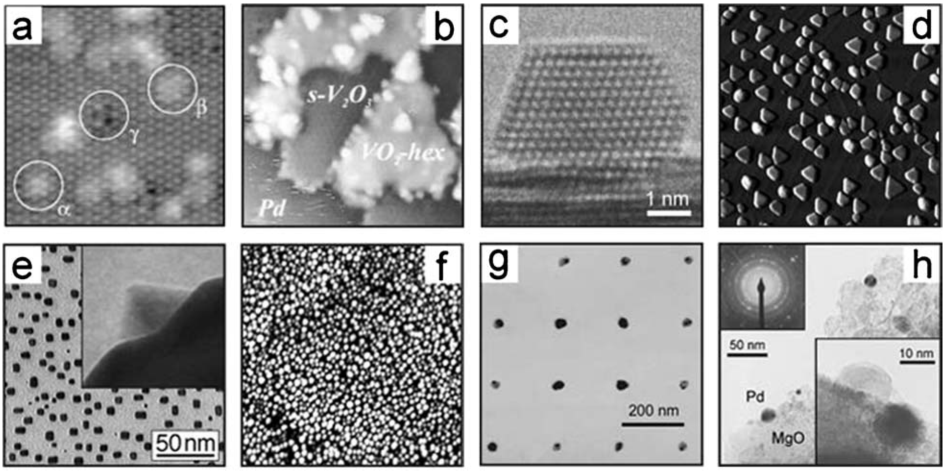

FIG. 3. Model catalysts most frequently used for investigations of elementary processes of heterogeneous catalysis. (a) Atomically resolved STM image of a (nominally) clean Pd(111) surface (6.0 x 6.6 nm; 4 pm corrugation; subsurface impurities are marked); adapted from Rose *et al.* (*85*); (b) STM image of an inverse model catalyst: vanadium oxide islands on Pd(111); adapted from Surnev *et al.* (*88*); (c) A Au particle on MgO(100); adapted from Giorgio *et al.* (*96*); (d) STM image of cuboctahedral palladium nanocrystals grown on Al_2O_3-NiAl(110) at 300 K; adapted from Heemeier *et al.* (*97*); (e) Pyramidal platinum particles (grown on NaCl(100)) supported by Al_2O_3 (*48*) (the inset shows a profile (side) view of a single particle); (f) STM image of palladium nanoparticles grown on Al_2O_3-NiAl(110) at 90 K; adapted from Heemeier *et al.* (*97*); (g) Platinum nanoparticle array grown on SiO_2 by electron beam lithography (*53*); (h) impregnated palladium-MgO catalyst with the inset showing a profile view (*105*). Adapted from (*84*) with permission from The Royal Society of Chemistry.

by epitaxially growing gold particles on MgO(100) microcubes by metal evaporation (*70,77,96,100*). Because the support crystals are typically insulators, charging or limited thermal conductivity often hampers experiments, and instead thin oxide films are generally better suited as supports (*73,82,101*). These planar model supports can be prepared by oxidation of metal or alloy single crystals, or by reactive evaporation of a metal in oxygen onto suitable substrates (*99,102,103*). The structure and long-range order of a thin oxide film may vary widely, depending on the preparation procedure. Structural homogeneity of the model support is thus difficult to achieve. A high level of support crystallinity is beneficial for the growth of regular metal nanoparticles on the thin model support. If the metal particles grow epitaxially on the support, homogeneous distributions of equal-sized particles with well-defined crystallographic shapes are typically obtained. For example, Fig. 3d shows an STM image of cuboctahedral palladium nanoparticles grown at 300 K on a thin-ordered Al_2O_3 film (which was grown on NiAl(1 1 0) (*83,97,101,104*)), and Fig. 3e shows an electron micrograph of half-octahedral (pyramidal) platinum nanoparticles (*48,52,74*) grown at 650 K on NaCl(1 0 0), which was subsequently replaced by an Al_2O_3 film. In both cases, the epitaxial growth leads to polyhedral metal particles (cuboctahedra and half-octahedra), which mainly expose (1 1 1) and (1 0 0) surface facets. The inset in Fig. 3e shows a TEM profile view of a truncated pyramid (half octahedron), which clearly reveals the particle morphology; the shapes of the cuboctahedra can be deduced from the height information provided by STM. The well-defined particle morphology is advantageous for the interpretation of experimental results, for a comparison with single-crystal results, and for theoretical calculations.

One may argue that such well-faceted particles may be "too perfect" to mimic the, sometimes, irregular metal particles grown on a high surface area oxide by industrially applied wet-chemical (impregnation) techniques. However, to produce nanoparticles with random orientations and more surface defects under UHV, metal deposition can be carried out at lower substrate temperatures. Figure 3f shows an STM image of palladium particles grown on Al_2O_3 at 90 K (*83,97,101,104*). The rounded profiles of these particles clearly indicate rough, stepped surfaces.

In the model catalysts described so far, the interparticle distances were more or less random, governed by the separation of substrate defects which control the nucleation and growth process of the metal particles (*74,101*). The position and separation of metal particles can be controlled accurately by electron beam lithography (EBL) (which has also been used to fabricate model catalysts), but the minimum size of the metal aggregates is currently still approximately 10 nm. Figure 3g shows an example of a platinum nanoparticle array on SiO_2 (mean size 28 nm; interparticle separation 200 nm) (*53,106,107*).

A further step toward technological catalysts is the use of medium-to-low surface area supports on which relatively large metal particles (~5 nm) of well-defined shape are grown. Figure 3h displays a TEM micrograph of palladium nanoparticles supported on MgO (*105,108*). In favorable cases, the powder oxide support also allows the use of scanning probe microscopy (AFM) or electron spectroscopy.

III. High-Pressure Surface-Sensitive Techniques

Fundamental investigations of the interactions of (reacting) gas molecules with single crystal and nanoparticle model catalysts have largely been carried out under UHV, with a number of surface-sensitive techniques, such as LEED, TPD, HREELS, IRAS, AES, XPS, UPS, and others being applied (*3,33,34*). Unfortunately, these methods typically cannot be used under catalytic reaction conditions (>1 bar), for example, because of mean free path restrictions of the involved electrons, atoms, or ions.

However, recent investigations have shown conclusively that the catalyst surface as well as the adsorbate geometry may change during the course of a catalytic reaction (*43,47,109*). Adsorbed molecules may restructure a surface, even under UHV ("adsorbate-induced restructuring" (*41,110*)), and this effect may be more pronounced at the high pressures and temperatures employed in the most catalytic reactions (*50*). These structural changes influence the adsorption and surface catalytic reactions. However, even when the catalyst surface would not change, the concentration (coverage) and the arrangement (structure) of adsorbed species during a high-pressure reaction may be quite different from what is observed in a pre- or post-reaction surface analysis in vacuum (*46,48,111,112*). Thus, dominant species observed in UHV investigations may turn out to be mere spectators in the high-pressure catalytic reaction, and these may hinder the catalytic reaction instead of participating in it. These issues have helped to fuel the ongoing debate about the relevance of UHV investigations to practical catalysis (*43,44*). The preference for investigation of catalysts under real reaction conditions is clear (*43,45,46*). For overviews of the methods, see References (*32,43,109*); several scientific meetings have focused on this topic (e.g., the Bunsen Discussion Meetings in Lahnstein (1992) and Berlin (2001), and symposia at American Chemical Society meetings (Dallas, 1998; Anaheim, 1999).

Adsorbed molecules and intermediates at high pressures can be detected by vibrational spectroscopies provided they can differentiate between gas phase and surface signals. For example, Fig. 4 shows a (conventional) IRAS spectrum of CO at 50 mbar on Pd(1 1 1) at 300 K (*113,114*). The signal of adsorbed on-top CO at approximately 2060 cm^{-1} is nearly obscured by the rovibrational absorption spectrum of the CO gas phase. In contrast, as shown below, SFG and PM-IRAS selectively probe the adsorbed surface species and thus provide surface-sensitive information, even in the presence of a gas phase. Investigations of the catalyst structure and composition under working conditions can be carried out by high-pressure (HP-) STM and (HP-) XPS, provided that the instruments are properly modified (*9,115*).

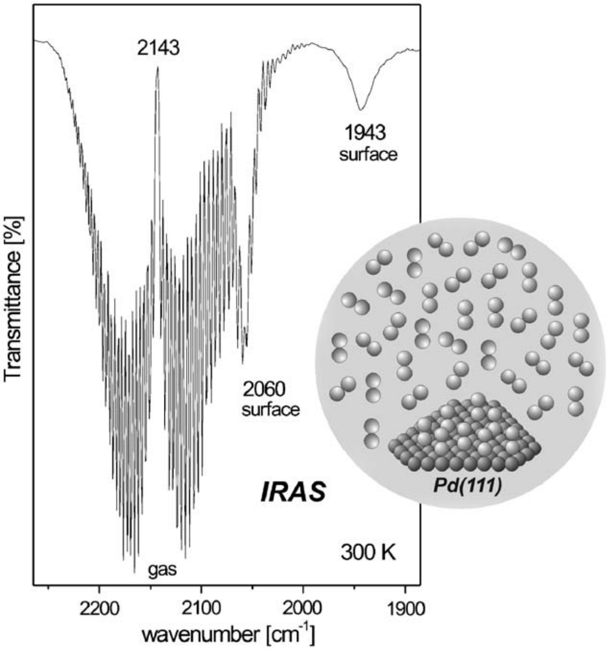

FIG. 4. IRAS spectrum of 50 mbar CO on Pd(1 1 1) at 300 K. Signals of adsorbed CO at approximately 2100 cm^{-1} are obscured by the rovibrational absorption spectrum of the CO gas phase (*113*).

Although monitoring of the surface is as important as monitoring of the adsorbed species, the latter topic is emphasized here, because this chapter is focused on vibrational spectroscopy. It is stressed that contamination occurs much faster at mbar pressures, and precautions must be taken to guarantee the cleanliness of samples used in high-pressure experiments.

A. Vibrational Sum Frequency Generation Spectroscopy

A.1. *Basics*

Nonlinear optical infrared-visible sum frequency generation (IR-vis SFG) is a versatile surface-specific vibrational spectroscopy that meets the requirements mentioned above. SFG provides vibrational spectra of molecules adsorbed on a surface, while the molecules in the gas phase do not produce a signal. Consequently, SFG can be operated in a pressure range from UHV to ambient conditions and still detects only the adsorbed species. A direct comparison of adsorbate structures under UHV and elevated pressure is therefore feasible. Furthermore, SFG can be applied to molecules adsorbed on single crystals, thin films, metal foils, and supported nanoparticles (*46,116–121*) and is thus a promising tool to extend surface science experiments to more realistic conditions.

The advantages of SFG spectroscopy have been outlined in a number of publications covering a wide range of substrate (interface)–adsorbate combinations (*46,122–127*). The first applications of SFG in catalysis research were reported in the 1990s by groups in Annandale (Exxon) (*123*), Berkeley (*128*), and Jülich (*129*). In these investigations, single-crystal surfaces such as Ni(1 0 0) (*123*), Pt(1 1 1), and Pt(1 1 0) (*129–131*) were used, because these "mirror-like" surfaces facilitated the optical experiment. The field was soon extended to less-ideal substrates such as thin oxide films (*116*) and polycrystalline foils (*117*). The first SFG spectra of CO on UHV-grown sub-10-nm palladium nanoparticles supported on Al_2O_3 were obtained by Dellwig *et al.* (*119*) and CO adsorption on lithographically fabricated platinum aggregates (30–1000 nm mean diameter) was reported (*132*). Most of the attention was directed to the adsorption of CO, NO, and small hydrocarbons.

Beyond solid–gas interfaces, SFG was also successfully employed to characterize a variety of "buried" interfaces, such as solid–liquid and liquid–liquid interfaces (*122,133–136*).

The principle of SFG and the components of an SFG spectrometer based on neodymium yttrium–aluminum–garnet (Nd:YAG), titanium sapphire (Ti:Sa), or free-electron lasers are described, and the reader is referred to these articles for details (*46,116,119,122–124,126,127,137–145*). Here, we restrict the discussion to those aspects that are important to understanding the advantages and limitations of the method.

To acquire an SFG vibrational spectrum of adsorbate molecules on a metal catalyst, two (picosecond) laser pulses are spatially and temporally overlapped on the sample (Fig. 5). One input beam is in the visible range at fixed frequency (ω_{vis}), and the second one is tunable in the mid-IR region (ω_{IR}) to probe the vibrational

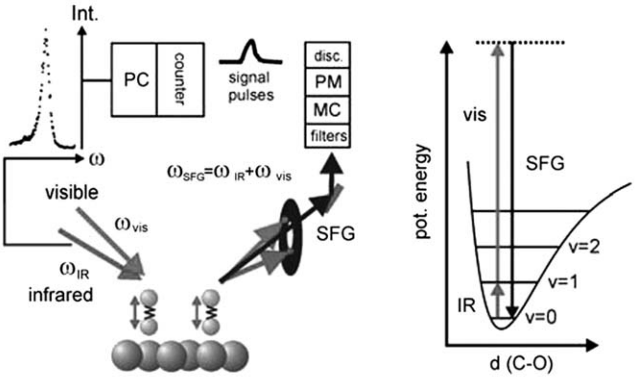

FIG. 5. Illustration of the IR-vis SFG process. The detection system employs spatial, spectral, and temporal filtering of the SFG signal (MC: monochromator; PM: photomultiplier; disc.: discriminator; adapted from (*48*) with permission from the PCCP Owner Societies).

modes of the surface species. In a simplified picture, when the IR beam is tuned through a vibrational resonance of the adsorbate, it induces a vibrational transition from the ground state to an excited state, and simultaneously the visible beam induces a transition to a higher-energy virtual state through an anti-Stokes Raman process. When the high-energy virtual state relaxes, light is generated at a frequency that is the sum of the frequencies of two incident optical fields ($\omega_{\mathrm{SFG}} = \omega_{\mathrm{IR}} + \omega_{\mathrm{vis}}$), resulting in a signal in the visible region and at an angle determined by the phase-matching condition ($\omega_{\mathrm{SFG}} \sin\,\theta_{\mathrm{SFG}} = \omega_{\mathrm{IR}} \sin\,\theta_{\mathrm{IR}} + \omega_{\mathrm{vis}} \sin\,\theta_{\mathrm{vis}}$). By tuning of the IR beam and monitoring of the intensity of the SFG output, an adsorbate vibrational spectrum is obtained as a plot of the SFG intensity against the IR wavenumber. This measurement can be called "conventional" SFG spectroscopy (i.e., the IR energy is varied), in contrast to "broadband" SFG spectroscopy, in which broadband IR pulses are used (*146–148*).

The inherent surface-specificity of SFG originates from its second-order nonlinearity. The beam mixing process induces a nonlinear polarization $P^{(2)}$:

$$P^{(2)}(\omega_{\mathrm{SFG}} = \omega_{\mathrm{IR}} + \omega_{\mathrm{vis}}) = \chi_s^{(2)} E(\omega_{\mathrm{IR}})\, E(\omega_{\mathrm{vis}}), \tag{1}$$

with $\chi_s^{(2)}$ being the surface nonlinear susceptibility and $E(\omega_{\mathrm{IR}})$ and $E(\omega_{\mathrm{vis}})$ the magnitudes of the local electric fields. The intensity of the SFG signal generated by the nonlinear polarization is proportional to the absolute square of $\chi_s^{(2)}$ and to the product of the incident light intensities I_{IR} and I_{vis}:

$$I_{\mathrm{SFG}} \propto \left|\chi_s^{(2)}\right|^2 I_{\mathrm{IR}} I_{\mathrm{vis}}. \tag{2}$$

The term $\chi_s^{(2)}$ has two components: a resonant contribution from the adsorbate vibrations $\chi_{\mathrm{R}}^{(2)}$ (incorporating the resonance condition (ω_{IR}–ω_q)) and a nonresonant contribution $\chi_{\mathrm{NR}}^{(2)}$ from the surface itself. In many cases, the applied light frequencies are far from resonances of the surface, and the response of the surface is therefore usually modeled by a frequency-independent nonresonant susceptibility

$\chi_{\mathrm{NR}}^{(2)}$ (assuming that this also incorporates the nonresonant contribution from higher-order multipole moments of the centrosymmetric bulk) (*149*). Consequently,

$$\chi_{\mathrm{s}}^{(2)} = \chi_{\mathrm{R}}^{(2)} + \chi_{\mathrm{NR}}^{(2)} = \sum_q \frac{A_{\mathrm{R}(q)}}{\omega_{\mathrm{IR}} - \omega_q + \mathrm{i}\Gamma q} + A_{\mathrm{NR}}\,\mathrm{e}^{i\Phi}, \tag{3}$$

where $\chi_{\mathrm{R}}^{(2)}$, $\chi_{\mathrm{NR}}^{(2)}$, $A_{\mathrm{R}(q)}$, ω_q, Γ_q, and ω_{IR} are the resonant nonlinear susceptibility, nonresonant nonlinear susceptibility, amplitude, resonance frequency, and damping constant (homogeneous linewidth $2\Gamma_q = \mathrm{FWHM}$) of the qth vibrationally resonant mode, and the IR laser frequency, respectively. A_{NR} is the amplitude of the vibrationally nonresonant susceptibility, and Φ is its phase relative to the resonant term. The term $\chi_{\mathrm{R}}^{(2)}$ incorporates the resonance condition (ω_{IR}–ω_q), and as the IR beam is tuned through vibrational resonances of surface species, the surface nonlinear susceptibility $\chi_s^{(2)}$ reaches a maximum. The amplitude of the vibrationally resonant susceptibility $A_{\mathrm{R}(q)}$ includes the adsorbate concentration (number density N) and the product of the IR and Raman transition moments of the vibration (T_q, M_q; $\delta\rho$ is the population difference between the vibrational ground and excited state):

$$A_{\mathrm{R}(q)} \propto N\, T_q\, M_q\, \delta\rho. \tag{4}$$

Equation (4) illustrates the selection rule for the SFG process. In order for a vibrational mode to be SFG active, it must simultaneously satisfy both IR and Raman selection rules. Therefore, SFG is not allowed in media with inversion symmetry (in the electric dipole approximation). The SFG signal vanishes in the bulk of centrosymmetric media but has a finite value at an interface where the inversion symmetry is broken. The dominant contribution to the SFG signal is hence generated by the modes of the adsorbed monolayer (ML), and the centrosymmetric bulk of face-centered cubic (fcc) metals and an isotropic gas phase give zero contribution to the signal (with the exception of the nonresonant background). SFG is frequently carried out in ppp geometry (*128*) (i.e., all beams are p-polarized), but other polarization combinations can also be employed to gain information about molecular orientations (*150*), as shown in Section IV.H.

A.2. *IR Gas-Phase Absorption Correction, Sensitivity toward Various Adsorbed Species, and SFG Lineshape*

According to Eq. (2), the intensity of an SFG signal (let us say for a data point at a specific frequency ω_{IR}) must be normalized by the (effective) light intensities I_{IR} (at ω_{IR}) and I_{vis} at the sample surface. For a given energy range (e.g., $1800-2300\,\mathrm{cm}^{-1}$), the variations in I_{IR} are typically small, and normalization (although certainly appropriate) has a minor effect in the investigations of UHV adsorption. However, in high-pressure measurements, strong frequency-dependent variations in the IR intensity may occur, and normalization becomes essential.

Although no SFG light is produced by the gas phase itself, at elevated pressure (e.g., ≥ 1 mbar for CO) a significant frequency-dependent IR absorption occurs in the gas phase via vibrational and rotational excitations (cf. Fig. 4), (*118,151*) modifying the effective IR intensity at the sample surface. Consequently, because the number of generated SFG photons depends linearly on the intensity of the IR pulse (and the vis pulse, which, however, is essentially constant), the SFG process is indirectly influenced by the gas pressure. The apparent (uncorrected) intensity of vibrational SFG resonances may therefore depend on whether they coincide with a gas-phase absorption line. For the apparatus shown in Fig. 8, the distance between the input window and the sample is only 1.5 cm (minimizing IR gas-phase absorption), which allows the measurement of "uncorrected" SFG spectra up to pressures of ~1 mbar of CO. For higher pressure or for experimental arrangements using longer beam paths, an IR absorption correction must be applied.

To correct (normalize) the SFG spectra for IR gas-phase absorption, reference measurements were performed on a GaAs crystal, which could be moved to the exact sample position using a linear motion (Fig. 6a) (*118,151*). As a consequence of its zincblende structure, GaAs has no inversion symmetry and produces a constant bulk SFG signal. Although the SFG signal is constant at 10^{-7} mbar of CO, the signals at 50, 100, and 200 mbar of CO vary strongly, as a consequence of IR gas-phase absorption (Fig. 6a; the P-branch of the unresolved rotational side bands is evident). Alternatively, the reflected IR light may be measured and used to calculate the IR intensity at the sample surface (if account is taken of the additional absorption between the sample position and the IR detector) (*121,152*). The "raw" SFG spectra were then normalized by dividing the experimental traces by the corresponding gas-phase absorption (correction) curves and by the vis intensity recorded with a photodiode (which is nearly constant).

For example, Fig. 6b shows the raw SFG spectrum of CO on Pt(1 1 1) in the presence of 200 mbar of CO at 300 K (open circles) together with the applied gas-phase compensation curve (solid line) and the corrected spectrum (black dots). To prevent the undesired attenuation of the IR beam by atmospheric CO_2 and water before entering the SFG cell, all beam lines were encapsulated and purged with dry nitrogen.

Apart from providing the vibrational characteristics of an adsorbed species, a quantitative analysis of SFG spectra adds further important information.

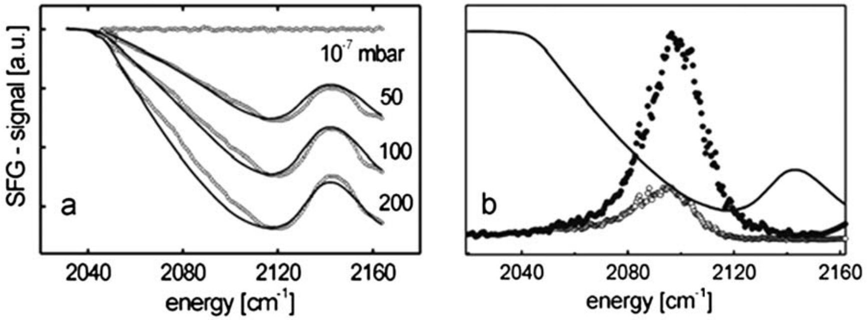

FIG. 6. (a) Influence of IR absorption by gas-phase CO on the SFG signal of a GaAs reference crystal located at the sample position. The data points (open circles) were fitted by using the Lambert–Beer equation to obtain compensation curves (solid lines). (b) The experimental (raw) SFG spectrum of Pt(1 1 1) in the presence of 200 mbar of CO at 300 K (open circles) is plotted together with the corrected spectrum (black dots) and the corresponding gas-phase compensation curve (solid line); adapted from (*151*) with permission. Copyright (2001) American Chemical Society.

According to Eq. (4), the amplitude of the SFG signal depends on the adsorbate concentration and also on the IR and Raman transition moments. Because the latter two terms are usually different for different adsorbate species (e.g., bridging vs. terminally bonded CO (*152*)) and may even depend on coverage, (*150,153*) the SFG signal cannot be easily correlated with the adsorbate concentration. This limitation is, however, not a drawback specifically of SFG, inasmuch as the same also holds for IR spectroscopy (apart from the Raman contribution, of course); thus, a direct quantitative analysis of different adsorbed species is usually difficult (*17*).

The IR absorbance of an adsorbed layer typically depends on coverage, often leading to the absorption maximum even well below the saturation coverage (*17*). However, in a low-to-medium coverage regime, a quantitative analysis of IR spectra may still be successful, whereas in SFG, one has to cope with the additional Raman contribution. An example is presented in Section IV.C. Nevertheless, attempts to place SFG on a quantitative basis are increasing (*153–155*).

The lineshape of an SFG spectrum may sometimes also be quite different from that observed by IR spectroscopy, because of the interference of the resonant SFG signal with the nonresonant background (Eq. (3)) (*126,141,156*). Depending on the amplitudes (A_R and A_{NR}) and the phase shift (Φ), the SFG lineshape may be strongly asymmetric. However, the resonant SFG signal is often much greater in intensity than the nonresonant background, producing almost Lorentzian-like lineshapes in the spectra. In most of the investigations described below, the nonresonant background was small, with a phase leading to rather symmetric SFG peaks. Further details of SFG intensities and lineshapes are discussed in Section IV.C and in Reference (*153*).

A.3. *Design of an SFG Spectrometer*

Because the second-order nonlinear optical process of SFG generally produces only a small signal, high-incident light intensities (i.e., pulsed lasers) are required. A number of SFG spectrometers, incorporating Nd:YAG, Ti:Sa, or free-electron lasers, have been described in detail (*116,119,122–124,126,138–144,157*). For example, a Nd:YAG-based "scanning" system is described here and depicted schematically in Fig. 7. The output of a Nd:YAG picosecond laser (1064 nm, 25 mJ/pulse, 25 ps, 50 Hz) is partly converted to 532- and 355-nm light by a second- and third-harmonic generator (SHG, THG). About 200 μJ/pulse, 532-nm light is used as a visible beam in the SFG experiment; the 1064- and 355-nm beams are mixed in an optical parametric generator/amplifier (OPG/OPA) to generate tunable IR light (3–6 μm, *ca.* 200 μJ/pulse, resolution ~5 cm^{-1}) in a difference frequency generation (DFG) stage. A strong reduction of the transmission of the DFG $AgGaS_2$ crystal at wavenumbers below 2000 cm^{-1} typically limits the frequency range to greater than approximately 1600 cm^{-1}. New DFG crystals (such as $AgGaSe_2$) are able to extend the range down to ~1000 cm^{-1}. The IR frequency can be calibrated to an accuracy of about ±1–2 cm^{-1} by measurements of the absorption bands of, for example, CO at high-pressure (absorption minimum at 2143 cm^{-1}) or of atmospheric CO_2 (at approximately 2350 cm^{-1}).

"Routine" SFG experiments are usually carried out with parallel-polarized IR and vis beams oriented at about 55° and 50° to the surface normal, respectively

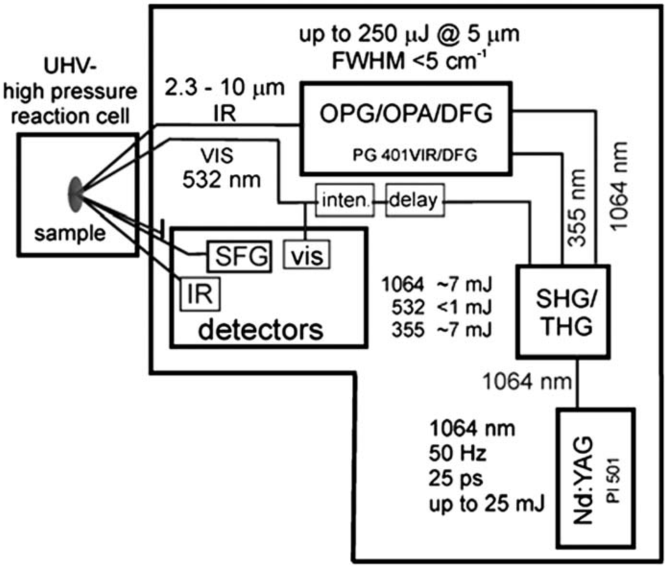

Fig. 7. Schematic illustration of an SFG spectrometer based on a Nd:YAG picosecond laser system.

(Fig. 5) (*118,151*). The difference in the incident angles is necessary to separate the SFG signal from the reflected pump beams by an aperture. However, even with a high-power laser system (producing a surface power density on the order of 1 GW/cm^2), the absolute SFG intensity is low. For example, in the case of CO on Pt(1 1 1) 10^{14}–10^{15} photons per pulse of incident light produce only a few counts in the detector (detector sensitivity ~0.1%). Therefore, a combination of spatial, spectral, and temporal filtering is required to remove contributions from the reflected pump beams (Fig. 5). The signal is filtered by an edge filter and a monochromator (both remove the 532-nm light and allow only the SFG light to pass) before it reaches a photomultiplier, the signal of which is directed to a gated boxcar integrator and sent to a PC via an A/D interface. A typical SFG spectrum (over a range of *ca.* 500 cm^{-1}) takes about 15–30 min to collect, depending on the type of adsorbate and coverage. Other modes of operation, for example, broadband techniques (*146,158*) and time-resolved SFG (pump-probe experiments) giving access to surface dynamics, (*148,157,159*) are treated in the following sections. The use of free-electron lasers allows the extension of the frequency range to the far-IR for characterization of metal-adsorbate vibrations (*140*).

A.4. *SFG-compatible UHV-High-pressure Reaction Cells*

To combine optical SFG spectroscopy with the more traditional surface analysis methods (e.g., LEED, AES, TPD, XPS), the basic requirement is to simply add IR-transparent windows (e.g., CaF_2 or BaF_2) to a UHV chamber. However, if SFG spectroscopy is to be carried out at high pressure or during catalytic reactions, instruments combining a UHV surface analysis system with an SFG-compatible

UHV-high-pressure reaction cell are preferable. Such an instrument that has been successfully applied for several years is shown in Fig. 8 (*48,84,118*). The UHV section (1×10^{-10} mbar) is equipped with tools for sample preparation (Ar ion gun, metal evaporator, quartz crystal microbalance) as well as sample characterization by LEED, AES, and thermal desorption spectroscopy (TDS). After analysis of the model catalysts under UHV, the samples are transferred (still under UHV) to the SFG cell. When the manipulator is lowered to the SFG level, the sample holder is

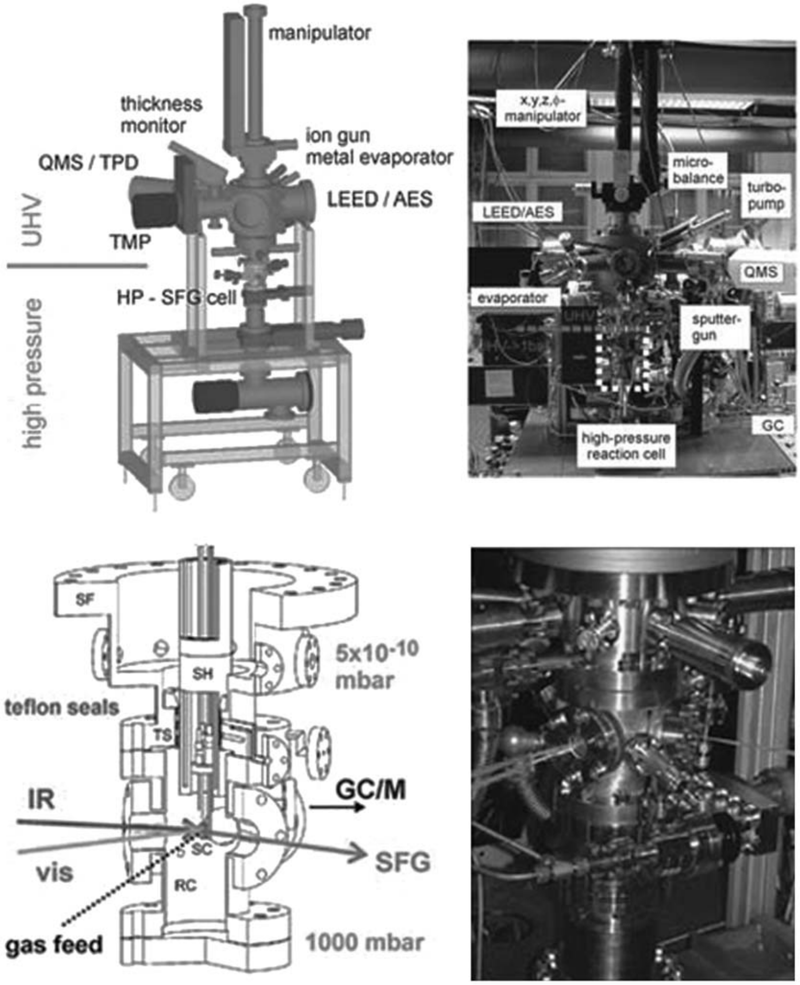

FIG. 8. (top) Experimental apparatus combining a UHV surface analysis chamber and an SFG-compatible UHV-high-pressure reaction cell. Pre- and post-reaction surface analysis under UHV can be performed by LEED, AES, and TDS. (bottom) Magnified cross section of the high-pressure cell showing the sample holder (SH), the sealing flange (SF) housing the differentially pumped spring-loaded Teflon® seals (TS), and the reaction cell (RC). A single crystal (SC) is spot welded to the sample holder that is inserted into the Teflon® seals (*48, 118*).

inserted into an arrangement of three differentially pumped spring-loaded Teflon seals, and the SFG cell is separated from the UHV part. The SFG cell can then be pressurized up to 1 bar, while the UHV chamber can still be kept at 5×10^{-10} mbar. The advantage of this design is that the sample is permanently attached (spot welded) via tantalum wires to two molybdenum rods providing good electrical and thermal contact. To minimize gas-phase absorption inside the high-pressure cell as much as possible, recessed windows reducing the IR path length are used.

Figure 9 shows a second SFG cell utilizing another transfer mechanism (*48,160*). In this case, the sample is mounted on a sample car that can be moved from the UHV chamber to the SFG cell with a magnetically coupled transfer rod. The high- and low-pressure sections are then separated by a gate valve. The advantage of this design is that several samples (sample cars) can be "stored" inside the UHV chamber (in a revolving "park deck"), allowing investigation of several samples without breaking of the vacuum. Furthermore, by use of a "load lock," new samples can be installed without venting of the whole UHV chamber.

In each of the SFG cells, the sample can be resistively heated to about 1300 K, and cooled with liquid N_2. To apply low exposures in UHV experiments, leak valves and ionization gauges are also connected to the SFG cells. CaF_2 windows are typically used to allow IR and visible light to enter and to allow sum frequency light to exit to the detector. The large CaF_2 windows (clear aperture 5 cm) of the cell in Fig. 9 even allow 2-IR 1-vis SFG (i.e., in this case, two IR beams can be overlapped with one visible beam and two different spectral ranges, such as C–O and C–H, can be observed simultaneously) (*160*). For catalytic tests, the SFG cells serve as recirculated batch reactors that are interfaced to a gas chromatograph for product analysis. To minimize wall reactions, the cells should be gold coated. After completion of kinetics measurements or high-pressure gas exposure, the samples are transferred back to the UHV section for post-reaction surface analysis.

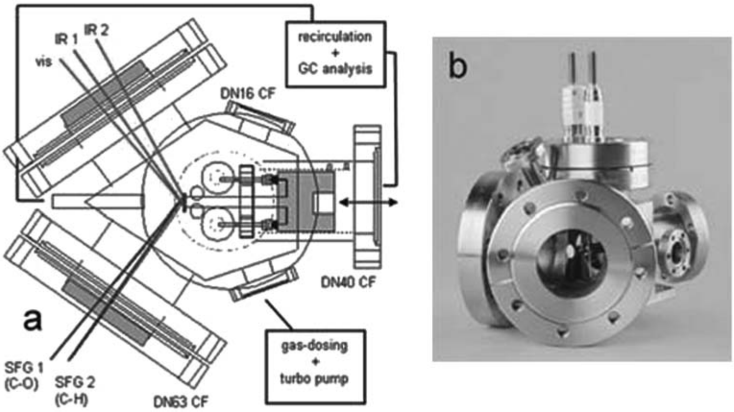

FIG. 9. An SFG-compatible UHV high-pressure reaction cell that allows the performance of 2-IR 1-vis SFG experiments (*48,160*). Three noncollinear laser beams (two IR, one visible beam) are spatially and temporally overlapped on the adsorbate/substrate interface, which allows simultaneous monitoring of two different spectral regions (reflected pump beams are not shown).

B. Polarization–Modulation IR Reflection Absorption Spectroscopy

B.1. *Basics*

IR spectroscopy is the most widely used technique to characterize catalysts and molecules adsorbed on them. It has been successfully applied to dispersed catalysts as well as to planar model catalyst. Comprehensive reviews by Sheppard and De la Cruz (*18,19*), Hoffmann (*17*), Chabal (*161*), and others (*162*) describe the basics, technical aspects, and applications of the technique to a variety of catalysts (considering, for example, catalyst preparation, activation and rejuvenation, and the state of the catalyst during the course of a catalytic reaction). The reader is referred to these reviews for details; here, we focus on recent developments and high-pressure applications.

Compared with SFG, IR spectroscopy offers advantages in the spectral range ($\sim$800 to 4000 cm^{-1}) and resolution ($<1\,\text{cm}^{-1}$) and in the acquisition time (several minutes) and thus in the signal-to-noise (S/N) ratio. Furthermore, SFG generally requires more maintenance and thus has higher running costs (flashlamps, dye, etc.) than PM-IRAS.

A sample of a supported metal (powder) for transmission IR spectroscopy is often made by pressing a few hundred milligrams of catalyst into a thin, self-supporting wafer. For a catalyst with a high metal dispersion (e.g., 90%), even a 1% metal loading produces a metal surface area of the order of several thousand square centimeters. If all of the metal contributes to the transmission IR spectrum, an acceptably strong surface signal can be obtained. In favorable cases, surface and gas-phase contributions to the vibrational spectrum can be differentiated, even in a mbar pressure range (e.g., by subtracting the gas-phase spectrum from the sample + gas-phase spectrum). However, the diffusion resistance to the molecules in the sample wafer may limit the intensity of the signal of adsorbed species.

IR spectra of a planar model catalyst can be acquired in reflection mode at gracing incidence (the dependence of the surface effective field on the incidence angle and polarization is described in Reference (*17*)). However, because the exposed metal area is typically $<1\,\text{cm}^2$, the surface signal is orders of magnitude smaller than the gas-phase absorption. Any reflectance IR spectrum is therefore dominated by the absorption of the gas molecules (Fig. 4). Of course, one can measure the gas-phase spectrum, which can then be subtracted from the sample + gas-phase spectrum. Gas-phase spectra can be obtained, for example, by acquiring spectra of the ‘‘hot’’ sample (i.e., at a high enough sample temperature that no adsorbates should be present) or of an inert sample (one not adsorbing the gas under investigation).

However, on a metal surface there is another (better) possibility, as illustrated in Fig. 10. If the spectrum is taken with s-polarized IR light (with the electric field vector parallel to the surface), the electric field is canceled at the surface and only the gas-phase absorption contributes to the spectrum (*17*). A spectrum acquired using p-polarized light (with the electric field vector nearly perpendicular to the surface) contains both the surface and gas-phase absorptions. Consequently, two spectra (in p and s polarization) must be measured and subsequently subtracted

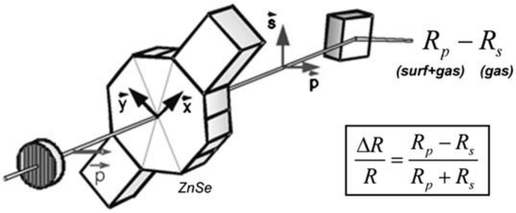

FIG. 10. Schematic illustration of polarization-modulated IR reflection absorption spectroscopy (PM-IRAS).

(both polarization states are equally sensitive to gas-phase absorption and the s-signal thus provides an online gas-phase reference). Unfortunately, because of the weak surface signals of a planar model catalyst, an accurate subtraction is still difficult if the spectra are measured one after another, in particular, in light of instabilities of the spectrometer and/or changes of the sample that occur on the timescale of a typical measurement (10–15 min).

The ploy to resolve this issue is to acquire the p (surface and gas-phase absorption) and s (gas phase) spectra simultaneously (or, at least, nearly simultaneously). This measurement can be achieved by polarization modulation (PM) (*163,164*) of the incident IR light using a fast photoeleastic modulator (PEM) that rapidly modulates the polarization state of the gracing incidence IR beam between p-polarized light and s-polarized light (Fig. 10). The PEM consists of a ZnSe optical element, enclosed between two quartz piezoelectric transducers. An electric field oscillating at $\omega = 37$ KHz is applied to the quartz crystals, resulting in strain with a broad maximum at the center of the ZnSe crystal. Therefore, orthogonal linear polarizations have different velocities after passing through the ZnSe crystal. As a result, the polarization of the transmitted beam is modulated between s- and p-polarization. After demodulation, a differential reflectivity spectrum $\Delta R/R$ is obtained, which constitutes the adsorbate vibrational spectrum whereas no bulk (gas-phase) species are detected, and there is no need for any further gas-phase correction.

An advantage of PM-IRAS over SFG is that PM-IRAS provides IR surface spectra (p–s) and gas-phase spectra (s) in parallel.[4] Thus, the catalytic turnover can be followed not only by gas chromatography, but also by PM-IRAS (cf. Figs 45 and 53). The efficiency of PM-IRAS has been demonstrated both with dispersed and Fourier-transformed IR spectrometers in the characterization of various metal surfaces (*114,164–177*).

B.2. *High-Pressure Reaction Cells for PM-IRAS and Experimental Design*

Figure 11a shows an instrument designed for applying PM-IRAS to model catalysts (*84,113*). The requirements are similar to those described for SFG. The

---

[4] Because the IR absorption of surface species is typically very weak (as compared to gas phase absorption), "p + s" spectra are often called "gas-phase" spectra below.

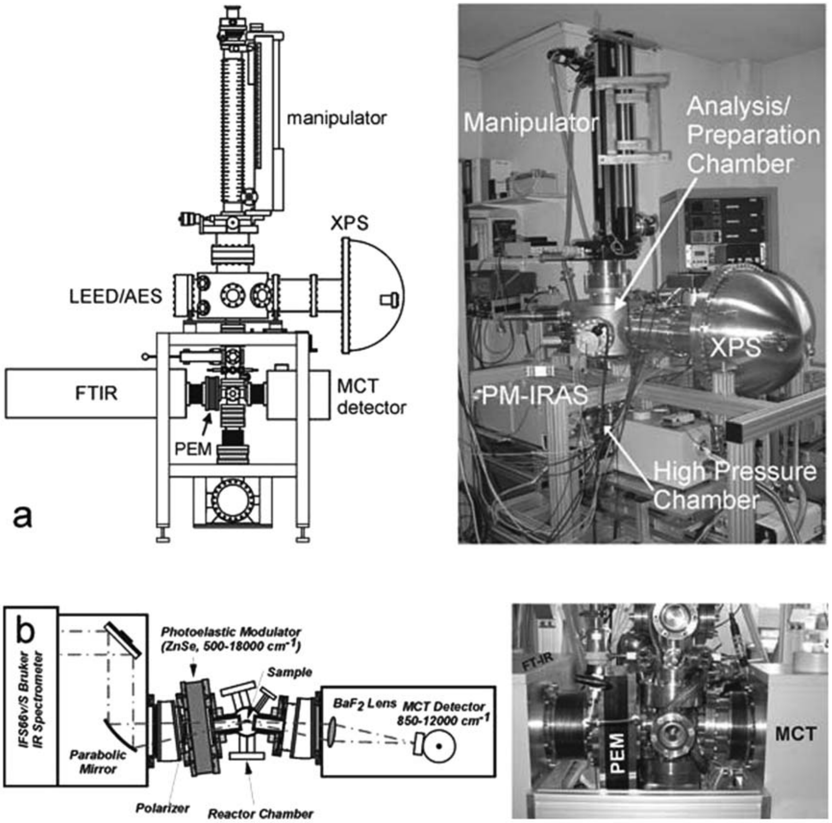

FIG. 11. (a) Experimental apparatus combining a UHV surface analysis chamber with a UHV-high-pressure reaction cell optimized for PM-IRAS spectroscopy. Pre- and post-reaction surface analysis under UHV can be performed by XPS, LEED, AES, and TDS. The optical equipment and the high-pressure cell used for the PM-IRAS experiments are shown in (b) (*84,113,114,171*).

apparatus again combines a UHV preparation and characterization chamber with a UHV-high-pressure reaction cell, this time optimized for PM-IRAS (i.e., the windows must allow grazing incidence geometry). This instrument is additionally equipped with the capability for XPS (Specs Phoibos 150 using MgKα with a resolution of ~1 eV), which is used together with LEED and TDS for pre- and post-reaction analysis.

Figure 11b shows the optical apparatus for PM-IRAS with the high-pressure cell and the photoelastic modulator (PEM) (Hinds-PEM-90) located between the vacuum FTIR spectrometer (Bruker IFS66v/S) and the detector (*113,171*). By the use of recessed windows, the IR path length inside the high-pressure cell is reduced to minimize gas-phase absorption. To avoid interference from atmospheric H_2O and CO_2, the IR spectrometer and beam path are evacuated, and only the PEM is purged with dry nitrogen. The IR spectrometer produces a parallel beam of about 40 mm diameter, which is focused on the sample by a parabolic mirror (250 mm focal length). Before entering the high-pressure cell, the IR beam is polarized via a metal grid polarizer and passed through the PEM (Fig. 10). After reflection from the sample, the beam is collected with a ZnSe lens into a nitrogen-cooled photovoltaic HgCdTe detector mercury cadmium telluride (MCT). The detector signal is finally sent to a demodulator that generates the sum and difference interferograms required for the $\Delta R/R$ spectrum. For catalytic tests, this apparatus can also be interfaced to a gas chromatograph.

C. High-Pressure X-ray Photoelectron Spectroscopy

C.1. *Introductory Remarks*

By analyzing the kinetic energy of photoelectrons (E_{kin}) produced by irradiating a surface with X-rays ($h\nu$), the binding energy (BE) of the photoelectrons can be determined ($\mathrm{BE} = h\nu - E_{\mathrm{kin}}$), allowing a chemical analysis of the surface *(30,33,178)*. Furthermore, in the presence of adsorbates, XPS allows one to distinguish, for example, molecular CO (C1s BE of ~286 eV) from amorphous/graphitic carbon (~284 eV). Moreover, XPS can differentiate between the various binding geometries of adsorbates (e.g., bridging and terminal CO) *(179–183)*. An advantage of XPS over SFG and PM-IRAS is that it also detects species that typically are not represented in a vibrational spectrum (such as carbon deposits); further advantages are its high sensitivity and ability to detect subsurface species, and it is also well suited to the determination of quantitative information. Consequently, the PM-IRAS chamber of Fig. 11a was equipped with XPS.

However, as an electron spectroscopic technique, core-level XPS is typically operated under UHV (or at pressures up to 10^{-6} mbar) and generally not suited to elevated pressure measurements. Of course, XPS can be used for pre- and post-reaction analysis if the surface species are stable (such as carbonaceous layers). However, if the adsorbed species are in equilibrium with the gas phase, they desorb upon evacuation, and the limitations discussed in the introduction are significant. It is preferable to carry out XPS under reaction conditions, at mbar pressures.

Early so-called high-pressure XPS investigations were performed by Roberts, Joyner, and coworkers in the late 1970s *(184–186)*. Using a specialized spectrometer construction (see below), they increased the working pressure up to 0.1−1 mbar, at least 5 orders of magnitude greater than the pressures of conventional XPS. The instrument was built by Vacuum Generators Co. (VG ESCALAB), and a second instrument was installed at the Boreskov Institute of Catalysis in Novosibirsk *(187)* (the HP-XPS data cited below were acquired with that instrument). Recently, the interest in HP-XPS has been revived, and improved apparatus was developed by the groups of Salmeron *(188)*, Schlögl *(189,190)*, and Steinrück *(191,192)*. More details are to appear in the next volume of *Advances in Catalysis* *(9)*.

C.2. *High-pressure Reaction Cells for XPS*

The XPS apparatus is described briefly here. The mean free path of electrons at ~1 mbar pressure is a few millimeters *(185)*. Consequently, if the path length of the photoelectrons can be reduced to this range, XP spectra can be acquired. The key goal is to produce a strong pressure gradient normal to the sample surface, so that the photoelectrons travel only a short distance through the mbar pressure surrounding the sample surface before they enter a vacuum zone. This goal can be achieved by using a number of differential pumping stages. Differential pumping of the energy analyzer and X-ray tube with diffusion pumps allows the sample pressure to be raised from UHV to $\sim 10^{-4}$ mbar. By insertion of a specialized gas cell into the UHV chamber (which provides another differential pumping stage surrounding the sample), the pressure can be increased up to 0.1 mbar (*193,194*).

The high-pressure XP spectra shown below were taken by using nonmonochromatized AlKα irradiation ($h\nu = 1486.6$ eV) with constant analyzer pass energy and a resolution of about 1.2 eV. The spectrometer was calibrated by using the Au4f$_{7/2}$ BE of 84.00 eV and the Cu2p$_{3/2}$ BE of 932.6 eV as references. The take-off angle between the analyzed photoelectrons and the substrate surface was 70°, with an X-ray incidence angle of 20°. The XPS intensity decreases by 20–30 times relative to that of UHV XPS, leading to collection times of about 2–3 h at $\sim$0.1 mbar, compared with approximately 30 min in UHV. To compensate for this effect, Bluhm, Ogletree, and coworkers (*61,188–190*) developed a differentially pumped electrostatic lens system, which collects the photoelectrons and focuses them into the object plane of a hemispherical energy analyzer (in other words, they increased the nominal collection angle of the detector). Thus, acquisition times comparable to those of UHV measurements were achieved. Synchrotron radiation improves the spectral resolution and also reduces acquisition times (*61,183,195*).

D. High-Pressure Scanning Tunneling Microscopy

Knowledge of the exact surface structure of a model catalyst is another important prerequisite for the types of fundamental investigations described here. For single-crystal surfaces, electron (LEED, RHEED) and atom (He) diffraction have typically been used to determine surface structure under UHV (*33,196*). These methods work well for systems with long- or medium-range order but are rather insensitive to local inhomogeneities (such as surface defects or small disordered domains), which can be important for catalysis. Furthermore, diffraction techniques provide a reciprocal space representation that typically requires modeling and calculation of diffraction intensities for interpretation, and a given structure cannot always be unambiguously identified. For structural characterization of UHV-grown nanoparticle samples, TEM was sometimes used, but the characterizations included sample transfer through air, which might have led to restructuring of the metal particles (*48,54,74,77,197,198*) (see below). Diffraction techniques can also be applied to (ordered) arrangements of adsorbed molecules, but the above-mentioned limitations still hold (local inhomogeneities may be undetected). In comparison, SFG, PM-IRAS, and XPS probe surface bonding, (nearly) regardless of order, but the exact assignment to a specific adsorption site is often difficult (*199,200*).

The advent of scanning probe microscopy in the mid-1980s, in particular of STM, has helped to overcome these limitations and was therefore a major breakthrough (*201,202*). In ideal cases, STM allows monitoring of the atomic structure of a (single crystal) surface as well as the arrangement of adsorbed (ordered and disordered) molecules in real space (e.g., see References (*86,203,204*)). Although STM images the tunneling probability at a position on a specimen, images can often be interpreted as being "atomic snapshots." As another major advantage, STM can be applied not only to single crystals but also to nanoparticle model catalysts (*34,73,77,101,205–210*). Consequently, investigations that were previously carried out by TEM (e.g., of nucleation and growth of metal particles, structural changes and sintering, oxidation/reduction, etc. (*74,77,197,198,211*)) can now be carried out in reactive atmospheres by STM. Recent improvements in the acquisition speed ("fast-STM") even allow recording of atomically resolved real-time movies of catalytic processes at low pressures ($<10^{-7}$ mbar) (*212–214*). The identification of adsorbed molecules by STM is not always straightforward, however, and parallel spectroscopic investigations (IRAS, XPS) are advisable to identify species.

With respect to the Pd/Al_2O_3 model catalysts described below, STM was used to examine the structure of the Al_2O_3 support and the nucleation and growth of metal deposits (e.g., References (*34,63,73,101,215*) and references cited therein), providing information about the size, shape, and height of palladium nanoparticles. In some cases, even atomically resolved images of individual palladium nanoparticles were obtained (*206*).

STM is mostly applied under UHV, but it can also be used at high gas pressures when the adsorbate is in equilibrium with the gas phase (see the chapter by the Besenbacher group in this volume (*115*)). The proximity of the probe (in the most favorable case a single-metal atom at the apex of the STM tip) and the sample, which are separated by just a few Angstroms, allows one to ignore the bulk of the high-pressure gas environment. The STM tip can remain in tunneling range when the pressure is increased, so that the same sample area can be imaged at various pressures. The first high-pressure STM instrument applied to the study of chemisorption and catalytic reactions was developed by Somorjai, Salmeron, and coworkers, (*216–219*) and similar and improved instruments were developed by other groups (*204,210,220–222*).

In the context of this chapter, STM data of (co-)adsorbed molecules under UHV and at elevated pressures provide complementary information. When available, such investigations were included here and are briefly discussed. Applications of STM in related fields are numerous; one fascinating example is single-molecule spectroscopy by inelastic tunneling spectroscopy (IETS) (*223–225*).

E. Environmental Transmission Electron Microscopy

Before the introduction of STM, high-resolution (HR-)TEM was the primary technique for determination of the surface structures of nanoparticle model catalysts (*14,54,74,77,197,198,211,226–230*). For technological catalysts, it is still the only method that provides a direct atomic-scale characterization of metal nanoparticles and of the oxide support (*211,231–238*). Although TEM is unable to detect adsorbed molecules (in contrast to the methods discussed above), it is briefly mentioned here because HR-TEM was sometimes employed to corroborate STM data characterizing model catalysts and, in particular, to demonstrate the internal

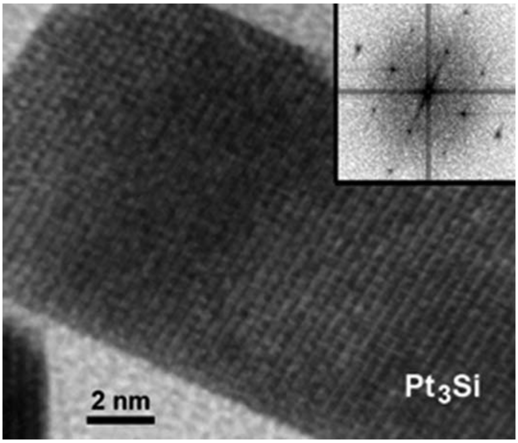

FIG. 12. HRTEM image and Fourier transform of a Pt_3Si nanoparticle observed after heating a Pt/SiO_2 model catalysts in H_2 to 873 K for 1 h (*247,248*).

structures of metal nanoparticles (Fig. 12). Furthermore, TEM methods were used to characterize various catalysts made by impregnation, which provided the basis for a meaningful comparison between real and model catalysts.

The major drawback of TEM is that it is typically used to characterize samples transferred to a microscope before or after a high-pressure gas exposure or catalytic reaction. Although sample transfer devices/holders have been developed that enclose the sample in a controlled atmosphere (e.g., argon), structural changes during the transfer can still not be fully excluded.

This limitation has been overcome by the development of electron microscopes that operate in the low mbar pressure range (*239–243*) (see the chapter by Hansen *et al.* in the preceding volume of *Advances in Catalysis* (*8*)). The catalyst sample is enclosed in a small housing ("environmental cell"), which has either small apertures or windows to allow the electron beam to pass through the specimen. As in high-pressure XPS, differential pumping allows a local pressure of the order of 1 mbar surrounding the sample, while the rest of the instrument still operates under high vacuum. High-resolution imaging and electron energy loss spectroscopy (EELS) can then be carried out at mbar pressures to determine structural and compositional changes induced by the gas environment (*244,245*). To date, primarily the effects of oxidizing or reducing atmospheres on the particle morphology and surface structure have been investigated (*241*). TEM investigations of working catalysts combined with kinetics measurements of the catalyst sample in the TEM may follow in the near future (*246*).

IV. Spectroscopy of Model Catalysts at Pressures Exceeding Ultrahigh Vacuum

This section is a summary of recent high-pressure investigations of model catalysts. The focus is on vibrational spectroscopy but, when data are available, complementary methods are briefly mentioned to provide a more complete picture of the processes. Investigations of adsorption are treated first, followed by investigations of coadsorption and catalytic reactions. Then the potential of polarization-dependent and time-dependent SFG measurements is illustrated with examples.

A. CO Adsorption at Pressures from Ultrahigh Vacuum to 1000 mbar: Introductory Remarks

The adsorption of CO is probably the most extensively investigated surface process. CO is a reactant in many catalytic processes (methanol synthesis and methanation, Fischer–Tropsch synthesis, water gas shift, CO oxidation for pollution control, etc. (*1,3–5,249,250*)), and CO has long been used as a probe molecule to "titrate" the number of exposed metal atoms and determine the types of adsorption sites in catalysts (*27,251*). However, even for the simplest elementary step of these reactions, CO adsorption, the relevance of surface science results for heterogeneous catalysis has been questioned (*43,44*). Are CO adsorbate structures produced under typical UHV conditions (i.e., by exposure of a few Langmuirs ($1\,\mathrm{L} = 10^{-6}\,\mathrm{Torr\,s}$) at $100-200\,\mathrm{K}$) at all representative of CO structures present under reaction conditions? How good are extrapolations over 10 or more orders of magnitude in pressure? Such questions are justified, because there are several scenarios that may account for differences between UHV and high-pressure conditions. Apart from pressure, attention must also be paid to the temperature.

In the temperature range of catalytic reactions (typically $>300-400\,\mathrm{K}$), the pressures usually applied in UHV investigations ($<10^{-6}\,\mathrm{mbar}$) may not be sufficient to produce the surface coverage required for a specific reaction. If the required active species is weakly bound, it may appear only at high pressure (close to saturation coverage) after all the more strongly adsorbing sites are already occupied by spectator species. Consequently, such species may be missed in UHV investigations (*46*). Of course, high coverages can also be obtained under UHV, but generally only at low temperatures (e.g., 100 K), and under these conditions, the low mobility of the adsorbed CO molecules may produce kinetically "trapped" adsorbate species, and the surface reaction may proceed in a way that may not be relevant for catalysis. It has also been suggested that high pressures may be able to give coverages that exceed the UHV saturation coverage, thereby producing new adsorbate structures that cannot even be reproduced under UHV. The occurrence of such "high-pressure species" would have a dramatic impact, shattering the foundation of the surface science approach to understanding catalysis.

Furthermore, because catalysts may undergo restructuring at elevated pressures and temperatures, (*14,15,48,51,216,222*) or even undergo changes in composition (*55,60,252*), the availability and nature of adsorption sites and adsorbate geometries at mbar pressures may be different from those existing under UHV, and the most incisive characterizations are those of catalyst under reaction conditions.

Vibrational spectroscopies such as IRAS and SFG are among the most successful techniques for investigation of the interactions of CO with metal surfaces; the techniques are facilitated by the high dynamic dipole moment of CO. The observed

CO stretching frequency is in many cases characteristic of the binding site, allowing one to differentiate between adsorption on three and fourfold hollow sites, bridge sites, on-top sites, steps, etc. (*17–19*). One should keep in mind, however, that this differentiation may not always be possible, in particular, when strong adsorbate–adsorbate interactions occur or when coadsorption of multiple species occurs (*199,200*).

B. GAS PURITY—PRECAUTIONS FOR EXPERIMENTS AT PRESSURES EXCEEDING UHV

The cleanliness of gases is critical. Although gas purification is often routinely applied for investigations of technological catalysts (e.g., by using the same or another catalyst to adsorb impurities before they reach the operating catalyst), such procedures are rather uncommon in surface science investigations, because only low pressures of high-purity gases are exposed to the model catalysts. However, impurity levels in the range of 10^{-3}% (present, for example, in "high-purity" 99.997% CO) that can be neglected for exposures of a few Langmuirs become significant at pressures of about 1 mbar (*120*). In particular, care has to be taken to avoid contamination by nickel or iron originating from nickel carbonyls and iron carbonyls produced by reaction of CO with the walls of steel gas cylinders. Figure 13a, trace (1), shows a mass spectrum taken from 1 mbar 99.997% CO without further purification. Gas sampling was made using a quartz capillary inlet connected to a differentially pumped mass spectrometer (*120*). Nickel carbonyls were identified that would decompose on the sample, leaving behind dispersed nickel. Figure 13b presents corresponding AE spectra of a clean Pd(1 1 1) surface (trace (3)) and the surface after exposure to "as-received (uncleaned)" 99.997% CO gas (>200 mbar) for several hours (Fig. 13b, trace (4)). Characteristic nickel signatures can be identified at 715, 782, and 847 eV, and the attenuation of the palladium signal depends on the amount of nickel. If CO then adsorbs on the nickel contaminant, peaks may be observed at 2020–2070 cm^{-1} (depending on the CO coverage (*118*)), which could be misinterpreted as "high-pressure species."

Iron carbonyls present a similar problem. Figures 13c and d show Fe2p and C1s XP spectra, respectively, measured at 400 K when 99.997% CO was used without further purification at various pressures. The Fe2p signals originate from the decomposition of iron carbonyls (*253*). Of course, nickel and iron deposits also change the chemical properties of a surface, for example, they may act as centers for CO dissociation. Figure 13d shows that on a contaminated surface, iron carbides, carbonaceous species, and metal carbonyls were present in addition to molecular CO. This result clearly shows that careful removal of impurities and also a compositional surface analysis are invariably needed for every high-pressure experiment.

Nickel and iron impurities can be removed by passing CO over a carbonyl absorber cartridge and through a cold trap filled with a liquid nitrogen/ethanol mixture (~170 K) (*120*). After passage through these traps, no impurities were detected with a differentially pumped mass spectrometer, or by AES or XPS (Fig. 13a, trace 2). A dedicated gas cleaning system is also described in Reference (*220*).

Water traces at high pressures constitute another problem, in particular, when experiments of long duration are carried out at temperatures below the desorption

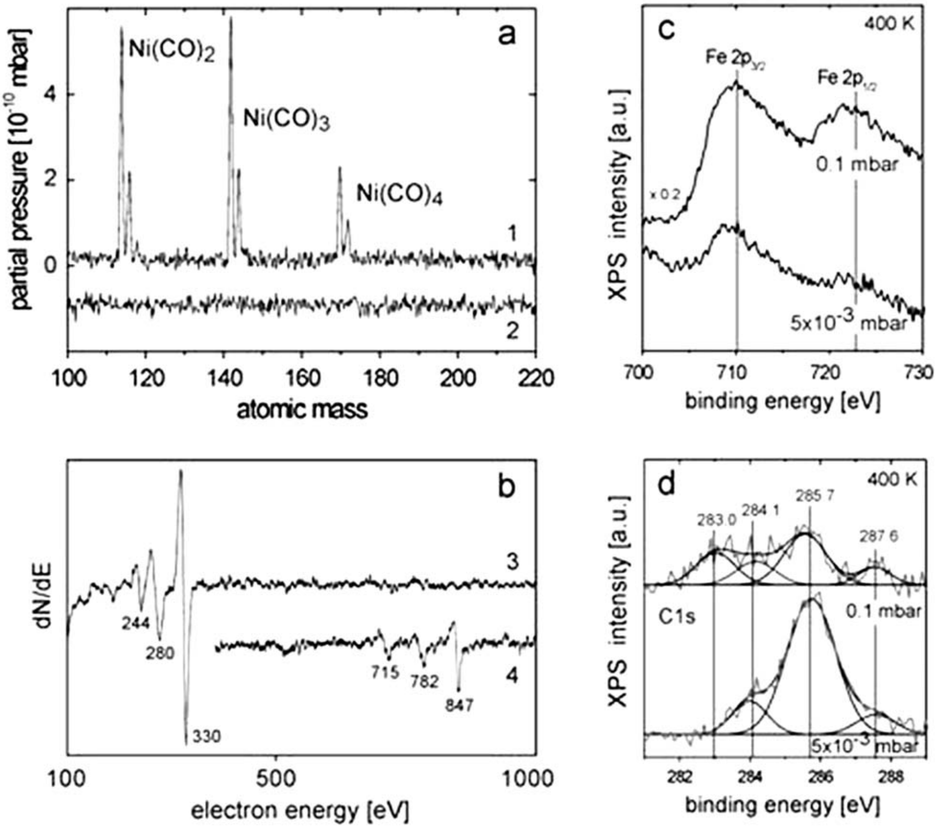

FIG. 13. (a) Mass spectra taken from 1 mbar 99.997% CO using a quartz capillary inlet to a differentially pumped mass spectrometer (1) and after passage of CO through a carbonyl absorber cartridge and a cold trap (2). (b) Auger spectra of Pd(1 1 1) (3) and after exposure to 99.997% CO (> 200 mbar) for several hours (4) demonstrating nickel contamination; adapted from (*120*) with permission from Elsevier. Fe2p (c) and C1s (d) core-level XP spectra obtained when CO was used without purification at 400 K, at 5×10^{-3} mbar and 0.1 mbar. Results of deconvoluting the C1s spectra are also shown: 283.0, carbide species (FeC); 284.1, graphite; 285.7, molecular CO; 287.6, metal carbonyl species; adapted from (*253*) with permission. Copyright (2003) American Chemical Society.

temperature of water (~160 K for platinum and ~175 K for palladium). For example, with CO/Pt(1 1 1), it was observed that coadsorbed water induced a 15-cm^{-1} redshift of the on-top CO frequency (*151*) that could also be wrongfully interpreted as high-pressure species. It is hence advantageous to carry out elevated pressure experiments at 190 K or higher temperatures. These temperatures also facilitate a CO mobility that is sufficient to avoid nonequilibrium layers with "kinetically trapped" CO molecules (*121*).

Gas cleanliness is particularly crucial when molecules with small sticking coefficients are examined (e.g., H_2 on copper (sticking coefficient ~3×10^{-11} at 298 K), (*204,220*) since even small amounts of CO or other impurities dominate adsorption because of their much higher sticking probabilities.

C. CO Adsorption and CO–H_2 Interactions on Pd(1 1 1) and Pd/Al_2O_3

Palladium is one of the most frequently used metals in heterogeneous catalysis, used for hydrogenation as well as oxidation reactions. As discussed below, a variety of palladium model catalyst surfaces were used to characterize CO adsorption and the coadsorption and reaction of CO with hydrogen, both under UHV and at atmospheric pressure. Figure 14 shows schematic models of smooth and stepped

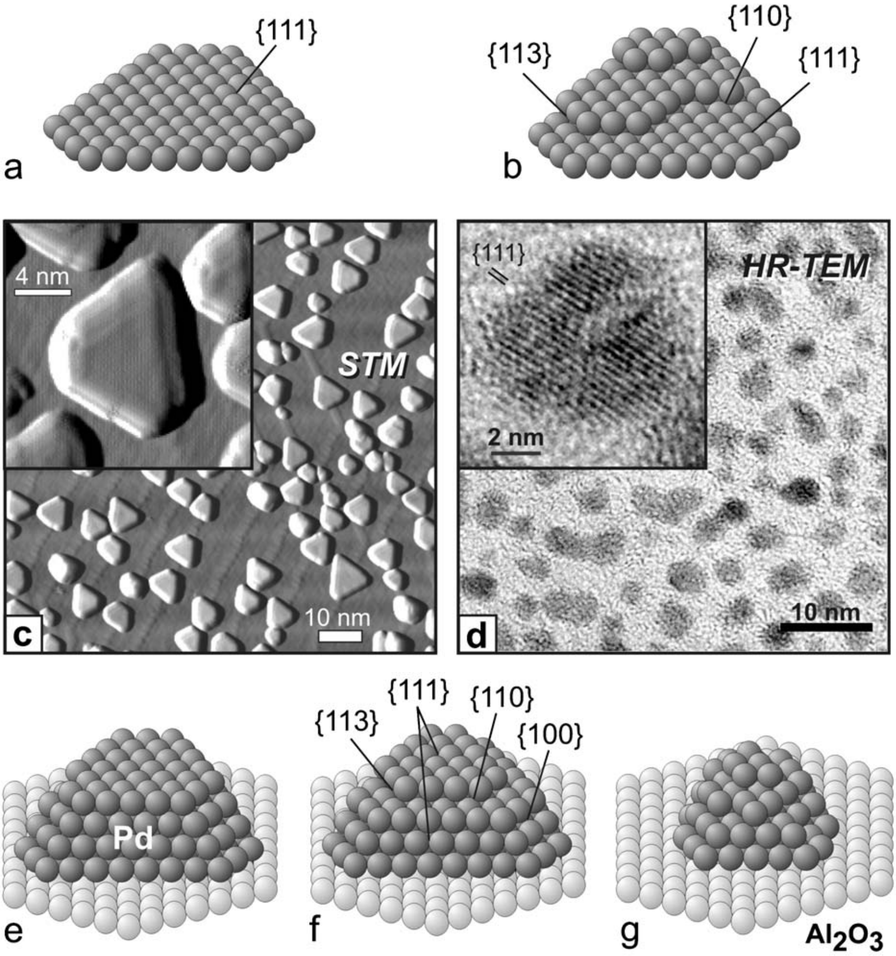

FIG. 14. Schematic illustration of palladium model catalysts used in the experiments described below: a well-ordered Pd(1 1 1) and a "defect-rich" Pd(1 1 1) surface including various defects are shown in (a,b). An STM image (100 × 100 nm, adapted from reference (*97,254*)) of palladium nanoparticles grown on Al_2O_3/NiAl(1 1 0) and transmission electron micrographs are displayed in (c, d). The insets in (c, d) show individual particles in higher magnification. Depending on the growth conditions, the palladium particles may have different morphologies and surface structures; for example, a well-faceted truncated cuboctahedron is shown in (e), with surface steps in (f), and a highly defective structure is shown in (g); adapted from (*152*) with permission. Copyright (2002) American Chemical Society.

(ion-bombarded) Pd(1 1 1), and of Al_2O_3-supported palladium nanocrystals of various surface structures, together with the corresponding STM and HRTEM images (*48,120,152*). The inset in Fig. 14c shows a well-faceted single crystalline palladium particle, and that in Fig. 14d displays a more irregular palladium particle, which exhibits both internal and surface defects. It is important that both types of surface structures are available via nanoparticle model catalysts, because nanoparticles of technological catalysts may vary in their microstructure and surface roughness, depending on preparation conditions. The exact properties of the model catalysts and the exposed surface sites are addressed below, together with the corresponding spectroscopic results.

C.1. *CO Adsorption on Pd(1 1 1) and on "Defect-rich" Pd(1 1 1)*

C.1.1. Ultrahigh Vacuum Investigations. Although inherent differences between single-crystal surfaces and facets on a metal nanoparticle do not allow a direct extrapolation of single-crystal results to heterogeneous catalysis, it is still true that single crystals provide inevitable reference information that is required to understand nanoparticle properties. CO adsorption on Pd(1 1 1) has been investigated under UHV conditions with nearly every available technique (including TDS (*255,256*), LEED (*257–262*), X-ray photoelectron diffraction (PED) (*199*), IRAS (*17,171,260,261,263–265*), XPS (*182,192*), STM (*86,266*), SFG (*120,152,265*), and density functional theory (DFT) calculations (*98,267–272*).

A variety of ordered CO structures were reported with a $(\sqrt{3}\times\sqrt{3})R30^\circ-1CO$ at 0.33 ML, a c(4 × 2)-2CO at 0.5 ML, a $(4\sqrt{3}\times 8)$rect at 0.63 ML, and a (2 × 2)-3CO at 0.75 ML being the most prominent.[5] The adsorbate layer rearranges as the coverage increases, and different adsorption sites are populated in different coverage regimes. The transitions between these regimes can produce even more complex structures (see, e.g., References (*112,121*)). As a consequence of the large number of overlayer structures, the vibrational spectrum of CO on Pd(1 1 1) might seem to be somewhat more interesting than, for example, that of CO on Pt(1 1 1) (Section IV.D).

Each CO adsorbate structure exhibits a characteristic SFG vibrational spectrum and LEED pattern. This point is illustrated in Fig. 15 for CO coverages of 0.5 ML and greater (for spectra at lower coverages, see Reference (*120*)). The coverages (θ) indicated in Fig. 15 were obtained from parallel TDS measurements (*273*). At coverages below and up to 0.33 ML, CO adsorbs in a $(\sqrt{3}\times\sqrt{3})R30^\circ$ structure on fcc threefold hollow sites with stretching frequencies of about $1850\,cm^{-1}$ (see, for example, Fig. 1 of Reference (*120*)). The binding configuration at about 0.5 ML CO is still under debate (*86,182,192,199,267*). At 0.5 ML of CO, a c(4 × 2) structure was observed, producing a single vibrational peak at $\sim 1925\,cm^{-1}$. According to PED and stretching frequency calculations (*199,267*), this structure was assigned to CO in fcc and hexagonal close-packed (hcp) threefold hollow sites. However, in a recent STM investigation, Rose *et al.* (*86*) resolved both CO molecules within the c(4 × 2)

---

[5] Here one ML equals the density of palladium atoms in the (1 1 1) plane; $1.53\times 10^{15}\,cm^{-2}$.

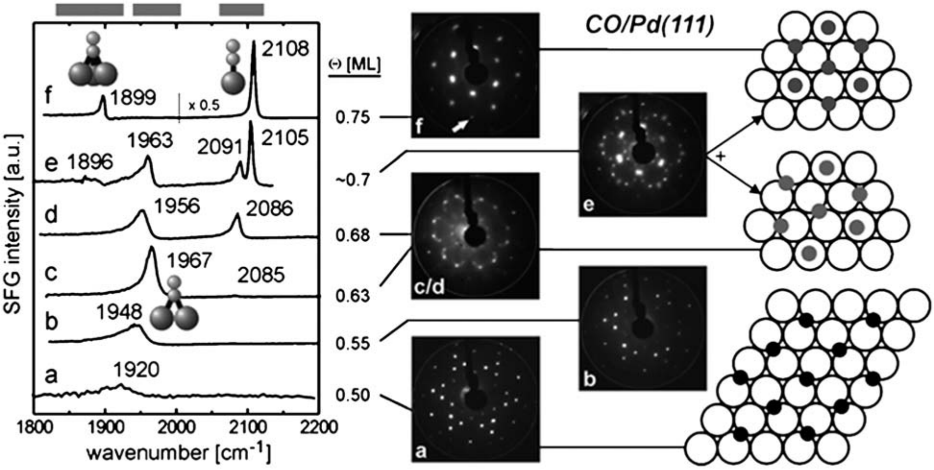

FIG. 15. SFG spectra and corresponding LEED patterns of various CO structures on Pd(1 1 1) (CO coverage indicated; approximate frequency ranges of hollow, bridge, and on-top CO indicated by bars) (*273*). The adsorbate layers can be produced by the following CO exposures: (a) 10^{-6} mbar at 350 K or 1 L at 95 K; (b) 10^{-6} mbar at 250 K or 2 L at 95 K; (c) 10^{-6} mbar during cooldown from 300 to 190 K (measurement without background gas) or 3–5 L at 95 K; (d) 10^{-6} mbar during cooldown from 300 to 190 K (measurement with background gas); (e) 10^{-7} mbar during cooldown from 300 to 90 K or 5–10 L at 90 K; (f) 10^{-6} mbar during cooldown from 300 to 90 K. The LEED pattern in (e) is a superposition of patterns (c, d) and (f). In the LEED pattern (f) one palladium substrate spot is marked with an arrow; adapted from (*273*) with permission. Copyright (2003) American Institute of Physics.

unit cell and showed that, near $\theta = 0.5$, two types of c(4 × 2) structures coexist, one with CO in fcc and hcp threefold hollow sites and one with bridge-bonded c(4 × 2) (as originally suggested on the basis of vibrational spectroscopy) (*17*). Furthermore, XPS measurements at 300 K (*182*) also indicated a coexistence of hollow- and bridge-bonded CO at $\theta = 0.5$. In the range between 0.5 and 0.6 ML, the CO peak continuously shifts to higher wavenumbers. At $\theta \sim 0.6–0.7$, CO is generally considered to be bridge bonded (and characterized by a frequency $> 1950\,\text{cm}^{-1}$) with a smaller amount of linear (on-top) CO at 2075–2085 cm^{-1}; the intensity of this band is sensitive to coverage (hollow CO cannot be fully excluded, however). When the coverage is further increased, the bridge site intensity decreases, that of the on-top signal increases, and a transition (*264*) from a bridge/on-top structure to a hollow/on-top structure occurs. At saturation (2 × 2; $\theta = 0.75$), two bands, at 1899 and 2108 cm^{-1} (fcc and hcp hollow and on-top CO), were observed (Fig. 15f).

The dosing procedure itself also strongly influences the structure of the adsorbed CO layer. A well-ordered (2 × 2) saturation structure can be obtained only by exposing the sample to a background pressure of CO at temperatures > 150 K and subsequent cooling to 100 K (Fig. 15f) (*120,121,264,265*). When CO is exposed to Pd(1 1 1) at temperatures < 120 K, "nonequilibrium structures" may be obtained, such as the one shown in Fig. 15e exhibiting hollow (1896 cm^{-1}), bridge (1963 cm^{-1}), and two on-top CO peaks (2091 and 2105 cm^{-1}). SFG and LEED showed that this structure originates from a superposition of domains with coverages between 0.63 and 0.68 ML (Figs 15c,d) and of 0.75 ML (Fig. 15f). Dosing at 90 K produced even broader SFG peaks. Apparently, the thermodynamic equilibrium (2 × 2) structure is kinetically not accessible at temperatures below 120 K as a consequence of the low mobility of CO at these temperatures; kinetically trapped structures will be produced. More detailed investigations under UHV (*121*) have shown that the formation of a well-ordered (2 × 2) saturation structure requires a sufficiently high CO mobility (temperatures of ~150 K to overcome the CO diffusion barrier) and a sufficient CO flux (e.g., corresponding to a CO pressure of ~10^{-6} mbar at 150 K) to avoid "quenching" of domains with lower coverage. This result demonstrates that adsorbate phases formed at cryogenic temperatures in UHV are not necessarily equilibrium structures (another example discussed below is CO/Pt(1 1 1)). Therefore, great care must be taken when UHV data are extrapolated to high-pressure catalytic reaction conditions (when the adsorbate is in equilibrium with the gas phase). Furthermore, when it is taken into account that even the seemingly simple CO/Pd(1 1 1) system exhibits quite complex adsorption behavior, it is clear that the interpretation of the spectra of adsorbates on nanoparticles is quite involved.

C.1.2. Atmospheric Pressure Investigations. It is now appropriate to ask whether similar adsorbate structures are also present at higher CO pressures and higher temperatures. SFG provides a direct answer. Figure 16a shows the results of a series of experiments at various pressures carried out with Pd(1 1 1) at 190 K. The spectrum at 10^{-6} mbar displays bridging (1955 cm^{-1}) and on-top CO (2087 cm^{-1}), in agreement with the corresponding spectrum in Fig. 15d. With increasing pressure, the bridged species disappeared, the band indicative of on-top CO increased in

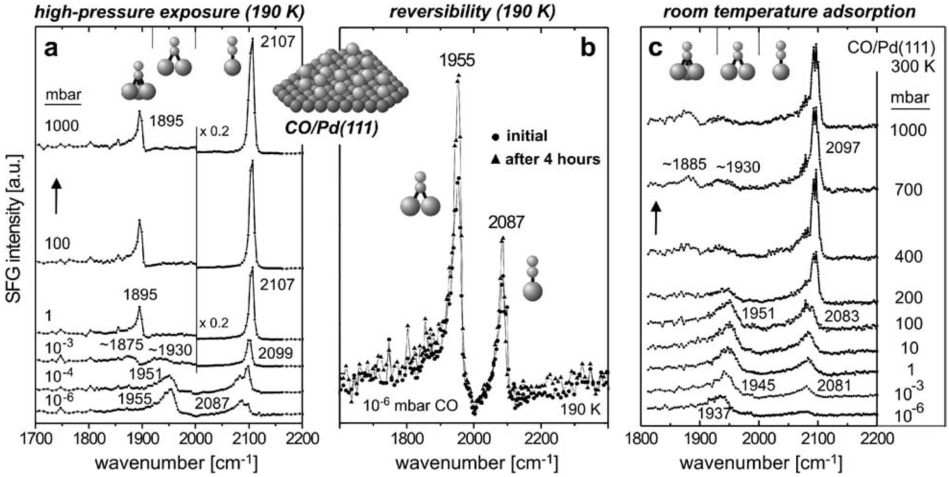

FIG. 16. (a) SFG spectra of CO on Pd(1 1 1) at pressures in the range of 10^{-6} to 1000 mbar and at 190 K. The (nonresonant) SFG signal from a thin Al_2O_3 film on NiAl(1 1 0) (*121*), on which CO does not adsorb, was used as a reference for IR normalization. Approximate frequency ranges of the CO species are indicated. The reversibility of the appearance of the spectra with cyclic changes in pressure is shown in (b), with the results of corresponding measurements at 300 K shown in (c) (*121, 152*).

intensity, and that indicating CO at a hollow site (1895 cm^{-1}) evolved. The "phase transition" between the bridged/on-top (at 0.63 ML) and the hollow/on-top (at 0.75 ML) structures (*152,264*) occurred at pressures between 10^{-3} and 1 mbar; between 1 and 1000 mbar, the on-top peak grows slightly, but otherwise the spectra were identical (spectra not shown; see Reference (*120*)). A comparison of Figs. 15–17 shows that very similar CO adsorbate structures were obtained at high pressure/high temperature and at low pressure/low temperature. No evidence for the formation of high-pressure species has been found. The spectra were fully reversible with cyclic changes in pressure, indicating the absence of major surface restructuring (Fig. 16b). At pressures of 10^{-4}–10^{-3} mbar, the two on-top species (characterized by bands at 2087 and 2099 cm^{-1}) and the coexistence of peaks indicating bridged species and those at hollows indicate a superposition of the domains at 0.63 and 0.75 ML, similar to the nonequilibrium structures discussed above (cf. Fig. 15e). A well-ordered (2 × 2) structure with hollow/on-top occupancy was formed only at 1 mbar. In summary, the saturation structures formed under UHV and at high pressure were identical, and less-ordered structures may be present in both cases.

Because catalytic reactions are usually carried out at higher temperatures, SFG spectra were also recorded at higher temperatures, at pressures between 10^{-6} and 1000 mbar characterizing CO on Pd(1 1 1) (*112,152,253*). At 10^{-6} mbar and 300 K, a peak at 1937 cm^{-1} indicated a coverage of about 0.5 ML (Fig. 16c). The coverage increased with pressure and reached about 0.63 ML at 100 mbar (1951 cm^{-1} characterizing bridged and 2083 cm^{-1} characterizing on-top CO). At 190 K, this structure (this coverage) was obtained even at 10^{-6} mbar. Upon a further increase in the pressure, the peak indicating bridged CO decreased in intensity, and the on-top peak increased in intensity. Within a broad pressure range (400–1000 mbar of CO), less-ordered structures, with CO at hollows and in bridging and on-top positions were again observed. These results suggest that at certain combinations of temperature and pressure (falling into the transition range between 0.63 and 0.75 ML), such structures may even be present during catalytic reactions. As shown below for CO hydrogenation, such imperfectly ordered adsorbate phases may play a role in catalytic processes. At 300 K, a saturation structure with CO exclusively in hollow sites and in on-top positions (coverage 0.75 ML) could not be obtained because this would require pressures >1 bar. The spectra measured at 300 K also indicated that the surface structures were formed reversibly, again indicating the absence of irreversible CO-induced surface restructuring. Measurements at 400 K are described in References (*253,274*).

Recently, high-pressure CO adsorption on Pd(1 1 1) was also investigated with PM-IRAS (*170,171,173*). Figure 17a displays a PM-IRAS spectrum of 170 mbar CO on Pd(1 1 1) at 190 K, typical of a (2 × 2)-3CO structure with CO bonded at hollow (1885 cm^{-1}) and on-top (2099 cm^{-1}) sites (coverage *ca.* 0.75 ML). This structure is in good agreement with the high-pressure SFG investigations described above (an SFG spectrum of 100 mbar CO is included for comparison in Fig. 17a). The offset in frequency between the PM-IRAS and SFG spectra probably originates from differences in the adsorbate layer (with different contributions of CO domains with coverage slightly lower than 0.75 (*121,273*), influencing the size of (2 × 2) domains). Spectra recorded at higher temperatures are presented in References (*170,173*).

C.1.3. Intensities and Lineshapes. The SFG spectra in Figs 15–17 qualitatively agree with corresponding IRAS data (*17,171,260,264*). The linewidths of the peaks associated with CO at on-top and hollow sites at 0.75 ML (5 and 8 cm^{-1}) and of the peak representing bridged CO at 0.6 ML (17 cm^{-1}) are similar to those obtained by IRAS (on-top, 8 cm^{-1}; hollow, 9 cm^{-1}; bridged, 18 cm^{-1}) (*17*). However, there are apparent differences in signal intensity that are attributed to the different selection rules of SFG and IRAS. For example, in the characterization of the (2×2) structure (Fig. 17), PM-IRAS yielded peaks characterizing CO at hollow and on-top positions of about similar size (hollow/on-top ratio 0.8:1). Because the unit cell of the (2×2) superstructure contains two (fcc and hcp) hollow-bonded CO molecules and one linear-bonded CO molecule, the real hollow/on-top-ratio is therefore 2:1. Apparently, it is difficult to determine the exact site occupation from IRAS, because the absorbance does not scale with the actual coverage or site occupation. The reason for this behavior may be related to different dynamic dipole moments of molecules on different adsorption sites. Furthermore, dipole coupling effects (*17*) as coverage increases and intensity borrowing (*275*) can alter the signal intensities of the various species.

We are now in a position to compare the hollow/on-top ratio determined from PM-IRAS data with that of the corresponding SFG spectrum (Fig. 17), recalling that the latter depends not only on the IR moment but also on the Raman scattering activity. Fitting the SFG spectrum indicated a hollow/on-top (amplitude) ratio of about 0.3:1. Consequently, threefold hollow-bonded CO is underestimated (or on-top CO is overestimated), as it has already been proposed (*120,152*). In SFG spectroscopy, the discrepancy between measured and real-site occupation originates not only from differing IR moments, but may also be attributed to the reduced Raman scattering activity of CO at hollow sites and/or an increased scattering

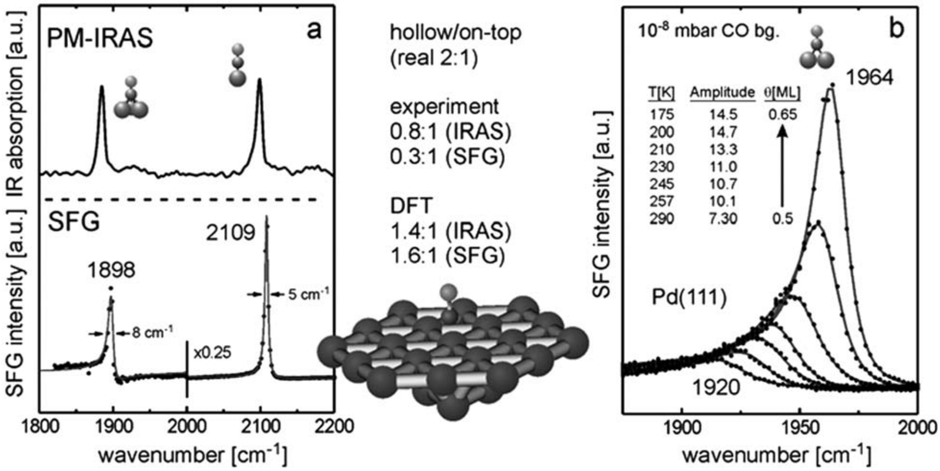

FIG. 17. PM-IRAS and SFG spectra of CO on Pd(1 1 1) at CO pressures of 170 and 100 mbar at 190 K, respectively. A comparison of the experimentally observed and calculated intensity ratios of peaks characterizing CO in hollow positions relative to CO in on-top positions is included (see text). (b) Dependence of the SFG intensity on coverage in the range 0.5 to 0.65 ML; adapted from (*153*) with permission from Elsevier.

activity of linear CO. Compared with IRAS, the overestimation of linear-bonded CO is therefore even larger for SFG, because of the additional influence of the Raman term. Similar intensity differences were observed for bridged and on-top bonded CO on Ni(1 1 1) (*116*) and on Pt(1 1 1) (*46,125,129,131,151*) (with bridging CO hardly being detected).

To better explain the SFG intensities, DFT cluster calculations were performed (*153*). Calculations were done for an isolated CO molecule on various sites on a Pd_{22} cluster (mainly exhibiting a (1 1 1) surface, Fig. 17), and the corresponding IR- and Raman cross-sections and singleton frequencies were calculated. The higher sensitivity of IRAS toward on-top bonded CO seems to be related to a ~25% higher dynamic dipole moment for linearly bonded CO than for CO bonded at hollow sites, but the argument of a significantly lower Raman activity of hollow-bonded CO leading to a strong overestimation of on-top CO was not supported by the calculations. DFT yielded a calculated hollow/on-top ratio of 1.4:1 for IRAS and 1.6:1 for SFG, with the latter value being notably different from the experimental value. However, adsorbate–adsorbate interactions (*276*) were neglected in the theoretical description, because they cannot be modeled for a cluster within reasonable processing time, especially when Raman scattering cross-sections are required.

The complications of coverage-dependent changes as well as intensity borrowing, for example, are illustrated by data showing that when the coverage increased from 0.5 and 0.65 ML the SFG amplitude of bridge-bonded CO doubled (Fig. 17b), whereas the IRAS signal intensity did not change significantly. The strong enhancement of the SFG amplitude may therefore be attributed to coverage-dependent (and increasing) Raman cross-sections (*150,153*). Interference effects between different SFG susceptibility tensor elements may also contribute, as shown by Baldelli *et al.* (*277*). More complex calculations at higher CO coverages are required for a full analysis of signal intensities (*278*).

A direct quantitative coverage analysis by simple integration of the SFG peak areas/heights is hence difficult (*120,152*) (the coverages shown in Fig. 15 were obtained from TDS data (*273*)). Nevertheless, for the particular case of the CO/Pd(1 1 1) system, coverages can still be deduced from the spectra; as shown below, the strong coverage dependence of the C–O stretching frequency allows a good estimation of the actual CO coverage under mbar pressure conditions, an inference that was confirmed by comparing SFG and (quantitative) HP-XPS measurements (*253*).

C.1.4. Summary. SFG spectra of CO on Pd(1 1 1) have shown that the high-pressure structures (existing at pressures up to 1000 mbar) were identical to the corresponding high-coverage structures observed under UHV with the "usual" CO adsorption sites (with CO bridging and in on-top and hollow sites). Even when the CO pressure was increased by 10 orders of magnitude, the UHV saturation coverage could not be exceeded. There is no evidence for the formation of high-pressure species that are different from those observed under UHV. Whereas high CO pressures disrupt rhodium nanoparticles (*51*) and restructure rhodium (*14*) and platinum single crystals (*216,222,279*), such an effect was absent for Pd(1 1 1) under the experimental conditions. No evidence for major surface rearrangements has been found. The spectra indicated that the structures were formed reversibly as a result of cyclic changes in pressure.

Notwithstanding these results, several scenarios can still be suggested to account for a "pressure gap." When elevated temperatures are required to stimulate reactions between molecules, typical UHV pressures (10^{-9}–10^{-6} mbar) may lead to rather low coverages. For example, at 300 K UHV exposures of Pd(1 1 1) to CO produce coverages <0.5 ML, whereas at pressures >100 mbar, coverages of 0.6–0.7 ML are obtained. Even more important than the simple coverage difference are differences in the site occupation. At 300 K, CO is bound to hollow sites under UHV, whereas mainly bridge bonded and linearly bonded CO are present at 100 mbar. Therefore, UHV investigations may not provide data that are characteristic of a specific reaction, such as when the reactive species is a weakly bound on-top CO which only appears at high coverages after the more strongly adsorbing sites (hollows, bridge positions) are occupied. Of course, application of low temperatures in UHV (~100 K) can produce high CO coverages, but this would simultaneously prompt another problem. At low temperatures, the reduced mobility of adsorbed CO molecules may produce different (kinetically hindered) adsorbate structures, and the catalytic reaction may proceed by a route different from that pertaining at higher temperatures. Consequently, to connect surface science and catalysis, one has to make sure that both types of investigations are carried out under comparable conditions, with identical surface coverages and identical adsorbate structures and site occupations.

C.1.5. Ion-bombarded (Defect-rich) Pd(1 1 1) Surfaces. The complex surface structure of a metal nanoparticle cannot be represented fully by low-index single-crystal surfaces, but higher Miller index (stepped and/or kinked) surfaces or defect-enriched (slightly misoriented or ion-bombarded) surfaces (*120,152*) should be more realistic models.[6] SFG was therefore performed to characterize "defect-rich" Pd(1 1 1) (Fig. 18), which can be imagined as being composed of (1 1 1) terraces and various sorts of "defects" including steps and kinks (the steps can also be regarded as (1 1 0) or (1 1 3) nanofacets; cf. Fig. 14). Comparison of the 10^{-6} mbar CO spectrum of Fig. 18 to the corresponding spectrum of CO on the well-ordered (1 1 1) surface (Fig. 16) shows an additional peak on the imperfect surface, at 1990 cm^{-1} (total coverage ~0.65 ML). This species is most likely related to CO adsorbed on step (low-coordination) sites, and the frequency range indicates that it is bridge bonded. The same species was also observed on a regular (1 1 1) surface after defects were produced by ion bombardment (*152*). Bridge-bonded species with peaks at about 1985 cm^{-1} have been assigned to CO on Pd(1 0 0) (*17,280,281*), Pd(1 1 0) (*282,283*), Pd(2 1 0) (*17*), and rough palladium thin films (*17*). This vibrational mode is expected to occur when CO is adsorbed on curved and rough surfaces of nanoparticles, and it has indeed been observed by IR spectroscopy on wet-chemically prepared Pd/SiO_2 (*263,284*) and on alumina- (*285,286*) and titania- (*282*) supported palladium model catalysts.

---

[6] Provided that finite size (or volume) effects (*68*) that may occur in the course of hydrogenation reactions are absent.

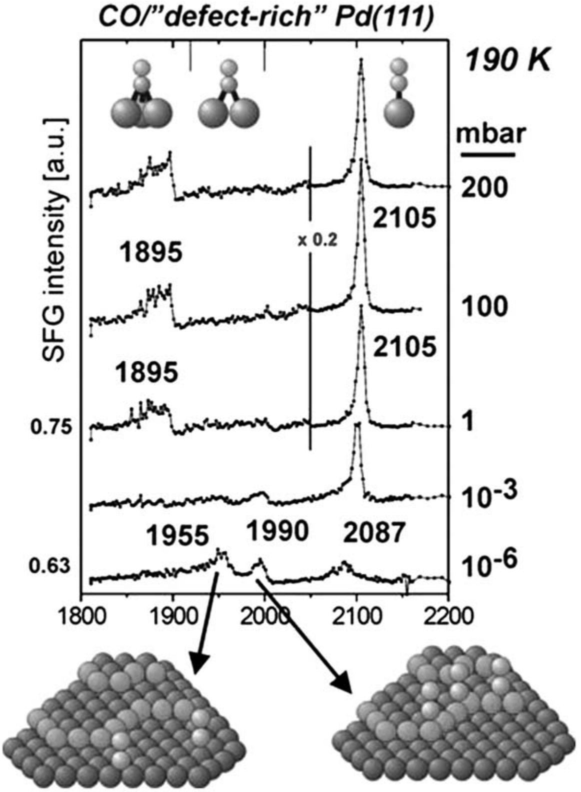

FIG. 18. SFG spectra of CO adsorption on "defect-rich" Pd(1 1 1) at 190 K at pressures in the range from 10^{-6} to 200 mbar. A peak at 1990 cm^{-1} appeared that was not evident for CO on the perfect (1 1 1) surface; adapted from (*120*) with permission from Elsevier.

The species indicated by the band at approximately 1990 cm^{-1} may originate from a specific binding site at a step edge, but it may also arise from coupling between CO molecules on a step and neighboring CO molecules on a (1 1 1) terrace. Greenler *et al.* (*287*) demonstrated that by dipole coupling of linear CO molecules on a step edge (where the metal atoms have coordination numbers <9) and ("subsequent") coupling to CO molecules adsorbed on the terrace sites (coordination number $= 9$), a resonance frequency is produced that is characteristic of the ensemble and not of a particular binding site.

When the CO pressure was increased in the presence of the imperfect Pd(1 1 1) crystal at 190 K, the bridge/on-top to hollow/on-top transition again occurred at about 10^{-3}–1 mbar (i.e., at a pressure nearly identical to that observed for CO on Pd(1 1 1)). Whereas the defect-related peak at ~1990 cm^{-1} was present at coverages below saturation, it could no longer be observed at coverages close to 0.75 ML. This result does not necessarily mean that high CO pressures restructure the surface and anneal out the defects. If the "packing density" of the CO molecules becomes high, lateral interactions between the CO molecules on the terraces and defects (step edges) may be responsible for the "disappearance" of the defect peak. Such an

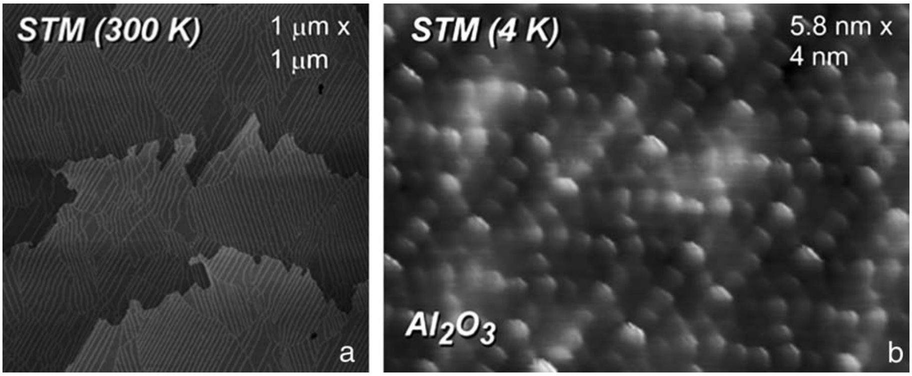

FIG. 19. STM images of the thin Al_2O_3 support, (left) at medium magnification (acquired at 300 K) and (right) at atomic resolution (acquired at 4 K); adapted from Freund *et al.* (*63,83,101*) and Kulawik *et al.* (*215*). Copyright (2003) American Physical Society.

effect has, for example, been observed on a stepped Pt(3 3 5) surface when co-adsorbed H strongly modifies the vibrational spectrum of CO along the step edges (*288*). Furthermore, after a reduction in the pressure, the defect-peak at about 1990 cm^{-1} reappeared, which is possible only if there is no restructuring or if the restructuring is fully reversible. Apparently, under high-pressure conditions, defects on a single-crystal surface may be obscured, suggesting the need to carry out investigations of palladium nanoparticles.

C.2. *CO Adsorption on Al_2O_3-supported Palladium Nanoparticles*

In the following section, CO adsorption on alumina supported palladium nanoparticles of various sizes and surface structures is examined and compared with the corresponding results for CO on Pd(1 1 1) and "rough" Pd(1 1 1) (*119,120,152,289*). The preparation and characterization of the alumina support and of deposited palladium nanoparticles have been described in detail (*63,68,73,83,101,290*) and only a brief summary is given here.

C.2.1. Pd/Al_2O_3 Preparation and Structural Properties. To prepare a thin well-ordered Al_2O_3 model support, a NiAl(1 1 0) alloy single crystal was oxidized in 10^{-5} mbar of O_2 at 523 K (*290*). The structure of the alumina film was examined by a variety of techniques (see Reference (*101*) and references cited therein), and recently it was even possible to image its atomic structure by STM at 4 K (Fig. 19) (*215*). The alumina film was only approximately 0.5 nm thick and hydroxyl-free,[7] and one should also keep in mind that its exact structure may deviate from those of bulk aluminas (*101,215,292,293*). Its properties are certainly influenced by the observed line defects (antiphase domain boundaries and reflection domain boundaries).

---

[7] Procedures have also been developed to create OH groups on the alumina film. For details, see References (*83,291*).

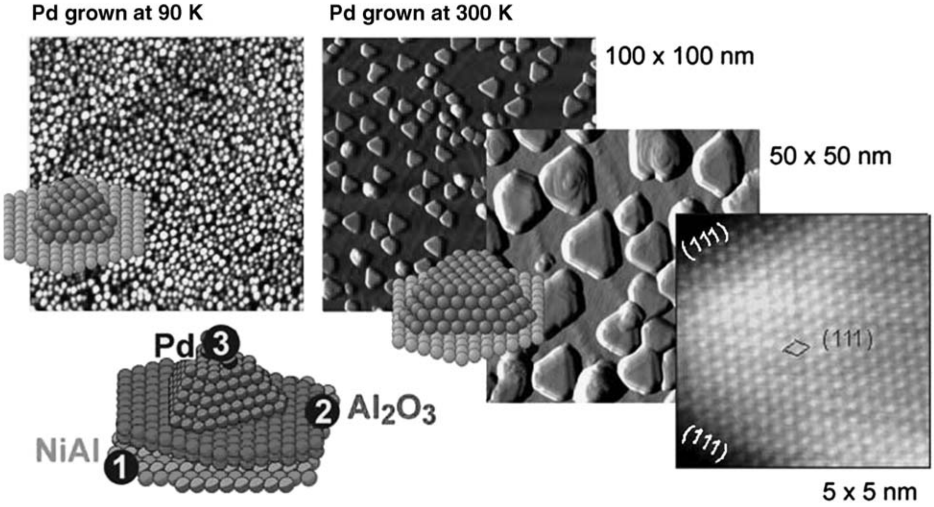

FIG. 20. STM images of palladium nanoparticles on Al_2O_3/NiAl(1 1 0), grown at 90 and at 300 K; adapted from Heemeier *et al.* (*97*), Frank and Bäumer (*254*), and Højrup Hansen *et al.* (*206*).

To obtain palladium nanoparticles, palladium was deposited onto the Al_2O_3 film either at 90 or at 300 K. Figure 20 shows typical STM images (*73,97,206,254*) of palladium particles of approximately 3 and 6 nm mean diameter. At 300 K, the palladium particles grew preferentially along line defects (nucleation density $\sim 1 \times 10^{12}$ particles cm^{-2}), whereas at 90 K, the reduced palladium mobility led to a higher nucleation density and thus to a more homogeneous distribution (nucleation density $\sim 5 \times 10^{12}$ particles cm^{-2}). The Al_2O_3 temperature during palladium deposition also influenced the particle morphology. Palladium particles grown at 90 K were of rounded (irregular, presumably hemispherical) shape. No high-resolution STM images could be obtained, but HRTEM images suggest a large number of low-coordination sites (defects, steps, etc.; cf. Fig. 14). Palladium particles grown at 300 K were of cuboctahedral shape. According to atomically resolved STM images, the particles exhibit a (1 1 1) top facet, and (1 1 1) and (1 0 0) side facets (*206*). By accurately controlling the amount of palladium and the alumina temperature during palladium evaporation, the mean palladium particle size and island density could be adjusted between ~1–10 nm and $\sim 1 \times 10^{12}$–1×10^{13} cm^{-2}, respectively, giving access to a wide variety of model catalysts. Table I is a summary of the structural parameters for a number of preparation conditions (for more details, see References (*101,254*)). A further stabilization procedure, described in Reference (*294*), increased the thermal stability of the palladium particles so that they withstood temperatures up to approximately 600 K.

Before turning to the SFG spectra of adsorbed CO, it is worthwhile to examine the statistics of surface metal atoms (*22*) by which is meant the exact particle surface structure that eventually governs the particle properties. Figures 21a and b show truncated (perfect) cuboctahedra of the same size (6.2 nm) but with different aspect (height/diameter) ratios, both exhibiting a (1 1 1) top facet, and (1 1 1) and (1 0 0)

TABLE I

Structural parameters of Pd/Al_2O_3 model catalysts and comparsion with Pd(1 1 1)

Nominal palladium film thickness (nm)/ substrate temperature during palladium evaporation (K)	Particle number density[a] (particles per cm^2 of sample area)	Mean particle diameter (nm)	Number of atoms per particle	Number of surface atoms per particle	Dispersion	Number of exposed surface atoms per cm^2 of sample area	Percentage of surface atoms/cm^2 relative to those on Pd(1 1 1) (1.53×10^{15} atoms cm^{-2})	Percentage of surface atoms/cm^2, considering only the particle (1 1 1) top facets, relative to those on Pd(1 1 1) (1.53×10^{15} atoms cm^{-2})
0.6/300	1×10^{12}	6.0	3940	820	0.21	8.2×10^{14}	53.6	~16
0.4/300	1×10^{12}	5.4	2720	640	0.24	6.4×10^{14}	41.8	~13
0.2/300	1×10^{12}	4.2	1360	400	0.30	4×10^{14}	26.1	~8
0.6/90	4.7×10^{12}	3.5	850	295	0.35	1.4×10^{15}	90.6	~27
0.4/90	6.4×10^{12}	2.9	430	185	0.44	1.2×10^{15}	77.4	~23
0.2/90	8.7×10^{12}	2.1	160	95	0.61	8.3×10^{14}	54.0	~16

[a] On the basis of STM structure characterization; see References (*63,97,101,254*) for details.

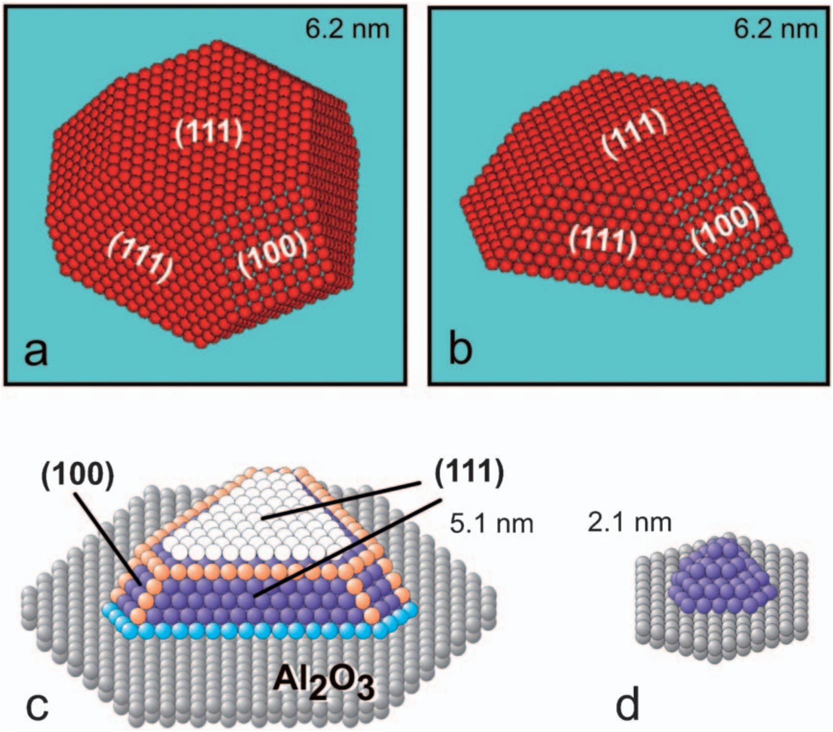

FIG. 21. Schematic models of truncated cuboctahedra of various sizes and aspect ratios, exhibiting a (1 1 1) top facet and (1 1 1) and (1 0 0) side facets. According to HRTEM images of palladium nanoparticles, the terraces may be incomplete, leading to surface facets with steps. For structural characteristics, see Table II.

side facets (for simplicity, no oxide support is shown). This picture may be too ideal, because HRTEM images of palladium nanoparticles (Fig. 14d) and of other metals (e.g., platinum (*48,74*) and rhodium (*54*)) indicated that the particle terraces may not always be perfect, leading to incomplete surface facets with steps. A model of an incomplete cuboctahedron is thus shown in Fig. 21c, together with a small (somewhat disordered) palladium particle. Table II is a summary of the structural properties of these nanoparticles, showing the breakdown of their surface atoms into various sites. Table II indicates that about 75–80% of the particle surface consists of (1 1 1) facets, with the remaining approximately 20–25% being (100) facets. Edge atoms and phase-boundary (adlineation) sites (*295*) each comprise about 10–15% of the number of surface atoms and can be regarded as minority sites. Particles smaller than 2 nm no longer exhibit well-developed facets, so that a separation into different surface sites is not appropriate (the "facets" typically contain only 4–8 atoms; an approximately 2-nm particle is shown in Fig. 21d). Further implications of the results of Table II are discussed below.

C.2.2. SFG Spectroscopy of CO on Palladium Nanoparticles. The first SFG spectra of CO on supported nanoparticles were obtained by using a Ti:Sa-based laser

TABLE II

Statistics of surface metal atoms for various types of nanoparticles[a]

Particle morphology	Mean particle diameter (nm)	Height (nm) (height/ diameter aspect ratio)	Number of atoms per particle	Number of surface atoms per particle	Dispersion	Number of atoms in (1 1 1) top facet per particle (percentage of surface atoms)	Number of atoms in (1 1 1) side facets per particle (percentage of surface atoms)	Number of atoms in (1 0 0) side facets per particle (percentage of surface atoms)	Number of edge atoms per particle (percentage of surface atoms)	Number of phase-boundary atoms (percentage of surface atoms)	Percentage of (1 1 1) facets per particle relative to the total particle surface
Perfect cuboctahedron with re-entrant facets (cf. Fig. 21a)	6.2	2.6 (0.42)	approximately 4100	997	0.25	170 (17)	474 (48)	147 (15)	135 (13)	72 (7)	65
Flat perfect cuboctahedron (cf. Fig. 21b)	6.2	1.8 (0.29)	approximately 2600	710	0.27	170 (24)	231 (32)	147 (21)	90 (13)	72 (10)	56
Flat incomplete cuboctahedron (cf. Fig. 21c)	5.1	1.2 (0.22)	~1100	315	0.29	44 (14)	108 (34)	18 (6)	90 (29)	54 (17)	48
Small particle (cf. Fig. 21d)	2.1	0.7 (0.3)	95	45	0.47	n.a.	n.a.	n.a.	n.a.	18 (40)	n.a.

[a] The most accurate way to calculate the nuber of specific surface atoms is to differentiate the surface atoms according to their coordination number, designating whether they belong to (111) faces, (100) faces, edges, or to the phase boundary. Each surface atom was thus counted only once (i.e., edge and phase-boundary atoms do not count as terrace atoms and phase boundary atoms do not count as edge atoms). Phase-boundary atoms are those atoms which are in immediate contact with the oxide support and which are accessible to the gas-phase molecules (adlineation sites).

When the number of edge atoms is split between (111) and (100) facets and the phase-boundary atoms are added to the respective faces, the surface of larger particles exhibits 75–80% (111) facets and 20–25% (100) facets.

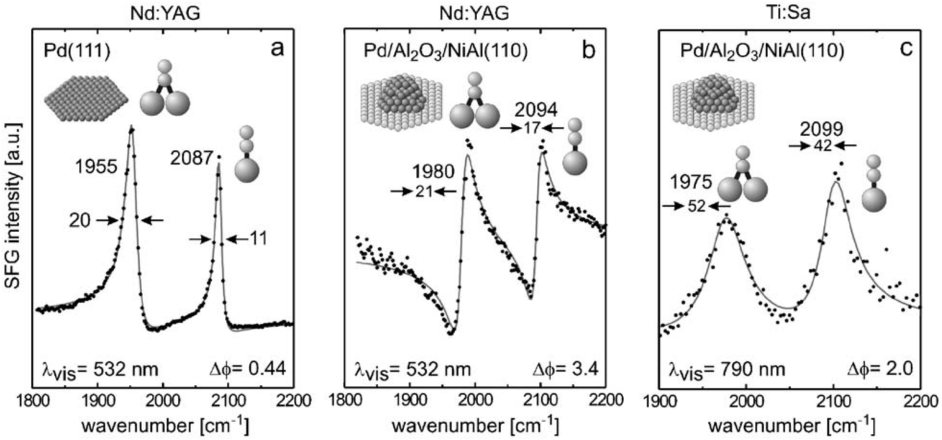

FIG. 22. SFG spectra of CO (near saturation coverage at 190 K) adsorbed on (a) Pd(1 1 1) and on (b,c) 3.5-nm palladium nanoparticles (grown at 90 K) acquired with Nd:YAG (a, b) and Ti:Sa (c) laser-based SFG spectrometers (*153*). Fitted spectra are included; adapted from (*153*) with permission from Elsevier.

system (*48,119,152*). An example is presented in Fig. 22c. Although the OPG/DFG unit used in these experiments had a resolution of only approximately 25 cm^{-1} (explaining the large linewidth of the peaks), these spectra still provided valuable information about adsorbate structures on palladium nanoparticles in the presence of high-pressure CO. Similar experiments were carried out by using the Nd:YAG-based laser system described in Section III.A, which has a resolution of about 5 cm^{-1} (Fig. 22b). Because the latter spectra revealed even more details (*68,296,297*) and are of the same resolution as those characterizing CO on Pd(1 1 1),[8] we focus on the Nd:YAG spectra.

Before we turn to the high-pressure experiments, the lineshapes of the SFG spectra deserve some attention. Figure 22 provides a comparison of UHV SFG spectra of CO adsorbed on 3.5 nm palladium nanoparticles acquired with the Ti:Sa and Nd:YAG laser systems. There is a clear improvement in resolution when the Nd:YAG laser is used (and good agreement in the observed resonance frequencies), but the most apparent difference between the two spectra is the different lineshapes; whereas rather symmetric peaks were observed with the Ti:Sa system, the Nd:YAG laser produced asymmetric CO resonances. This effect can be understood by considering Eq. (3), indicating that the SFG signal originates from the interference between the resonant signal and the nonresonant background. Accordingly, the SFG lineshape is governed by the nonresonant amplitude A_{NR} and even more important, the phase difference Φ to the resonant contribution. For both laser systems, the nonresonant background was much higher for palladium nanoparticles than for Pd(1 1 1), which is attributed to electronic transitions in the NiAl(1 1 0) substrate (*153,296*). Furthermore, in the measurements with the Nd:YAG system, a

---

[8] The heterogeneity of supported nanoparticles with respect to particle size and surface structure generally leads to CO peaks that are broader than those on Pd(1 1 1).

phase difference Φ occurred that produced an asymmetric lineshape (which was independent of the crystal azimuthal orientation and the pulse energy).

Although the exact origin of these effects is not fully understood, an interband transition in the NiAl(1 1 0) substrate at about 2.5 eV (*298*) is most likely the key process responsible for the altered SFG lineshape. Whereas for the Nd:YAG system the wavelength of the resulting SFG signal (481 nm for 2000 cm^{-1}; 2.58 eV) or the vis pump beam itself (532 nm; 2.3 eV) coincide with the NiAl interband transition (~2.5 eV) (*298*), the SFG signal obtained with the Ti:Sa system (682 nm for 2000 cm^{-1}; 1.82 eV) and the vis pump beam (790 nm; 1.6 eV) are outside the interband transition range, which may explain the different phases observed in the spectra. Similar changes in lineshape upon variation of the excitation vis-wavelength were reported, for example, for octadecanethiol (*299*) and biphenyl -3-methenethiol (*300*) on gold surfaces, respectively, and attributed to the excitation of electronic s–d interband transitions in the gold substrate. For completeness, we also mention that the observed asymmetric lineshape is not a Fano-effect (*301,302*), but it is rather a simple optical interference phenomenon (see Reference (*153*) for details). In any case, applying Eq. (3) to fit the experimental results allows one to extract the relevant parameters from the Nd:YAG cluster spectra, as shown in Fig. 22b.

C.2.3. UHV CO Spectra and Assignment of Bands. Figure 23 displays SFG spectra of CO on palladium particles of 6 and 3.5 nm mean diameters. The model catalysts were cooled from 225 to 105 K in 10^{-6} mbar of CO (to avoid nonequilibrium structures), resulting in a CO saturation coverage. For interpretation of the spectra, the resonance positions are marked with dashed lines in Fig. 23.

First, consider CO adsorption on well-faceted 6-nm palladium particles. In light of the predominance of (1 1 1) facets (accounting for approximately 80% of the particle surface), one might expect that the particles would behave similarly to a Pd(1 1 1) single-crystal surface. Furthermore, the CO molecules adsorbed on the side facets are tilted with respect to the NiAl substrate and produce a smaller SFG signal than CO on the (1 1 1) top facet.[9] Similar considerations may also hold for (tilted) CO on the edge sites. Therefore, although the metal atoms that are on the (1 1 1) top facet account for only 20–30% of the particle surface atoms, the CO of the (1 1 1) top facet accounts for approximately 50–60% of the SFG signal (depending on the height/diameter aspect ratio); in other words, the SFG spectrum is dominated by the (1 1 1) top facet. Nevertheless, as shown in the following, even the adsorbate properties of well-faceted nanoparticles are quite different from those of Pd(1 1 1). In particular, the influence of minority sites (small facets, edges, steps, etc.) must be taken into account.

---

[9] Note that the surface electric field, induced by the incident IR radiation characterizing the thin-film model catalysts, is mainly determined by the NiAl substrate. Consequently, because only the components of the dynamic dipole moment that are perpendicular to the metallic substrate contribute to the SFG signal, the effective dipole moment of tilted molecules is reduced. As a result, the intensity of the signal characterizing tilted molecules is smaller than that of CO molecules oriented perpendicular to the substrate (such as those on the particle top facet).

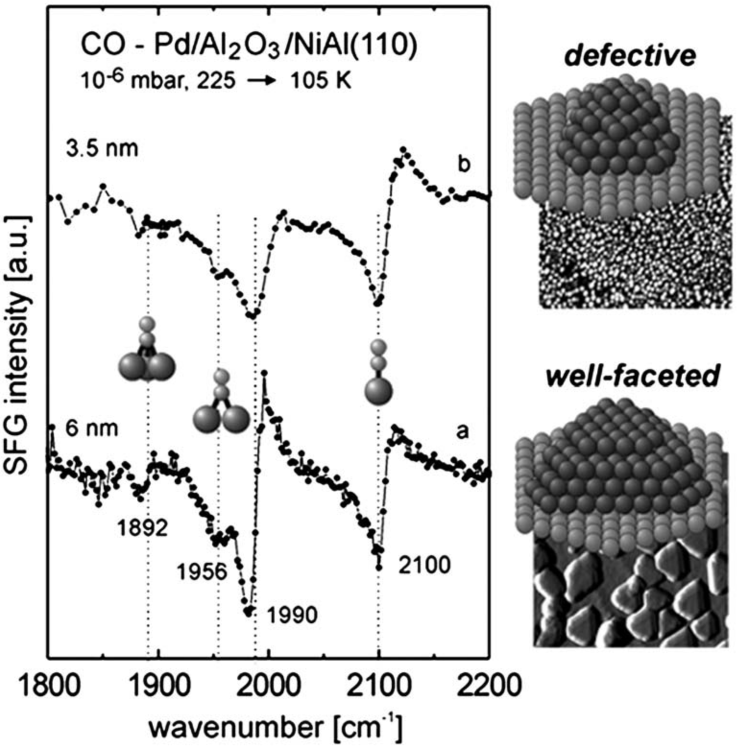

FIG. 23. SFG spectra of CO adsorbed on 3.5 nm and 6 nm palladium nanoparticles on alumina (near saturation coverage at 190 K; Nd:YAG-based SFG spectrometer). Well-faceted 6-nm palladium particles were grown at 300 K, and defective 3.5 nm palladium particles were grown at 90 K. A higher fraction of on-top CO is observed on the "rough" 3.5-nm palladium particles; adapted from Unterhalt (*296*).

In a consideration of the SFG spectrum shown in Fig. 23, two parameters should be considered when comparing palladium nanoparticles and Pd(1 1 1): the CO resonance frequencies and the relative intensities of the various species.[10] Four CO species were detected on well-faceted 6-nm palladium particles: the SFG spectrum exhibits a dominant bridge peak (1990 cm^{-1}) and a somewhat smaller on-top peak (2100 cm^{-1}) as well as a pronounced shoulder at 1956 cm^{-1} and a small peak at 1892 cm^{-1}. On the basis of a comparison with the single-crystal results shown above, these resonances can be assigned to bridging CO at particle steps/edges (1990 cm^{-1}), on-top CO (presumably on (1 1 1) facets; 2100 cm^{-1}), bridging CO on (1 1 1) facets (1956 cm^{-1}), and CO on hollow sites of (1 1 1) facets (1892 cm^{-1}). The main difference between nanoparticle and single-crystal spectra is that on particles defect-related bridging CO (1990 cm^{-1}) dominates, whereas bridged CO on (1 1 1) facets (1956 cm^{-1}) dominates on Pd(1 1 1). This result seems to contradict the

---

[10] As discussed above, no quantification of site populations can be made but trends can still be recognized.

expectations developed from the surface structure analysis by STM and HRTEM, but several explanations may account for the apparent contradiction.

(i) *Structure effects*. Even well-faceted palladium nanoparticles exhibit more defect sites than Pd(1 1 1). The models of half-octahedral particles shown in Figs 20 and 21a,b are idealized, because for a given particle diameter, a truncated cuboctahedron with *complete* surfaces would require a "magic number" of atoms. During the particle growth by vapor deposition, the number of palladium atoms per particle increases continuously, and consequently some surface steps must be present even on well-faceted nanoparticles. The particle will have monoatomic steps that can be imaged by HRTEM (*48*) and STM (*254*). This structure is equivalent to the presence of {1 1 0} and {1 1 3} nanofacets, which are included in the ball model of Fig. 23. It is therefore not surprising that the bridging CO frequency is characteristic of CO on step sites. Furthermore, density functional investigations of CO adsorption on cuboctahedral palladium nanoparticles have indeed shown that the band at approximately 1980 cm^{-1} originates from CO molecules bound to particle edges (*303*).

(ii) *Intensity borrowing*. According to the site statistics (Table II), the fraction of edge sites is only 10–15%, which is too small to explain the large intensity of the peak at about 1990 cm^{-1} by structural effects alone (adding a few surface steps would not increase the fraction much). Both SFG (Fig. 23) and IRAS spectra (*285*) indicated a weaker band (shoulder) at about 1950 cm^{-1}, which is characteristic of CO bridge-bonded to (1 1 1) terraces. Because the SFG signal intensities of edge- and terrace-related bridge-bonded CO are apparently inversely proportional to the respective number of these sites on a palladium nanoparticle, intensity borrowing from the low-frequency bridging CO species (on terraces) to the high-frequency bridging CO species (on steps and edges) seems to be responsible for the strong intensity of the 1990-cm^{-1} peak (*17,275*).

(iii) *Palladium(100)*. According to the frequency, the intense bridging peak could also originate from CO on (1 0 0) facets (*17*). However, in light of the particle shape, the contribution of the tilted (1 0 0) facets is again too small (~20% in area and ~15% in intensity) to explain the strong 1990-cm^{-1} peak.

After explaining the origin and intensity of the defect-related peak, we are now able to analyze the structure of the CO adsorbate layer on 6-nm palladium particles. Apart from the population of step/edge sites (1990 cm^{-1}), the coexistence of bridged/on-top (1956/2100 cm^{-1}) and hollow/on-top (1892/2100 cm^{-1}) structures under saturation conditions suggests that a 0.75-ML (2×2) structure may be obtained on part of the particle surface, presumably on the (1 1 1) top facet. The heterogeneity of the particle surface (steps, defects) most likely prevents the phase transition from occurring fully. It remains unclear, however, whether two domains with different CO coverages may coexist on a single palladium nanoparticle (i.e., whether Fig. 23a is characteristic of adsorption on a single particle), or whether different nanoparticles exhibit different surface coverages (i.e., whether Fig. 23a is a superposition of the different SFG spectra of different particles). In light of the limited terrace size on nanoparticles, the latter seems more probable.

Figure 23b shows the corresponding SFG spectrum of CO at saturation on 3.5-nm palladium particles (about 850 atoms/particle; ~300 surface atoms). These particles were grown at 90 K, and as mentioned above, the reduced palladium mobility led to a higher nucleation density, to a smaller particle size, and to less-ordered surfaces with more low-coordination sites. As a consequence of the "rougher" surface, SFG peaks appeared at 1990 and 2100 cm^{-1}, typically with an increased fraction of on-top CO (*48,119,152*). On rough particles, many defect sites (e.g., protruding palladium atoms) are available, and lateral CO interactions are much reduced; this situation presumably favors a higher fraction of on-top CO (*285,304*). Because well-developed (1 1 1) facets were absent, SFG signals attributed to bridging (approximately 1950 cm^{-1}) or hollow-bonded CO (approximately 1890 cm^{-1}) are typically absent from spectra characterizing particles prepared at 90 K. The weak signals at approximately 1950 and 1890 cm^{-1} (Fig. 23b) occur only because this sample had been previously annealed at a temperature of approximately 250 K (*296*). In any case, the lack of pronounced (1 1 1) facets prevents the formation of (2 × 2)-like hollow-bonded/on-top structures, either by saturation under UHV or at high gas pressures (see below).

C.2.4. High-pressure CO Adsorption. Figure 24 is a collection of spectra representing CO on 6-nm palladium particles at pressures between 10^{-6} and 600 mbar of CO at 190 K (spectra were smoothed for clarity). The SFG spectra were reversible with pressure, i.e., there were no indications for surface restructuring under these conditions. At 10^{-6} mbar peaks at approximately 1990 and approximately 2100 cm^{-1} were observed, with only a small shoulder at about 1950 cm^{-1}. Increasing the pressure from 10^{-6} to 0.1 mbar decreased the intensity of the 1990 cm^{-1} peak and increased the on-top CO intensity. In addition, the evolution of hollow bonded CO was observed at about ~0.1 mbar, which is similar to the situation on

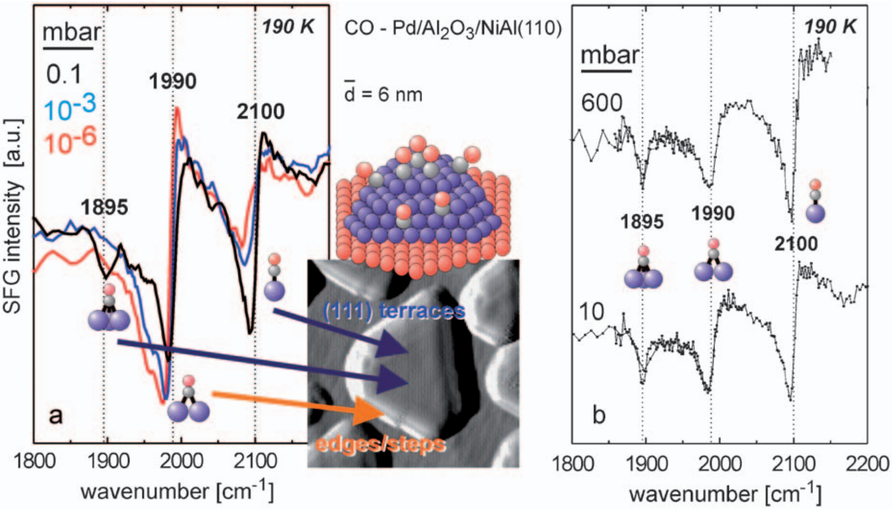

FIG. 24. High-pressure CO SFG spectra on 6-nm palladium nanoparticles (Nd:YAG-based SFG spectrometer) (*296, 297*).

Pd(1 1 1) (*48,296*). Increasing the pressure up to 600 mbar did not induce any further (major) changes.

This indicates that a bridge/on-top to hollow/on-top transition occurs, at least on part of the particle surface or on a fraction of particles. The apparent reduction in the intensity of the 1990 cm^{-1} peak does not indicate that the population of edge sites is reduced, but rather that the amount of intensity borrowing decreases as a result of the reduction of bridging CO on (1 1 1) facets (which relocated to hollow sites with increasing coverage). Another point to note is that the "bridge on edge" species (1990 cm^{-1}) persists up to atmospheric pressure while this species was absent on Pd(1 1 1) and even bridging CO on Pd(1 1 1) fully disappeared at pressures above ~1 mbar at 190 K. Gelin et al. (*263*) and Rainer *et al.* (*286,305*) reported a similar behavior for palladium particles on silica and alumina, respectively.

High-pressure spectra were also acquired characterizing CO on smaller (3.5 nm) defective palladium particles (not shown). As a consequence of the absence of well-developed facets the structural rearrangements of the CO overlayer were rather minor. At 200 K and 10^{-8}–10^{-6} mbar CO, the particles were saturated yielding SFG spectra with bridge and on-top CO peaks (similar to Fig. 23b). Because the particles were already saturated with CO, increasing the pressure up to 600 mbar did not induce significant changes (see, e.g., Fig. 8 of (*48*)). No hollow-bonded CO was detected on the rougher particles, indicating that the number of defects is too great to allow the formation of a (2 × 2) structure (*296*). In any case, bridge-bonded CO could again be detected up to 600 mbar, whereas this species was absent from Pd(1 1 1).

High-pressure spectra were also taken at temperatures of 300 K and higher (*119,152*). At 300 K and 10^{-7} mbar, only a very small on-top peak was observed, even for 3.5-nm palladium particles (*119,152*). This result can be understood on the basis of TPD results indicating that on-top CO desorbs at about 250 K. At pressures exceeding 1 mbar, the on-top peak became more intense, but to obtain an adsorption site occupancy similar to what was observed at 10^{-6} mbar and 190 K (cf. Fig. 24), a pressure of about 200 mbar was required at 300 K (see, e.g., Fig. 11 of Reference (*152*)).

As mentioned, the 10^{-6} mbar particle spectra could be reproduced after the high gas pressure was pumped out, and no indications of *CO-induced* particle disruption were observed. However, annealing in vacuum or CO led to pronounced spectral changes attributed to a reduction in the number of (surface) defects. For example, when "rough" 3.5-nm palladium particles grown at 90 K were heated in vacuum or CO from 90 to approximately 300 K, the intensity of the peak representing on-top species decreased significantly (*152*), indicating surface reordering even at this temperature. After the sample had been annealed at room temperature, the spectrum was rather similar to a spectrum of CO on well-faceted particles grown at 300 K.

In summary, a Pd(1 1 1) single-crystal surface is not sufficient to model the complex adsorption behavior of palladium nanoparticles, even for nanoparticles which mostly exhibit (1 1 1) facets. High Miller index stepped or kinked single-crystal surfaces may provide better models of nanoparticles. However, one should remember that CO adsorbed on defects of defect-rich Pd(1 1 1) became "invisible" at high coverages! Furthermore, it will be demonstrated in a following section that the mere limitation in size/volume of palladium nanoparticles, which cannot be modeled accurately by macroscopic single crystals, has a strong impact on the nanoparticle properties.

C.2.5. Comparison of SFG Intensities of CO on Palladium Nanoparticles and Pd(1 1 1). Figure 22 also provides a comparison of the SFG signal intensities of CO adsorbed on palladium nanoparticles and on Pd(1 1 1). Before a discussion of the details, it is essential to consider the number of exposed Pd surface atoms on each type of sample. According to Table I, for a given sample area (e.g., the approximately 0.5-cm^2 sample area illuminated by the laser beams), the total number of Pd surface atoms exposed by nanoparticle model catalysts is about 40–90% of the corresponding value for Pd(1 1 1). Assuming similar CO surface concentrations (coverages) on the two types of catalysts, the number of CO molecules on a model catalysts would also be 40–90% of the number of CO molecules adsorbed on Pd(1 1 1) (per unit area). Neglecting the effect of tilted CO molecules on palladium particles for the moment, we infer that the resonant amplitudes A_R of CO on nanoparticles could at most be 2.5 times smaller than A_R for CO on Pd(1 1 1), according to Eq. (4). The SFG intensities of CO on nanoparticles would then at most be about 6 times smaller than on Pd(1 1 1) (Eq. (2)). Such ratios of amplitudes and intensities correspond roughly to what has been observed,[11] which excludes SFG enhancement effects on palladium nanoparticles. Enhancement effects were reported for large (50-nm) platinum particles, as discussed in Section IV.D.2.

C.2.6. PM-IRAS of CO on Nanoparticle Model Catalysts. For completeness, we mention that investigations of CO adsorption on palladium nanoparticle catalysts were also carried out by PM-IRAS. The observed adsorbate species essentially agree with those observed by SFG, and References (*175,306,307,453*) provide more information.

C.2.7. Comparison with CO Adsorption on "Real" Catalysts. Investigations of model catalysts are meaningful only if the results are representative of the behavior of comparable technological catalysts. In this section, CO adsorption on palladium/Al_2O_3/NiAl(1 1 0) model catalysts is compared with adsorption on wet-chemically prepared supported catalysts. In such comparisons, high surface area catalysts must be used that are well characterized with respect to particle morphology. Furthermore, residues resulting from the synthesis (such as chlorine or alkali or alkaline earth metals (*308*)) can complicate adsorption and reactivity profiles and should be avoided. Lear *et al.* (*26,27*) applied a novel synthesis route, using thermally unstable tetramminepalladium(II) tetraazidopalladate(II) ($[Pd(NH_3)_4][Pd(N_3)_4]$) (*309*) rather than conventional $PdCl_2$ or $Pd(NO_3)_2$ as precursors. The catalyst was prepared by a controlled explosion of the precursor, producing well-defined palladium crystallites.

---

[11] We emphasize, however, that although SFG intensities are normalized to the intensity of the incident light, variations in the optical alignment of the various detectors (which can hardly be avoided) still make it difficult to compare exactly experiments with different samples on different days.

Figures 25a–c show (HR)TEM images of a 7% Pd/Al_2O_3 catalyst (94 $m^2 g^{-1}$; dispersion approximately 13%). The palladium particles exhibited a distinct hexagonal structure, consistent with cuboctahedra, presenting (1 1 1) and (1 0 0) low-index planes, and the particle diameters clustered at about 5 and 15 nm.The palladium particles were often composed of crystalline sub-units separated by grain boundaries, twin planes, etc., but nevertheless they were still dominated by well-developed low-index facets with a low level of surface defects. Figure 25d shows a diffuse reflectance spectrum for CO saturation coverage at room temperature. The spectrum is atypical for CO chemisorption on a (conventional) supported palladium catalyst, in that there is effectively no contribution from linear CO at 2050−2100 cm^{-1} (*18*). A corresponding spectrum of a conventional Pd/γ-Al_2O_3 catalyst prepared from $Pd(NO_3)_2$, exhibiting a contribution from linear CO, is shown for comparison in Fig. 25e. The spectrum in Fig. 25d has two intense, symmetrical peaks: a broad one at 1923 cm^{-1} and a sharp feature at 1984 cm^{-1}.

On the basis of CO adsorption investigations of single crystal and nanoparticle model catalysts, (*18,119,182,199*) the 1923-cm^{-1} band can be assigned to CO bonded at threefold hollow sites and to bridge-bonded CO on the (1 1 1) planes of the particles. The origin of the sharp 1984-cm^{-1} feature is more complex. As described above, it may originate from CO adsorbed on (1 0 0) facets and/or from CO bridge-bonded to particle edges and steps (*303*). Taking into account the same "site statistics" considerations stated above for the model catalysts, the high intensity of the 1984-cm^{-1} peak is probably the best attributed to intensity borrowing from

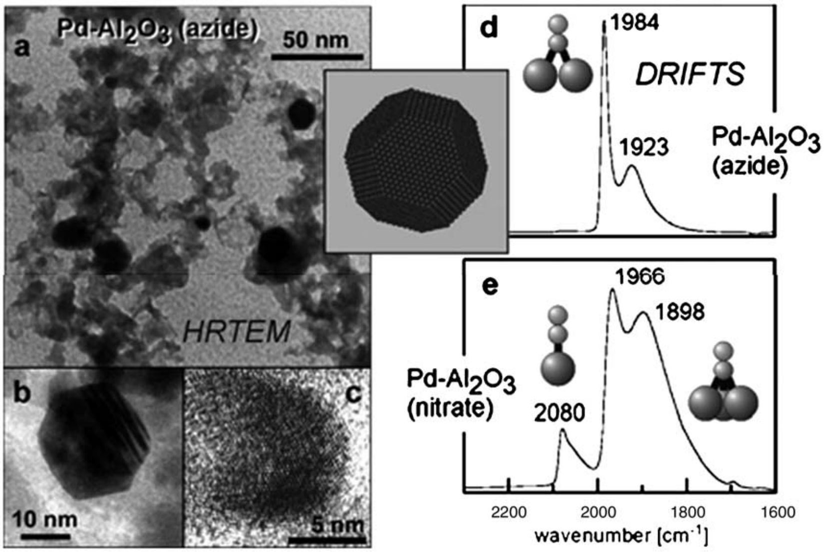

Fig. 25. (a) Transmission electron micrograph of the Pd/Al_2O_3 catalyst prepared from the azide. Images (b) and (c) show a higher magnification of single particles, demonstrating their crystalline structure as well as internal defects. (d and e) Diffuse reflectance IR spectra (4-cm^{-1} resolution) for a saturation coverage of CO at 293 K on (d) the Pd/Al_2O_3 catalyst prepared from the azide and (e) 1% Pd/Al_2O_3 prepared by wet impregnation of γ-Al_2O_3 with $Pd(NO_3)_2$; adapted from Lear *et al.* (*26*) with permission from the PCCP Owner Societies.

bridging CO on (1 1 1) facets (characterized by a peak at 1923 cm^{-1}) (275). The observed spectrum agrees nicely with vibrational spectra of CO on (UHV-grown) well-faceted palladium nanoparticles, corroborating the well-ordered particle surface as determined by HRTEM. Because investigations of Pd/Al_2O_3 model catalyst showed that more intense linear bands were observed for rougher surfaces (101,119,285), the effective absence of on-top CO is a clear indication that the palladium particles in the azide-prepared catalyst have a low concentration of surface defects. The Al_2O_3-supported catalyst prepared from the azide was quite active for propyne hydrogenation, with 100% conversion and 100% selectivity to propane (reaction in a continuous flow reactor at 293 K for a hydrogen:propyne mixture in a 3:1 molar ratio (26,27)). Corresponding spectra of CO on palladium particles derived from other precursors, demonstrating effects of residues, are given in Reference (27).

The similarity in CO adsorption properties of impregnated and model catalysts is mainly attributed to the well-defined palladium particle morphology and is not restricted to alumina supports. A Pd/MgO catalyst (2.5 wt% Pd) was prepared by impregnation of $Mg(OH)_2$ with solutions of $PdCl_2$, followed by drying, calcination, and reduction (105). According to TEM (Fig. 26), the palladium particles had a mean diameter of 15 ± 3.5 nm and frequently had polygonal outlines and straight edges suggesting the presence of low-index facets. The shape was roughly cuboctahedral, again indicating a strong contribution of (1 1 1) and (1 0 0) faces. However, the corners were often truncated, leading to a somewhat rounded appearance at low magnification. Palladium particles located at thin edges of the MgO support allowed side-on views, and a height/diameter aspect ratio of approximately 0.6–0.75 was found, illustrating the three-dimensional nature of the particles. The

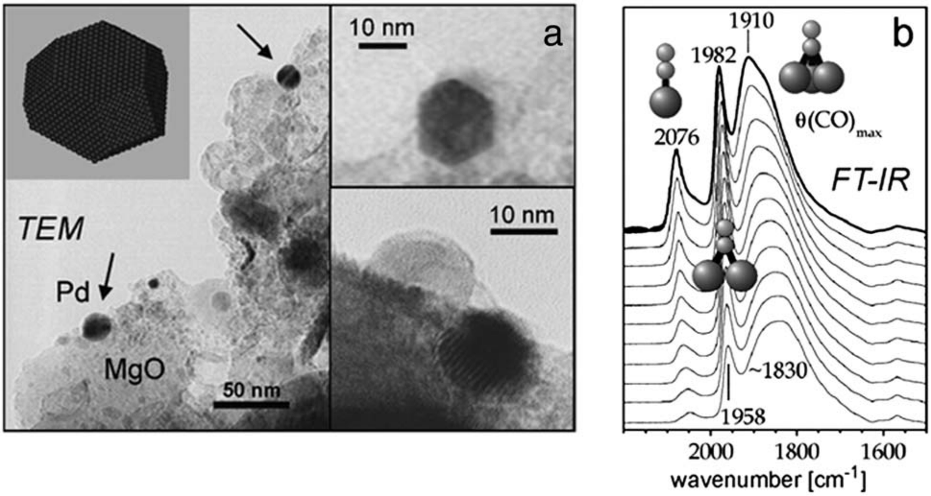

FIG. 26. (a) Transmission electron micrograph of an impregnated Pd/MgO catalyst (2.5 wt% Pd; made from $PdCl_2$). The inset shows particles with various shapes in higher magnification and in profile view, respectively. (b) Transmission IR spectra of CO adsorbed at 300 K; adapted from Bertarione *et al.* (105) with permission. Copyright (2004) American Chemical Society.

crystalline structure of the palladium particles was evident from electron diffraction, showing a typical ring pattern of randomly oriented metal particles (Fig. 3h, with Pd{1 1 1}, {2 0 0}, and {2 2 0} reflections).

The transmission IR spectra of Fig. 26b show bands at 1910, 1982, and $2076\,\mathrm{cm}^{-1}$ (*105*), which again agree well with those observed for Pd/Al_2O_3/NiAl(1 1 0) model catalysts. Accordingly, they are attributed to hollow/bridge bonded CO on (1 1 1) facets, to bridging CO at particle edges/steps and (1 0 0) facets, and to linearly bonded CO, respectively. Although the presence of the on-top band shows that the particle facets were not as perfect as those of the azide-derived catalyst, Fig. 26 is another example demonstrating that Pd/Al_2O_3/NiAl(1 1 0) is a well-chosen model system to represent technological catalysts.

C.3. *CO Dissociation on Palladium Surfaces*

The CO SFG and PM-IRAS spectra and post-"high pressure" AES of the palladium model catalysts did not show indications of CO dissociation (such as decreasing SFG/IR intensity or growing AES lines at 272 eV that would be attributed to carbon formation). Although this result agrees with previous UHV investigations of Pd(1 1 1) (*180,258,310–312*), partial CO dissociation at high pressures cannot be ruled out, because vibrational spectroscopy and AES may not be sensitive enough. A number of investigations of platinum (*279,313*) and rhodium (*14,314*) led to the conclusion that at high (mbar) pressures, CO dissociated even on the (initially) close-packed (1 1 1) surfaces, leading to carbon deposition. Surface roughening at mbar pressures was considered to be responsible for CO dissociation, whereas CO dissociation was absent under UHV. Furthermore, in a number of investigations of mica-, alumina-, and MgO-supported palladium nanoparticles, carbon deposits were also observed, resulting from CO dissociation or disproportionation via the Boudouard reaction (*306,315–318*). However, there are also conflicting reports regarding supported palladium, according to which CO dissociation was not observed (*70,119,152,318–320*).

To explain the disagreement between various investigations of palladium nanoparticles, Henry *et al.* (*70*) suggested that CO dissociation proceeds on a particular type of defect site, which is present only on "ill-shaped" (rough) clusters and not on well-faceted nanoparticles. This suggestion was supported by an XPS study in which partial CO dissociation occurred on a sputtered palladium foil, but was absent on a well-annealed foil (*317*). Another suggestion that may help to explain the observed disagreement is metal–support interactions, as described by Matolín *et al.* (*318*). Apparently, the exact origin of possible CO dissociation on palladium is not fully understood. According to DFT calculations, the direct scission of the C–O bond ($CO \rightleftarrows C + O$) is energetically unfavorable (endothermic by about 2 eV and with an activation barrier > 2 eV) (*321–323*). However, if the reaction proceeds in a concerted motion with the reaction of oxygen with CO ($O + CO \rightleftarrows CO_2$), the net process is the Boudouard reaction ($2CO \rightleftarrows C + CO_2$), which is strongly exothermic. If this reaction is kinetically not hindered, C–O bond scission would be energetically possible.

It is clear that the detection of carbon originating from CO dissociation requires a method that unambiguously reveals the chemical composition of adlayers;

core-level XPS is the apparent method of choice. XPS allows one to distinguish molecular CO (C1s BE of approximately 286 eV) from amorphous/graphitic carbon (approximately 284 eV). Moreover, XPS can also distinguish between the various binding geometries of molecular CO on Pd(1 1 1) (the BE difference is approximately 0.7 eV between hollow-bonded or bridge and on-top CO (*182,192*)) and on other surfaces (*180,181*). Being element-specific and quantitative, XPS also provides direct information about the amount of, for example, CO or carbon deposits (*186*). High-pressure XPS allows the establishment of an equilibrium coverage of CO during measurements at 300 K and higher temperatures; and a further advantage of XPS measurements on reacting samples is that there is no possible contamination during pump down.

The possibility of CO dissociation on Pd(1 1 1) at high pressures was therefore examined by combining HP-XPS and vibrational SFG spectroscopy, in a pressure range from 10^{-6} to 1 mbar at 200–400 K (*253,274,324*). To investigate the influence of surface defects, ion-bombarded Pd(1 1 1) was also investigated. Figure 27 shows SFG and XP spectra of CO adsorbed on perfect (“p”) and defect-rich (“d”) Pd(1 1 1) at 300 K. Comparison of “p” and “d” SFG spectra at 10^{-6} mbar CO (Fig. 27a) shows that ion sputtering gave rise to an additional feature, at 1980 cm^{-1}, which is attributed to CO bridge-bonded to defects (*152*). The two common features, at 1935 and approximately 2075 cm^{-1}, originate from CO on bridge and on-top sites on (1 1 1) terraces, respectively (cf. Figs 15 and 16).

XPS C1s core-level spectra at 10^{-6} mbar of CO are very similar for “p” and “d” surfaces, exhibiting a single peak at 285.6 eV, with a slightly asymmetric shape (Fig. 27b, traces 1 and 2). According to SFG, the C1s peak corresponds to CO at bridge and/or threefold hollow sites at a coverage of about 0.55 ML. However, the CO on the “d” surface, is characterized by a C1s BE that is slightly higher (285.8 eV) than that characterizing CO on perfect Pd(1 1 1), as illustrated by the difference spectrum in Fig. 27c (trace 2-1). Notwithstanding the small value of this shift (approximately 0.2 eV), the corresponding SFG data (Fig. 27a) suggest an additional CO state. Therefore, the C1s BE of 285.8 eV was tentatively assigned to CO bridge-bonded to sputtering-induced defects such as steps, kinks, or vacancies. High-resolution XPS (*182,325*) obtained by using synchrotron radiation would be required for testing of this interpretation.

Raising the CO pressure to 1 mbar shifted the frequency of each of the CO species (dipole coupling) and increased their intensity, especially for on-top CO (Fig. 27a). In agreement with SFG results, the C1s intensity increased (Fig. 27b, traces 3, 4), with the change attributed to a growing feature at about 286.2 eV (Fig. 27c, difference spectrum 4-2), which arises from on-top CO (*182*). The C1s feature at approximately 290 eV originates from gas-phase CO and typically occurred at pressures $>10^{-2}$ mbar. Carbon deposits (amorphous, graphitic, etc.) which would appear at about 284.5 eV (marked by an arrow in Fig. 27b), and palladium carbonyl species (287–288 eV (*326*)) and carbides (<283.5 eV) were not detected. Even if carbon had dissolved in the palladium bulk near the surface region, the escape depth of the C1s electrons (about 2 nm) should be sufficient to have allowed its detection. (The results of similar measurements at 400 K are presented in References (*253,274*).)

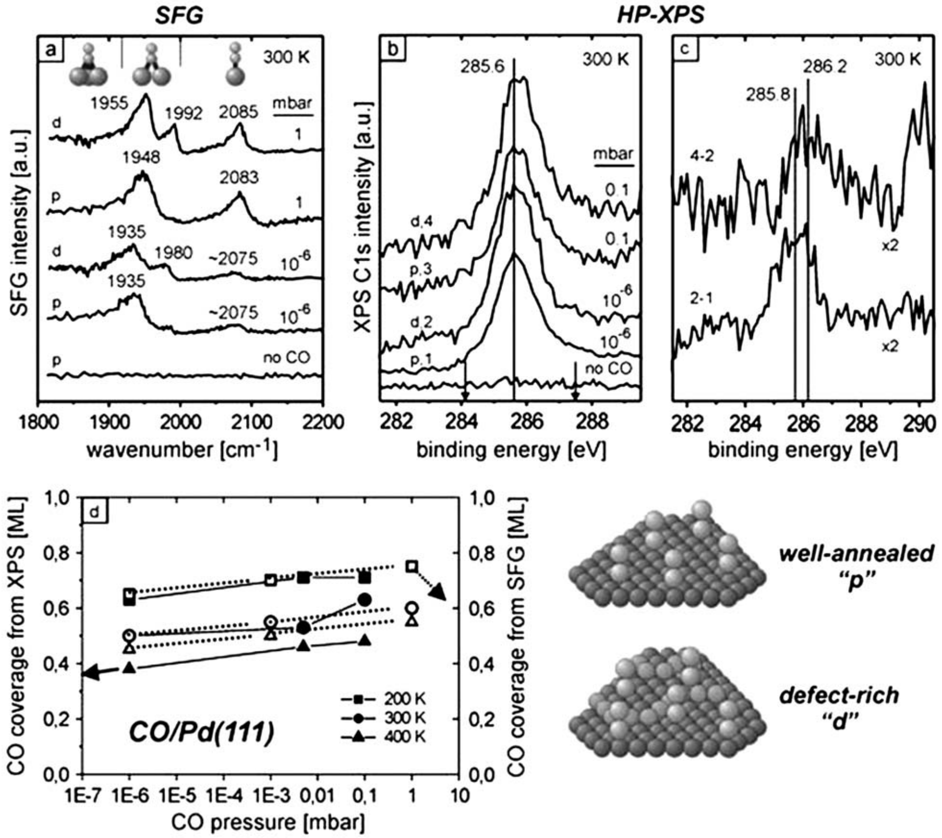

FIG. 27. (a) SFG and (b) XPS C1s core-level spectra measured during CO adsorption at 300 K; "p" and "d" refer to well-annealed (perfect) and defect-rich (ion-bombarded) Pd(1 1 1) surfaces, respectively. In (c) difference spectra are shown indicating adsorption on defect (2-1) and on-top (4-2) sites. XP spectra were normalized to the Pd3d$_{5/2}$ integral intensity at 334.9 eV. (d) Coverage vs. pressure dependence determined from XPS (full symbols, full lines) and from SFG (open symbols, dashed lines); adapted from (*274,324*) with permission from Elsevier.

On the basis of the combined HP-XPS/SFG data, a quantitative analysis of CO coverages at various pressures and temperatures was carried out (*253*). Figure 27d displays the CO coverage on Pd(1 1 1) as a function of the CO background pressure. It is emphasized again that gas cleanliness is crucial to the success of such experiments. When CO was used as received (purity 99.997%), iron and nickel impurities were detected on the surface, and these caused dissociation of CO and produced various carbon species (cf. Fig. 13d) (*253*).

In summary, even in the mbar pressure regime, both methods indicated that CO adsorbed in "regular" adsorption sites (such as hollow, bridge, and on-top sites), and no indications of CO dissociation or carbonyl formation were found. In a simple picture, the upright (perpendicular) adsorption geometry of CO on Pd(1 1 1) (*150,327*) may be one of the reasons explaining the nonoccurrence of CO dissociation. A tilted CO molecule would allow for a better overlap between the CO 2π* orbitals and the metal valence electron density, thus weakening the CO bond (*180,328*). Indeed, CO dissociation was reported for rhodium (*329*), iron (*330*), and chromium (*331*) surfaces, on which CO adopts a tilted geometry. The ability of CO to adopt a tilted geometry on early transition metals has been explained in terms of their ability to accept electrons (attributed to their d electron deficiency) (*332*). In contrast to the above-mentioned metals, palladium has a filled d-band ($4d^{10}$), and CO adsorbs perpendicularly on Pd(1 1 1) (*150,327*). For CO molecules adsorbed on sputter-induced defects, the situation is more complex, but presumably CO is still not tilted enough to provide the geometry required for CO dissociation.

High-pressure SFG spectra of CO on palladium nanoparticles also failed to indicate CO dissociation. With respect to the reported CO dissociation on small palladium particles, it appears that an additional influence may come from the oxide support (interface sites, metal–support interactions, hydroxyl groups, etc.). Along these lines, discrepancies between various investigations of Pd/Al_2O_3 were attributed to differences in catalyst preparation/composition, for example, Matolín *et al.* (*318*) reported PdAl alloys produced by partial reduction of the alumina support. In this case, carbon and oxygen of the CO molecule may bind to Pd and Al, respectively, and the tilted geometry may lead to CO dissociation. Potassium may promote CO decomposition on palladium particles on mica (*315,333*). Increased impingement rates and higher temperatures (e.g., in experiments at 185 mbar and >600 K (*306*)) were also reported to induce CO dissociation, in particular at defect sites of palladium particles.

C.4. *Hydrogen Adsorption, Absorption, and Palladium Hydride Formation on Pd/Al_2O_3 and on Pd(1 1 1)*

Supported palladium is frequently used to catalyze hydrogenation reactions, which explains the large number of investigations of palladium–hydrogen interactions on low- and high-index single-crystal surfaces (e.g., see References (*98,334–336*)). In contrast, there are very few results characterizing well-defined UHV-grown palladium nanoparticles (*68,104,319,337*). Furthermore, there is basically only a single surface science study of hydride phases in palladium nanoparticles (*68*), although palladium hydride is certainly present at high hydrogen pressures[12] and low reaction temperatures. To allow for a better comparison, results characterizing Pd(1 1 1) and palladium nanoparticles are discussed together below.

Well-faceted cuboctahedral palladium nanoparticles, similar to those shown in Figs 14 and 20, were again used (mean size, 5 nm; height, approximately 2 nm; number of atoms/particle, approximately 3000; number of surface atoms/particle, approximately 600; number of particles/cm^2, approximately 1×10^{12}). It is again emphasized that about 75–80% of the surface of the palladium nanoparticles consisted of (1 1 1) facets, with the remaining approximately 20% being (1 0 0) facets.

We focus on dissociative hydrogen adsorption, hydrogen dissolution, and palladium hydride formation (*68*). Figure 28 provides a comparison of H_2-TDS spectra

---

[12] The threshold hydrogen pressure for hydride formation at room temperature is about 20 mbar.

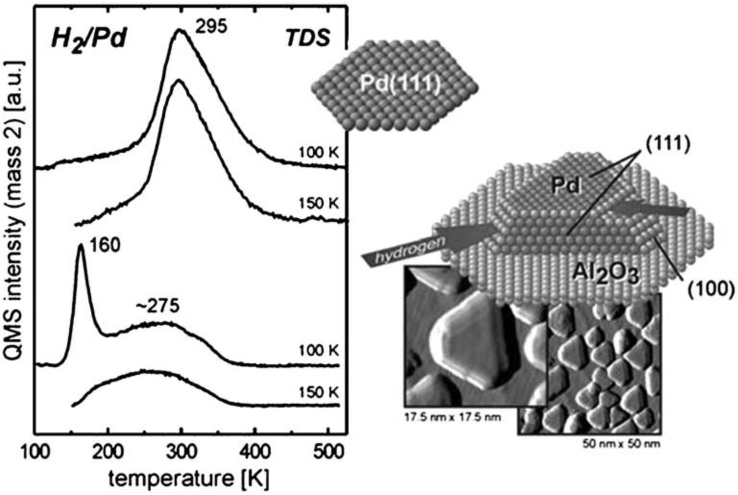

FIG. 28. Thermal desorption spectra of hydrogen acquired after exposure of Pd/Al_2O_3 and Pd(1 1 1) to H_2: Cooling in 2×10^{-7} mbar of H_2 from 300 to 100 K (approximately 80 L; upper traces) and cooling in 2×10^{-7} mbar of H_2 from 300 to 150 K (approximately 150 L; lower traces). Schematic models and STM images of the palladium model catalysts are shown on the right. For simplicity, the ball model shows a smaller particle but with the correct proportions; adapted from *(68)* with permission from Elsevier.

of Pd/Al_2O_3/NiAl(1 1 0) and Pd(1 1 1). We distinguish (i) adsorbed surface hydrogen; (ii) subsurface hydrogen (which is not necessarily restricted to positions between the first and second substrate layers, but may instead be situated within the first 5–10 layers below the surface *(338–340)*; these species are sometimes called near-surface hydrogen or near-surface hydride); and (iii) bulk hydrogen dissolved deep below the surface. Exposure of Pd(1 1 1) to H_2 during cooling from 300 to 100 K (approximately 80 L) produced a H_2-desorption peak at 295 K, attributed to recombinative hydrogen desorption from surface sites (with possible small contributions of subsurface and bulk hydrogen). In contrast, in experiments with Pd/Al_2O_3, a sharp desorption peak appeared at 160 K, followed by a broad desorption at temperatures up to about 350 K. Whereas the latter mostly originates from surface H atoms, the 160 K peak indicates subsurface/dissolved hydrogen. Assuming that the broad peak appearing at about 250 K corresponds to a hydrogen coverage (θ) of 1 ML, the average particle composition is roughly $PdH_{0.3}$ (including surface and dissolved H). When the palladium particles were exposed to more H_2 (approximately 5500 L at 120 K), the 160-K peak increased, and the amount of subsurface hydrogen exceeded that of surface hydrogen by three times (i.e., there was more hydrogen below the surface than on the surface), yielding an average particle stoichiometry of $PdH_{0.8}$. Therefore, the 160-K peak (which is reminiscent of "hydrogen explosion" phenomena *(341,342)*) is attributed to the decomposition of a palladium hydride. Here the term "palladium hydride" includes solid solutions (α-phase) as well as hydride phases with varying stoichiometry and structure (β-phase).

A "near-surface hydride," similar to that shown in Fig. 28 for palladium particles, was also reported for Pd(1 1 1), but its formation required much higher exposures (approximately 5000 L at 115 K) (*340*). An easier hydride formation was reported for more open "rougher" surfaces, for example, at temperatures <140 K, approximately 300 L are sufficient on Pd(1 0 0) (*343*); approximately 50 L are sufficient on Pd(1 1 0) (*344*); approximately 200 L are sufficient on Pd(3 3 1) (*345*); and approximately 40 L are sufficient on Pd(2 1 0) (*338*). This comparison indicates that the activation barriers for hydrogen atom surface to subsurface diffusion for more open surfaces are smaller than for the close-packed Pd(1 1 1). Consequently, because hydride formation is strongly facilitated for palladium nanoparticles (as compared with Pd(1 1 1)), it must proceed predominantly via the small (1 0 0) facets and defects. Apparently, the minority sites ((1 0 0) facets ($<20\%$) and/or edges/steps/and defects ($<10\%$)) govern the hydrogen absorption properties of palladium nanoparticles, rather than the more abundant (1 1 1) facets. The effect of hydrogen surface-to-subsurface diffusion via defects is also corroborated by observations that, after roughening Pd(1 1 1) by ion bombardment, or on (rough) palladium films, hydride formation increased (*319,340*); theoretical calculations of diffusion barriers provide confirmation (*98*).

After H_2 exposure during cooling from 300 to 150 K (approximately 150 L), the 160-K peak was not observed (Fig. 28), because the subsurface hydride is not stable at 150 K. Nevertheless, the onset temperature of hydrogen desorption was still about 70 K lower for Pd/Al_2O_3 than for Pd(1 1 1), a difference that may be attributed to the small particle volume (*68,337*). When the temperature was increased during TPD, hydrogen on Pd(1 1 1) has the additional option of diffusing deeper into the bulk (*98,273*), whereas for nanoparticles hydrogen is restricted to the small particle volume, which provides a reservoir that can supply hydrogen rapidly to the surface. As shown below, this effect has a strong impact on CO–hydrogen coadsorption, and the behavior cannot be mimicked by macroscopic single crystals.

C.5. *CO–H Interactions on Pd(1 1 1) and Pd/Al_2O_3 under UHV*

Catalytic CO hydrogenation on transition metals is among the most important catalytic reactions. Depending on the metal (and support), a variety of products can be obtained, such as CH_4 (in methanation, for example, on nickel or rhodium), CH_3OH (methanol synthesis, for example, on copper or palladium), or higher molecular weight hydrocarbons (Fischer–Tropsch synthesis, for example, on iron or cobalt) (*1,3,249,250,346,347*). Hydrogenation of molecules other than CO is no less important (see, for example, the section on ethene hydrogenation below).

In this section, the coadsorption of CO and hydrogen on palladium nanoparticles and on Pd(1 1 1) under UHV conditions is described. Although the UHV behavior cannot necessarily be extrapolated to high-pressure reactions, the UHV experiments clearly demonstrate the enormous diversity of CO–H interactions on palladium surfaces. The seemingly simple CO–H system becomes complex because of the large number of well-ordered CO structures on palladium surfaces and the various states of adsorbed and absorbed (dissolved) hydrogen, as discussed above. Therefore, it is not surprising that some controversy still persists regarding the mechanism of CO hydrogenation on palladium catalysts (*249,348*). Taking into account that the adsorption of CO and the interaction with H_2 are quite different for palladium nanoparticles and Pd(1 1 1), we also expect significant differences for coadsorption of CO and hydrogen.

The number of investigations of CO–H coadsorption is much smaller than the number of investigations of adsorption of the individual species CO or hydrogen. Furthermore, investigations of coadsorption have typically been carried out by sequential dosing, whereas it is a mixture of these reactants that interacts with the surface during catalysis. Nevertheless, several effects have been reported, exemplified by blocking of hydrogen adsorption by CO (*344,349,350*), formation of subsurface hydrogen (H) and absorption of H (*343,344,351–353*), CO-induced hydrogen dissolution in the palladium bulk (*273,350,354,355*), differences in catalytic activity of surface and bulk H (*356–358*), etc. Recent STM investigations by the Salmeron group provided images of a hydrogen-induced compression of CO and oxygen islands on Pd(1 1 1), as well as of hydrogen dissociation and dissolution (*85,86,203,359,360*). Investigations of coadsorption on nanoparticles are scarce, and those discussed below were carried out with well-faceted palladium nanoparticles of cuboctahedral shape (mean size, 5 nm; height, approximately 2 nm; number of atoms/particle, approximately 3000; number of surface atoms/particle, approximately 600) (*68*). It was found that, apart from structural differences between palladium nanoparticles and Pd(1 1 1), the limited volume of palladium nanoparticles is crucial in determining their properties for coadsorption of CO and hydrogen. In the following, both types of gas exposure, sequential dosing and co-dosing experiments, are described, and it is shown that the resulting CO–H coadsorbate structures strongly depend on (i) the palladium surface structure, (ii) the surface temperature, and (iii) the type of gas exposure.

C.5.1. CO Adsorption Followed by Hydrogen Adsorption. It is well known that preadsorbed CO effectively prevents hydrogen adsorption, which may either be an undesired poisoning effect or a desired means of controlling selectivity (*361*). On CO-precovered Pd(1 1 1) ($\theta_{CO} = 0.75-0.33$) and CO-precovered palladium nanoparticles, dissociative adsorption of H_2 did not occur (*98,273,362*). This point is illustrated in Figs 29a and b for Pd(1 1 1), as no changes were observed by SFG or LEED after H_2 exposure (for LEED and TDS results, see Reference (*273*)). Although the CO structure on Pd(1 1 1) formed at 0.75 ML is quite dense (Fig. 30a), purely steric arguments cannot explain the observed site blocking. However, DFT calculations determined a large activation barrier, which renders H adsorption on a CO-precovered surface very unlikely (*98*). A practical means for visualizing the potential energy surface (PES) of a H_2 molecule approaching the palladium surface is the so-called elbow plot. The potential energy is scanned along two of the six degrees of freedom of the molecule (height and H–H distance), with all other degrees of freedom (two angles and the horizontal position of the adsorbate) kept fixed. Figure 30b shows the PES of a H_2 molecule in bridge-top-bridge configuration (*363*) above CO-precovered Pd(1 1 1). For the adsorption geometry chosen, the transition state lies almost 5 eV above the energy of the desorbed H_2 molecule (i.e., the minimum energy path (MEP) is strongly endothermic (CO molecules were not allowed to relax)). When all adsorbates were allowed to relax, the transition state was still approximately 2.5 eV higher in energy than the initial state (atomic

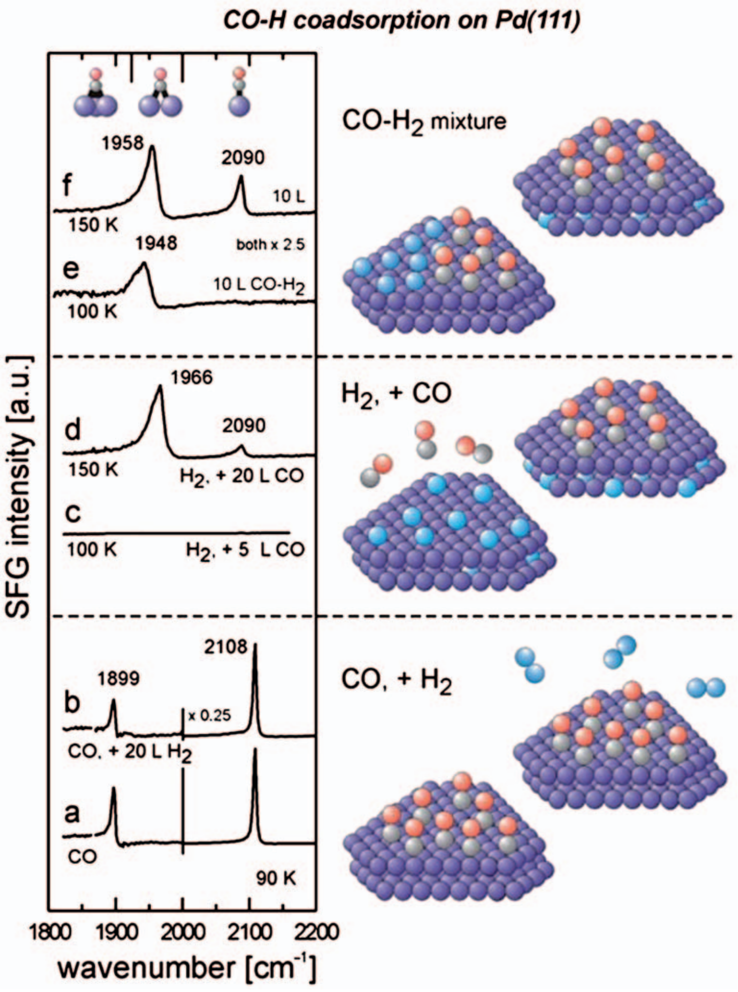

FIG. 29. SFG spectra of CO–H coadsorbate structures on Pd(1 1 1) demonstrating the difference between sequential dosing of CO and H_2 (a–d) and the dosing of CO + H_2 mixtures (e, f). After saturating Pd(1 1 1) with approximately 1000 L of CO by cooling in 3×10^{-6} mbar of CO from 300 to 90 K (a), 20 L of H_2 were dosed at 90 K (b). After cooling of Pd(1 1 1) in 1×10^{-7} mbar of H_2 from 300 to 100 K (approximately 100 L), 5 L of CO were dosed (c). After cooling of Pd(1 1 1) in 1×10^{-7} mbar of H_2 from 300 to 150 K (approximately 50 L), 20 L of CO were dosed (d). Exposure of Pd(1 1 1) to 10 L of a 1:1 (molar) CO:H_2 mixture at 100 K (e) and 150 K (f); adapted from *(98)* with permission from Elsevier.

configuration shown in Fig. 30c). When CO-precovered palladium particles were exposed to H_2, no indication of significant hydrogen adsorption was found.

C.5.2. Hydrogen Adsorption Followed by CO Adsorption. When the gas dosing sequence was reversed, the coadsorption behavior became more complex and depended on the temperature and the palladium surface structure. We start with measurements at 100 K. On hydrogen-precovered Pd(1 1 1), no CO adsorption was

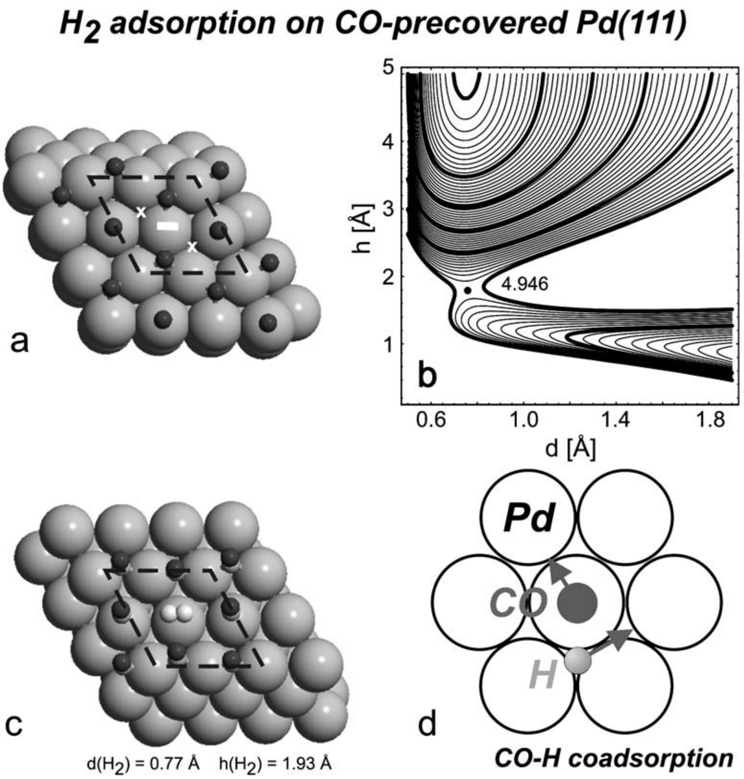

FIG. 30. (a) The (2 × 2)-3CO structure on Pd(1 1 1). The white bar indicates the position and orientation of the adsorbing H_2; "x" marks the final H adsorption positions (98). (b) Elbow plot of the vertical approach of a H_2 molecule in bridge-top-bridge configuration above CO precovered ($\Theta =$ 0.75 ML) Pd(1 1 1). All coordinates besides h and d of the molecule were kept fixed. (c) Transition state along the dissociative adsorption pathway of H_2 above CO-precovered Pd(1 1 1). The CO molecules initially adsorbed at fcc hollow sites are pushed towards bridge positions. (d) "Destabilization" of on-top CO by neighboring hydrogen; adapted from (98) with permission from Elsevier.

observed (Fig. 29c), in agreement with DFT calculations indicating an unstable CO adsorption configuration under these conditions. At 100 K, adsorbed H cannot overcome the diffusion barrier of about 0.5 eV between an fcc threefold hollow surface adsorption site and a subsurface octahedral site (98). Consequently, H is confined to the surface[13] and prevents CO adsorption.

In contrast, when the H-precovered Pd(1 1 1) surface was exposed to CO at 150 K (Figs 29d and 31a), a different structure was observed, including bridge (1966 cm^{-1}) and on-top (2090 cm^{-1}) bonded CO, typical of approximately 0.65 ML of CO. The SFG spectrum is even identical to a corresponding measurement without preadsorbed hydrogen, suggesting that surface hydrogen was absent—that is, there

---

[13] Assuming a prefactor of $10^{13}\,\mathrm{s}^{-1}$, a temperature of about 150 K would be required to produce a measurable subsurface population of H within a few minutes (98).

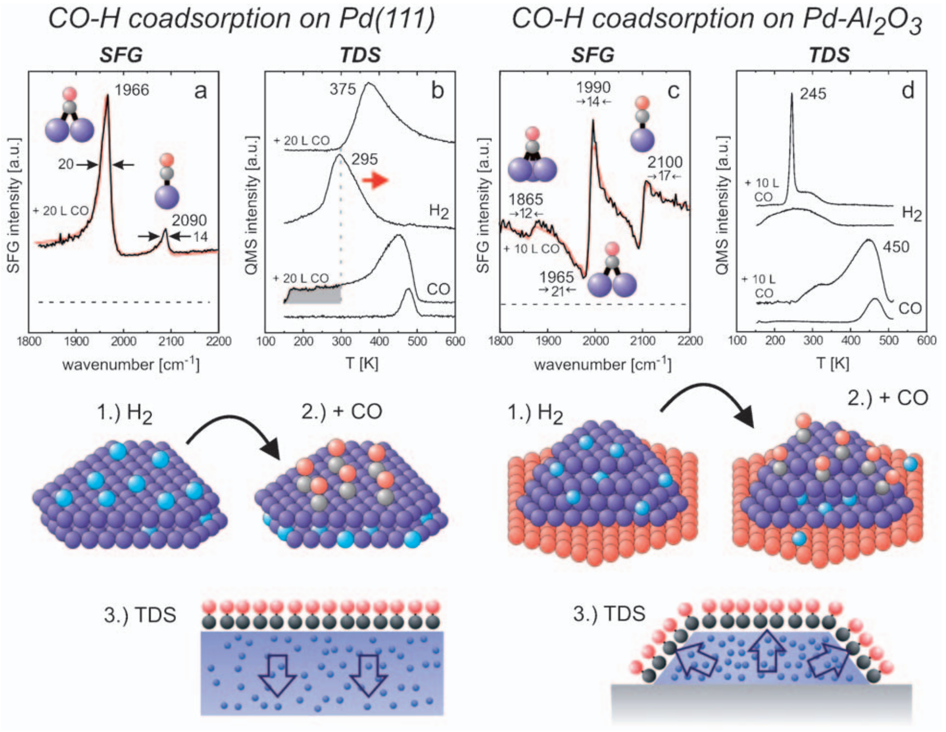

FIG. 31. Sequential dosing of H_2 and CO on Pd/Al$_2$O$_3$ and Pd(1 1 1): After cooling in H_2 at 2×10^{-7} mbar from 300 to 150 K (approximately 150 L), SFG (a, c), and TDS (b, d) measurements were made (lower traces). After a repeat of the H_2 exposure and subsequent adsorption of 10–20 L of CO at 150 K, SFG and TDS spectra were again acquired (a–d; upper traces). The models illustrate the locations of CO and hydrogen; adapted from (*68*) with permission from Elsevier.

was a complete removal of surface hydrogen by CO. This result was confirmed by CO-TDS indicating a CO-saturated surface (Fig. 31b (*273*)). After adsorption of 20 L CO on H-precovered Pd(1 1 1) at 150 K, H_2-TDS indicated a H_2 desorption peak that was shifted from 295 to 375 K and had a pronounced high-temperature tailing, typical of diffusion-controlled desorption kinetics (Fig. 31b) (*339,343,344,349,364*). This result indicates that at 150 K CO removes/replaces adsorbed hydrogen from the surface, which moves into the palladium bulk (see schematics in Fig. 31). CO may in fact promote H dissolution by reducing the H surface to subsurface diffusion barrier, or as suggested by Eriksson and Ekedahl (*354*), by temporarily increasing the concentration of local surface hydrogen, which promotes dissolution of H.

The coadsorption of CO and hydrogen on Al$_2$O$_3$-supported palladium nanoparticles was found to be quite different from that on the single crystal. As shown in the preceding section on palladium hydride formation (Section IV.C.4), H subsurface/bulk dissolution occurs more easily in palladium nanoparticles. Consequently, preadsorbed H can be replaced from the palladium particle surface even at 100 K, leading to a CO-saturated surface (cf. Fig. 31c); thus, in contrast to the observations made with Pd(1 1 1), there is no blocking of CO adsorption on the nanoparticles at 100 K.

Figures 31c and d show results of a UHV coadsorption experiment at 150 K,[14] with H_2 dosed first and CO second. After saturation with hydrogen, H_2-TDS traces as described above were observed (Figs 28 and 31d). No SFG signals (apart from the nonresonant background; dashed line) were detected, because the Pd—H stretch (at approximately 500 cm^{-1}) was out of range. The small peak in CO-TDS (Fig. 31d) indicates a negligible amount of residual CO (*273*). After dosing of CO onto the H-covered particles at 150 K, SFG detected a dominant CO peak at 1990 cm^{-1}, with additional weaker signals at 2100, approximately 1965, and approximately 1865 cm^{-1}, typical of a near saturation coverage (Fig. 31c; resonance frequencies and linewidths are indicated; fitted spectra in red). As discussed above, the intense peak at about 1990 cm^{-1} originates from CO bridge-bonded to particle edges and steps (*152,303*), with a possible small contribution from CO on (1 0 0) facets (*17*). Intensity borrowing from bridging CO on (1 1 1) facets (peak at about 1965 cm^{-1}) presumably enhances the 1990-cm^{-1} peak (*17,63*). The peaks at 2100 and about 1865 cm^{-1} are attributed to on-top and hollow-bound CO on (1 1 1) facets, respectively.

The amount of CO adsorbed on the palladium particles can be deduced from CO-TDS (Fig. 31d). The CO-TDS spectrum was identical to that observed after dosing of the same amount of CO on the clean particles, demonstrating that the particles were fully covered with CO and that H was replaced from the palladium surface. However, H had not desorbed because the H_2-TDS experiment (Fig. 31d) indicated that the overall amount of hydrogen was unchanged. Apparently, CO had displaced surface H to the subsurface and bulk of the palladium nanoparticles (see schematics in Fig. 31; partial H spillover to the support is unlikely because no OH groups or H_2O were detected).

Up to this point in the discussion, the coadsorption behavior of CO and hydrogen on palladium particles is roughly similar to that on Pd(1 1 1), that is, in both cases, CO displaced surface H into the palladium bulk (ignoring for the moment the different behavior at 100 K). However, it is important that there are striking differences between palladium particles and Pd(1 1 1) with respect to the *desorption* of dissolved hydrogen (Fig. 31). Approximately 50% of the hydrogen desorbed from the palladium particles in a very sharp peak (Fig. 31d), similar to the decomposition of the hydride phase represented in Fig. 28. This result indicates that CO had displaced H to the subsurface of the nanoparticles, increasing the near-surface H concentration and producing a hydride-like phase, even at 150 K. As a consequence of the CO overlayer on the palladium particles, the hydrogen desorption maximum shifted to 245 K, but desorption still occurred *before* CO desorption started. In contrast, on Pd(1 1 1), the replacement of surface H by CO did not produce such a sharp H_2 desorption peak (Fig. 31b), and H_2 desorption started only after a considerable amount of CO had desorbed, generating free sites for H recombination (shaded area in Fig. 31b). Apart from the differences between Pd/Al_2O_3 and

---

[14] Hydrogen dosage was carried out by cooling of the sample in 2×10^{-7} mbar of hydrogen to exclude residual CO adsorption, but hydrogen exposure at 150 K yields the same result.

Pd(1 1 1) discussed above, the "explosive" desorption of the hydride phase "through" a CO-layer which occurs only for palladium nanoparticles is remarkable.

The reason for this behavior is not easily understood. At first, one may expect that structure effects are responsible, that is, that there are sites on palladium nanoparticles that allow hydrogen recombination in the presence of a CO overlayer. However, because the reverse process (hydrogen adsorption on a CO-covered surface) does not occur, these sites must have been produced during the TDS experiment. Another possibility is that it is rather the finite particle size or limited volume of the nanoparticles that is important. When palladium hydride decomposition generates a hydrogen "pressure" inside a palladium nanoparticle, the small volume does not allow it to accommodate excess hydrogen. Thus, surface CO is pushed aside, enabling hydrogen desorption "through" the CO overlayer. In contrast, when CO prevents H_2 desorption from Pd(1 1 1), near-surface hydrogen has the additional option of diffusing deeper into the bulk during the TPD experiment (which leads to the high-temperature tailing shown in Fig. 31b).

To differentiate between structure and volume effects, Pd(1 1 1) and Pd(1 1 0) crystals were exposed to large amounts of hydrogen (*ca.* 10 000 L at 130 K) to produce near-surface hydrides (*340,344*), followed by 20 L of CO to replace surface hydrogen. In subsequent TDS experiments, hydrogen desorption started only at temperatures exceeding 300 K (maximum approximately 370 K; similar to Fig. 31b), including a high-temperature tail. Similar results were reported for Pd(1 1 0) and Pd(1 0 0) (*344,355*). Consequently, for Pd(1 1 1), (1 1 0), and (1 0 0) single crystals, it seems to be easier to decompose a near-surface hydride by bulk dissolution of H than by replacing surface CO and subsequent desorption. Such a route is not feasible on palladium nanoparticles, which suggests that the observed hydrogen desorption in the presence of a CO layer is in fact related to the limited volume of the palladium nanoparticles and not to their particular surface structure. Apparently, a volume on the scale of a cubic nanometer cannot be modeled by macroscopic single crystals. A contribution involving desorption via the metal oxide interface cannot, however, be excluded.

C.5.3. Adsorption of CO+H_2 Mixtures. Because exposure of the surface to premixed $CO + H_2$ is more representative of catalytic reaction conditions than sequential dosings, a number of experiments have been done with these mixtures. When a 1:1 (molar) $CO:H_2$ mixture was used for dosing, the adsorbate structures were again found to be temperature-dependent for Pd(1 1 1) and independent of temperature for palladium particles. Dosing of a $CO + H_2$ mixture onto Pd(1 1 1) at temperatures less than about 125 K produced a single CO resonance in SFG (1948 cm^{-1}) (Fig. 29e). Dosing of CO alone under the same conditions yielded a strong additional on-top CO peak at approximately 2090 cm^{-1}, which demonstrates that, in the presence of adsorbed H, the formation of on-top CO was strongly suppressed. This result is surprising because separate islands of CO and H are formed upon coadsorption (*86*), and it is difficult to understand how the CO islands are affected by H.

An explanation emerged from DFT calculations, which indicate the absence of on-top CO to H atoms diffusing between hollow sites via bridge sites, thereby destabilizing neighboring on-top CO molecules[15] (Fig. 30d). The CO–H interaction at the island boundaries is "passed on" to inner CO island regions (*86*), ultimately resulting in the absence of on-top CO. A destabilization of on-top CO (and its shift to bridge sites) upon adsorption of hydrogen has also been reported for Pt(1 1 1) (*365*), Pt(3 3 5) (*288*), Ni(1 1 1) (*366*), and Ni(1 0 0) (*367*).

When a $CO + H_2$ mixture was adsorbed on Pd(1 1 1) at 150 K (Fig. 29f), hydrogen was no longer confined to the surface, and CO was able to replace surface hydrogen, which moved to palladium subsurface/bulk sites. SFG (and LEED and TDS (*273*)) allowed detection of CO adsorbate structures identical to those observed after exposure to pure CO. Adsorption of mixtures of $CO + H_2$ on palladium nanoparticles yielded CO-saturated surfaces, both at 100 and 150 K, attributed to the facile CO-induced displacement of adsorbed H into the particle volume. The SFG spectra were qualitatively the same as that in Fig. 31c.

C.5.4. Summary. Although the coadsorption behavior of CO and hydrogen on palladium is quite complex and depends sensitively on a number of parameters, it can be explained by considering the mutual site blocking by CO and H, and whether H is confined to the palladium surface under the experimental conditions. The latter depends on the probability of H surface-to-subsurface/bulk diffusion, which, in turn, depends on the palladium surface structure (mainly on the number of minority sites other than (1 1 1)) and on the exposure temperature. For palladium nanoparticles, smaller surface-to-subsurface diffusion barriers are very likely (although this point needs further theoretical checking), and H can thus more easily escape to the subsurface. Therefore, site blocking or destabilization effects of hydrogen on CO are absent from palladium nanoparticles even at 100 K, and the elimination of these effects drastically changes the coadsorption behavior of CO and hydrogen on nanoparticles. Furthermore, finite size effects influence the interaction of CO and hydrogen by confining H to the small volume of a palladium particle. In contrast, on palladium single crystals, hydrogen can diffuse into the palladium bulk so that CO–H interactions are avoided. The onset temperature of hydrogen diffusion into the palladium bulk was investigated for Pd(1 1 1), both experimentally and theoretically (for details, see Reference (*98*)), indicating that bulk diffusion of H occurred at about 125–150 K. Thus, TDS reactivity investigations of palladium single crystals can be quite misleading, because the surface concentration of H may change markedly during the TDS experiment.

Evidently, palladium hydrides deserve more attention by surface scientists. In the course of a typical high-pressure catalytic hydrogenation reaction at room temperature or higher temperatures, hydrogen can easily enter the palladium subsurface/volume region, but whether dissolved hydrogen is present in an appreciable amount will depend on the hydrogen partial pressure.

---

[15] In fact, an energy of approximately 0.6 eV is gained when a hydrogen atom moves between two hollow sites via an adjacent bridge site and an on-top CO molecule is pushed to the bridge site farthest away from the hydrogen atom (*98*).

C.6. *CO Hydrogenation on Pd(1 1 1) and Pd/Al_2O_3 at Atmospheric Pressure*

C.6.1. High-pressure Spectroscopy. The diverse behavior of CO–H coadsorbate structures under UHV, which depends on the palladium surface structure, adsorption temperature, and type of gas exposure, makes predictions of adsorbate geometries under catalytic reaction conditions difficult. Consequently, SFG spectra were also acquired under the high-pressure/high-temperature conditions of technological catalysis (*249,348,368*), when a dynamic equilibrium between gas phase and surface species is established (Figs 32a–c) (*68,98,152,273*). A CO:H_2 molar ratio of 1:10 was chosen for high-pressure experiments to increase the probability of the presence of surface H, which is required for catalytic hydrogenation (as shown above, CO rapidly displaces surface H (*68,98,273*)). In practical catalysis, the sum of the partial

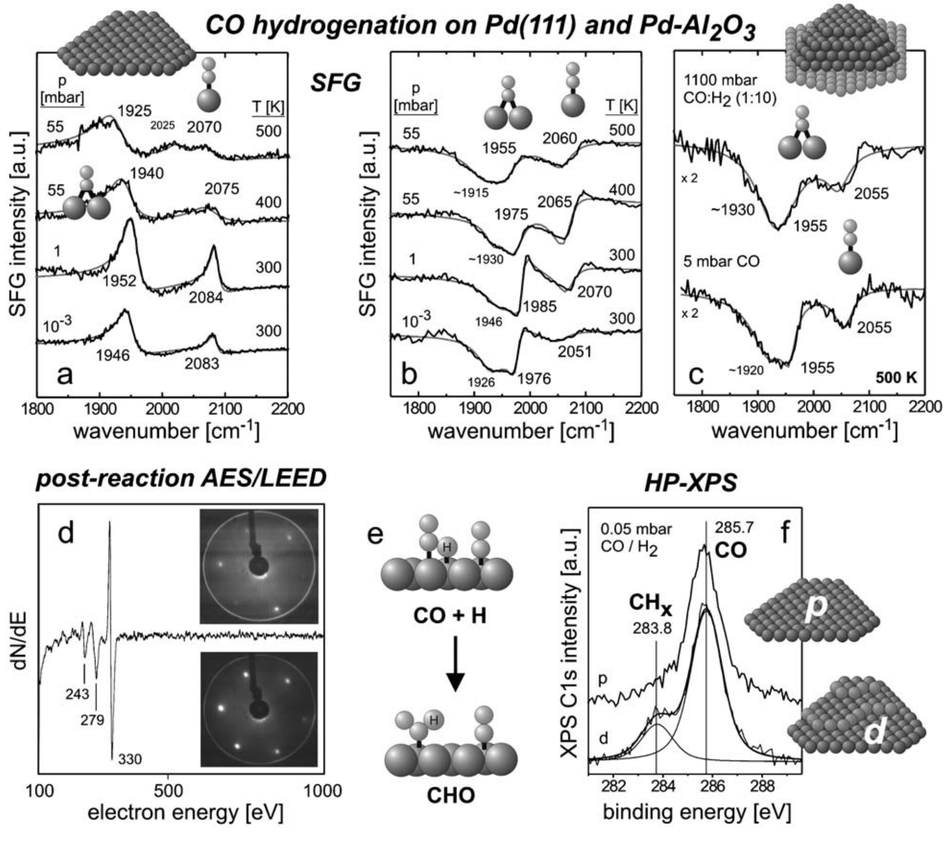

FIG. 32. High-pressure SFG spectra of a 1:10 (molar) CO:H_2 mixture on Pd(1 1 1) (a) and on Pd/Al_2O_3 (b, c) (*68*). Pressures and temperatures are indicated. (d) LEED patterns recorded before (lower) and after (upper) high-pressure gas exposure to Pd(1 1 1) (*273*). The post-reaction AE spectrum indicates that the surface remained clean during 6 h of gas exposure. (e) Schematic illustration of the reaction of on-top CO with hollow-bonded H to adsorbed formyl. (f) C1s XP spectra of smooth (perfect "p") and defect-rich ("d") Pd(1 1 1), acquired with the sample in 0.05 mbar of CO + H_2; the "d" spectrum shows an additional peak at 283.8 eV, attributed to carbonaceous deposits (*324*).

pressures of $CO + H_2$ (10–25 bar) is still higher, but increasing the pressure by up to six orders of magnitude was found to induce only small changes in the CO coverage (Fig. 32). At 500 K, the CO frequency is redshifted, a result that is attributed to a reduction in coverage; there was also a temperature-induced line broadening (*17*). Nevertheless, the SFG spectrum at a pressure of 1.1 bar characterizing $Pd/Al_2O_3/NiAl(1\,1\,0)$ (Fig. 32c) is very similar to IR spectra reported by Hicks and Bell (*368*) for 5% Pd/SiO_2 at about 10 bar, indicating that the Pd/Al_2O_3 model catalysts mimic a sample resembling a technological catalyst quite well.

Under all the conditions investigated (Fig. 32), SFG indicated high CO coverages (approximately 0.5 ML on Pd(1 1 1) and close to saturation on palladium particles). Under static UHV conditions, such high CO coverages prevent dissociative hydrogen adsorption, because of the approximately 2.5-eV activation barrier indicated by DFT calculations for hydrogen adsorption on CO-covered Pd(1 1 1) (*98*). Furthermore, recent STM observations of H/Pd(1 1 1) suggest that dissociative hydrogen adsorption requires at least three neighboring empty Pd sites (*203*), which are rare at such high CO coverages and render hydrogen adsorption even more unlikely. It therefore might at first be considered somewhat puzzling that CO hydrogenation works at all on technological catalysts, although it is often true that only a small fraction of the surface sites of a catalyst are active.

However, a static (UHV) picture is not appropriate here. Under the dynamic equilibrium conditions of a high-pressure/high-temperature catalytic reaction, even the unlikely event of hydrogen adsorption has a nonzero probability because of the adsorption/desorption equilibrium of CO and the high hydrogen impingement rate (which is about 40 times higher than that of CO and of the order of 10^8/Pd surface atom × s). Isotope exchange experiments with a mixture of ^{13}CO and ^{12}CO on Pd(1 1 1) indicated that even at 200 K a CO layer was exchanged within minutes at mbar pressures (*152*). On the basis of TDS spectra, an exchange (or desorption) rate of $\sim$0.1–1 ML s^{-1} is estimated to pertain at 450 K. Even if only a negligible number of free adsorption sites were present (resulting from thermal fluctuations on the CO-covered surface), for example, one site per 10^6 Pd atoms, the high H_2 impingement rate allows for a nonnegligible hydrogen adsorption. At high temperatures, the increased fraction of high kinetic energy hydrogen molecules may also raise the reaction probability.

There is also another effect (apart from the impingement rates) that may facilitate the reaction. The high-pressure spectra shown in Figs 32a and b were different from corresponding UHV spectra for $\theta_{CO} \sim 0.5$. On Pd(1 1 1) at 500 K, a peak at 1920 cm^{-1} was accompanied by weak features at about 2025 and 2070 cm^{-1}, the latter two pointing to on-top CO (Fig. 32a). In low-temperature (UHV) CO spectra, a bridge- (or hollow-) bonded CO signal at about 1925 cm^{-1} did not occur in combination with on-top CO (cf. Fig. 15) (*273*). Consequently, the species characterized by the peaks at 2070 and 2025 cm^{-1} may indicate that the Pd(1 1 1) surface is (partially) roughened under reaction conditions (in particular, the low-frequency on-top CO species should originate from CO bonded to low-coordinated sites). An adsorbate structure different from that indicated by UHV spectra was also observed for Pd/Al_2O_3, whereby a bridging species characterized by a peak at 1955 cm^{-1} was accompanied by an on-top feature at about 2060 cm^{-1} (Fig. 32b). Such an on-top CO species characterized by a low-frequency peak does not occur under UHV (285,296), and the result again points to a possible surface roughening. However, it is evident that the high-pressure adsorbate phase was not induced by hydrogen, because corresponding spectra obtained with the sample in pure CO were nearly identical. In any case, post-reaction LEED (Fig. 32d for Pd(1 1 1) (273)) and CO-SFG did not indicate any surface reconstruction or modified spectrum, demonstrating that any CO-induced roughening must be either reversible or rather moderate, if present at all.

Alternatively, the additional on-top CO species observed at mbar pressures may rather originate from an imperfectly ordered CO phase, which may facilitate CO–H interactions. Taking into account DFT calculations favoring the CO + H reaction on a single metal atom (321), the on-top CO species would react with hollow-bonded H to produce CHO (formyl; Fig. 32e). Although further experiments and calculations are required to understand this adsorbate structure, it is evident that the equilibrium conditions of a high-pressure reaction led to adsorbate arrangements that could not be reproduced under static UHV conditions.

In any case, the observed high CO coverage may still be responsible for the low CO hydrogenation rate on palladium catalysts. Gas chromatographic and mass spectroscopic analysis detected only trace amounts of reaction products (methanol or methane), consistent with a low turnover frequency (TOF) in the reaction catalyzed by unpromoted palladium under the applied conditions (the TOF was of the order of $5 \times 10^{-4}\,s^{-1}$ at 1000 mbar of $CO + H_2$ (in a molar ratio in the range of 1:4 to 1:2) at 550 K (284,348,369,370)), and in particular, with the low palladium surface area of the model catalysts (approximately 0.25–0.5 cm^2), which may only produce about 6×10^{-4} mbar of methanol (or methane) after 6 h (which is below the GC/MS detection level). Nevertheless, the SFG spectra closely resemble IR spectra recorded by Hicks and Bell with technological catalysts, and we refer to Reference (368) for a description of kinetics data.

A final point concerns the state of adsorbed hydrogen. We have deliberately chosen reaction conditions that avoid the formation of β-palladium hydride (on the basis of phase diagrams for palladium hydride formation in bulk palladium), which would restructure the palladium lattice and destroy the well-defined structure of the Pd(1 1 1) single crystal. However, surface H diffuses easily into the palladium bulk under reaction conditions, and large amounts of H_2 were actually detected by post-reaction H_2-TDS. Although β-palladium hydride is not stable under the applied reaction conditions, there was a considerable amount of dissolved hydrogen, and its involvement in the catalytic reaction cannot be ruled out (for a discussion on the potential activity of palladium hydrides, see Section IV.I.2 regarding C_2H_4 hydrogenation). Furthermore, under technological reaction conditions ($CO:H_2$ (molar) approximately 1:3, 25 bar, 550 K), it is possible not only that significant amounts of hydrogen are dissolved in the palladium bulk but also that (initial stages of) palladium hydride phases are present (bulk phase diagrams may not be entirely appropriate for palladium nanoparticles). This hydrogen would change the atomic structure of the nanoparticles and further modify their catalytic properties. It has been suggested that dissolved (subsurface) hydrogen may exhibit catalytic properties different from those of adsorbed hydrogen, for example, in catalytic hydrogenation or hydrodechlorination reactions (337,356–358).

C.6.2. Selectivity of CO Hydrogenation on Palladium Surfaces. The reaction selectivity in CO hydrogenation on transition metals is frequently discussed in terms of the metal's ability to dissociate CO and produce a surface carbon species ($CO \leftrightarrows C + O$) (*249,348*). Because oxygen can react easily with CO ($O + CO \leftrightarrows CO_2$), the net process is the Boudouard reaction ($2CO \leftrightarrows C + CO_2$). Accordingly, metals that readily dissociate CO produce methane or higher molecular weight hydrocarbons by the stepwise hydrogenation of surface carbon, whereas those metals which do not dissociate CO mainly produce compounds with intact C–O bonds, such as methanol, ethanol, dimethyl ether, etc. Indeed, for methanation ($CO + 3H_2 \leftrightarrows CH_4 + H_2O$) at atmospheric pressure (*371,372*), an order of decreasing activity Ru > Fe > Ni > Co > Rh > Pd > Pt > Ir has been found, related to the CO dissociation probability on these metals.

Apart from the type of metal itself, structure sensitivity is another key effect determining the CO dissociation probability (e.g., Rh(1 1 1) and (1 0 0) single-crystal surfaces do not dissociate CO (*373,374*), whereas Rh(2 1 0) (*375*) and rhodium nanoparticles with diameters of about 2–3 nm do (1 0 1)).

As shown above, CO does not dissociate on smooth and rough palladium surfaces even at mbar pressures. CH_3OH should therefore be the main product on palladium catalysts, but CH_4 formation was also detected experimentally (*371,372*). This observation suggests that the mechanism must include other routes apart from CO dissociation, for example, the direct hydrogenation of CO ($CO + xH \leftrightarrows CH_xO$), followed by C–O bond scission ($CH_xO \leftrightarrows CH_x + O$) and hydrogenation to give methane (or further dehydrogenation of CH_x), as illustrated in Fig. 33. Accordingly, it is worthwhile to examine the adsorption and dissociation of CO even during catalytic CO hydrogenation (i.e., in the presence of hydrogen).

Figure 32f shows HP-XP spectra of $CO + H_2$ at 0.05 mbar in a 1:10 molar ratio at 300 K. SFG detected high CO coverages (approximately 0.65 ML) under these conditions, as discussed above. On smooth Pd(1 1 1), XPS (Fig. 32f) did not give any indication of carbon(aceous) deposits, but on ion-bombarded Pd(1 1 1), XPS indicated (besides a peak at 285.7 eV: molecular CO; *ca.* 0.6 ML) another peak, at 283.8 eV, typical of carbonaceous species (carbon or CH_x; roughly 0.1 ML).

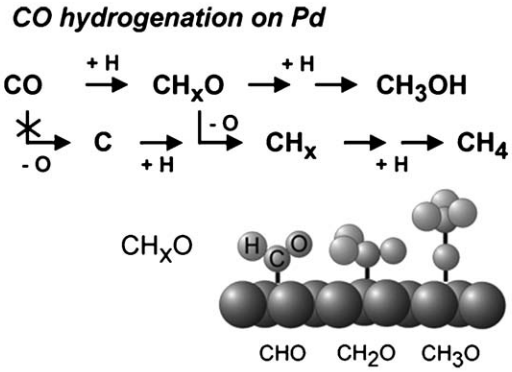

FIG. 33. Schematic illustration of potential CO hydrogenation routes on palladium catalysts.

On the basis of these observations, the following picture of CO hydrogenation is suggested (Fig. 33). Because (pure) CO does not even dissociate on the sputtered surface, the dissociative mechanism on that surface can be excluded. CH_xO species, formed from CO and H via a nondissociative mechanism, must be the precursors for subsequent hydrogenation or C–O bond cleavage. Furthermore, the formation of CH_xO seems to be facilitated by surface defects. This statement agrees with the results of investigations of CO hydrogenation on supported palladium catalysts, indicating CH_xO species (*376,377*), and with density functional calculations (*321*), suggesting the formation of CHO (by CO insertion into a Pd–H bond) as the rate-limiting step of CO hydrogenation. The absence of carbonaceous species on perfect Pd(1 1 1) indicates that CH_xO formation from CO and H does not occur (or is very slow), because the decomposition of CH_xO to CH_x (if produced from other sources, e.g., methanol; see Section IV.K.1) is fast even on Pd(1 1 1).

The probability of C–O bond scission within CO or CH_xO is probably related to the adsorption geometry of these species. Whereas CO adsorbs perpendicularly on Pd(1 1 1), the C–O bond in CHO (and CH_2O) species is tilted with respect to the palladium substrate (*378*). The tilted arrangement may allow for a better overlap between the CH_xO orbitals and the metal valence electron density, thus weakening the C–O bond.

What are the implications of these statements with regard to catalysis? Gusovius *et al.* (*348*) showed that on unpromoted Pd/SiO_2 catalysts, CH_3OH/dimethyl ether, and CH_4 were produced in a ratio of approximately 1:2 (molar), whereas on group 1 or 2 (Li, Ca)-promoted Pd/SiO_2, methanol selectivities up to approximately 99% were obtained (*379*). On the basis of these results indicating the absence of CO dissociation, one can suggest that for unpromoted Pd/SiO_2 the reaction proceeds via a CH_xO intermediate, which is either hydrogenated stepwise to produce methanol or which undergoes C–O bond cleavage and subsequent hydrogenation of CH_x to give methane. At least one of these reactions must be structure sensitive to explain the particle size-dependent selectivity of CO hydrogenation (*376*). On promoted Pd/SiO_2, the C–O bond cleavage in CH_xO seems to be suppressed, thus leading to high CH_3OH selectivities.

Another influence may arise from the oxide support (SiO_2, Al_2O_3, TiO_2, La_2O_3, MgO, ZnO, etc.). Although the discussion of the role of the support in CO hydrogenation is still controversial (*249*), strong support effects on activity and selectivity are well established (*368,370,380,381*). Spillover processes were observed (*382*), and possible intermediates (e.g., formate) were found to be bound to the oxide (*379*).

D. CO Adsorption, Dissociation, and Oxidation on Pt(1 1 1) and Platinum Nanoparticles Supported on SiO_2

D.1. *CO Adsorption on Pt(1 1 1)*

The adsorption of CO on Pt(1 1 1) can be regarded as one of the foundation systems (if not the *Drosophila*) of surface science (along with CO on nickel surfaces). Because of its high dynamic dipole moment, CO is an ideal probe molecule that can adopt various adsorption geometries and thus provide information about the surface site distribution. An extensive database has been acquired under UHV (cf. references cited in References *111,151,383–386*), and the importance of extending these investigations to higher pressures is apparent.

As described in Sections III.A.1 and III.A.2, when high-pressure CO adsorption is investigated by SFG, it is important to know the effective surface intensity of the incident IR and vis beams at a given pressure to properly normalize the SFG signal (e.g., via reference measurements of a GaAs crystal (*118,151*)). Figure 34 displays room temperature SFG spectra of CO on Pt(1 1 1) from submonolayer coverages up to a pressure of 500 mbar (the relatively broad peaks are attributed to the IR source (Ti:Sa laser system) with a resolution of about 25 cm^{-1}) (*112,151*). The nonresonant response from the clean platinum surface was constant over the spectral region and

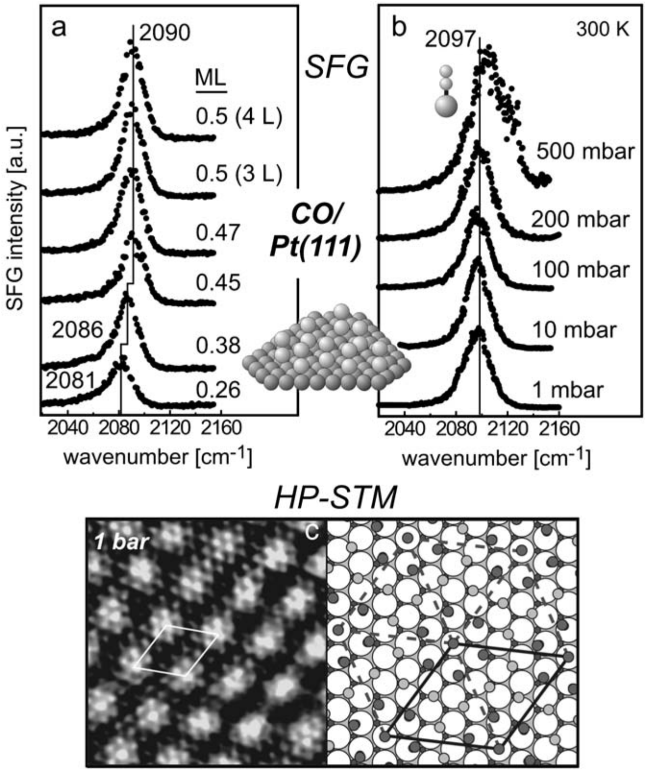

FIG. 34. SFG spectra of CO adsorbed on Pt(1 1 1) at 300 K at submonolayer coverages (a), and in the pressure range from 1 to 500 mbar (b) (*112,151*). Spectra recorded at pressures > 1 mbar were corrected for absorption by gas-phase CO. On-top CO was the only species detected (Ti:Sa laser system); adapted from (*151*) with permission. Copyright (2002) American Chemical Society. (c) High-resolution STM image (55 × 51 Å^2) of the Moiré pattern formed by CO on Pt(1 1 1) at 1 bar (only one rotational domain shown). An illustration of the ($\sqrt{19} \times \sqrt{19}$)R23.4°-13CO structure is included (unit cell marked by the solid line); adapted from Kruse Vestergaard *et al.* (*393*) with permission. Copyright (2002) American Physical Society.

only about 5% of the maximum resonant CO signal. Under UHV, values of surface coverages by CO were determined by TDS by using the c(4×2) saturation structure as a reference ($\theta = 0.5$) (*384*) (see Reference (*151*) for details). At 0.26 ML of CO (exposure approximately 0.5 L at 300 K), a single resonance feature at 2081 cm^{-1} was observed, which is characteristic of the C–O stretching vibration of terminally bonded (on-top) CO (*387*). With increasing coverage, the peak shifted to 2090 cm^{-1} as a result of dynamic dipole coupling, in good agreement with previous IRAS, HREELS, and SFG investigations (*129,131,140,385,388–391*). At saturation (0.5 ML; *ca.* 4 L), a c(4×2) LEED pattern was observed (*384*), corresponding to a superstructure in which equal numbers of CO molecules occupy on-top and bridge sites, as confirmed by a comparison of experimental and simulated STM images (*392*). The absence of bridge-bonded CO (peak expected at about 1850 cm^{-1}) in the SFG spectra may be accounted for by different reasons (several groups have reported difficulties in detecting this species on Pt(1 1 1), platinum foil, and Ni(1 1 1)). Its absence may be attributed to a low Raman polarizability of bridge-bonded CO (which could be affected by neighboring on-top CO) (*46,116,125,131*), an inherently broad linewidth of bridged CO at 300 K (*129*), and/or an interference effect between various SFG susceptibility tensor elements (as discussed by Baldelli *et al.* (*277*)).

Increasing the CO pressure to 1 mbar and then up to 200 mbar further increased the dipole coupling and shifted the frequency to 2097 cm^{-1}, but the spectra were found to be quite similar to those taken under UHV, with on-top CO being the only species detected (Fig. 34b). If the maximum value of the SFG signal is simply taken as a measure of the on-top CO concentration (using 0.5 ML CO at 10^{-7} mbar as a reference), a CO coverage of about 0.7 can be calculated for high pressures (*151*). This value and the presence of on-top CO are in excellent agreement with a recent high-pressure STM investigation of CO/Pt(1 1 1) by the Besenbacher group (*386,393*) (see below). The spectrum recorded at 500 mbar of CO also shows a center peak frequency near 2100 cm^{-1}, but the peak width was nearly doubled (most likely because of the strong IR absorption and low S/N ratio under these conditions). Similar spectra were recorded at temperatures between 160 and 400 K and also with CO on stepped platinum (*151*). The spectra were formed reversibly with changes in pressure, which suggests that under these conditions there was no surface restructuring induced by the high CO pressure.

SFG investigations of CO at mbar pressures on Pt(1 1 1) were also carried out by Somorjai *et al.* (*160,313*) and by Härle et al. (*131*); and recently PM-IRAS data were obtained by Andersen *et al.* (*176*). All SFG investigations reported spectra similar to those of Fig. 34 (with sometimes weak bridge signals). PM-IRAS was able to detect clearly bridging CO over the whole pressure range (see Fig. 4 in Reference (*176*)). Early investigations (*111,130,391*) had led to the statement that on-top CO strongly decreased at pressures >15 mbar of CO at 300 K, and carbonyl-like species platinum–$(CO)_n$ ($n = 1, 2, 3, 4$) at about 2050 cm^{-1} were suggested, as a result of displacive reconstruction of platinum atoms at high CO pressures. However, subsequent investigations (*160,313*) with improved (smaller) high-pressure cells (minimizing IR gas-phase absorption) and with improved IR normalization showed that the attenuation and frequency shift of terminal CO was an artifact, which had originated from IR gas-phase absorption.

SFG and PM-IRAS detected on-top and bridge-bonded CO on Pt(1 1 1) at pressures between 10^{-7} and 500 mbar and temperatures from 100 to 400 K. The adsorption geometry of CO did not change with pressure; thus, under all conditions, the high BE on-top sites were populated by CO and no high-pressure species appeared. However, the exact overlayer structure cannot be deduced from SFG. It is therefore unclear whether the high-pressure CO phase is comparable to the known UHV/low-temperature structures (e.g., $c(4 \times 2)$ 0.5 ML; $c(\sqrt{3} \times 5)$rect 0.6 ML; $(\sqrt{3} \times 3)$rect 0.66 ML; $c(\sqrt{3} \times 7)$rect 0.71 ML) (*384,390,394*).

STM can provide direct evidence to clarify the issue. Using HP-STM, the Berkeley group (*395*) observed a hexagonal Moiré pattern (periodicity approximately 12 Å) at about 250–1000 mbar of CO at 300 K, different from the (nonhexagonal) structures formed under UHV, and they suggested the formation of a new (nonrotated) incommensurate hexagonal CO overlayer with only one rotational orientation (*395,396*). It was further concluded that such an incommensurate CO overlayer could be produced only in a high-pressure environment. Subsequent HP-STM investigations by Kruse Vestergaard *et al.* (*386,393*) also led to the identification of a hexagonal Moiré pattern at 1 bar of CO. However, these authors suggested a commensurate CO overlayer structure, and the analysis of the orientation relationship between CO and platinum was significantly refined (Fig. 34c). Two rotational domains were found, rotated ~24° with respect to the platinum substrate. The individual CO molecules could even be resolved, a result that suggests a $(\sqrt{19}x\sqrt{19})R23.4°$-13CO commensurate structure (0.68 ML coverage; the brightest protrusions in Fig. 34c are associated with on-top CO). Furthermore, by annealing a CO overlayer at temperatures of about 170 K, this Moiré structure could also be prepared under UHV, a result that shows it is not restricted to the mbar pressure range (*384,386,393*). However, this structure could not be obtained at 100 K, a finding that is attributed to the low mobility of CO at this temperature (likewise, a perfect (2×2)-3CO structure cannot be obtained at 100 K on Pd(1 1 1) (*121*); cf. Fig. 15e). This result shows that differences between UHV and high-pressure experiments may be attributed not only to pressure, but may depend on exact pressure/temperature conditions, and hence originate from different experimental procedures as well. According to HP-STM, the high-pressure CO structure incorporates 47% more on-top CO than the 0.5 ML $c(4 \times 2)$-2CO room temperature UHV saturation structure. This result is in excellent agreement with the approximately 40% coverage increase observed by SFG at pressures between 10^{-7} and 500 mbar (*151*) (Fig. 34b).

In summary, at 300 K, SFG, PM-IRAS, and HP-STM indicated the absence of high-pressure species (such as carbonyls or adsorbate structures not accessible under UHV) on Pt(1 1 1), and surface roughening was not detected. Nevertheless, great care has to be taken when UHV data are extrapolated to high-pressure catalytic reaction conditions. The structures formed at cryogenic temperatures in UHV are not necessarily similar to the high-pressure/high-temperature structures that are in equilibrium with the gas phase.

D.2. *CO Adsorption on Platinum Nanoparticles Supported by SiO_2*

Because the adsorption properties of highly dispersed metals may differ significantly from those of single-crystal surfaces, especially if the metal particles are very small (*397*), CO adsorption on platinum nanoparticles supported on SiO_2 (particle diameter $>6\,nm$) is contrasted in the following section with that on Pt(1 1 1), with particular emphasis on the SFG signal intensities (*132*).

EBL was used to fabricate uniform platinum nanoparticle arrays on SiO_2 (mean platinum particle diameter 30–1000 nm (*52,53,106,107,398*)), and evaporation techniques were used to prepare smaller particles and a continuous platinum film. The EBL microfabrication technique allows the production of model catalysts consisting of supported metal nanoparticles of uniform size, shape, and interparticle distance. Apart from allowing investigations of the effects of particle size, morphology, and surface structure (roughness) on catalytic activity and selectivity, these model catalysts are particularly well suited to examination of diffusion effects by systematic variations of the particle separation (interparticle distance) or particle size. The preparation process (see Fig. 1 in Reference (*106*)) is described only briefly here, and detailed descriptions can be found in References (*53,106,399*).

The first step was to spin-coat an electron-sensitive polymer (polymethylmethacrylate (PMMA)) onto an oxidized Si(1 0 0) wafer (which serves as a SiO_2 support). The desired pattern is subsequently "written" into the polymer layer by a highly collimated electron beam, followed by the selective dissolution of the polymer damaged by the electron exposure. A thin film of platinum is then deposited on this mask, and after the remaining polymer resist is removed completely by dissolution, metal particles remain on the substrate and are located at the positions of the prior electron irradiation, typically forming an ordered array of nanoparticles.

To facilitate the interpretation of vibrational spectra, the platinum particle arrays were characterized by HRTEM, microdiffraction, dark-field imaging, and atomic force microscopy (AFM) (*52,53,107,398*). Figure 35a shows a medium-magnification micrograph of a Pt/SiO_2 model catalyst with a mean particle diameter of $40 \pm 1\,nm$ and an interparticle distance of 220 nm (yielding approximately 2×10^9 particles cm^{-2}). Microdiffraction patterns of individual particles and dark-field images (Figs 35b and d (*52,107*)) indicated that the platinum particles were polycrystalline with domain sizes of about 5 nm.This observation is evident from Fig. 35c showing a HRTEM image of a single platinum particle (mean size about 25 nm) of another EBL model catalyst (cf. Fig. 3g). The polycrystalline structure is apparent, and Moiré fringes (0.44 nm) appear where crystal grains overlap. The FFT in Fig. 35c′ demonstrates a (1 1 0) orientation of the particle area marked by a square in Fig. 35c. The height of the platinum particles determined by AFM was $20 \pm 0.5\,nm$, in agreement with the film thickness measurements by a quartz crystal oscillator during metal deposition. These images and the rounded profiles of the particles suggest that the surface of the platinum exhibits many defects (steps, kinks, vacancies), being similar to high Miller index facets.

One would therefore expect that vibrational spectra of CO adsorbed on the platinum particle array should resemble spectra of CO on stepped high Miller index platinum single crystals. However, in preparation for UHV experiments, the

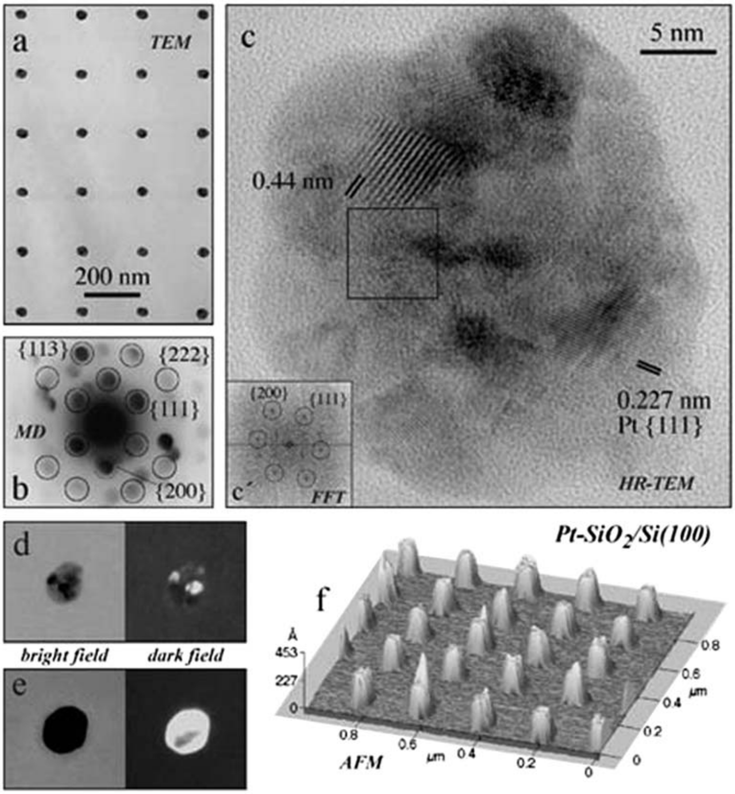

Fig. 35. (a) Transmission electron micrograph of a platinum nanoparticle array on SiO_2; (b) microdiffraction pattern of an individual platinum particle (spots originating from a (1 1 0) oriented crystalline grain within the polycrystalline platinum particle are marked by circles); (c) HRTEM micrograph and (c′) fast Fourier transform (FFT) of the section marked in (c); bright-field and dark-field images indicate the particle crystallinity before (d) and after (e) annealing to 973 K; (f) AFM image of a platinum nanocluster array after several reaction-cleaning cycles (*106, 107, 398*).

platinum nanoparticles must be cleaned, such as by oxidation–reduction cycles and/or annealing, and their internal and surface structures change during these treatments (*52,53,107*). Microstructural changes upon annealing under vacuum, in hydrogen, and in oxygen (1 bar), described in References (*52,53,107*), did not affect the particle arrangement but did lead to crystallization of the platinum particles. The changes are clearly evident in a comparison of dark-field images of platinum particles as prepared (Fig. 35d) and after annealing under vacuum at temperatures up to 973 K (Fig. 35e). Figure 35f shows an AFM image after several cleaning cycles.

SFG spectroscopy of CO adsorbed on SiO_2-supported platinum nanoparticle arrays (with 30-, 40-, 45-, 200-, and 1000-nm mean particle diameters), evaporated platinum nanoparticles (6-nm mean diameter), and a thin platinum film (all at approximately 1 bar) was reported by Baldelli *et al.* (*132*). Unfortunately, the EBL samples had to be prepared under nonUHV conditions and were cleaned by a rather unconventional method (treated with concentrated HNO_3/H_2SO_4 solution,

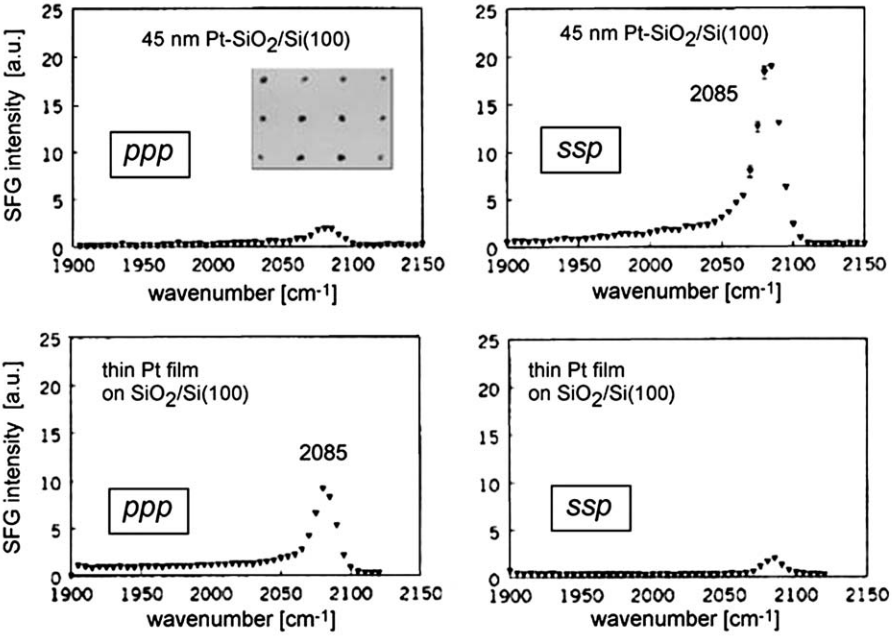

FIG. 36. SFG spectra of CO at approximately 1 bar on an array of 45-nm platinum particles prepared by EBL (interparticle spacing 150 nm) and on a thin platinum film 132(ssp (s-SFG, s-vis, p-IR) and ppp refer to the polarization combination); adapted from Baldelli *et al.* (*132*) with permission. Copyright (2000) American Institute of Physics.

rinsed with H_2O, then dried with N_2). Although no HRTEM images were obtained after the cleaning, it is likely that the particles retained their polycrystalline structures. Nevertheless, interesting CO adsorption spectra were obtained for the various samples and for various polarization combinations of the IR, vis, and SFG light.[16] For example, Figure 36 shows ppp and ssp (s-SFG, s-vis, p-IR) CO spectra for an array of 45-nm platinum particles (interparticle spacing 150 nm) and the corresponding spectra of CO on a thin platinum film. In both cases, a single peak at about 2085 cm^{-1} was observed, which can be attributed to on-top CO on platinum, because no resonances occurred between 1800 and 2150 cm^{-1} for the pure SiO_2 film. Because this frequency is about 15 cm^{-1} lower than that characterizing CO on polycrystalline platinum or Pt(1 1 1), Baldelli *et al.* (*132*) attributed the shift to coadsorbed water resulting from the cleaning procedure (a similar effect was reported in Reference (*151*)). However, the shift may also be attributed to the stepped surfaces of the nanoparticles, as shown in the HRTEM images of Fig. 35, leading to a lower resonance frequency. In any case, the authors (*132*) reported how the SFG signal intensity depends on particle size and light polarization.

---

[16] For a description of polarization-dependent SFG spectroscopy, see Section IV.H.

First consider the "surface statistics" of the large EBL particles. A platinum particle of 45 nm diameter consists of about 1×10^6 atoms, with approximately 30 000 surface atoms (dispersion 3%; assuming cylindrical particles 15 nm in height). When there are about 4×10^9 particles cm^{-2}, the number of Pt surface atoms per cm^2 of sample is approximately 1×10^{14} (i.e., about 8% of the number per cm^2 on a Pt(1 1 1) single-crystal surface or thin film). Surprisingly, even though the number of exposed Pt atoms and thus the number of CO molecules per sample area is quite small for the 45-nm platinum array, the observed CO signal is comparable (ppp) or even stronger (ssp) than the SFG signal from the platinum film (Fig. 36; note that there is a second-order dependence of I_{SFG} on N, Eqs. (2–4)). Baldelli *et al.* (*132*) normalized the SFG intensity over the platinum (or CO) surface coverage (using the platinum film as reference) and found an enhancement factor of approximately 250 and approximately 11 800 for ppp and ssp polarization, respectively. This strong enhancement effect was attributed to a surface plasmon resonance in the platinum particles (enhancing the local fields of the laser beams *ca.* 180 times for approximately 50-nm particles), and the polarization dependence was attributed to the dielectric properties of a metal film on a dielectric $\mathrm{SiO_2}$ substrate (the support-induced enhancement is approximately 70 × for 45-nm particles). The total enhancement is therefore approximately 10^4 for 50-nm particles for ssp polarization (i.e. approximately 70% is attributed to plasmon resonance and approximately 30% to the substrate effect).

The data also allow an examination of the particle size dependence of these effects (cf. Fig. 4 in Reference (*132*)). Larger and smaller platinum particles showed a much smaller enhancement, although nanoparticles prepared by EBL typically consist of platinum grains of about 5 nm diameter, independent of the total diameter of the platinum particles (cf. TEM images in Fig. 35). This result indicates that the SFG signal is averaged over the entire particle, because the electrons in the entire particle are polarized. The particle size-dependent enhancement was explained by a particle size-dependent surface plasmon enhancement and by changes in the substrate optical properties resulting from changes in the platinum loading. Increasing the platinum loading on the $\mathrm{SiO_2}$ layer changes the surface from an insulator to a metal, with a strong impact on the optical properties (e.g., the ppp signal is stronger for the more metallic surfaces). In contrast, at low platinum coverages, the optical properties are dominated by the $\mathrm{SiO_2}$ film although the SFG signal originates from adsorbed CO. Therefore, the polarization spectra do not provide a probe of various molecular orientations of CO (as described in Section IV.H), but instead the polarization dependence reflects the changing dielectric properties of the surface as the platinum coverage increases.

What is surprising is that platinum nanoparticle arrays with similar mean particle diameters still exhibited very different SFG intenities (*132*). For example, for 40-nm platinum particle arrays, the enhancement for ssp polarization was the relatively "small" value of approximately 4200 (whereas for 45-nm platinum articles it was approximately 11 800). Indeed, the calculations suggested the same enhancement for these particle sizes. For 6-nm platinum particles evaporated onto $\mathrm{SiO_2}$, the calculations suggest a plasmon enhancement of 28 and a substrate enhancement of 76, yielding a total enhancement of approximately 2100 for ssp. However, an approximately 140-fold enhancement was observed for ssp, and a sevenfold enhancement for ppp polarization. As discussed in Section IV.C, ssp and ppp SFG spectra of CO on approximately 6-nm palladium nanoparticles did not show an enhancement effect when compared with the signal intensity of CO on Pd(1 1 1).

In summary, although there are open questions, the possible enhancement of SFG signals of CO on metal nanoparticles on dielectric substrates deserves further attention, and UHV experiments carried out with better controlled samples (particle morphology, cleanliness) are recommended.

D.3. *CO Dissociation and CO Oxidation on Pt(1 1 1)*

At temperatures of 300–400 K, SFG did not provide evidence of CO dissociation, in agreement with the known inability of platinum to dissociate CO (*180,384*). However, at temperatures >673 K and pressures of approximately 40 mbar of CO, an irreversible redshift of the frequency of CO on Pt(1 1 1) to about 2050 cm^{-1} was reported, and post-exposure AE spectra showed strong carbon signals at 273 eV (*279,313,400*). The irreversible shift was attributed principally to the influence of coadsorbed carbon originating from CO dissociation. A CO-induced surface roughening producing defect sites (with the driving force being the formation of platinum carbonyls) was judged to be responsible for CO dissociation on Pt(1 1 1) at high pressures and high temperatures.

This result should have significant implications for the catalytic properties of platinum. Because the CO dissociation temperature was found to coincide with the ignition temperature characterizing catalytic oxidation of CO on Pt(1 1 1), it was suggested that CO dissociation may be part of an important alternative pathway during CO oxidation. Similar investigations were carried out with Pt(1 0 0) and Pt(5 5 7) (*279,400,401*). Unfortunately, the AE spectra presented in References (*279,313*) do not show results for energies >550 eV, which would be necessary to exclude conclusively any influence of nickel or iron carbonyls (which may also serve to dissociate CO). STM, LEED, and XPS investigations would be valuable to examine a possible surface roughening in detail. For further information about CO oxidation and the involvement of potential high-pressure species (e.g., an incommensurate CO overlayer), see References (*124,402*). PM-IRAS investigations of the effect of exposure of CO-precovered Pt(1 1 1) to H_2 at 1 bar at various temperatures are described in Reference (*176*).

E. CO Adsorption, Dissociation, and Oxidation on Rh(1 1 1)

E.1. *CO Adsorption and Dissociation on Rh(1 1 1)*

Supported rhodium is used in many catalytic processes, and rhodium is an active component in the automobile catalytic converter (rhodium catalyzes the reduction of NO to N_2, as well as the oxidization of CO to CO_2) (*1*), which explains the large number of investigations of adsorption under UHV (e.g., references cited in Reference (*403*)). As rhodium surfaces are able to dissociate CO (*373–375*), CO adsorption may be accompanied by CO dissociation. CO dissociation on rhodium is structure-sensitive: Rh(1 1 1) (*374*) and Rh(100) (*373*) surfaces do not break the C–O bond under UHV, whereas rougher surfaces such as Rh(2 1 0) (*375*) do. Consequently, CO dissociation on supported rhodium nanoparticles is strongly dependent on particle size ((*101*) and references therein). Rhodium particles with diameters of 2–3 nm have the highest activity, because this size range exhibits the highest relative fraction of low-coordinated (edge and corner) sites (*22*). As evidenced by HRTEM images (*14,54,404*), oxidation–reduction treatments can be used to increase the number of low-coordinated sites on Rh/Al_2O_3, and thus, the CO dissociation (methanation) and hydrocarbon hydrogenolysis activity.

In any case, close-packed rhodium surfaces such as Rh(1 1 1) are known not to dissociate CO under UHV. This observation may not hold true in the high-pressure gas environment of a catalytic reaction, because the pressure is at least 10 orders of magnitude higher than under UHV conditions. Processes that are too slow under UHV may hence gain more importance at high pressure. Indeed, Hayek *et al.* (*14*) reported that at mbar pressures, CO dissociated on Rh(1 1 1), most likely as a result of surface roughening under high pressure. Carbon deposits from CO dissociation were detected by AES, and the strong restructuring of the Rh(1 1 1) single crystal was even visible optically.

CO adsorption on Rh(1 1 1) at 300 K at coverages >0.5 ML was investigated by high-pressure STM (*219,396,400*). This investigation is important because it is not clear whether the high-coverage structures observed under UHV at low temperature are equilibrium phases or metastable phases. Figure 37a displays a HP-STM image typical of those acquired at CO pressures between 5 and 900 mbar. The structure was identified as the (2×2)-3CO saturation structure known from low-temperature UHV investigations (Fig. 37b; with a corrugation of 0.2 Å). According to a LEED investigation, the CO molecules are bound to top sites and threefold hollow sites (*405*) (comparable to the situation on Pd(1 1 1); see Section IV.C.1). Because on-top CO sits higher, STM detects only these molecules (and no hollow-bonded CO), and only one bright spot appears per unit cell (*266*). No strong surface restructuring was observed in these investigations, but the change of the preferred CO adsorption sites from on-top (at low coverage) to hollow may be related to a CO-induced restructuring of the rhodium surface. LEED crystallography (*405*) indicated that the first

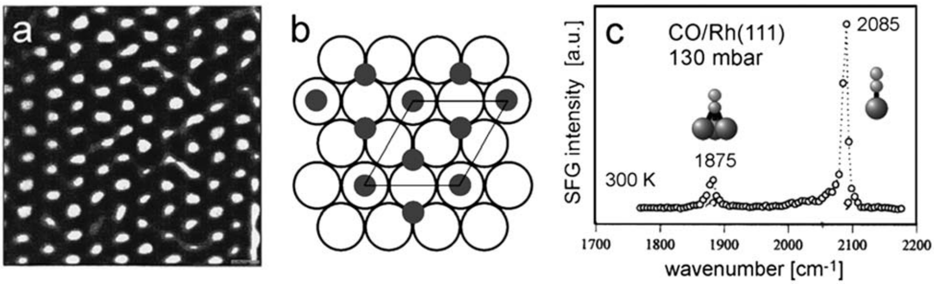

Fig. 37. Topographic 50×50-Å^2 STM image (a) and schematic representation (b) of the (2×2)-3CO structure observed in the presence of CO at 930 mbar on Rh(1 1 1) at 300 K; adapted from (*219*). (c) SFG spectrum of CO on Rh(1 1 1) in the presence of 130 mbar of CO at 300 K (*396*).

layer of rhodium atoms shifted upward by about 0.07 Å when the 0.75 ML (2 × 2) structure was present. However, no indications of CO dissociation were found. At a lower CO coverage (about 0.5 ML), when the sample was investigated by exposing Rh(1 1 1) at 300 K to approximately 10^{-8}–10^{-5} mbar of CO, a (2 × 1) overlayer and two types of $(\sqrt{7} \times \sqrt{7})R19^\circ$ structures were detected (*219*). In contrast to the low-coverage regime (≤0.33 ML) in which CO populates only on-top sites, the structures at about half a ML coverage exhibit both hollow-bound and on-top CO. These "intermediate" structures were not reported in UHV investigations and may also be quite important for catalysis.

Adsorption of CO at high pressures on Rh(1 1 1) at temperatures in the range from 125 to 300 K was also investigated by SFG (*46,396*). At low coverages (≤0.33 ML; e.g., 1 L of CO at 300 K), a single peak at about 2040 cm^{-1} characteristic of on-top CO was observed. After saturation of the Rh(1 1 1) (e.g., by application of a CO background pressure of approximately 5 mbar at 300 K), the SFG spectrum indicated two peaks, at 1875 and at approximately 2070–2085 cm^{-1} (cf. Fig. 37c). The first peak is attributed to hollow-bonded CO and the second to on-top CO (shifted to higher frequency as a result of dipole coupling), suggesting a (2 × 2)-3CO saturation structure, such as those observed under UHV (*405,406*). Figure 37c shows an SFG spectrum recorded at 130 mbar of CO.[17]

Increasing the pressure to approximately 900 mbar reduced and down-shifted the on-top CO peak and produced an additional weak and broad peak at *ca.* 2020–2050 cm^{-1} (*46,396*). Because a similar (but much stronger) low-frequency peak was also observed on an ion-bombarded (rough) Rh(1 1 1) surface under UHV, it was assigned to CO adsorbed on defect sites presumably resulting from a CO-induced surface restructuring/roughening. Such an effect was also observed by STM, when CO exposure was found to disrupt rhodium nanoparticles (*51*). In light of the (unexpected) intensity decrease with increasing pressure, it is inferred that the spectral changes may also be caused by partial CO dissociation and carbon formation, similar to what was reported for Pt(1 1 1) at higher temperatures (*279*) (but no AE spectra were reported in Reference (*396*)). Depending on the temperature and duration of the CO exposure, the structural changes on the Rh(1 1 1) surface, and therefore, the SFG spectra, were also more or less reversible with changes in pressure.

In light of the open questions related to CO adsorption/dissociation on Rh(1 1 1), Pery *et al.* (*314*) carried out a systematic SFG/AES study of CO on Rh(1 1 1), at pressures from 10^{-8} to 1000 mbar and temperatures from 300 to 800 K. Figures 38a and b show a series of SFG spectra recorded at 300 K and a comparison of spectra at 10^{-6} mbar before and after the atmospheric pressure gas exposure. All spectra are dominated by a single vibrational peak at 2053–2075 cm^{-1}, typical of CO terminally bonded to a single Rh atom, with a small peak at about 1900 cm^{-1} characterizing CO on threefold hollow sites (see, e.g., the 500-mbar spectrum). The intensity difference between the two peaks again points to the lower sensitivity of

---

[17] The intensity difference between the two CO species is similar to that on Pd(1 1 1); see, for example, Fig. 15.

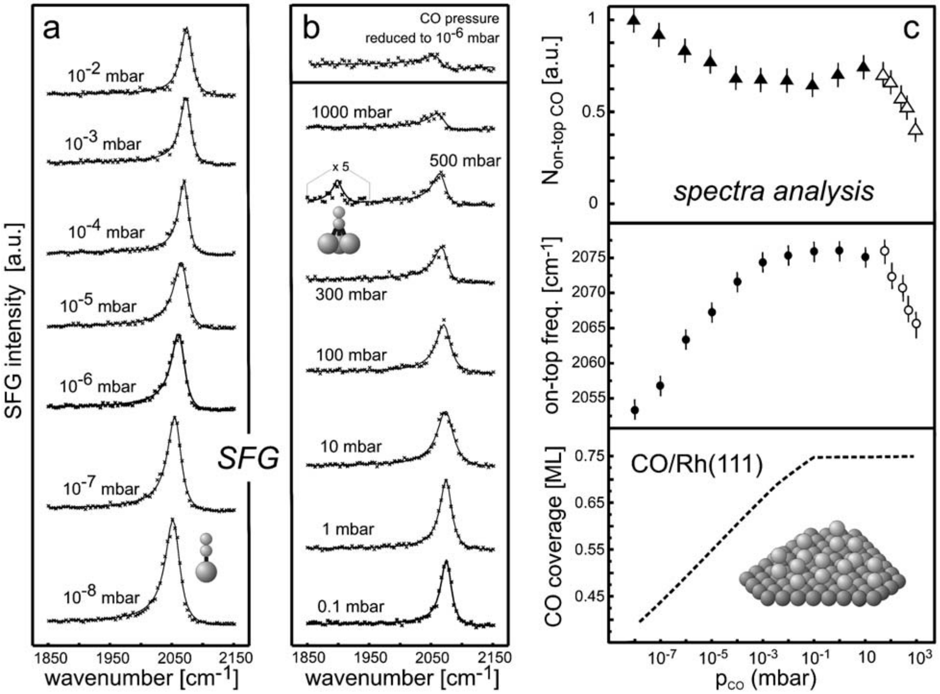

FIG. 38. (a, b) SFG spectra of CO adsorbed on Rh(1 1 1) at 300 K at pressures between 10^{-8} and 1000 mbar. (c) Analysis of the on-top CO intensity (surface density), resonance position, and CO coverage as a function of the CO pressure. The open symbols indicate the pressure range of irreversible CO adsorption. The equilibrium CO surface coverage in (c) was calculated from adsorption/desorption kinetics; adapted from Pery *et al.* (*314*). Copyright (2002) The Combustion Institute.

SFG toward multiple-coordinated CO. The spectra agree with those reported by Somorjai *et al.* (*46,396*) for CO chemisorption at pressures below 900 mbar and indicate a (2 × 2)-3CO saturation structure (0.75 ML) (*219*).

Figure 38c displays an analysis of the on-top CO intensity (surface density *N*, according to Eq. (3)), resonance position, and coverage as a function of the CO pressure. The frequency shift of on-top CO reflects the coverage increase with pressure (CO dipole coupling) and occurs mainly between 10^{-8} mbar (2053 cm^{-1}) and 10^{-2} mbar (2075 cm^{-1}). With further increases in pressure, the frequency then remained almost constant up to 100 mbar, indicating that saturation (0.75 ML) was reached at about 10^{-2} mbar at 300 K (for comparison, on Pt(1 1 1), saturation is reached at 2 L (*151*), whereas on Pd(1 1 1), saturation cannot even be reached at 1000 mbar at 300 K (*152*)). Strong repulsive interactions between the CO molecules apparently prevent coverage exceeding the UHV saturation coverage. The decrease of the on-top CO signal up to a pressure of about 10^{-1} mbar and small increase up to about 10 mbar are attributed to structural rearrangements of the CO layer. At 0.33 ML and below, CO occupies only on-top sites, whereas at higher coverages hollow sites are occupied as well, which first decreases the total amount of on-top CO (on-top/hollow ratio for approximately 0.6 ML: 1:3) and then slightly

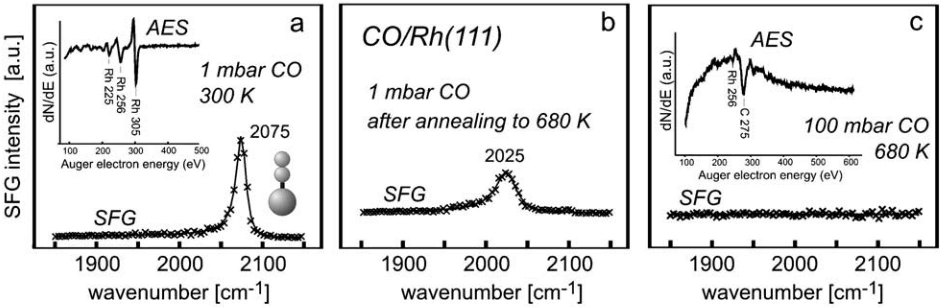

FIG. 39. SFG spectrum of CO on Rh(1 1 1) at 1 mbar and 300 K. The inset shows an AE spectrum of the clean surface. (b) SPG spectrum taken after increasing the temperature to 680 K. (c) SFG spectrum taken after increasing the pressure to 100 mbar at 680 K. The inset shows the AE spectrum after cooling of the sample to 300 K and evacuation; adapted from Pery *et al.* (*314*). Copyright (2002) The Combustion Institute.

increases it again (on-top/hollow ratio for 0.75 ML: 1:2; for details see References (*219,314*)).

Whereas reversible molecular adsorption of CO was observed up to about 100 mbar, exposure to CO at higher pressure continuously decreased the CO frequency, which reached 2065 cm^{-1} at 1000 mbar (open symbols in Fig. 38c). Even more important, there was an irreversible decrease in CO intensity (or adsorbate density; cf. the two 10^{-6} mbar spectra in Fig. 38). This result is similar to the observations reported (*46,396*) (attributed to surface roughening), but Pery *et al.* (*314*) attributed these effects to dissociative CO adsorption. To test this suggestion, high-pressure measurements were performed at temperatures up to 750 K. At pressures $\leq 10^{-4}$ mbar, only reversible (molecular) CO adsorption was observed. However, at pressures ≥ 1 mbar of CO, low-frequency contributions to the vibrational spectra were observed at temperatures ≥ 600 K, marking the onset of CO dissociation (*314*). To illustrate this point, Fig. 39 is a comparison of SFG and AE spectra under various conditions. Figure 39a shows an AE spectrum of the clean rhodium surface and an SFG spectrum of CO at 1 mbar and 300 K. After an increase in the temperature to 680 K, the spectrum in Fig. 39b was observed. Apart from the frequency shift and reduction in intensity, a new, very weak feature at the low-frequency side is evident. After an increase in the pressure to 100 mbar at 680 K (Fig. 39c), no CO adsorption was observed, not even after the temperature was reduced (showing the irreversibility of dissociative CO adsorption). These results can be understood by considering the post-exposure AE spectrum (Fig. 39c) showing a considerable carbon signal. It indicates that the rhodium surface is (nearly) fully covered with carbon, pointing to the high-pressure CO dissociation pathway. The absence of any oxygen signal in AES was taken as an indication that CO dissociation on Rh(1 1 1) proceeds via the exothermic Boudouard reaction ($2CO \rightleftarrows C + CO_2$).

In summary, the irreversible intensity decrease and downshift of the on-top CO frequency at 300 K for pressures > 100 mbar and the appearance of low-frequency features at elevated temperatures and pressures (≥ 600 K; ≥ 1 mbar) most likely indicate the onset of CO dissociation resulting in CO molecules coadsorbed with carbon. Unfortunately, LEED images were not presented, and the AE spectra in Reference (*314*) do not show the energy range above 700 eV, required to exclude unambiguously a possible interference from carbonyl impurities. LEED and STM investigations during or after various stages of CO adsorption/dissociation and quantitative XPS measurements would be required to examine a possible restructuring of the Rh(1 1 1) surface. The restructuring process may precede CO dissociation (i.e., CO would then dissociate on high-index rhodium facets or steps rather than on the Rh(1 1 1) surface), or alternatively, the restructuring may be induced by carbon deposition during CO dissociation (such as the carbon-induced reconstruction of Ni(1 0 0) (*407*)).

E.2. *CO Oxidation on Rh(1 1 1)*

CO oxidation on Rh(1 1 1) was investigated by SFG at a total pressure of 20 mbar (CO:O_2:Ar = 1:2:7 molar). And temperatures between 300 and 700 K (Fig. 40a)

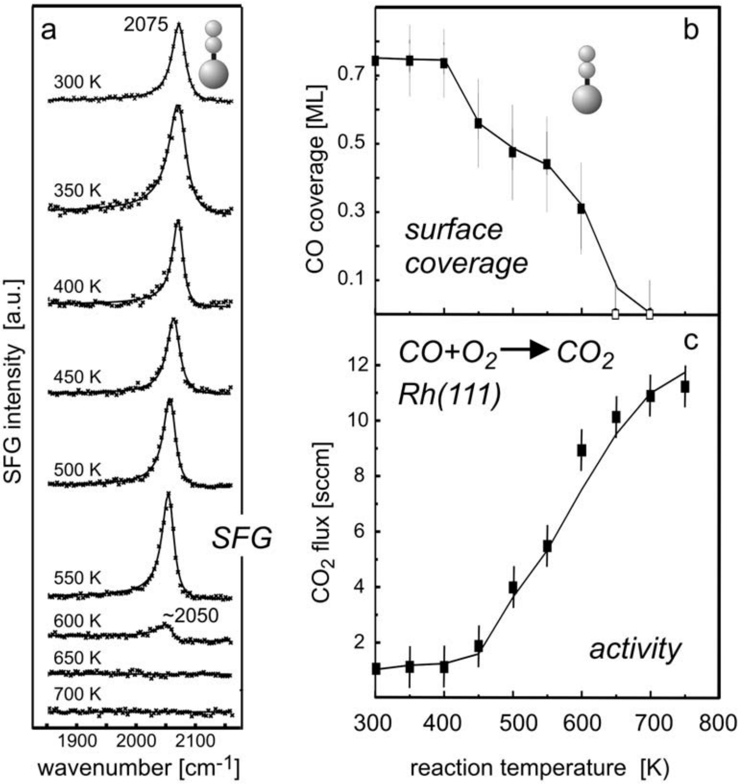

Fig. 40. (a) SFG spectra recorded during CO oxidation at temperatures between 300 and 700 K at a total pressure of 20 mbar (CO:O_2:Ar = 1:2:7 molar). CO surface coverage (b) and CO_2 production rate (c) are shown as a function of the oxidation (substrate) temperature; adapted from Pery *et al.* (*314*). Copyright (2002) The Combustion Institute.

(*314*). During the oxidation reaction, on-top CO was observed as the only surface species with frequencies from 2075 to about 2050 cm^{-1}. The dependence of the CO stretching frequency on coverage, calibrated by results of SFG/TPD investigations (*314*) (cf. Fig. 38c), allowed the researchers to deduce the CO coverage at various reaction temperatures (Fig. 40b); the CO_2 production rate was measured simultaneously by mass spectrometry (MS) (Fig. 40c). At temperatures up to about 400 K, a saturated CO layer was detected, and the CO_2 production rate was rather low because of the inhibition of oxygen adsorption by CO. At temperatures between 400 and 600 K, the CO equilibrium coverage decreased linearly with temperature, with a parallel increase in the CO_2 production rate. In this temperature window, dissociative oxygen adsorption (which competes with CO adsorption) is the rate-limiting step (*408*). A sudden decrease in the CO coverage at temperatures above 600 K indicated a transition from a mainly CO-covered surface to an O-covered surface, apparently yielding the highest CO_2 production rate. Post-reaction AES indicated only trace amounts of carbon or rhodium surface oxides. Previous investigations had reported rhodium surface oxides at oxygen pressures >500 mbar, which, however, deactivated the Rh(1 1 1) surface (*408*). Nevertheless, the involvement of (metastable) rhodium surface oxide phases under reaction conditions cannot be excluded, as long as no unambiguous HP-XPS or HP-STM investigations of working catalysts are available.

The experimental kinetics data were also compared with numerical reactive flow simulations (*314,409*), yielding the lines in Figs 40b and c. The postulated surface reaction mechanism was based on the Langmuir–Hinshelwood (LH) model (including adsorption and desorption of CO, dissociative adsorption of oxygen, and CO_2 formation), accounting for the strong decrease in the oxygen sticking probability with increasing CO coverage (0.9 for a clean surface vs. approximately 0.01 for 0.3 ML of CO). The good agreement between experiment and the simulations suggests that under these conditions (which are typical for exhaust gases of internal combustion engines) Rh(1 1 1)-catalyzed CO oxidation can be quantitatively described by a mean field model, which incorporates a Langmuir–Hinshelwood reaction scheme as well as kinetics data from surface science investigations of Rh(1 1 1).

F. CO Adsorption on Gold, Nickel, Iridium, Iron, and Ruthenium Single Crystals

Gold catalysis has attracted much attention because of the somewhat unexpected activity of an "inert" metal for low-temperature CO oxidation or hydrogenation (*410*). This has already stimulated a number of model investigations under UHV (*411–414*) and a few high-pressure investigations of gold single crystals. Room temperature CO adsorption on Au(1 1 1) at pressures from 10^{-3} to 1000 mbar was investigated by Piccolo *et al.* (*415*) using a combination of HP-STM, PM-IRAS, and DFT. STM revealed CO-induced structural changes, such as step roughening and modifications of the terrace structure. Figure 41 shows the Au(1 1 1) surface with the "herringbone" $22\times\sqrt{3}$ reconstruction (Fig. 41a) and large terraces. With increasing pressure, the $22\times\sqrt{3}$ reconstruction is transformed to an unreconstructed 1×1 surface, which can be clearly observed in the presence of 330 mbar of

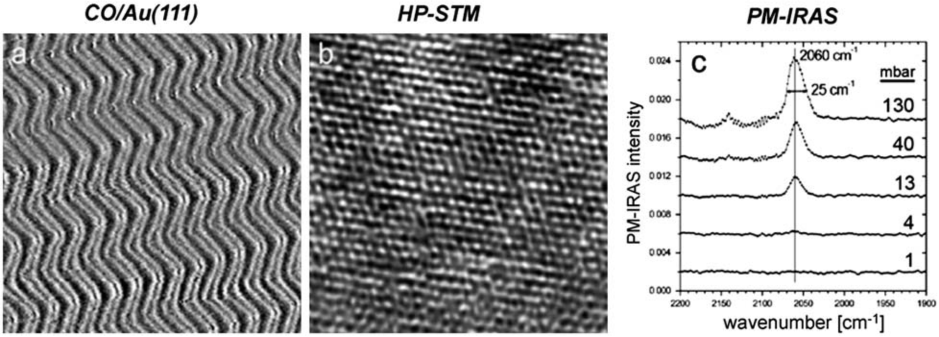

FIG. 41. STM images of the Au(1 1 1) surface at 295 K (a) under 10^{-9} mbar ($130 \times 130\,\text{nm}^2$); (b) under 330 mbar of CO ($7.5 \times 7.5\,\text{nm}^2$); (c) shows the corresponding PM-IRAS spectra; adapted from Piccolo *et al.* (*415*) with permission from Elsevier.

CO (Fig. 41b). On a larger scale, additional surface changes were detected. At approximately 1 mbar of CO, step edges roughened, and at approximately 130 mbar, two-dimensional islands appeared near the steps (strongly increasing the number of step and kink sites); these results indicate high mobility of the gold. The structural changes were irreversible with changes in pressure (i.e., evacuation of CO did not restore the original surface structure). These effects are inferred to be induced by CO, because no changes were observed in experiments with the sample in the presence of 660 mbar O_2.

Vibrational spectroscopy determined by PM-IRAS indicated on-top-bonded CO, with a peak at 2060 cm^{-1}, but only at pressures exceeding about 1 mbar at 300 K (Fig. 41c). The frequency shift with pressure is negligible, probably because of the low CO coverage (<0.1 ML according to DFT calculations (*415*)). These calculations, performed for various smooth, stepped, and kinked surfaces, indicated a strong structure sensitivity of CO adsorption on gold, and also that the on-top site is the most stable adsorption site on all the surfaces. The CO stability increased with decreasing coordination number of the gold atom to which CO binds (i.e., CO binds more strongly to rougher gold surfaces). A comparison of experimental and calculated vibrational frequencies suggests that CO is mainly chemisorbed on steps and kinks at low coverages and 300 K, with the best agreement for the kinked Au(874) surface. The surface roughening observed by STM creates such defect sites and allows CO adsorption; alternatively, the creation of favorable CO adsorption sites may be the driving force for the structural rearrangements. Similar investigations of Au(1 1 0) also indicated on-top CO (with a peak at about 2110 cm^{-1}) at pressures $>10^{-3}$ mbar, but they also showed even more pronounced surface restructuring under CO pressure (disappearance of the 1×2 missing-row reconstruction and formation of monatomic-height isotropic steps (*174*)).

SFG spectra of CO adsorbed on nickel have been reported (*116,118,416,417*), as have spectra characterizing NH_3 adsorption/dissociation on Fe(1 1 1) (*418*). UHV SFG investigations of formic acid decomposition on NiO(1 1 1) were also reported (*419,420*). Investigations of ruthenium surfaces (*147,148,157,421–425*) and of CO adsorbed on Ir(1 1 1) are also available (*426*).

G. BROADBAND SFG SPECTROSCOPY AND PUMP-PROBE EXPERIMENTS

The SFG experiments described so far refer to spectra acquired in "scanning mode" (the IR frequency was tuned over the spectral range of interest; cf. the SFG spectrometer shown in Fig. 7). As a result, one spectrum may take 15–30 min to acquire, depending on the surface coverage and type of molecule/bond being investigated. However, by using femtosecond lasers, an SFG experiment can also be performed in the broadband mode, which allows one to reduce the acquisition time considerably. The groups of Richter and Stephenson (*146*) and Wolf and Ertl (*147,421*), and more recently Domen (*427*), King (*423,425,426*), and Bonn (*424,428,429*) have been active in this field. Although the author is not aware of an application of broadband SFG to high-pressure catalytic measurements, this is certainly a promising approach and is briefly described here.

Broadband SFG takes advantage of ultrashort and thus spectrally broad IR laser pulses (e.g., 150 fs; width, approximately 150 cm^{-1}), with a spectrum covering a IR region of interest, for example, centered at about the CO stretching frequency (e.g., Fig. 12, Reference (*48*)). The broadband IR pulse is overlapped with a narrowband visible pulse (e.g., 7 ps; width, 2 cm^{-1}), but only that part of the IR spectrum that is in resonance with a vibrational transition will be upconverted to generate a sum frequency signal. Accordingly, the broadband approach allows the capture of the whole SFG vibrational spectrum in a single laser shot without tuning of the IR wavelength. The SFG spectrum is then dispersed by a spectrograph and recorded by a CCD camera. To obtain a good S/N ratio, it is usually necessary to average the results of several thousand shots (which requires about 10 min at 10 Hz (*425*) or several seconds at 1 kHz (*147,421*)).

Broadband femtosecond SFG was used, for example, to examine CO adsorption on Ru(10-10) (*425*) in the coverage range of 0.11–1.22 ML. A strong frequency shift (71 cm^{-1}) of on-top CO was observed, and with the help of isotope experiments, the various contributions were disentangled (34 cm^{-1} of the shift was attributed to chemical shift, 37 cm^{-1} to dipole–dipole coupling). The broadband technique also enables the performance of time-resolved pump-probe SFG experiments. For example, after photoexcitation of the surface with an intense near-IR femtosecond-laser pulse ("pump"), a time-delayed weak SFG (IR + VIS) "probe" is employed to monitor the changes in the vibrational properties of the adsorbate–substrate complex by taking snapshots of the transient vibrational spectrum (*48*). Systems investigated include CO desorption (*147,148,157,417,421,422*) and formic acid decomposition on NiO(1 1 1) (*419,420*).

H. MONITORING MOLECULAR ORIENTATION BY POLARIZATION-DEPENDENT SFG

The SFG spectra discussed in the preceding sections were obtained in ppp-polarization combination (i.e., by detecting a p (parallel)-polarized SFG signal produced by a p-polarized visible and a p-polarized IR beam). This combination is typically used for adsorption/reaction investigations of metal surfaces because it produces the most intense adsorbate SFG signal (*46,430*). However, it is also possible to use other polarization combinations, for example, ssp (s ("senkrecht," i.e., perpendicular)-polarized SFG, s-polarized visible, and p-polarized IR; see Fig. 9 of Reference (*48*) for an illustration). The IR beam is always p-polarized because the light field of an s-polarized IR beam is screened by the conduction electrons of metal surfaces (*17*).

Comparing the intensity of corresponding peaks in ppp and ssp SFG spectra allows one to deduce the molecular orientations of adsorbed molecules. However, the analysis is quite involved and not always unambiguous (see discussion in Reference (*150*)). Details of the theory and analysis of such spectra can be found elsewhere (*125,149,150,277,431*).

The technique was applied to CO and NO adsorption on Pt(1 1 1) under UHV (*125,432*). The results indicate an upright orientation of both on-top and bridge-bonded CO and a tilted geometry of adsorbed NO (at high coverage). A tilt angle of about 20° was obtained for NO, in agreement with near-edge X-ray absorption fine structure (NEXAFS) results (*433*). Polarization-dependent SFG of CO on Pd(1 1 1) (*150*) confirmed that CO adsorbs perpendicularly on the surface (*327*). Bandara *et al.* (*116*) also investigated CO and NO adsorption, but on a NiO(1 1 1) thin film grown on Ni(1 1 1). Polarization-dependent measurements for CO adsorbed on supported palladium nanoparticles were reported (*296*). To date no polarization-dependent measurements of molecular orientation have been performed at high (mbar) pressures. The geometries of adsorbed species may well be coverage- and temperature-dependent, and knowledge of how would represent useful information for determining catalytic reaction mechanisms.

I. ETHENE ADSORPTION, C_2H_4–HYDROGEN COADSORPTION, AND C_2H_4 HYDROGENATION ON Pd(1 1 1) AND Pd/Al_2O_3

Among the platinum metals, palladium is considered the most selective for hydrocarbon hydrogenation (dehydrogenation to undesired carbonaceous species is much slower than hydrogenation). Because alkene hydrogenation is structure-insensitive and thus particle size independent, ethene can be regarded as a prototype for longer alkenes.[18] Although selectivity is not an issue in C_2H_4 hydrogenation, investigations of ethene adsorption and hydrogenation still provide valuable information about adsorption geometry, reaction mechanisms, and deactivation processes. Ethene hydrogenation takes place even at room temperature, presumably by the stepwise hydrogenation of ethene, as proposed by Horiuti and Polanyi in 1934 (*434*). In this section, the various ethene adsorbate species and their coadsorption with hydrogen are described, both under UHV and mbar pressure conditions.

I.1. *Ethene Adsorption and C_2H_4–Hydrogen Coadsorption on Pd(1 1 1) under UHV*

Ethene adsorption, in particular on platinum and palladium surfaces, has received much attention. The atomic structure of the various adsorbed ethene

---

[18] One should note, however, that isomerization on palladium is structure sensitive and particle-size dependent.

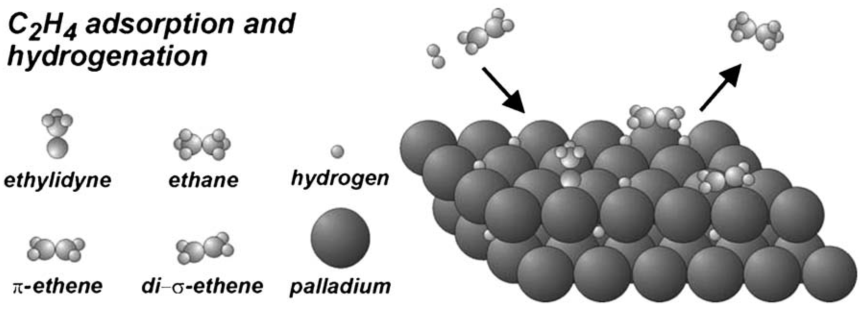

FIG. 42. Schematic illustration of the various adsorbed ethene species and their adsorption positions on Pd(1 1 1).

species was determined by applications of a variety of techniques, including LEED surface crystallography, TDS, UPS, HREELS, XPS, IRAS, NEXAFS, DFT, etc. (*19,83,435–447*). Figure 42 shows a schematic illustration of C_2H_4 adsorption and hydrogenation.

I.1.1. C_2H_4 Adsorption under UHV. Ethene exhibits three adsorption configurations, which are described briefly here. C_2H_4 molecules can interact weakly with the surface via π-coordination (typically at low temperature) (i.e., ethene is physisorbed with its C–C bond parallel to the surface, and the distance between the two sp^2 carbon atoms is almost unchanged with respect to the gas-phase molecule) (*435–438*). π-Bonded ethene is considered to adsorb on-top of a single Pd atom. In the case of a stronger molecule–substrate interaction, the (gas phase like) carbon–carbon double bond is broken, and the carbon atoms attain nearly sp^3 hybridization. Two σ-bonds are formed with the underlying palladium surface, and this species is therefore called di-σ-bonded ethene. At adsorption temperatures of about 100 K, the two species may coexist, but there is still some debate as to their relative abundances. Whereas vibrational and photoelectron spectroscopy of C_2H_4 adsorption at about 100 K detected predominantly di-σ-bonded ethene (e.g., References (*19,68,83,444,445*)), theoretical investigations rather suggest a combination of di-σ-bonded C_2H_4 at bridge sites and π-bonded C_2H_4 at top sites (*446,447*). When the temperature is increased to approximately 300 K, a hydrogen shift occurs from one carbon atom to the other to form ethylidene ($=CH–CH_3$) (*448*) followed by further dehydrogenation to form ethylidyne $\equiv C–CH_3$, which is oriented up-right and located at an fcc threefold hollow metal site (Fig. 42; the resultant hydrogen desorbs as H_2 at about room temperature) (*68,435–438,441,444,445,449,450*). Ethylidyne is then stable at temperatures up to about 400 K, and at higher temperatures, dehydrogenation continues, producing CH_x species and finally graphitic precursors. Nearly the same ethene adsorption states had been observed previously for Pt(1 1 1) (see below).

Ethene adsorption on Pd(1 1 1) was investigated by SFG spectroscopy (*68,83,84,98,120*). Figure 43 shows SFG spectra after adsorption of ethene at various temperatures. At 100–200 K, ethene adsorbed in a di-σ configuration with a characteristic peak at 2910 cm^{-1} ($\nu_S(CH_2)$; Fig. 43a). The second, weak peak at

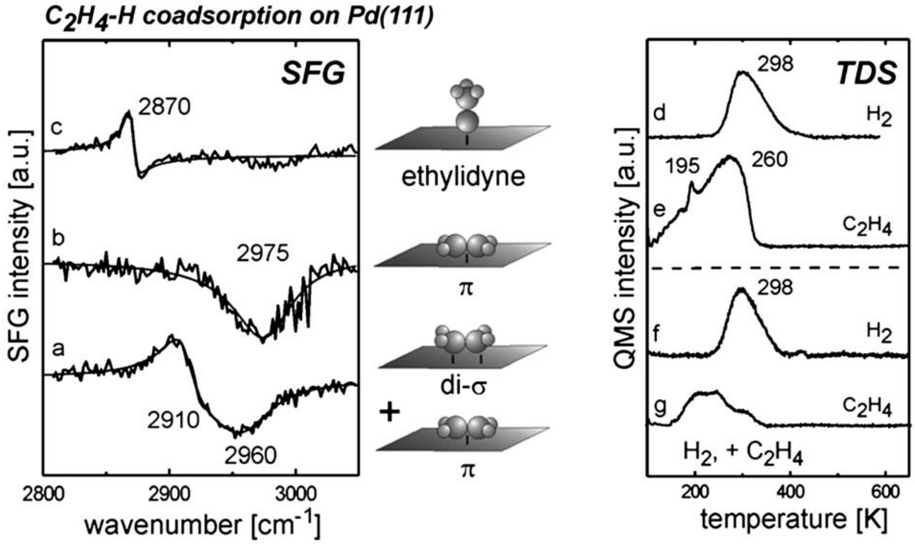

FIG. 43. SFG spectra of C_2H_4 species on Pd(1 1 1). Exposures were 2.5 L of C_2H_4 at 100 K (a), 1 L of H_2 followed by 2.5 L of C_2H_4 at 100 K (b). Spectrum (c) was acquired at 300 K after annealing of the sample in 5×10^{-7} mbar of C_2H_4 at temperatures from 100 to 300 K. (d–g) TD spectra of hydrogen (mass 2) and C_2H_4 (mass 27) from Pd(1 1 1). TD spectra of the individual components are shown in (d and e), those of coadsorption in (f and g). Exposures were as follows: (d) 1 L of H_2 at 95 K; (e) 1 L of C_2H_4 at 95 K; (f) and (g) display the desorption traces after exposures of Pd(1 1 1) to 1 L of H_2 and subsequently to 1 L of C_2H_4 at 95 K; adapted from *(68,98)* with permission from Elsevier.

about 2960 cm^{-1} can be attributed to the $\nu_S(CH_2)$ of π-bonded ethene. In the spectra of ethene on single-crystal surfaces, the $\nu_S(CH_2)$ signal for π-bonded C_2H_4 (with the C–H bonds nearly parallel to the metal surface (*447*)) is very weak, a result attributed to the surface-dipole selection rule for metal surfaces (dynamic dipoles parallel to the surface plane are canceled by image dipoles inside the metal (*17*)); furthermore, the surface concentration of π-bonded C_2H_4 may be low. The identification of π-bonded ethene is therefore ambiguous (the SFG peak was identified only indirectly; a better fit was obtained by assuming two resonances).

When the ethene layer of Fig. 43a was heated to room temperature, nearly all of the ethene desorbed and only a small amount was dehydrogenated to ethylidyne (*254,445*). Compared with Pt(1 1 1) (see below), palladium has a weaker tendency to produce ethylidyne. Only after adsorption of ethene at room temperature (*68,449*) could a signal for ethylidyne ($M{\equiv}C{-}CH_3$) be observed, at 2870 cm^{-1} ($\nu_S(CH_3)$; Fig. 43c).

I.1.2. C_2H_4–Hydrogen Coadsorption under UHV. A Pd(1 1 1) surface, covered only with π-bonded ethene ($\nu_S(CH_2)$ at 2975 cm^{-1}), was produced by first adsorbing hydrogen (which blocked threefold hollow sites), followed by ethene adsorption at 100 K (Fig. 43b), as evidenced by IRAS (*444,451,452*) and SFG (*68*). Preadsorbed oxygen has a similar effect as preadsorbed hydrogen (*445*). The coadsorption of C_2H_4 and hydrogen was also examined by TDS (Figs 43d–g) (*98*). Desorption spectra of the individual components are presented in Figs 43d and e for comparison.[19] Comparable to CO, preadsorbed C_2H_4 prevents hydrogen adsorption, and 1 L of hydrogen was thus adsorbed before 1 L of C_2H_4 was dosed at 95 K (Figs 43f and g). In contrast to CO, C_2H_4 was able to adsorb on a H-precovered surface (Fig. 43g) at 95 K, but C_2H_4 was now (mainly) bonded in a π-configuration, which desorbed at lower temperature. The difference between CO and C_2H_4 is presumably related to the preferred adsorption sites of the two molecules. Preadsorbed H (or O) occupies threefold hollow sites and thus blocks the most stable CO adsorption site, whereas π-bonded C_2H_4 can still adsorb at on-top sites (whereas di-σ-bonded ethene is (partially) blocked). The change in the C_2H_4 adsorption configuration as observed by SFG and TDS demonstrates that C_2H_4 and H coexist on the surface at 95 K (although electronic effects of subsurface hydrogen were also suggested to influence C_2H_4 adsorption (*454*)). During the TDS experiment, a small amount of ethene decomposed into ethylidyne (C_2H_3) at about 300 K (*98,104,435,445,449,450*), and its further decomposition led to the small H_2 peak at about 425 K (Fig. 43f).

Now consider the formation of ethane under UHV conditions: On the basis of investigations of hydrogen absorption described in Sections IV.C.4 and IV.C.5 (*98*), dissolution of H in the bulk metal should also be expected to occur during TPD of the H/C_2H_4 system at temperatures between approximately 125 and 200 K. This dissolution leads to a reduction of the surface hydrogen concentration and to a (partial) separation of H (in the bulk) and C_2H_4 (on the surface) (similar to what occurs in the case of CO and hydrogen), which decreases the probability of a catalytic reaction between C_2H_4 and H (*98*). Indeed, TDS investigations of C_2H_4 hydrogenation on Pd(1 1 1) (*337,444,455*) indicated only small amounts of desorbing ethane (less than a few percent of C_2H_4 were hydrogenated). At temperatures at which H returns to the surface from the bulk (and desorbs recombinatively at about 300 K; Fig. 43f), C_2H_4 has already mostly desorbed. This explanation is also supported by the observation that TDS detects the maximum of C_2H_6 formation/desorption from Pd(1 1 1) at about 270 K (*444,455*) (i.e., about 80 K higher than from palladium particles (for which bulk dissolution of hydrogen is apparently limited; see below). Consequently, the low activity of Pd(1 1 1) in TDS is attributed to an effectively small H surface concentration at about 200 K, rather than to an inherently low activity of Pd(1 1 1) for C_2H_4 hydrogenation.

I.2. *Ethene Adsorption and C_2H_4–Hydrogen Coadsorption on Pd/Al_2O_3 under UHV*

SFG, TDS, and IRAS investigations of C_2H_4 adsorption and C_2H_4–hydrogen coadsorption were also carried out with Al_2O_3-supported palladium nanoparticles (mean diameter, 6 nm). Because of the confinement of hydrogen within the palladium particles, a loss of surface hydrogen (to the palladium bulk, as for palladium single crystals) does not occur, leading to a higher conversion of C_2H_4 to C_2H_6, consistent with what has been observed experimentally (*68,337*).

---

[19] The broad 260 K peak in Fig. 43e can be attributed to (mainly) di-σ-bonded ethene, whereas the small features at 195 K are attributed to order–disorder transitions during C_2H_4 desorption (*98,453*).

With respect to ethene adsorption, C_2H_4-SFG signals characterizing adsorbates on palladium particles turned out to be too weak for detection, but IRAS spectra were reported by Frank *et al.* (*254,456*). The relative ratio of di-σ- to π-bonded ethene depends on the palladium particle size, with a preference for di-σ-bonded ethene for larger particles (*254*). This preference is likely best attributed to the fact that on small palladium particles, bridge sites for a di-σ configuration are rarer than on-top sites for the π-configuration. Similar to the situation on Pd(1 1 1), most of the ethene desorbed upon heating under UHV (*254*). Because di-σ-bonded ethene is the precursor for ethylidyne, more ethylidyne was formed on larger particles, about 30% on 3.5-nm palladium particles, about 10% on palladium particles with diameters <1.5 nm (*104,254*). Investigations of C_2H_4–hydrogen coadsorption in the absence of distinct palladium hydride phases were also reported (*83,104,337*); as was mentioned, conversions of only a few percent were observed.

In the following, we focus on the specific activity of palladium hydride phases for C_2H_4 hydrogenation, because the involvement of dissolved hydrogen in catalytic reactions has been proposed (*337,356–358,457*). Figure 44 provides a comparison of TDS traces of H_2 (mass 2), C_2H_4 (monitored by mass 27), and C_2H_6 (monitored by mass 29) measured after adsorption of the individual components (Fig. 44a, b) as well as after C_2H_4–hydrogen coadsorption (Fig. 44c). Adsorption of 50 L of H_2 on well-faceted 6-nm palladium nanoparticles at 120 K produced a TDS pattern typical of adsorbed H and palladium hydride (approximately $PdH_{0.3}$) (cf. Fig. 28; C_2H_4 and C_2H_6 desorption traces are also displayed to exclude the adsorption of residual

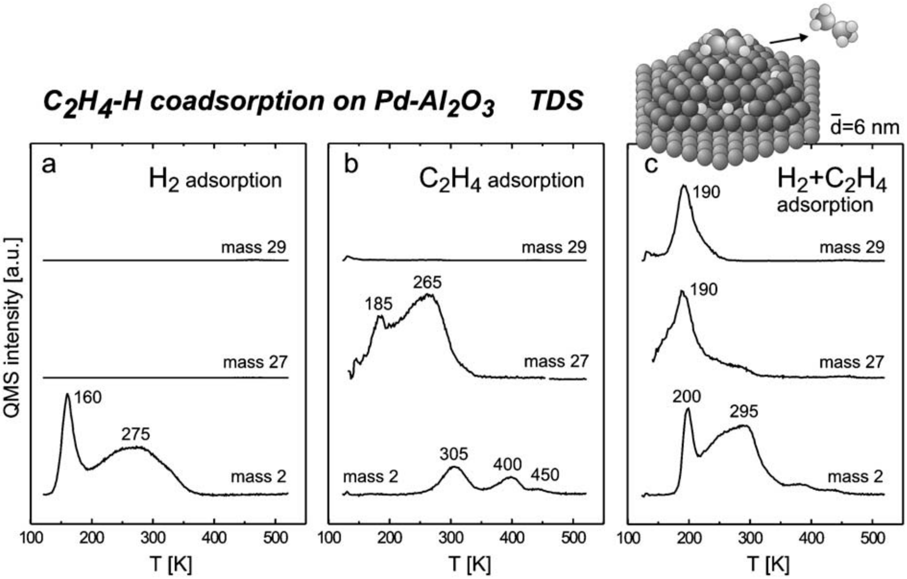

FIG. 44. TD spectra characterizing H_2 (mass 2), C_2H_4 (monitored by mass 27), and C_2H_6 (monitored by mass 29) on Pd/Al_2O_3 (mean particle diameter, 6 nm). The spectra were measured after adsorption of H_2 (a), C_2H_4 (b), and after C_2H_4–hydrogen coadsorption (c). Exposures were 50 L of H_2 at 120 K (a), 1.5 L of C_2H_4 at 120 K (b) and 50 L of H_2 followed by 1.5 L of C_2H_4 at 120 K (c); adapted from (*68*) with permission from Elsevier.

gases). After adsorption of 1.5 L of C_2H_4 at 120 K (Fig. 44b), C_2H_4-TDS indicated a broad peak with a maximum at 265 K and a small desorption feature at 185 K. The TDS trace is quite similar to that representing Pd(1 1 1) (cf. Fig. 43e), indicating that the spectrum is dominated by desorption from the (1 1 1) particle facets (C_2H_4 desorption from Pd(1 0 0) is not too different (*439*)). Taking into account corresponding SFG spectra characterizing Pd(1 1 1) and IRAS spectra characterizing palladium nanoparticles (*19,254,456*), we attribute the 265-K peak to di-σ-bonded ethene; the 185-K feature is most likely attributable to π-bonded ethene or to order–disorder transitions in the ethene layer upon desorption (*98,453*). This interpretation agrees with the results of theoretical investigations suggesting a combination of di-σ-bonded C_2H_4 at bridge sites and π-bonded C_2H_4 at top sites at low adsorption temperatures (*446,447*). Some ethene decomposed into ethylidyne at about 300 K, which was further dehydrogenated at higher temperatures, and these results explain the H_2 desorption indicated in Fig. 44b (*68,104,435,445,449,450*).

In the C_2H_4–hydrogen coadsorption experiment (Fig. 44c), 50 L of hydrogen were adsorbed on Pd/Al_2O_3 at 120 K, immediately followed by 1.5 L of C_2H_4 (preadsorbed C_2H_4 would prevent hydrogen adsorption). As is evident from SFG (Fig. 43), IRAS (*444,451*), and TDS data (Fig. 44c), C_2H_4 was now mostly bonded in a π-configuration, and the amount of di-σ-bonded ethene was strongly reduced. This result can be understood by considering that preadsorbed H occupies threefold hollow sites and influences the adsorption of di-σ-bonded ethene (at bridge sites (*446,447*)), whereas π-bonded C_2H_4 can still adsorb at on-top Pd atoms. The change in the C_2H_4 adsorption configuration points to the coexistence of C_2H_4 and H on the particle surface at 120 K (although H displacement to the subsurface (*68,273*) and electronic effects of subsurface H cannot be excluded (*454*)).

The most interesting result of the experiments characterizing coadsorption of C_2H_4 and hydrogen on palladium nanoparticles is, however, related to the H_2 and C_2H_6 desorption traces shown in Fig. 44c. First, the H_2 desorption peak attributed to the decomposition of palladium hydride was shifted from 160 to 200 K. This is less than the corresponding shift for H–CO coadsorption (85 K; cf. Fig. 31), but still indicates an effect of the C_2H_4 overlayer on H_2 desorption (either by stabilization of the hydride or, more likely, by hindrance of hydrogen recombination). Second, and most interestingly, C_2H_6 was produced and desorbed at about 190 K with a C_2H_6 TDS-desorption signal (monitored by mass 29) nearly as intense as that of C_2H_4 (monitored by mass 27) (Fig. 44c). This result is remarkable because previous TDS investigations of C_2H_4–hydrogen coadsorption with Pd/Al_2O_3, carried out in the absence of distinct hydride phases, had led to reports of a C_2H_6 desorption signal that was typically much smaller than that of C_2H_4 (with a ratio of signals of the order of a few percent (*337,455*)).[20]

---

[20] TDS investigations of C_2H_4 hydrogenation typically monitor mass 30 or 29 for C_2H_6 and mass 28, 27, or 26 for C_2H_4. Variations in the masses used (e.g., 30/28 vs. 29/27) induce only minor sensitivity changes that are much smaller than the effect reported here. The cracking pattern of C_2H_6 (mass/percent) 30/28%, 29/23%, 28/100%, 27/35%, and 26/24%; of C_2H_4 (mass/percent) 28/100%, 27/63%, 26/54%.

When an accounting is made for the fragmentation of ethene and ethane in the mass spectrometer, the data indicate that the conversion of C_2H_4 was nearly 100% in the presence of palladium hydrides (cf. Fig. 44c). This result apparently indicates a direct involvement of palladium hydride in the catalytic hydrogenation reaction. The conclusion of an inherently higher catalytic activity of dissolved hydrogen (palladium hydrides or subsurface H) than of surface hydrogen is, however, not unambiguous. One must take into account that when palladium hydride is present, its decomposition will supply H to the surface and thus increase the concentration of surface hydrogen at the reaction temperature of about 190 K, and this higher surface concentration of H may simply cause the high C_2H_4 conversion.

On the other hand, it is still remarkable that the presence of only 50% more hydrogen bound as palladium hydride [21] leads to a conversion (in the TDS experiment) that is about 20 times higher than was observed in corresponding experiments without palladium hydride. Although the activity increase is much higher than the increase in available hydrogen, further experiments are required to establish whether there is an inherently higher reactivity of dissolved hydrogen than of surface hydrogen. In any case, under UHV conditions, palladium nanoparticles are still (somewhat) more active for C_2H_4 hydrogenation than Pd(1 1 1) (*68,337*). Hydrogen dissolution in palladium nanoparticles is restricted to the small volume, whereas hydrogen dissolution in the bulk of Pd(1 1 1) may lead to a depletion of surface hydrogen, which decreases the reaction probability.

I.3. *Ethene Hydrogenation on Pd(1 1 1) and Pd/Al_2O_3 at Atmospheric Pressure*

Ethene hydrogenation at a total pressure of 1 bar was investigated by using the high-pressure reaction cells described in Sections III.A and III.B, which were coupled to an online gas chromatograph for product analysis (*68,83,84,118,120,453*). SFG and PM-IRAS spectroscopy were employed to characterize the functioning catalysts with simultaneous rate measurements by GC analysis of the products. On the basis of previous investigations (e.g., References (*18,19,68,83,104,138,254,337*)) and the results of the coadsorption experiments described above, one may expect π-bonded ethene to be the most likely reactive intermediate in the catalytic hydrogenation.

I.3.1. Reaction on Pd(1 1 1). Under reaction conditions of 5 mbar of C_2H_4, 5 mbar of H_2 and 990 mbar of Ar, a TOF of $\sim 1\,s^{-1}$ was observed at 300 K—the activity was relatively high. Nevertheless, SFG spectra acquired during C_2H_4 hydrogenation did not give evidence of any resonances (not shown), suggesting that both di-σ-bonded ethene and ethylidyne were absent or present in only small amounts (*83,84*). In light of the high activity, π-bonded ethene may therefore be suggested to be the reactive species. As was mentioned, π-bonded ethene produces

---

[21] Under the given conditions, assuming a surface H coverage of 1 ML, the amount of dissolved H is equivalent to 0.5 ML (cf. TDS in Fig. 44a), yielding an average particle composition of $PdH_{0.3}$. For corresponding experiments in the absence of palladium hydride, a surface H coverage of 1 ML can be assumed.

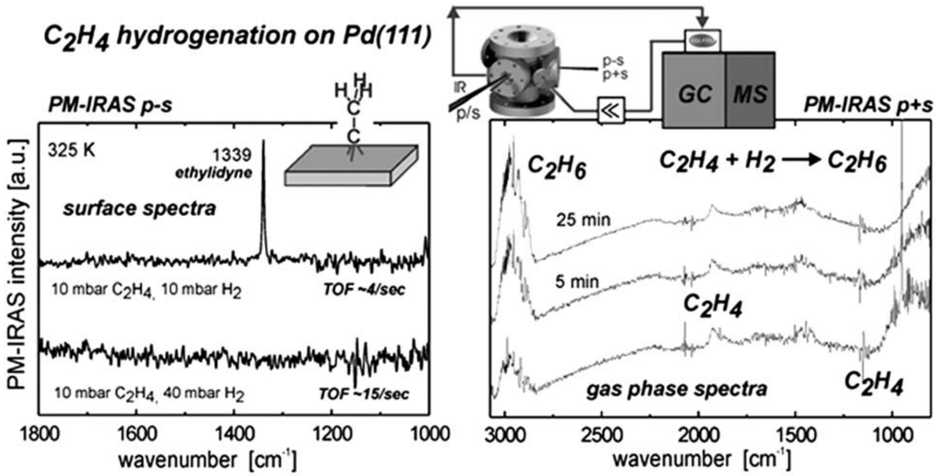

FIG. 45. PM-IRAS surface and gas-phase spectra of C_2H_4 hydrogenation on Pd(1 1 1) at 300 K; adapted from Borasio (*453*).

only a small SFG signal in the C–H stretching frequency range, as a consequence of its nearly parallel geometry on the (1 1 1) surface and its presumably small concentration. However, it is clear that SFG provided only indirect indications in support of this conclusion. In contrast, the detection of the deformation modes of π-bonded ethene at about 1000 cm^{-1} would be a direct demonstration. Because this frequency range is inaccessible to SFG, PM-IRAS experiments were performed.

Figure 45 is a collection of PM-IRAS surface (p−s) and gas-phase (p + s) spectra acquired during C_2H_4 hydrogenation on Pd(1 1 1) for two sets of experimental conditions (10 mbar of C_2H_4, 10 or 40 mbar of H_2, and 990 mbar of Ar at 325 K) (*452,453*). For a C_2H_4: H_2 molar ratio of 1:1, the TOF measured by GC was about 4 s^{-1}, and a single peak was detected at 1339 cm^{-1} in the PM-IRAS surface spectrum, characteristic of ethylidyne (δCH_3 of $\equiv C–CH_3$) (Fig. 45 (p−s)) (*254,449,456*). When a fourfold excess of hydrogen was used, the TOF was approximately 15 s^{-1}, and PM-IRAS did not give evidence of any surface species, indicating that C_2H_4 dehydrogenation to ethylidyne was suppressed (H adsorbed in hollow sites seems to block the sites required for ethylidyne formation). Apparently, under reaction conditions, the C_2H_4 surface concentration must be very low. π-Bonded ethene still seems to be the most likely intermediate, but a contribution of di-σ-bonded ethene cannot be excluded.

Ethylidyne, on the other hand, is only a spectator in C_2H_4 hydrogenation. C_2H_3 was present only under hydrogen-lean conditions that allowed (undesired) C_2H_4 dehydrogenation (decomposition), which finally led to catalyst deactivation by CH_x poisoning. This conclusion was corroborated by the observation that once an ethylidyne layer had been formed it could not be hydrogenated away by increasing the hydrogen pressure.

PM-IRAS also allowed the acquisition of gas-phase (p + s) spectra simultaneously with the surface (p−s) spectra. In this way, catalytic turnover could be

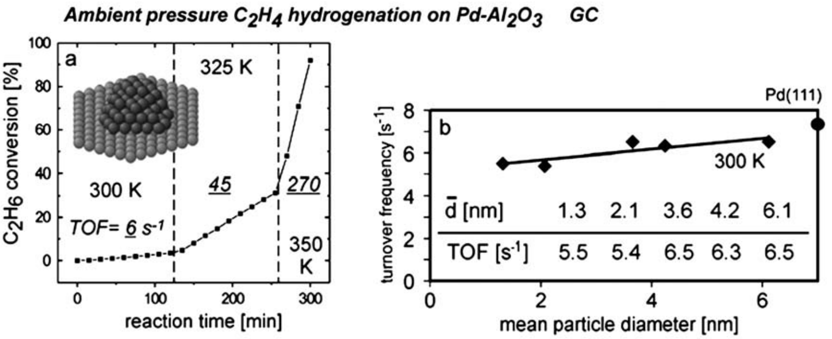

Fig. 46. (a) Ethene hydrogenation on a $Pd/Al_2O_3/NiAl(1\,1\,0)$ model catalyst with a mean palladium particle diameter of 3.5 nm. The reaction was carried out with 50 mbar of C_2H_4, 215 mbar of H_2, and 770 mbar of He at temperatures in the range of 300–350 K. Because the SFG cell was used as a recirculation batch reactor, the conversion increased with time. Turnover frequencies for the various temperatures are indicated. (b) Ethene hydrogenation activity of various $Pd/Al_2O_3/NiAl(1\,1\,0)$ model catalysts (mean palladium particle diameter of 1–6 nm), illustrating the structure insensitivity of this reaction. The TOF characterizing the reaction on Pd(1 1 1) is marked by the circle; adapted from (*83,120*) with permission from Elsevier.

followed by GC and also by IR. Figure 45 is a summary of the corresponding IR gas-phase spectra showing the evolution of C_2H_6.

I.3.2. Reaction on Pd/Al_2O_3. The hydrogenation activity of palladium–Al_2O_3/NiAl(1 1 0) model catalysts was also investigated under ambient conditions, with the SFG cell (Fig. 8) used as a recirculated batch reactor, with the catalytic reaction rate (TOF) measured by online GC (*83,84,120*). The model catalysts were exposed to 50 mbar of ethene, 215 mbar of H_2, and 770 mbar of helium at various temperatures (Fig. 46). The nanoparticle catalysts were found to be stable under reaction conditions, and the observed steady-state turnover frequencies, reaction orders (ethene: −0.3; hydrogen: 1), and the activation energy (about 50–60 kJ/mol) were very similar to values reported for impregnated powder catalysts (*458,459*). Figure 46a shows conversion vs. time plots for palladium particles of 3.5 nm mean diameter, and Fig. 46b shows the observed TOF values at 300 K as a function of palladium particle size. The data show that TOF is essentially independent of particle size, as expected for a structure-insensitive reaction. The results indicate that Pd/Al_2O_3 model catalysts are well suited to catalytic tests at ambient pressure and closely mimic the properties of conventional (impregnated) catalysts. Unfortunately, SFG spectroscopy of palladium nanoparticles under reaction conditions did not give evidence of any adsorbed ethene species, similar to the situation for Pd(1 1 1) (cf. Fig. 45). Although π-bonded ethene is again the most likely reactive species, no conclusive demonstration for this expectation has been obtained so far.

Under the reaction conditions (pressures of mbar), a nearly identical TOF was observed for Pd(1 1 1) (indicated by the circle in Fig. 46b) as for the supported palladium nanoparticles. Thus, the activity difference between palladium particles and Pd(1 1 1) observed in UHV-TDS experiments (*337*) does not occur under realistic reaction conditions when a sufficient surface population of hydrogen atoms is present on both the nanoparticle and single-crystal model catalysts. Furthermore, it is emphasized that, depending on the reaction conditions, palladium hydrides may or may not be present, and these deserve further attention.

J. Ethene Adsorption and Hydrogenation on Pt(1 1 1); Effect of Coadsorbed CO

In the following section, ethene adsorption on Pt(1 1 1) is discussed and contrasted to the corresponding adsorption on Pd(1 1 1). The interaction of C_2H_4 with H_2 and CO under UHV and at mbar pressure is also included, because the interaction of CO and ethene, for example, is important in the selective hydrogenation of acetylene/ethene mixtures when traces of CO are added to suppress ethene hydrogenation. This procedure can be understood by considering the results of the SFG experiments summarized below, which show that CO strongly blocks ethene adsorption (*160,460*) (whereas the adsorption of acetylene is less affected). Traces of CO are also beneficial for the selective hydrogenation of 1,3-butadiene to give butenes (when butane formation must be avoided (*361*)). More complex SFG investigations of alkene hydrogenation, such as propene hydrogenation (*461*), C_6 hydrocarbon hydrogenation (*462*), and cyclohexene hydrogenation/dehydrogenation (*46,138,463,464*) have also been reported.

J.1. *C_2H_4 Adsorption and Hydrogenation on Pt(1 1 1) under UHV and at mbar Pressure*

The atomic structures of the various ethene species on platinum surfaces were examined by a variety of techniques including LEED, UPS, HREELS, IRAS, NEXAFS, etc. (*407,465–467*) (cf. Fig. 42). At temperatures below 50 K, C_2H_4 adsorbs in π-coordination on top of single Pt atoms (*407,466,467*). At temperatures between 60 and 240 K, di-σ-bonded ethene is the most stable species (*468,469*), occupying fcc threefold hollow sites, with the molecular axis of di-σ ethene tilted 23° away from the surface plane (*407,467*). At higher temperatures, ethylidene (= CH–CH_3) is produced (*448*), followed by further dehydrogenation to form ethylidyne ≡C–CH_3, which is oriented up-right and still located at the same fcc threefold hollow metal site. At temperatures above 450 K, dehydrogenation continues, producing CH_x species (graphitic precursors).

The various ethene adsorbate species can be identified by vibrational spectroscopy (cf. Fig. 43) (*46,138,448,470–475*). Calibration SFG spectra recorded under UHV include three vibrational features, at 2880, 2910, and 3000 cm^{-1} (*138*), which are similar to those characterizing the adsorbates on Pd(1 1 1). The peak at 2880 cm^{-1} is attributed to the $\nu_S(CH_3)$ stretch vibration of ethylidyne (M≡C–CH_3), the feature at 2910 cm^{-1} results from the $\nu_S(CH_2)$ of chemisorbed di-σ-bonded ethene, and the very weak peak at 3000 cm^{-1} represents the $\nu_S(CH_2)$ of physisorbed π-bonded ethene. As has been stated, the $\nu_S(CH_2)$ signal characterizing π-bonded molecules on single-crystal surfaces is very weak and explained by the surface-dipole selection rule for metal surfaces (*17*).

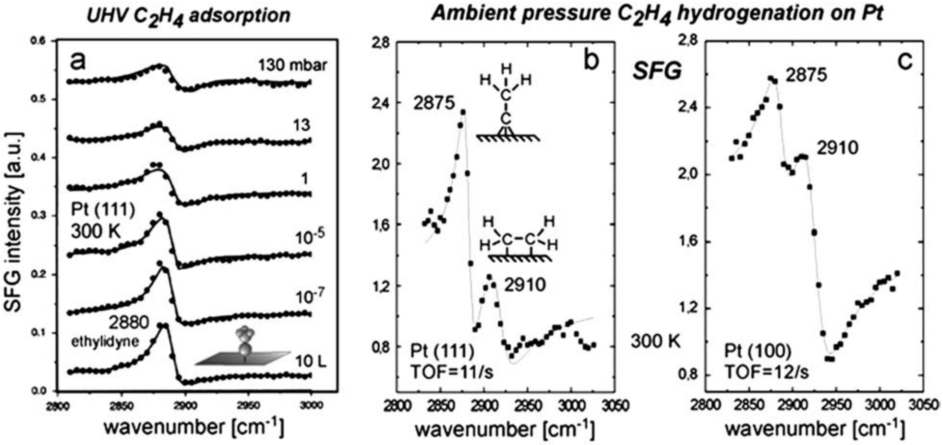

FIG. 47. (a) SFG spectra characterizing ethene adsorption on Pt(1 1 1) at 300 K, showing a strong signal from ethylidyne; adapted from Chen *et al.* (*460*). (b, c) SFG spectra acquired to characterize adsorption on platinum single-crystal surfaces during ethene hydrogenation catalysis with 45 mbar of C_2H_4, 130 mbar of H_2, and 830 mbar of helium at 300 K. The absence of a correlation between the spectral intensities and the observed catalytic activity (TOF) indicate that ethylidyne and di-σ-bonded ethene are spectator species; adapted from McCrea and Somorjai (*138*) with permission from Elsevier.

Fig. 47a shows SFG spectra characterizing room temperature adsorption of ethene on Pt(1 1 1) from UHV to a pressure of about 130 mbar, with the peak at 2880 cm^{-1} clearly indicating the presence of ethylidyne. At the relatively high pressure, the ethylidyne peak decreases, which may indicate the coadsorption of di-σ-bonded ethene. Ohtani *et al.* (*476*) observed by IRAS that C_2H_4 at about 1 mbar reduced the formation of ethylidyne on Pt(1 1 1), which the authors attributed to the reversible adsorption of di-σ-bonded ethene. Di-σ-bonded ethene was converted to ethylidyne at temperatures of 260–300 K in the presence of ethene at 1 mbar, whereas it was already converted at 240–260 K in vacuum. Vacant sites adjacent to di-σ-bonded ethene seem to be necessary for ethylidyne formation, which are occupied by di-σ-bonded ethene if the surface is equilibrated with gaseous ethene.

Ethene hydrogenation catalysis at atmospheric pressure was investigated by Somorjai and coworkers using SFG and gas chromatographic detection of the product ethane; the catalysts were Pt(1 1 1) and Pt(1 0 0) (*46,138,160,430,472,473*). When the reactant partial pressures were in the ranges of 13–26 mbar of ethene, 50–160 mbar of H_2, (and 780–910 mbar of He) a TOF of about 11 s^{-1} was observed for reaction on Pt(1 1 1) at 300 K (Fig. 47b; the ethene conversion was nearly 100% after about 1 h). SFG spectra indicated that ethylidyne (C_2H_3; 2875 cm^{-1}) and di-σ-bonded ethene (2910 cm^{-1}) were present during the reaction both on Pt(1 1 1) and Pt(1 0 0) (Fig. 47c) (*138*). Although the ratio of C_2H_3 to di-σ-bonded C_2H_4 was different for the two surfaces, the same activity was observed, indicating that both strongly bound species are only spectators. Further experiments, carried out under various reaction conditions, corroborated the result that the hydrogenation rate did not scale with the surface concentration of C_2H_3 and/or di-σ-bonded ethene (see References (*46,138*) for details). Weakly bound π-bonded ethene and ethyl were thus proposed as reactive intermediates, but (similar to the situation on palladium) they could not be unambiguously identified spectroscopically (*138*).

J.2. *C_2H_4–CO Coadsorption and Hydrogenation on Pt(1 1 1) at Pressures Ranging from UHV to 500 mbar*

The coadsorption of ethene with CO is of interest because CO may either favorably modify selectivity (e.g., in acetylene/ethene hydrogenation) or act as an inhibitor. In a normal scanning SFG experiment, the frequency regions of C–O and C–H stretching vibrations, which are about 800 cm^{-1} apart, can be measured only one after another, which requires long acquisition times. This limitation can be overcome by the SFG-compatible UHV-high-pressure cell (*48,160*) represented in Fig. 9. The large windows of this design (aperture of approximately 5 cm) allow one to carry out 2-IR 1-visible SFG by combining two optical parametric systems (the principle is also shown in Fig. 9). Two different spectral regions can be acquired at a time, for example, the C–O and C–H stretching vibrations, and the acquisition time for the spectra is hence shortened, and more important, two (or more) types of species can be monitored simultaneously.

This design was employed to examine the coadsorption of CO and ethene on Pt(1 1 1) over a wide pressure range (*160,460*). When ethene was exposed to a CO-covered Pt(1 1 1) surface (0.5 ML bridge and on-top bonded CO) at 300 K, ethene was unable to adsorb even at 45 mbar pressure, indicating a strong site-blocking effect of CO (the C_2H_4 impingement rate was $\sim 10^7$ molecules/(Pt surface atom × s) under these conditions). The adsorption of ethene requires fcc threefold hollow sites (for di-σ-bonded ethene) or on-top sites (for π-bonded ethene) that are both blocked by CO. As a result of Pauli repulsion, the ethene molecules may not even reach the platinum surface (*98*). Thus, an adsorbed monolayer of CO inhibits the hydrogenation reaction, even when mbar pressures of ethene are present.

Consequently, Pt(1 1 1) was first exposed to 10 L of ethene at 330 K, producing a saturation (0.25 ML) layer of ethylidyne, as is evident from a single peak at 2880 cm^{-1} in the C–H stretching frequency range (cf. Fig. 48b). In the experiments described in the following, various amounts of CO were exposed to the C_2H_3-precovered Pt(1 1 1) surface at 300 K (Fig. 48a,b). At 10 L (or *ca.* 10^{-7} mbar) of CO, a peak at about 2020 cm^{-1} appeared in the C–O stretching frequency range, typical of on-top CO. However, the peak was redshifted and about seven times weaker than that of on-top CO on clean Pt(1 1 1) (at 2080–2095 cm^{-1}). Apparently, some CO can still adsorb on on-top sites in the presence of ethylidyne (which is located in threefold hollow sites), but the frequency shift indicated a more strongly bonded CO species. The stronger bonding may result from electron donation from ethene to the substrate, leading to an increased electron back-donation from platinum to CO. A reduction in CO dipole coupling by ethylidyne may also contribute to the observed shift (see Reference (*460*) for a detailed discussion). In the C–H stretching frequency range, the peak at 2880 cm^{-1} indicated that ethylidyne was not affected by coadsorbed CO.

Increasing the CO partial pressure led to an increase in the CO peak intensity (Fig. 48a), a decrease in its linewidth, and a shift to higher wavenumbers, while the intensity of the ethylidyne peak decreased. At CO partial pressures exceeding about

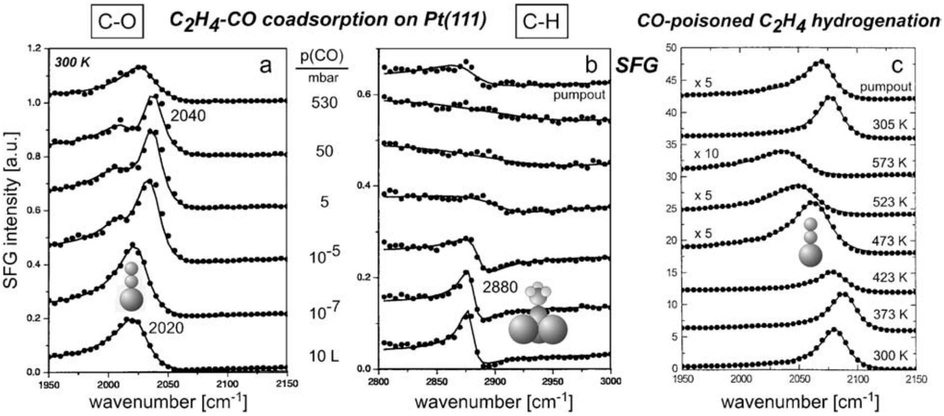

FIG. 48. (a,b) SFG spectra of CO adsorbed at 300 K on a Pt(1 1 1) surface that had been pre-exposed to 10 L of ethene. The C–O as well as the C–H stretching frequency range are displayed, measured simultaneously by 2-IR 1-visible SFG *(160,460)*. (c) Effect of CO poisoning on ethene hydrogenation on Pt(1 1 1) at 13 mbar of C_2H_4, 130 mbar of H_2, 850 mbar of Ar, and 4 mbar of CO as observed by SFG; adapted from Chen *et al.* *(460)* with permission from Elsevier.

1 mbar, the CO peak position shifted to 2040 cm^{-1}, and no clear resonance was no longer observed in the C–H stretching region. This change indicates that a high partial pressure of CO leads to partial displacement of ethylidyne from the Pt(1 1 1) surface. If ethylidyne would be fully displaced, a CO peak would be expected to occur at 2095 cm^{-1} (and should also be four times more intense than the one observed). Furthermore, the presence of two CO peaks at high pressures may also point to the presence of ethylidyne. Chen *et al.* *(460)* suggested that the 2040-cm^{-1} component in the high-pressure CO spectra most likely originates from CO molecules within CO islands, whereas the weaker shoulder at about 2020 cm^{-1} was tentatively assigned to isolated CO molecules neighboring ethylidyne molecules. The decrease in the ethylidyne peak intensity with increasing CO partial pressure may also be attributed to an orientational change of the ethylidyne molecules, which usually adsorb upright. If the ethylidyne molecules were tilted in the presence of CO, the net dynamic dipole moment along the surface normal would be reduced and part of their vibrational intensity lost *(460)*. An observation that supports this picture is the partial restoration of the ethylidyne SFG signal (and original ethylidyne orientation?) upon evacuation (Fig. 48b).

The effect of strong CO inhibition (or poisoning) on ethene hydrogenation catalysis was also investigated at mbar pressure *(400,460)*. The ethane production rate on Pt(1 1 1) was measured for a mixture of 13 mbar of C_2H_4, 130 mbar of H_2, and 850 mbar of Ar, with various partial pressures of CO (10^{-7}–4 mbar). Whereas at CO partial pressures below 0.1 mbar no strong effect was observed, in the presence of 4 mbar of CO, no ethane was produced at 300 K. Temperatures greater than about 423 K were needed to induce some hydrogenation activity (with a TOF three orders of magnitude lower than that without CO). This result can be understood by consideration of the corresponding SFG spectra of Fig. 48c, which show a strongly decreasing CO coverage with increasing temperature (note the scaling factors and the shift to lower wavenumbers). Furthermore, the activation energy for the CO-inhibited reaction was approximately 86 kJ/mol^{-1}, which is much higher than the activation energy observed in the absence of CO (45 kJ/mol^{-1}). Indeed, the activation energy for CO-poisoned ethene hydrogenation is identical to the enthalpy of adsorption of CO (i.e., the reaction becomes CO desorption limited). Even at temperatures exceeding the (UHV) CO desorption temperature (approximately 420 K), the reaction remains inhibited (the catalyst remains poisoned), because an equilibrium is set up between surface and gas-phase CO. CO poisons alkene hydrogenation apparently by blocking sites for ethene adsorption (and it also partially displaces adsorbed ethene) and by blocking sites for hydrogen adsorption/dissociation. The reaction proceeds only at temperatures at which CO desorbs (about 400 K). HP-STM investigations are needed for a full understanding of these processes, and the first results characterizing coadsorbate structures and adsorbate mobility have been reported *(477)*.

K. METHANOL DECOMPOSITION AND OXIDATION ON Pd(1 1 1) AND Pd/Al_2O_3

The previous sections described investigations of (co)adsorption and reaction of relatively simple molecules. Realistic catalysis typically deals with more complex molecules exhibiting a variety of different chemical bonds that can be activated, and selectivity becomes a critical issue. Consideration of methanol decomposition and methanol oxidation constitutes a step toward more complex reactions. CH_3OH decomposition has two competing pathways, dehydrogenation to give CO and H_2 (when the C–O bond stays intact) and C–O bond scission (cleavage of the C–O bond within a CH_yO species; $y = 1$–4) yielding carbonaceous deposits CH_x ($x = 0$–3). In the presence of oxygen, CH_3OH may be partially oxidized to give formaldehyde or fully oxidized to give CO_2.

SFG, HP-XPS, and PM-IRAS were employed to characterize elementary steps of these reactions. As shown below, processes that have a minor impact under UHV (such as C–O bond scission on Pd(1 1 1)) may dominate a reaction at ambient pressure. Thus, once again, we have a demonstration that UHV results cannot generally be extrapolated to conditions of technological catalysis.

K.1. *Methanol Decomposition on Pd(1 1 1) under UHV and at Elevated Pressures*

Methanol adsorption and decomposition on noble metals have been the subject of many surface-analytical investigations (e.g., References *94,171,320,350,378, 478–494*). CH_3OH dehydrogenation on palladium catalysts could be a valuable source of synthesis gas or hydrogen, but unfortunately catalyst deactivation by carbon deposits (coking) seriously limits this process *(495–498)*. In this respect, the probability of O–H vs. C–O bond scission is important, the first path resulting in CO and H_2, and the second in carbon or carbonaceous species (CH_x; $x = 0$–3), CH_4, and H_2O (see scheme in Fig. 49; details are discussed below).

K.1.1. UHV Investigations of Pd(1 1 1) under Adsorption/Desorption Conditions. A classical surface science approach to the surface reactions of methanol involves adsorption of methanol at cryogenic temperatures and monitoring of changes upon

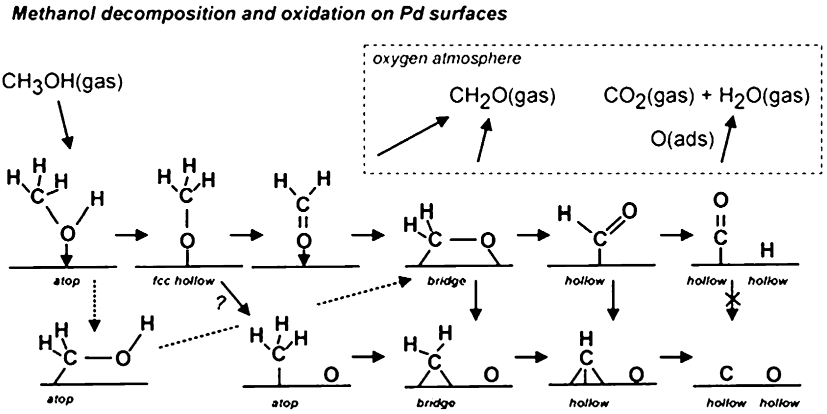

FIG. 49. Schematic illustration of CH_3OH decomposition and oxidation on palladium surfaces.

annealing by various spectroscopic methods. The results of such experiments indicated that the dehydrogenation of methanol proceeds via O–H bond scission with formation of CH_3O (methoxy) as the first intermediate at temperatures above about 150 K, followed by stepwise hydrogen abstraction to give CH_2O, CHO, and (at about 250–300 K) CO (*350,378,478–487*). A simultaneous formation of CH_3O and CH_3 species by dehydration of two adsorbed neighboring methanol molecules was also suggested (*489,493*).

The time- and temperature-dependent evolution of CO/CH_yO and of CH_x was investigated by combining XPS and PM-IRAS (*171*). After exposures of a few Langmuir, both methods indicated that adsorbed CH_3OH desorbed intact upon annealing to 300 K—that is, it largely desorbed before reacting to give CO (for spectra see Reference (*171*)). At temperatures exceeding 150 K, only a very small CO signal was observed, which indicates that desorption dominated over dehydrogenation and the yield to CO and H_2 was rather small (of the order of a few percent).

The probability of methanolic C–O bond scission on Pd(1 1 1) is still debated. In a number of UHV investigations, there was no report of any C–O bond scission at all (*479,483–486*), whereas in others, there were reports of (low) reactivity for the breaking of the methanolic C–O bond (*171,489,493,494*). XPS investigations indicated an upper limit of 0.05 ML of CH_x (*171,489*). To explain the differing results, it was suggested that methanolic C–O bond scission on Pd(1 1 1) may proceed on surface defects (*350,480,490–492*) or require near monolayer methanol coverage (*488,489,499*).

Another reason for the contrasting UHV reports may be simply related to the kinetics of the different routes of methanol decomposition. Besides fast dehydrogenation, methanolic C–O bond scission most likely also takes place on Pd(1 1 1), but at a low rate that is difficult to measure in typical UHV experiments. However, when the pressure is increased to the mbar regime (increasing the molecule impingement rate by at least six orders of magnitude), even a slow reaction may gain considerable importance; in this case, producing carbon species through methanolic C–O bond scission. Apparently, UHV results cannot be easily extrapolated to a

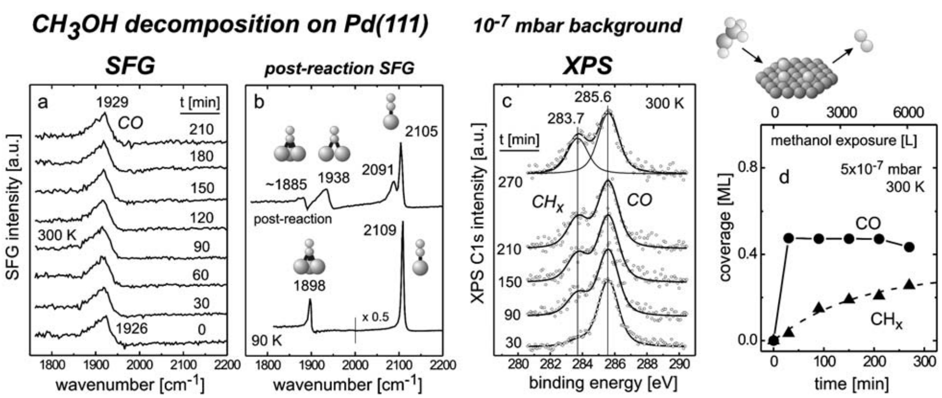

FIG. 50. SFG (a) and XPS C1s core-level (c) spectra measured during exposure of Pd(1 1 1) to 5×10^{-7} mbar of methanol at 300 K. The quantitative analysis of the XP spectra is shown in (d), pre- and post-reaction CO adsorption is compared in (b). The dashed line in (d) is the calculated rate of CH_x formation obtained by assuming a simple kinetics model in which the CH_x formation rate is proportional to the number of vacant sites; adapted from Morkel *et al.* (*94*) with permission. Copyright (2004) American Chemical Society.

catalytic regime; investigations at elevated pressures are therefore discussed in the next section.

K.1.2. Elevated Pressure Investigations of Pd(1 1 1). Combined SFG and HP-XPS experiments were carried out at higher pressures (10^{-7}–0.1 mbar) and higher temperatures (300–450 K), with the goal of facilitating dehydrogenation and methanolic C–O bond scission. Figure 50 includes SFG and C1s XP spectra, acquired at 5×10^{-7} mbar of CH_3OH at 300 K in intervals of 30 and 60 min, respectively (*94,274*). The SFG spectra (Fig. 50a) exhibit a single peak at about 1930 cm^{-1}, typical of hollow- or bridge-bonded CO (local coverage approximately 0.5 ML) (*17,86,120,182,253,260,273*). The corresponding C1s XP spectra include two overlapping peaks, at 285.6 and 283.7 eV (the original data points as well as traces of fitting two components to the spectra are included in Fig. 50c). Figure 50d displays the quantitative information extracted from these data. The peak at 285.6 eV remained constant and may be assigned to a CH_yO species ($y = 0$–4), such as CH_3OH, CH_3O, other dehydrogenation products (CH_2O, HCO), or CO. A quantitative analysis of the 285.6-eV peak indicated a coverage of about 0.5 ML, and because the same coverage was observed for CO by SFG, the peak at 285.6 eV is attributed principally to adsorbed CO. This conclusion is also supported by the results of previous investigations in which CO was the only species observed at 300 K (*481,483,486*).

In contrast to the result characterizing the dehydrogenation product CO, the coverage of the second feature (283.7 eV) increased with time (Figs 50c,d). On the basis of typical C1s binding energies of carbon(aceaous) species (282–285 eV) (*500*), the growing C1s peak at 283.7 eV was assigned to adsorbed CH_x ($x = 0$–3) species. After 210 min, approximately 0.2 ML of CH_x was present, but this amount was apparently too low to induce significant changes in the CO-SFG spectrum (Fig. 50a). Nevertheless, the binding site of the CH_x species could be examined by comparing

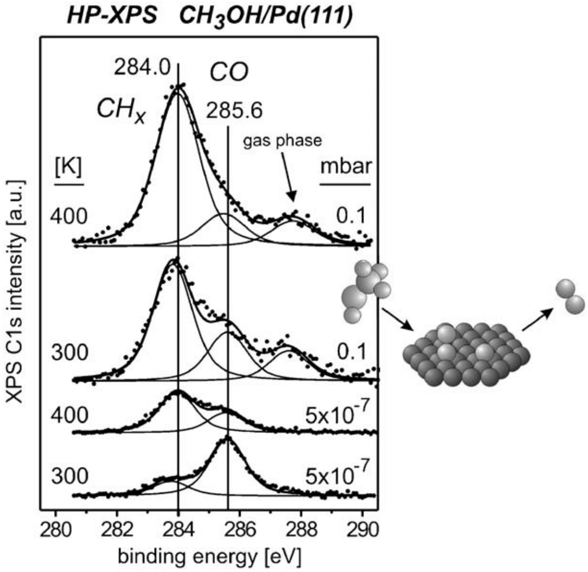

FIG. 51. C1s XP spectra of Pd(1 1 1) in presence of 5×10^{-7} mbar of CH_3OH and in presence of 0.1 mbar of CH_3OH at 300 and at 400 K (exposure time 90 min) indicating carbonaceous deposits; adapted from (*274*) with permission from Elsevier.

pre- and post-reaction CO adsorption spectra (Fig. 50b), which provide evidence of the availability of adsorption sites. On the clean Pd(1 1 1) surface, the typical (2 × 2)-3CO saturation structure (0.75 ML) was observed, with CO bonded to fcc and hcp threefold hollow sites and to on-top sites (Fig. 50b; cf. Fig. 15) (*120,273*). After methanol decomposition (210 min) at 300 K, a different saturation structure was observed, exhibiting hollow (approximately 1885 cm^{-1}), bridge (1938 cm^{-1}), and two on-top CO features (2091 and 2105 cm^{-1}) (Fig. 50b). These observations, together with the approximately twofold reduced intensity of hollow (and on-top) bonded CO, indicate that a fraction of the hollow sites were blocked by CH_x.

The preferred binding of CH_x to hollow sites may also indicate its stoichiometry. According to theoretical investigations (*501,502*), CH_x fragments ($x = 0$–3) tend to restore their tetravalency on the surface: adsorbed carbon atoms and CH species prefer hollow sites, CH_2 preferentially binds to bridge sites, and CH_3 bonds on top of Pd atoms. Consequently, the partial blocking of hollow sites suggests the presence of carbon atoms and/or CH species. However, because this stoichiometry cannot be unambiguously demonstrated, carbonaceous species are still termed "CH_x" below.

Corresponding SFG/XPS experiments were also carried out at 400 K and at pressures up to 0.1 mbar (*94,274*). Figure 51 provides a comparison of SFG and XP spectra acquired after 90 min at different pressures. SFG indicated adsorbed species, as described above (at 400 K only weak signals of hollow-bonded CO appeared), whereas XPS indicated three peaks (CO at 285.6 eV; CH_x at 283.8–284.0 eV; gas-phase CH_3OH at 287.6 eV appeared at pressures exceeding 10^{-2} mbar). Quantitative XPS analysis indicated the following approximate results: 0.5 ML of CO and

0.2 ML of CH_x at 5×10^{-7} mbar and 300 K; 0.2 ML of CO and 0.35 ML of CH_x at 5×10^{-7} mbar and 400 K; 0.5 ML of CO and 1 ML of CH_x at 0.1 mbar and 300 K; and 0.3 ML of CO and 1.5 ML of CH_x at 0.1 mbar and 400 K (for a complete table of results of time-dependent measurements, see Reference (*94*)). Obviously, increasing the temperature or CH_3OH partial pressure increased the amount of carbon(aceous) deposits. According to the XP spectra in Fig. 51, relatively large amounts of CO and CH_x coexist (e.g., about 0.5 ML of CO and about 1 ML CH_x at 0.1 mbar and 300 K). This coadsorption can occur only if carbon either partly moves to subsurface regions (*95,503*) or produces three-dimensional carbon clusters on the palladium surface (*500*). GC investigations of methanol decomposition at pressures up to 100 mbar and temperatures of 300–550 K did not lead to detection of any products (such as CO, CH_4, or H_2O), and the CH_3OH GC-signal remained constant for several hours. Apparently, carbonaceous deposits rapidly poisoned the palladium surface under catalytic conditions.

K.1.3. Kinetics of C–O Bond Scission. Another interesting point is related to the rate of CH_x formation, which was fast in the initial stages but then leveled off after a CH_x coverage of about 0.2 ML was reached (both at 300 and at 400 K; cf. Fig. 50d (*94*)). At first, one could assume that these observations indicate a fast C–O bond scission on defects (which were then rapidly poisoned by CH_x), followed by slow C–O bond scission on (1 1 1) terraces (*320*). Although a low concentration of defects on the single-crystal surface cannot be excluded, one can also suggest that, instead of a defect-induced mechanism, C–O bond scission was initially fast on the clean surface (and at low CH_x coverage) but then slowed down with increasing CH_x coverage (cf. Fig. 50d) (*94*). The decomposition of adsorbed CH_3OH, CH_3O, or other CH_xO species into CH_x will require one or more vacant metal sites, where products/fragments of the C–O bond scission reaction can reside. With increasing CH_x coverage, the number of vacant sites is successively reduced, leading to a decreasing bond-scission rate.[22] The evolution of the CH_x surface concentration can be represented by a simple first-order kinetics model, according to which the CH_x formation rate is proportional to the number of vacant surface sites:

$$r(CH_x)_t = d\Theta(CH_x)/dt = k_1\Theta(^*)_t\Theta(CH_3OH)^0 \qquad (5)$$

Assuming a zero-order dependence of the rate on methanol surface concentration[23] and $\Theta(^*)_t = \Theta(^*)_{t=0}–\Theta(CH_x)_t$, it follows that $\Theta(CH_x)_t = \Theta(^*)_{t=0}\,(1 - e^{-k_1 t})$, with k_1 being the rate constant of CH_x formation and $\Theta(^*)_{t=0}$ the initial concentration of vacant surface sites. The dashed line in Fig. 50d represents the calculated rate (amount) of CH_x formation and fits the data reasonably well. This comparison

---

[22] In comparison, CH_3OH dehydrogenation was very fast, leading immediately to CO saturation; cf. Fig. 50d.

[23] On the timescale of the SFG/HP-XPS experiment, Pd(1 1 1) was exposed to about 10 000 L of CH_3OH. Only a few monolayers (if at all) of CH_3OH were converted to CO, H_2, and CH_x—that is, the CH_3OH coversion was negligible and the CH_3OH pressure unchanged (pseudo zero-order dependence in CH_3OH).

suggests that C–O bond scission may also occur on Pd(1 1 1) under these conditions and that a defect-induced mechanism must not be invoked to explain the time-dependence of CH_x formation.

Of course, surface defects may still exhibit the highest bond-breaking activity but, on the other hand, they will also be rapidly poisoned by carbon (*95,320*). Consequently, their influence may show up only in the initial stages of the reaction. Increasing the number of surface defects on Pd(1 1 1) by ion-bombardment had only a small influence on the C–O bond scission activity (*171*). In any case, at elevated pressure, methanolic C–O bond scission readily occurs even on Pd(1 1 1).

For completeness, we mention that SFG was able to detect the final product of CH_3OH decomposition (CO), whereas the frequency range of intermediate products such as formaldehyde was not accessible. Similarly, HP-XPS carried out with a laboratory X-ray gun cannot accurately differentiate CO from CH_xO. In contrast, the wider frequency range of PM-IRAS allowed the identification of, for example, CH_2O (in addition to CO) at elevated methanol partial pressures on a strongly CH_x-poisoned surface (*177*). As these PM-IRAS investigations are relevant to methanol oxidation, they are discussed below.

K.2. *Methanol Decomposition on Pd/Al_2O_3 under UHV and at Elevated Pressures*

CH_3OH decomposition at pressures from 10^{-7} to 100 mbar was also examined on Al_2O_3-supported palladium nanoparticles (mean diameter about 6 nm) (*362*), with SFG used for detection of the product CO. The results are similar to the corresponding measurements characterizing reaction on Pd(1 1 1); notwithstanding the continuous formation of CH_x species, only minor changes occurred in the CO-SFG spectra at 300 K over time (CO spectra are similar to those in Fig. 23 and are not included here). Because HP-XPS during reaction has not been performed for this system, the presence of CH_x was confirmed postmortem by XPS for a number of reaction conditions (*320,452,453,504*). The coverage of CH_x typically exceeded the surface coverage of CO (e.g., with 5×10^{-7} mbar of CH_3OH at 300 K, approximately 0.6 ML of CH_x and 0.5 ML of CO were observed after 200 min), suggesting that CH_x was present both on the facets and edges of the palladium nanoparticles. Furthermore, the absence of any products detected by GC indicated a rapid deactivation of the entire palladium particle surface.

When methanol decomposition was carried out at 400 K and pressures up to 100 mbar (Fig. 52), SFG indicated rapidly vanishing CO bands, pointing to an increasing CH_x poisoning (*362*). Even when the catalyst was in the poisoned state, methanol peaks still appeared in the C–H stretching region ($\nu_{a_s}(CH_3)$, 2950 cm^{-1}; $\nu_s(CH_3)$, 2830 cm^{-1}) (Fig. 52), indicating reversible methanol adsorption on the alumina support at elevated pressure. This result could be demonstrated conclusively because these bands disappeared upon evacuation of the sample (excluding CH_x to cause them), and also appeared on Al_2O_3/NiAl(1 1 0), but did not show up on Pd(1 1 1). For UHV investigations of methanol decomposition on palladium–Al_2O_3/NiAl(1 1 0), refer to References (*320,505*).

Regarding the mechanism of C–O bond scission, an interesting question is related to the origin of the carbon deposits. Do CH_x species originate directly from

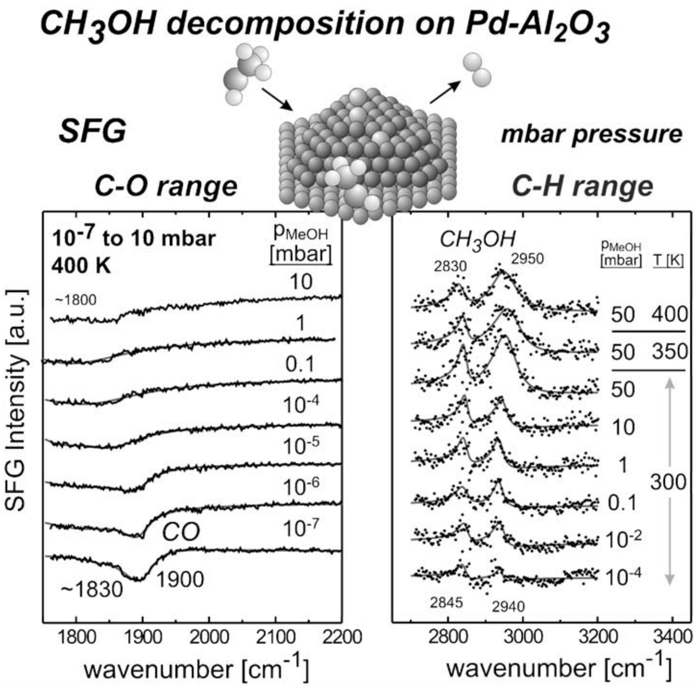

FIG. 52. SFG spectra acquired during methanol decomposition on Pd/Al_2O_3. Both the C–O and C–H stretching frequency ranges are shown; adapted from Morkel (*362*).

CH_3OH (via CH_yO (*492*) or dehydration (*489,493*)), or do they originate from dissociation of the decomposition product CO? As shown in Section IV.C.3, the latter possibility can be excluded, because, even after hours of high-pressure CO exposure, no indications of CO dissociation were found by SFG, PM-IRAS, and HP-XPS (cf. Figs 16, 17, and 27). Consequently, carbonaceous species must originate directly from CH_3OH/CH_yO precursors (Fig. 49). One can also ask why Pd(1 1 1) breaks the C–O bond within CH_3OH but not within (molecular) CO. Apart from the influence of the additional hydrogen atoms in the CH_3OH molecule, according to the arguments discussed in Section IV.C.3, the orientation of the C–O bond may be important. Whereas the upright adsorption geometry of CO on Pd(1 1 1) may be one of the reasons for the nonoccurrence of CO dissociation, during CH_3OH decomposition a CH_3O group bonded to the surface via the oxygen atom has to turn over in order to produce CO bonded via the carbon atom (*84,274,378*) (Fig. 49). During this process, adsorption geometries occur whereby the C–O axis deviates from a perpendicular orientation and can thus be broken. Along these lines, formaldehyde (CH_2O) and formyl (CHO), which incorporate a C–O bond that is parallel or inclined to the Pd(1 1 1) surface, may be the precursors of CH_x species (Fig. 49). The dehydration of two methanol molecules yielding CH_3O, CH_3, and H_2O also seems plausible, as deduced from the CH_3OH oxidation experiments described below.

K.3. Methanol Oxidation on Pd(1 1 1) and on Pd/Al_2O_3 at mbar Pressures

The oxidation of CH_3OH on palladium catalysts is interesting with respect to two possible reaction routes. First, methanol partial oxidation may provide a route to formaldehyde (CH_2O), and second, CH_3OH total oxidation to give CO_2 and H_2O can be considered as a model reaction for the oxidation of volatile organic compounds, which is important in waste treatment. On the basis of the experimental results presented above, it is clear that UHV coadsorption investigations are not necessarily relevant to technological systems, and consequently only experiments at pressures of about tens of mbar are discussed below (*177,504*).

K.3.1. High-pressure Methanol Oxidation on Pd(1 1 1). Figures 53a and b show PM-IRAS surface (p−s) and gas-phase (p + s) spectra acquired during methanol exposure and oxidation at mbar pressures. The gas-phase composition, determined by GC and by PM-IRAS,[24] respectively is shown in Figs 53c and d. After exposure of Pd(1 1 1) to 5 mbar of CH_3OH at 300 K, PM-IRAS was used to identify adsorbed CO (ν_{CO} at approximately 1840 cm^{-1}, typical of approximately 0.3 ML coverage) as well as formaldehyde (ρ_{CH_2} of formaldehyde in two different adsorption geometries (*506*), at 1305 and 1255 cm^{-1})[25] and formyl (CH bending or ν_{CO} at 1200 cm^{-1} (*507*)) (and minute amounts of methoxy characterized by a peak at about 2900 cm^{-1}; not shown; cf. Fig. 54a). These species result from the dehydrogenation of methanol via methoxy, formaldehyde, and formyl to give CO. According to the HP-XPS data summarized above (Fig. 51), at least 1 ML of CH_x was simultaneously present (the amount of CH_x may have been even larger because of the 50-times higher methanol partial pressure). Consequently, in the absence of oxygen, the surface was poisoned by CO, CH_2O, and CH_x (and small amounts of CHO and CH_3O; a contribution of formate (*508*) cannot be excluded but will not be considered here). As a result, no activity for methanol decomposition was detected by GC analysis (Fig. 53c), and furthermore, the corresponding PM-IRAS (p + s) gas-phase spectra showed only the reactant CH_3OH (Fig. 53b). Under UHV conditions, intermediate species in methanol decomposition were typically observed only at lower temperatures. For example, using HREELS, Davis and Barteau (*486*) observed formaldehyde species at about 170 K, leading to adsorbed CO and hydrogen atoms on Pd(1 1 1) at about 300 K. At 110 K, CHO was observed by Bhattacharya *et al.* (*481*) during CH_3OH decomposition on Pd(1 1 0). Using IRAS, Barros *et al.* (*506*) observed formaldehyde on Ru(0 0 0 1) at 190 K. As discussed in more detail below, formaldehyde seemed to be stabilized on a CH_x-poisoned surface.

When O_2 at 5 mbar was added to the gas phase, all the surface species were stable at temperatures up to 350 K, and no products were detected by GC (which indicated a mixture of CH_3OH and O_2 at partial pressures of 5 mbar each, with the remainder

---

[24] Fig. 53d was obtained by integration of the gas-phase peaks in the (p + s) PM-IRAS spectra. The plotted lines only *qualitatively* show the disappearance/evolution of the different components because the peak areas were not calibrated.

[25] According to (*506*), formaldehyde is adsorbed in bridging and chelating geometry. However, a contribution of formate is very likely (*508*).

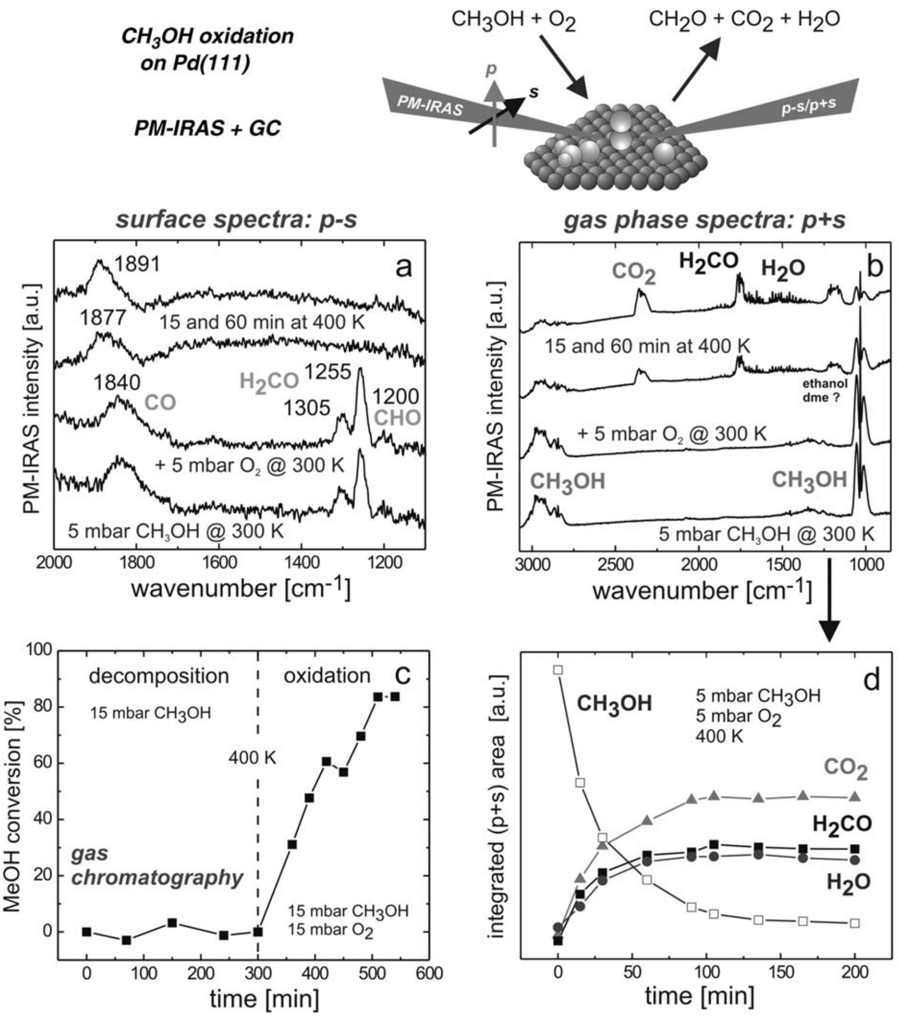

FIG. 53. PM-IRAS surface (a) and gas phase (b) spectra measured during CH_3OH oxidation on Pd(111). The methanol conversion was monitored by GC (c) and PM-IRAS (d); adapted from Borasio *et al.* (*177*) with permission. Copyright (2005) American Chemical Society.

being He and the total pressure being 1 bar). This result agrees with the results of SFG/HP-XPS investigations indicating that CH_x and CO species could not be oxidized at temperatures below 400 K (*94*). A surface covered with CH_x, CO, and CH_2O seems to provide no sites for dissociative oxygen adsorption, or the oxidation reaction may simply be too slow to measure at 300 K (*509*). The onset of catalytic activity was observed at 400 K, with CH_2O, CO_2, and H_2O being identified as gas-phase products by GC and PM-IRAS (p + s) spectroscopy (Fig. 53b). The CH_3OH conversion after 3 h at 400 K was about 84%, yielding a TOF of 7 s^{-1} (the initial value was 15 s^{-1}), and with a product distribution of *ca.* 10% CH_2O and 25% CO_2

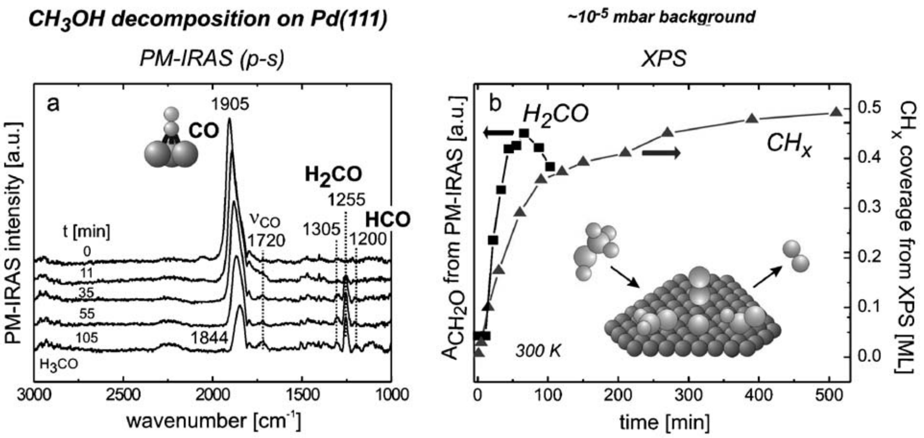

FIG. 54. (a) PM-IRAS spectra measured during CH_3OH decomposition on Pd(1 1 1) at 300 K and approximately 10^{-5} mbar. The time-dependent evolution of CH_2O (integrated intensity from (a)) and of CH_x (deduced from XPS) are compared in (b); adapted from Borasio *et al.* (*177*) with permission. Copyright (2005) American Chemical Society.

(molar).[26] On the surface, PM-IRAS indicated only CO; formaldehyde and formyl had disappeared. Apparently, at 400 K, CH_2O and CHO had reacted away, either by dehydrogenation to give CO and/or by desorption. The amount of CH_x present under reaction conditions, as deduced from post-reaction XPS, was about 0.4 ML (*177*). The reduction in the amount of CH_2O and CH_x present under reaction conditions generated more free surface sites and led to a higher CO surface coverage, indicated by the shift of the CO peak to about 1890 cm^{-1} (typical of approximately 0.4 ML of CO; Fig. 53a).

From these observations one can conclude that methanol oxidation proceeds via dehydrogenation to CH_2O, which either desorbs or is further dehydrogenated to CO, which is subsequently oxidized to CO_2 (cf. scheme in Fig. 49). During the various dehydrogenation steps, the reaction of hydrogen and oxygen produces water. Apparently, the surface concentrations of CH_2O and CHO are below the detection limit under reaction conditions. Hollow-bonded CO was identified by PM-IRAS, but the possibility that these molecules are spectators and that CO_2 formation rather proceeds via short-lived CO that is more weakly bonded cannot be excluded (isotope experiments may provide an answer to this question in the future).

K.3.2. Effect of Carbonaceous Species on Reaction Selectivity. A long-standing question is whether CH_x species present during a reaction are only undesired contaminants lowering the activity or whether CH_x may affect the selectivity. For example, CH_x may increase the yield of CH_2O by hindering its further dehydrogenation to CO. One observation supporting this possibility is that at reaction

---

[26] Both GC and PM-IRAS also found small amounts of ethanol and dimethyl ether, which will be disussed below.

temperatures of 500 K or higher, when the CH_x concentration is low (<0.1 ML), only CO_2 and water were produced. However, because this observation cannot demonstrate an involvement of CH_x in the oxidation reaction, the time dependences of the evolution of the surface CH_x and CH_2O concentrations were compared. Because CH_x formation was quite fast under mbar reaction conditions, these experiments were performed at a reduced pressure.

Figure 54 is a comparison of PM-IRAS (p−s) and XP spectra acquired during methanol exposure at 300 K and approximately 10^{-5} mbar. The PM-IRAS spectra shown in Fig. 54a indicated that CO was the only initial surface species, with a coverage of about 0.4 ML, in agreement with the XPS data. Under UHV conditions, methoxy, formaldehyde, and formyl are typically not observed at 300 K, and their absence might be attributed to the absence of CH_x species. However, at a pressure of about 10^{-5} mbar, PM-IRAS showed that formaldehyde and formyl surface species developed with time (peaks at 1255 and 1305 cm^{-1}, and at about 1200 cm^{-1}, respectively), which are intermediate species in methanol dehydrogenation to CO. The growing peak at about 1720 cm^{-1} may be tentatively assigned to ν_{CO} of a formyl species (*507*) or to ν_{CO} of formaldehyde (*510*) (its weak intensity suggests that CH_2O is adsorbed with the C–O bond oriented (nearly) parallel to the surface). In this case, XPS cannot differentiate between CO and CH_2O, but it did indicate that the evolution of formaldehyde was paralleled by the evolution of CH_x (Fig. 54b) (*177*). According to results of a previous study (*94*), CH_x is most likely elemental carbon located in threefold hollow sites of Pd(1 1 1). However, the value of x may be in the range of 0–3, because C–O bond scission could occur within methoxy, formaldehyde, and/or formyl, followed by further dehydrogenation (Fig. 49). Nevertheless, CH_2O seems to be the most likely precursor for C–O bond cleavage, because of its adsorption geometry (*84*). When the CH_x coverage exceeded 0.4 ML, the CH_2O signal decreased as a consequence of significant surface poisoning. A comparison between the time-dependent evolution of CH_2O[27] and CH_x is displayed in Fig. 54b, which suggests that the formation of these species is correlated.

An involvement of the CH_x species in steering the reaction selectivity is thus likely. For example, carbon atoms may prevent further dehydrogenation of CH_2O to CO by poisoning the required (hollow) surface sites. On the basis of the experimental findings and DFT calculations of Neurock, Mavrikakis, and others (see references cited in References (*378,494,511*)), the following model is suggested (Fig. 49). On a clean Pd(1 1 1) surface, CH_3OH adsorbs at on-top sites and is dehydrogenated via CH_3O (on threefold hollow sites), and via CH_2O (on bridge sites), and via CHO (on hollow sites) to give CO adsorbed on hollow sites. Because CH_x species occupy hollow sites, CH_3O formation on a (partially) CH_x-covered surface is hindered, and CH_3OH instead reacts to give hydroxymethyl (CH_2OH), which binds to the free on-top sites. CH_2OH is then dehydrogenated to CH_2O, and further dehydrogenation to CHO and CO is presumably hindered, because the required hollow sites are occupied by CH_x. Accordingly, a clean surface would preferentially produce CO_2, whereas a partly CH_x-deactivated surface would also produce CH_2O.

---

[27] The relative amount was determined by integrating the PM-IRAS peaks at 1255 and 1305 cm^{-1}.

Furthermore, one has to take into account that GC and PM-IRAS also provided evidence of small amounts of ethanol and dimethyl ether. Because ethanol can be produced from the reaction of CH_2OH with CH_3, and dimethyl ether from methoxy (CH_3O) and CH_3, both products indicate an involvement of CH_3 groups. Consequently, the dehydration pathway ($2CH_3OH \rightarrow CH_3O + CH_3 + H_2O$) and C–O bond scission within CH_3OH or CH_3O (although energetically unfavorable (*494*)) should not be neglected, because both produce the required methyl groups. It is emphasized that a complete understanding has not yet been obtained, consistent with the large number of potential surface species (CH_3OH, CH_3O, CH_3, CH_2OH, CH_2O, CHO, CO, H, CH_x, O, CO_2, H_2O, and possibly formate). Apart from geometric effects, CH_x species may also change the electronic structure of neighboring palladium sites (*95*). Detailed GC investigations of selectivity combined with XPS measurements of reacting surfaces will be required to assess this model critically.

K.3.3. Oxidation State of Surface Palladium under Reaction Conditions. The oxidation state of the palladium in the Pd(1 1 1) surface in the presence of 5 mbar of O_2 at 400–500 K is another important issue. Surface oxides of palladium (Pd_5O_4 overlayer) (*56,58,252*) (and of other metals (*57,512,513*)) have recently drawn much attention and may contribute to the reaction by supplying oxygen. However, post-reaction XPS, acquired in the O1s and Pd3d region, did not indicate any surface oxidation (*177*).[28] Furthermore, because the CO species observed by PM-IRAS during the oxidation reaction were typical of adsorption on metallic palladium, the oxidation of the palladium surface is inferred to have been minor, if it occurred at all.

K.3.4. High-pressure Methanol Oxidation on Pd/Al_2O_3. CH_3OH oxidation was also investigated on Pd/Al_2O_3/NiAl(110) (mean particle diameter 6 nm), monitored in parallel by GC and SFG (Figs 55a and b) (*297,362,453*). In the presence of 15 mbar of CH_3OH and 15 mbar of O_2 (in a balance of He to give a total pressure of 1 bar), GC indicated that a temperature of at least 400 K was (again) required for the reaction to proceed (with CO_2, H_2O, and CH_2O as products). At lower temperatures, the palladium particles were covered (poisoned) by CO and very likely by CH_x and CH_2O as well. Only at 400 K and higher temperatures were CH_x and CH_2O (partially) reacted away, producing cleaner particle surfaces and thereby increasing the CO coverage to near saturation under reaction conditions (Fig. 55b).

Post-reaction XPS detected considerable amounts of CH_x (about 0.7 ML), indicating that CH_x may again have been involved in the reaction, and also a Pd3d BE shift (approximately 0.6 eV), which points to a partial oxidation of the palladium nanoparticles during the reaction (*297,504*) (Fig. 55c). It is inferred that the oxidation was not complete, because the frequencies of adsorbed CO were still characteristic of CO on metallic palladium (Fig. 55b), and full oxidation to PdO particles would result in BE shifts of about +1.5 eV (*514*). The observed BE shift (characteristic of oxidized palladium) could be (partly) reversed by reaction

---

[28] Reference investigations of Pd(1 1 1) oxidation at 10^{-5} mbar of O_2 indicated the onset of surface oxidation at approximately 600 K, with clear shifts in the Pd3d and O1s lines of 0.5 and approximately 2 eV, respectively (*58*).

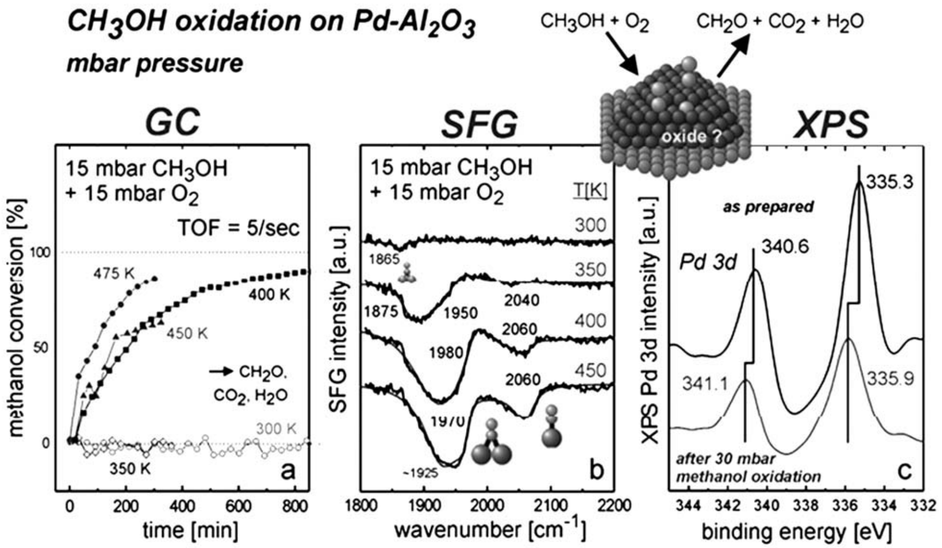

FIG. 55. Methanol oxidation on Pd/Al_2O_3 (mean particle diameter 6 nm): (a) CH_3OH conversion vs. reaction time, as monitored by GC. (b) Corresponding SFG spectra are displayed. (c) Palladium 3d XP spectra obtained before and after methanol oxidation on Pd/Al_2O_3. The shift indicates a partial oxidation of the palladium particles during the oxidation reaction. Because the particles were covered by CO after the reaction, the clean sample was also exposed to CO, responsible for the shift from 334.9 to 335.3 eV (*297,362,453*).

(reduction) of the surface oxide with CO at 300 K. This clearly excludes palladium particle sintering as alternative explanation for the observed 0.6 eV BE shift because palladium particle redispersion is very unlikely under such mild treatment conditions.

Considering that under reaction conditions identical to those stated just above the Pd(1 1 1) single-crystal surface remained metallic, palladium nanoparticles are apparently easier to oxidize than bulk palladium, possibly because of the higher abundance of surface defects. The palladium oxide phase may be located not only on the particle surface but also at the palladium/alumina interface (*515*). Partial oxidation of palladium particles has been observed previously for combustion reactions on technological catalysts and may lead to complex hysteresis phenomena (see Refs (*514,516*) and references therein).

V. Outlook and Directions of Future Research

This final section includes a brief outline of suggested future research directions, aimed at applying spectroscopy of functioning catalysts to more complex catalysts and reactions, mimicking technological systems even more closely. It is emphasized that such model investigations will have to sacrifice part of the control of surface structure and composition and cope with problems similar to those occurring on real catalysts.

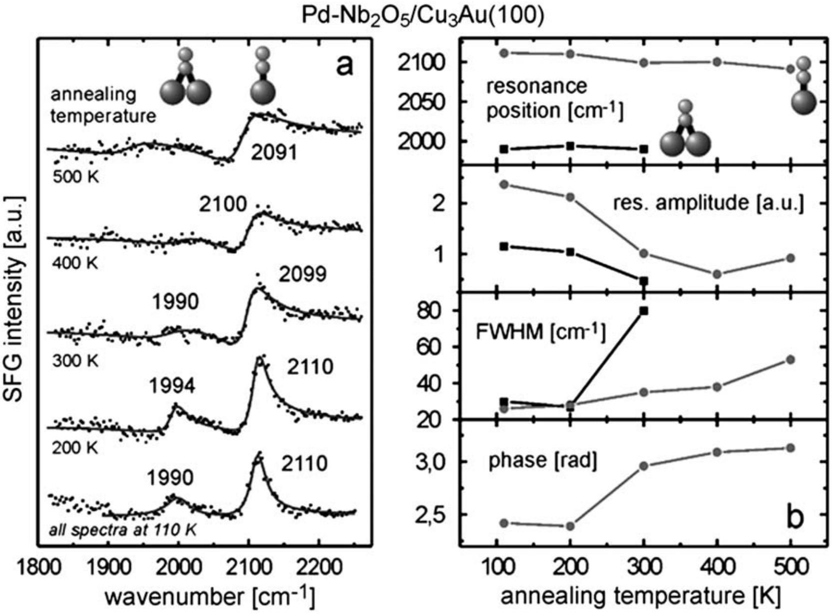

FIG. 56. CO adsorption on palladium nanoparticles grown at 90 K on $Nb_2O_5/Cu_3Au(1\,0\,0)$. (a) SFG spectra acquired in 10^{-6} mbar of CO at 110 K, after annealing of the model catalysts to the temperatures indicated. Values obtained for the peak position, resonant amplitude, peak width (FWHM), and phase ϕ of the spectra are displayed in (b), both for on-top and bridge-bonded CO. Metal–support interactions resulting from annealing of Pd/Nb_2O_5 led to an irreversible loss of the CO adsorption capacity and formation of a mixed $Pd–NbO_x$ phase; reprinted from (*523*) with permission from Elsevier.

New model supports and metal–support interactions: In the future, such spectroscopy should be applied to other and more complex catalysts than Pd/Al_2O_3. When silver particles are grown on $Al_2O_3/NiAl(1\,1\,0)$, as a consequence of the low BE of CO to silver (CO desorbs from Ag(1 1 1) at 55 K (*517*)), adsorption investigations at elevated temperatures can be performed only by high-pressure spectroscopy (e.g., about 10 mbar is required at 150 K to detect adsorbed CO by SFG (*518*)). Recent advances in the preparation of thin iron oxide films (FeO, Fe_2O_3, and Fe_3O_4) allow their use as model supports (*515,519–522*). Low-temperature CO oxidation on Fe_3O_4-supported gold nanoparticles (*410*) has drawn considerable interest and already stimulated a number of model investigations under UHV (*411–414*).

Figure 56a shows SFG spectra of CO adsorbed on palladium nanoparticles on a Nb_2O_5 support (*523–526*). Heating of the $Pd/Nb_2O_5/Cu_3Au(1\,0\,0)$ model catalyst to temperatures above 300 K was found to lead to an irreversible 50% decrease in the CO adsorption capacity and a modification of the remaining adsorption sites. Changes in the vibrational frequencies and phase between resonant and nonresonant SFG signals upon annealing of the sample (Fig. 56b) indicate a change in the electronic structure of the surface, which excludes palladium sintering or migration of Nb_2O_5 over palladium particles as causes of the observed effect and rather suggests the formation of mixed $Pd–NbO_x$ sites (*523*). These effects were observed

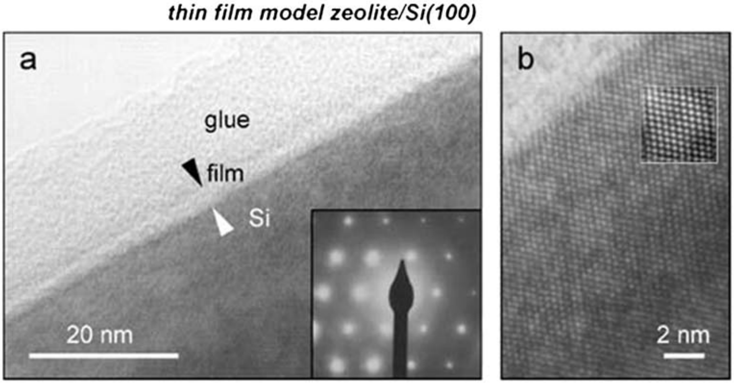

FIG. 57. (a) Transmission electron micrograph of a cross-section of an approximately 3-nm-thick zeolite film on Si(1 0 0), with the inset showing a diffraction pattern. The atomically resolved interface area is shown in (b); the inset displays an image area enhanced by Fourier filtering; adapted from (*25*) with permission from Elsevier.

both under UHV and at ambient pressure and may contribute to the catalytic properties of Nb_2O_5-supported metal nanoparticles. The interest in the Nb_2O_5 support stems from the excellent performance of Co/Nb_2O_5 catalysts in Fischer–Tropsch synthesis (*250,527*), and the first SFG spectra of CO on cobalt particles have already been obtained (SFG signal at $2080\,cm^{-1}$) (*518*).

Because SiO_2 is another widely used support material, the availability of well-ordered thin silica films will have strong impact on future fundamental investigations (*102,103*). There have also been recent efforts to prepare thin-film zeolites (*25*). Figure 57 shows a roughly 3-nm-thick film of silicalite precursors spin coated on a Si(1 0 0) wafer. The film was found to be flat over a distance of microns, and if the further processing can be successfully managed, a model zeolite film suitable for surface science investigations could be obtained.

More complex model reactions (selective butadiene hydrogenation): Apart from being accessible to surface spectroscopy, model catalysts also have the advantage that the nanoparticle morphology and surface structure can be accurately measured. This advantage allows the determination of the relative abundance of specific surface sites and calculation of surface site statistics, as shown, for example, in Table II.[29] Knowledge of the exact number and type of available surface sites then allows calculation of more accurate (and perhaps more meaningful) turnover frequencies of catalytic reactions.

In the following, we use the selective hydrogenation of 1,3-butadiene on $Pd/Al_2O_3/NiAl(1\,1\,0)$ model catalysts (mean particle diameter in the range of 2–8 nm) to illustrate this point (reactions were carried out at ambient pressure; cf. Fig. 8) (*361,528,529*). Figure 58a shows the kinetics of the reaction on approximately

---

[29] Of course, such a statistics can also be calculated for real catalysts, but in view of the uncertainties in the structure characterization, they are regarded only as estimates.

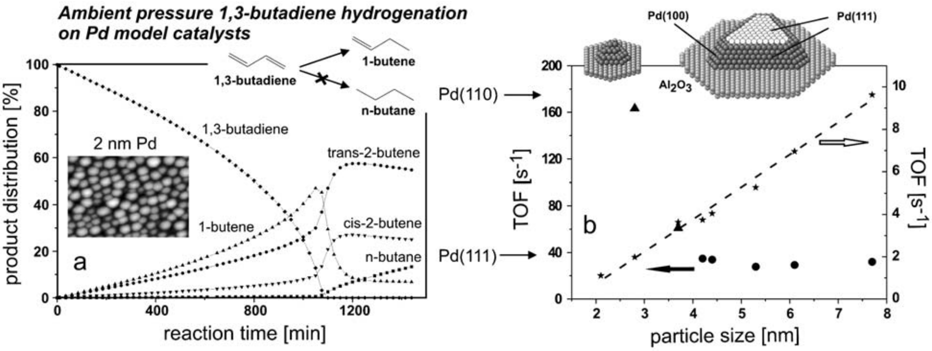

FIG. 58. (a) Product distribution as a function of reaction time for 1,3-butadiene hydrogenation at 373 K on Pd/Al_2O_3/NiAl(1 1 0). Reaction conditions: 5 mbar of 1,3-butadiene; 10 mbar of H_2; Ar added to give a total pressure of 1 bar. (b) Hydrogenation activity (TOF) data characterizing the various Pd/Al_2O_3/NiAl(1 1 0) catalysts as a function of mean particle diameter, normalized by the total number of Pd surface atoms (★ and dashed line; right axis), and normalized by the number of Pd atoms on incomplete (1 1 1) facets (●; left axis), using a truncated cubo-octahedron as a structural model (shown as inset; incomplete layers on side facets are not displayed). TOF values for Pd(1 1 1) and Pd(1 1 0) under identical reaction conditions are indicated; adapted from Silvestre-Albero *et al.* (*529*) with permission from Elsevier.

2-nm palladium particles. Butadiene hydrogenation gives four products (1-butene, *trans*-2-butene, *cis*-2-butene, and *n*-butane); typically, 1-butene is the desired product. The kinetics and selectivity are particle size-dependent (see References (*528,529*) for details), and here we only discuss the initial activity.

Butadiene hydrogenation is structure-sensitive and thus regarded as particle size-dependent (*530–536*). When the total number of Pd surface atoms on the nanoparticles is used for rate normalization, a size-dependent rate is indeed observed (stars and dashed line in Fig. 58b; the data show the number of butadiene molecules reacted per Pd surface atom per second within 1 h). Apparently, this TOF increases linearly with particle size, indicating that larger palladium particles are more active than smaller ones, in agreement with what is commonly reported for this reaction (see References (*530,537*) and references cited therein).

However, the exact microscopic information characterizing the shape and surface structure of the palladium nanoparticles provided by STM (*83,206,254*) also make it possible to relate the activity to specific surface sites. Using a realistic model of the palladium nanoparticles, a cuboctahedron with incomplete (1 1 1) terraces (inset, Fig. 58b), the number of Pd surface atoms present in (1 1 1) and (1 0 0) facets as well as at edges and at the metal–support boundary were calculated for various cluster sizes (cf. Table II). With these values, a more accurate TOF can be calculated by dividing the total hydrogenation activity by the number of specific surface sites. It was found that when the number of Pd atoms in incomplete (1 1 1) facets was used for normalization, the TOF of butadiene hydrogenation was clearly independent of particle size (Fig. 58b; filled circles). This result suggests that the reaction takes place preferentially on the (1 1 1) facets of the palladium nanoparticles, at least for a mean particle diameter exceeding 4 nm.

This model was validated by reference measurements carried out with Pd(1 1 1) and Pd(1 1 0) single crystals (*361,528*). The specific activity of larger palladium particles and that of Pd(1 1 1) show excellent agreement (Fig. 58b), which corroborates the inference that the reaction occurs on (1 1 1) particle facets. Another implication is that one can now demonstrate on a quantitative basis that in this case suitably large palladium particles behave identically to Pd(1 1 1) single crystals, whereas palladium particles with diameters <4 nm do not. Such a demonstration has been anticipated for a long time, but it had never been quantified for a structure-sensitive reaction.

Such a normalization is more difficult for small palladium particles (mean diameter about 2–3 nm), because these particles (with edge lengths of only a few atoms) do not exhibit well-developed facets (the "facets" typically contain only 4–8 atoms; an approximately 2-nm particle is shown in Fig. 58b; these data points are symbolized by ▲). Nevertheless, the TOF values suggest that the catalytic activity of small palladium particles approaches that of Pd(1 1 0). Again, recall that although measurements with single crystals clearly showed that 1,3-butadiene hydrogenation is structure-sensitive (*361,536*), the reaction is in fact particle size independent if the correct morphology of the palladium nanoparticles is taken into account. This is a very clear example of a bridge of the materials gap between single crystals and metal nanoparticles on the basis of measurements of absolute reaction rates.

Spectroscopic investigations of alkenes (*68,83,104,254,337,456,538*) have suggested π-bonded or di-σ-bonded species as possible reactive intermediates. However, the complexity of butadiene allows for a large number of adsorbate configurations (*539,540*), and future spectroscopic investigations are needed to explore the reaction mechanism of diene hydrogenation.

VI. Conclusions and Perspective

The case studies presented here illustrate how vibrational SFG spectroscopy and PM-IRAS can be applied to characterize the adsorption, coadsorption, and reaction of small molecules on model catalyst surfaces over wide pressure ranges—from UHV to ambient conditions. The broad aim of these investigations is to bridge the pressure gap between surface science investigations and heterogeneous catalysis, with the ultimate goal of elucidating the elementary steps of catalytic reactions. The examples include CO adsorption and dissociation, CO–H coadsorption, CO hydrogenation, CO oxidation, ethene adsorption and hydrogenation, and CH_3OH decomposition and oxidation. The model catalysts include low-index single-crystal surfaces, defect-rich (stepped or ion-bombarded) single-crystal surfaces, and oxide-supported metal nanoparticles. This complete approach allows addressing the materials gap problem and demonstrates the inherent differences between supported nanoparticles and single crystals. Structure analysis by high-pressure scanning tunneling microscopy (HP-STM) and composition analysis by high-pressure photoelectron spectroscopy (HP-XPS) have been discussed briefly, because they provide inevitable complementary information.

The adsorbate geometries that were observed under atmospheric pressure conditions on palladium, platinum, rhodium, gold and other surfaces were essentially comparable to the corresponding high-coverage structures known from UHV investigations, that is, high-pressure species were absent. For example, even by increasing the CO pressure by 10 orders of magnitude, the UHV saturation coverages could not be exceeded. Nevertheless, differences between UHV and high-pressure experiments may still occur, for example, as a consequence of differences in the adsorption site occupancy and coverage or of nonequilibrium structures that may be formed at cryogenic temperatures under UHV. When coadsorption occurs, the situation becomes more complex, in particular when strong mutual site blocking occurs and when one reactant (e.g., H) may dissolve in the noble metal. Scenarios have been described, for example, for CO hydrogenation on palladium, whereby the high-pressure adsorption configuration could not be mimicked under UHV conditions.

Investigations of supported palladium nanoparticles clearly demonstrated that the specific particle surface structure and finite size cannot be modeled by single-crystal surfaces. For example, palladium hydride formation proceeds predominantly via minority sites on palladium nanoparticles (defects and (1 0 0) facets), and "explosive" hydrogen desorption in the presence of a CO overlayer originates from the confinement of dissolved hydrogen within the limited nanoparticle volume. Such effects do not occur in/on macroscopic single crystals. The presence of palladium hydride phases also was found to lead to a very high catalytic activity for C_2H_4 hydrogenation indicating a potentially enhanced activity of hydride phases. Carbonaceous overlayers that were observed during methanol oxidation catalysis may not only poison a palladium catalyst but may also favorably influence its selectivity for partial oxidation. The accurate surface site characterization of nanoparticle model catalysts may allow refinement of the concepts of structure-sensitivity and particle size dependence. Polarization-dependent SFG spectroscopy can be used to determine the orientation of molecules on metal and oxide surfaces. Time-resolved broadband SFG ("pump-probe") provides insight into the transient behavior of reacting molecules. The latter two methods await their application under mbar reaction conditions.

Nanoparticle model catalysts together with high-pressure spectroscopic techniques are needed to simultaneously bridge the materials and pressure gaps between surface science and heterogeneous catalysis. Although the work carried out so far deals primarily with small molecules, the benefits of high-pressure methods for characterization of working catalysts are apparent. If these methods can be successfully extended to more complex molecules and surfaces in the future, our understanding of heterogeneous catalysis will deepen substantially.

Acknowledgments

I am very grateful for the contributions of previous and current coworkers whose names appear in the list of references and especially to my former colleagues at the Fritz Haber Institute (T. Dellwig, H. Unterhalt, L. Hu, P. Galletto, M. Morkel, O.

Rodriguez de la Fuente, M. Borasio, F. Höbel, B. Kell, J. Silvestre-Albero, and A. Bandara). I am particularly indebted to H.-J. Freund for continuous support. STM images of Pd/Al_2O_3 are courtesy of M. Heemeier, M. Frank, K. Højrup Hansen, M. Kulawik, and M. Bäumer. Fruitful collaborations with V. I. Bukhtiyarov and V. V. Kaichev (Boreskov Institute of Catalysis), K. Hayek (University of Innsbruck), R. Schlögl and D. S. Su (Fritz Haber Institute), J. J Calvino and J. A. Perez-Omil (University of Cadiz; also kindly providing the particle models in Figs. 21 a,b), and G. A. Somorjai (University of California, Berkeley) are gratefully acknowledged. Part of the electron microscopy was performed at the National Center for Electron Microscopy at the Lawrence Berkeley National Laboratory. I also thank those colleagues who have supplied original data for figures.

References

1. Ertl, G., Knözinger, H. and Weitkamp, J. (Eds.), "Handbook of Heterogeneous Catalysis." VCH, Weinheim, 1997.
2. Ertl, G., and Freund, H.-J., *Phys. Today* **52**, 32 (1999).
3. Somorjai, G.A., "Introduction to Surface Chemistry and Catalysis." Wiley, New York, 1994.
4. Thomas, J.M., and Thomas, W.J., "Principles and Practice of Heterogeneous Catalysis." VCH, Weinheim, 1997.
5. Chorkendorff, I., and Niemantsverdriet, J.W., "Concepts of Modern Catalysis and Kinetics." VCH, Weinheim, 2003.
6. Schlögl, R., and Abd Hamid, S.B., *Angew. Chem. Int. Ed.* **43**, 1628 (2004).
7. Banares, M.A., *Catal. Today* **100**, 71 (2005).
8. Datye, A.K., Hansen, P.L., and Helveg, S., *Adv. Catal.* **50**, 77 (2006).
9. Schlögl, R. et al., *Adv. Catal.*, to be published.
10. Lopez-Cartes, C., Perez-Omil, J., Pintado, J., Calvino, J., Kang, Z.C., and Eyring, L., *Ultramicroscopy* **80**, 19 (1999).
11. Blanco, G., Calvino, J.J., Cauqui, M.A., Corchado, P., López-Cartes, C., Colliex, C., Pérez-Omil, J.A., and Stephan, O., *Chem. Mater.* **11**, 3610 (1999).
12. Rupprechter, G., Calvino, J.J., López-Cartes, C., Fuchs, M., Gatica, J.M., Pérez-Omil, J.A., Hayek, K., and Bernal, S., *Stud. Surf. Sci. Catal.* **130**, 2021 (2000).
13. Tauster, S.J., Fung, S.C., and Garten, R.L., *J. Am. Chem. Soc.* **100**, 170 (1978).
14. Hayek, K., Fuchs, M., Klötzer, B., Reichl, W., and Rupprechter, G., *Top. Catal.* **13**, 55 (2000).
15. Rupprechter, G., Seeber, G., Goller, H., and Hayek, K., *J. Catal.* **186**, 201 (1999).
16. Sheppard, N., *Ann. Rev. Phys. Chem.* **39**, 589 (1988).
17. Hoffmann, F.M., *Surf. Sci. Rep.* **3**, 103 (1983).
18. Sheppard, N., and De La Cruz, C., *Adv. Catal.* **41**, 1 (1996).
19. Sheppard, N., and De La Cruz, C., *Adv. Catal.* **42**, 181 (1998).
20. Schwab, G.M., and Schultes, H., *Z. Phys. Chem. B* **9**, 265 (1930).
21. Boudart, M., Aldag, A., Benson, J.E., Dougharty, N.A., and Harkins, C.G., *J. Catal.* **6**, 92 (1966).
22. van Hardeveld, R., and van Montfoort, A., *Surf. Sci.* **4**, 396 (1966).
23. Schwab, G.-M., *Adv. Catal.* **27**, 1 (1978).
24. Che, M., and Bennet, C.O., *Adv. Catal.* **36**, 55 (1989).
25. Doyle, A.M., Rupprechter, G., Pfänder, N., Schlögl, R., Kirschhock, C.E.A., Martens, J.A., and Freund, H.-J., *Chem. Phys. Lett.* **382**, 404 (2003).
26. Lear, T., Marshall, R., Gibson, E.K., Schütt, T., Klapötke, T.M., Rupprechter, G., Freund, H.-J., Winfield, J.M., and Lennon, D., *Phys. Chem. Chem. Phys.* **7**, 565 (2005).
27. Lear, T., Marshall, R., Lopez-Sanchez, J.A., Jackson, S.D., Klapötke, T.M., Bäumer, M., Rupprechter, G., Freund, H.-J., and Lennon, D., *J. Chem. Phys.* **123**, 174706 (2005).

28. Somorjai, G.A., *Surf. Sci.* **299/300**, 849 (1994).
29. Ertl, G., *Surf. Sci.* **299/300**, 742 (1994).
30. Ertl, G., and Küppers, J., "Low Energy Electrons and Surface Chemistry." VCR Verlagsgesellschaft, Weinheim, 1985.
31. Walls, J.M., and Smith, R. (Eds)., "Surface Science Techniques," Special Issue of Vacuum, Pergamon, New York, 1994.
32. Somorjai, G.A., and Rupprechter, G., *J. Chem. Edu.* **75**, 161 (1998).
33. Woodruff, D.P., and Delchar, T.A., "Modern Techniques of Surface Science." Cambridge University Press, New York, 1986.
34. Freund, H.-J., *Angew. Chem. Int. Ed. Engl.* **36**, 452 (1997).
35. Somorjai, G.A., *Chem. Rev.* **96**, 1223 (1996).
36. Madix, R.J., *Surf. Sci.* **299/300**, 785 (1994).
37. Goodman, D.W., *Surf. Sci.* **299/300**, 837 (1994).
38. Bradshaw, A.M., *Surf. Sci.* **299/300**, 49 (1994).
39. Ibach, H., *Surf. Sci.* **299/300**, 116 (1994).
40. Heinz, K., *Surf. Sci.* **299/300**, 433 (1994).
41. Van Hove, M.A., and Somorjai, G.A., *Surf. Sci.* **299/300**, 487 (1994).
42. King, D.A., *Surf. Sci.* **299/300**, 678 (1994).
43. Thomas, J.M., and Somorjai, G.A. (Eds.), *Top. Catal.* 8 (1999) (Special Issue on "*In-Situ* Characterization of Catalysts").
44. Schlögl, R., and Zecchina, A. (Eds.), *Top. Catal.* 15 (2001) (Special Issue on "*In-Situ* Characterization of Catalysts").
45. Somorjai, G.A., *Z. Phys. Chem.* **197**, 1 (1996).
46. Somorjai, G.A., and Rupprechter, G., *J. Phys. Chem. B* **103**, 1623 (1999).
47. Somorjai, G.A., *Langmuir* **7**, 3176 (1991).
48. Rupprechter, G., *Phys. Chem. Chem. Phys.* **3**, 4621 (2001).
49. Scheibe, A., Günther, S., and Imbihl, R., *Catal. Lett.* **86**, 33 (2003).
50. Somorjai, G.A., *Nature* **430**, 730 (2004).
51. Berkó, A., Ménesi, G., and Solymosi, F., *J. Phys. Chem.* **100**, 17732 (1996).
52. Rupprechter, G., and Freund, H.-J., *Top. Catal.* **14**, 3 (2001).
53. Eppler, A., Rupprechter, G., Anderson, E.A., and Somorjai, G.A., *J. Phys. Chem. B* **104**, 7286 (2000).
54. Rupprechter, G., Hayek, K., and Hofmeister, H., *J. Catal.* **173**, 409 (1998).
55. Stampfl, C., and Scheffler, M., *Surf. Sci.* **433–435**, 119 (1999).
56. Leisenberger, F.P., Koller, G., Sock, M., Surnev, S., Ramsey, M.G., Netzer, F.P., Klötzer, B., and Hayek, K., *Surf. Sci.* **445**, 380 (2000).
57. Over, H., Kim, Y.D., Seitsonen, A.P., Wendt, S., Lundgren, E., Schmid, M., Varga, P., Morgante, A., and Ertl, G., *Science* **287**, 1474 (2000).
58. Lundgren, E., Kresse, G., Klein, C., Borg, M., Andersen, J.N., De Santis, M., Gauthier, Y., Konvicka, C., Schmid, M., and Varga, P., *Phys. Rev. Lett.* **88**, 246103 (2002).
59. Reuter, K., Frenkel, D., and Scheffler, M., *Phys. Rev. Lett.* **93**, 116105 (2004).
60. Knop-Gericke, A., Hävecker, M., Schedel-Niedrig, T., and Schlögl, R., *Top. Catal.* **15**, 27 (2001).
61. Ketteler, G., Ogletree, D.F., Bluhm, H., Liu, H., Hebenstreit, E.L.D., and Salmeron, M., *J. Am. Chem. Soc.* **127**, 18269 (2005).
62. Goodman, D.W., *Chem. Rev.* **95**, 523 (1995).
63. Freund, H.-J., Bäumer, M., and Kuhlenbeck, H., *Adv. Catal.* **45**, 412 (2000).
64. Davis, S.M., Zaera, F., and Somorjai, G.A., *J. Am. Chem. Soc.* **104**, 7453 (1982).
65. Goodman, D.W., *Surf. Sci.* **123**, L679 (1982).
66. Zhdanov, V.P., and Kasemo, B., *J. Catal.* **170**, 377 (1997).
67. Freund, H.-J., *Faraday Discuss.* **114**, 1 (1999).
68. Morkel, M., Rupprechter, G., and Freund, H.-J., *Surf. Sci. Lett.* **588**, L209 (2005).
69. Levin, M.E., Williams, K.J., Salmeron, M., Bell, A.T., and Somorjai, G.A., *Surf. Sci.* **195**, 2807 (1988).
70. Henry, C.R., Chapon, C., Goyhenex, C., and Monot, R., *Surf. Sci.* **272**, 283 (1992).

71. Glassl, H., Kramer, R., and Hayek, K., *J. Catal.* **68**, 397 (1981).

72. Hayek, K., *J. Mol. Catal.* **51**, 347 (1989).

73. Bäumer, M., Libuda, L., Sandell, A., Freund, H.-J., Graw, G., Bertrams, T., and Neddermeyer, H., *Ber. Bunsenges. Phys. Chem.* **99**, 1381 (1995).

74. Rupprechter, G., Hayek, K., Rendón, L., and José-Yacamán, M., *Thin Solid Films* **260**, 148 (1995).

75. Gunter, P.L.J., Niemantsverdriet, J.W.H., Ribeiro, F.H., and Somorjai, G.A., *Catal. Rev.—Sci. Eng.* **39**, 77 (1997).

76. Stone, P., Poulston, S., Bennett, R.A., and Bowker, M., *Chem. Commun.* 1369 (1998).

77. Henry, C.R., *Surf. Sci. Rep.* **31**, 235 (1998).

78. Datye, A.K., *Top. Catal.* **13**, 131 (2000).

79. Heiz, U., and Schneider, W., *J. Phys. D: Appl. Phys.* **33**, R85 (2000).

80. Thüne, P., Loos, J., de Jong, A., Lemstra, P., and Niemantsverdriet, J.W., *Top. Catal.* **13**, 67 (2000).

81. Campbell, C.T., Grant, A.W., Starr, D.E., Parker, S.C., and Bondzie, V.A., *Top. Catal.* **14**, 43 (2001).

82. Goodman, D.W., *J. Catal.* **216**, 213 (2003).

83. Freund, H.-J., Bäumer, M., Libuda, J., Risse, T., Rupprechter, G., and Shaikhutdinov, S., *J. Catal.* **216**, 223 (2003).

84. Rupprechter, G., *Annu. Rep. Progr. Chem, Sect. C* **100**, 237 (2004).

85. Rose, M.K., Borg, A., Mitsui, T., Ogletree, D.F., and Salmeron, M., *J. Chem. Phys.* **115**, 10927 (2001).

86. Rose, M.K., Mitsui, T., Dunphy, J., Borg, A., Ogletree, D.F., Salmeron, M., and Sautet, P., *Surf. Sci.* **512**, 48 (2002).

87. Ribeiro, F.H., Gerken, C.A., Rupprechter, G., Somorjai, G.A., Kellner, C.S., Coulston, G.W., Manzer, L.E., and Abrams, L., *J. Catal.* **176**, 352 (1998).

88. Surnev, S., Kresse, G., Ramsey, M.G., and Netzer, F.P., *Phys. Rev. Lett.* **87**, 086102 (2001).

89. Bonzel, H.P., and Krebs, H.J., *Surf. Sci.* **117**, 639 (1982).

90. Bonzel, H.P., *Surf. Sci. Rep.* **8**, 43 (1987).

91. Nørskov, J.K., Holloway, S., and Lang, N.D., *Surf. Sci.* **137**, 65 (1984).

92. Groß, A., *Appl. Phys. A* **67**, 627 (1998).

93. Gravil, P.A., and Toulhoat, H., *Surf. Sci.* **430**, 176 (1999).

94. Morkel, M., Kaichev, V.V., Rupprechter, G., Freund, H.-J., Prosvirin, I.P., and Bukhtiyarov, V.I., *J. Phys. Chem. B* **108**, 12955 (2004).

95. Stolbov, S., Mehmood, F., Rahman, T.S., Alatalo, M., Makkonen, I., and Salo, P., *Phys. Rev. B* **70**, 155410 (2004).

96. Giorgio, S., Henry, C.R., Chapon, C., Nihoul, G., and Penisson, J.M., *Ultramicroscopy* **38**, 1 (1991).

97. Heemeier, M., Stempel, S., Shaikhutdinov, S., Libuda, J., Bäumer, M., Oldman, R.J., Jackson, S.D., and Freund, H.-J., *Surf. Sci.* **523**, 103 (2003).

98. Rupprechter, G., Morkel, M., Freund, H.-J., and Hirschl, R., *Surf. Sci.* **554**, 43 (2004).

99. Rupprechter, G., Seeber, G., Hayek, K., and Hofmeister, H., *Phys. Stat Sol. (a)* **146**, 449 (1994).

100. Giorgio, S., Henry, C.R., and Chapon, C., *J. Cryst. Growth* **100**, 254 (1990).

101. Bäumer, M., and Freund, H.-J., *Prog. Surf. Sci.* **61**, 127 (1999).

102. Schroeder, T., Adelt, M., Richter, B., Naschitzki, N., Bäumer, M., and Freund, H.-J., *Surf. Rev. Lett.* **7**, 7 (2000).

103. Chen, M.S., Santra, A.K., and Goodman, D.W., *Phys. Rev. B* **69**, 155404 (2004).

104. Shaikhutdinov, S., Heemeier, M., Bäumer, M., Lear, T., Lennon, D., Oldman, R.J., Jackson, S.D., and Freund, H.-J., *J. Catal.* **200**, 330 (2001).

105. Bertarione, S., Scarano, D., Zecchina, A., Johanek, V., Hoffmann, J., Schauermann, S., Frank, M., Libuda, J., Rupprechter, G., and Freund, H.-J., *J. Phys. Chem. B* **108**, 3603 (2004).

106. Eppler, A., Rupprechter, G., Guczi, L., and Somorjai, G.A., *J. Phys. Chem. B* **101**, 9973 (1997).

107. Rupprechter, G., Eppler, A.S., Avoyan, A., and Somorjai, G.A., *Stud. Surf. Sci. Catal.* **130**, 369 (2000).

108. Bertarione, S., Scarano, D., Zecchina, A., Johanek, V., Hoffmann, J., Schauermann, S., Frank, M., Libuda, J., Rupprechter, G., and Freund, H.-J., *J. Catal.* **223**, 64 (2004).

109. *Ber. Bunsenges. Phys. Chem.* **97** (3) (1993) (Special Issue on "In situ Investigations of Physico-Chemical Processes at Interfaces").

110. Somorjai, G.A., and van Hove, M.A., *in* "Structure and Bonding" (J.D. Dunitz, J.B. Goodenough, P. Hemmerich, J.A. Albers, C.K. Jørgensen, J.B. Neilands, D. Reinen and R.J.P. Williams, Eds.), Springer, Berlin, 1979.

111. Su, X., Jensen, J., Yang, M.X., Salmeron, M.B., Shen, Y.R., and Somorjai, G.A., *Faraday Disc. Chem. Soc.* **105**, 263 (1996).

112. Rupprechter, G., Unterhalt, H., Morkel, M., Galletto, P., Dellwig, T., and Freund, H.-J., *Vacuum* **71**, 83 (2003).

113. Galletto, P., Rodriguez de la Fuente, O., Borasio, M., Rupprechter, G., and Freund, H.-J., Proceedings of the European Conference on Catalysis, 2003.

114. Rodriguez de la Fuente, O., Borasio, M., Galletto, P., Rupprechter, G., and Freund, H.-J. Proceedings of the European Conference on Surface Science, Prague, Czech Republic, 2003.

115. Lauritsen, J.V., and Besenbacher, F., *Adv. Catal.* **50**, 97 (2006).

116. Bandara, A., Dobashi, S., Kubota, J., Onda, K., Wada, A., Domen, K., Hirose, C., and Kano, S., *Surf. Sci.* **387**, 312 (1997).

117. Härle, H., Lehnert, A., Metka, U., Volpp, H.R., Willms, L., and Wolfrum, J., *Chem. Phys. Lett.* **293**, 26 (1998).

118. Rupprechter, G., Dellwig, T., Unterhalt, H., and Freund, H.-J., *Top. Catal.* **15**, 19 (2001).

119. Dellwig, T., Rupprechter, G., Unterhalt, H., and Freund, H.-J., *Phys. Rev. Lett.* **85**, 776 (2000).

120. Rupprechter, G., Unterhalt, H., Morkel, M., Galletto, P., Hu, L., and Freund, H.-J., *Surf. Sci.* **502–503**, 109 (2002).

121. Morkel, M., Unterhalt, H., Salmeron, M., Rupprechter, G., and Freund, H.-J., *Surf. Sci.* **532–535**, 103 (2003).

122. Shen, Y.R., *Surf. Sci.* **299/300**, 551 (1994).

123. Hall, R.B., Russell, J.N., Miragliotta, J., and Rabinowitz, P.R., *in* "Chemistry and Physics of Solid Surfaces (Springer Series in Surface Science)" (R. Vanselow and R. Howe, Eds.), Springer, Berlin, p. 77–87, 1990.

124. Somorjai, G.A., and McCrea, K.R., *Adv. Catal.* **45**, 385 (2000).

125. Metka, U., Schweitzer, M.G., Volpp, H.R., Wolfrum, J., and Warnatz, J., *Z. Phys. Chem.* **214**, 865 (2000).

126. Tadjeddine, A., Le Rille, A., Pluchery, O., Vidal, F., Zheng, W.Q., and Peremans, A., *Phys. Stat. Sol. (a)* **175**, 89 (1999).

127. Williams, C.T., and Beattie, D.A., *Surf. Sci.* **500**, 545 (2002).

128. Cremer, P.S., McIntyre, B.J., Salmeron, M., Shen, Y.R., and Somorjai, G.A., *Catal. Lett.* **34**, 11 (1995).

129. Klünker, C., Balden, M., Lehwald, S., and Daum, W., *Surf. Sci.* **360**, 104 (1996).

130. Su, X., Cremer, P.S., Shen, Y.R., and Somorjai, G.A., *J. Am. Chem. Soc.* **119**, 3994 (1997).

131. Härle, H., Mendel, K., Metka, U., Volpp, H.R., Willms, L., and Wolfrum, J., *Chem. Phys. Lett.* **279**, 275 (1997).

132. Baldelli, S., Eppler, A.S., Anderson, E., Shen, Y.R., and Somorjai, G.A., *J. Chem. Phys.* **113**, 5432 (2000).

133. Richmond, G.L., *Ann. Rev. Phys. Chem.* **52**, 357 (2001).

134. Eisenthal, K.B., *Chem. Rev.* **96**, 1343 (1996).

135. Bonn, M., Roke, S., Berg, O., Juurlink, L.B.F., Stamouli, A., and Müller, M., *J. Phys. Chem. B* **108**, 19083 (2004).

136. Baldelli, S., *J. Phys. Chem. B* **109**, 13049 (2005).

137. Shen, Y.R., "The Principles of Nonlinear Optics." Wiley, New York, 1984.

138. McCrea, K.R., and Somorjai, G.A., *J. Mol. Catal. A* **163**, 43 (2000).

139. Caudano, Y., Peremans, A., Thiry, P.A., Dumas, P., and Tadjeddine, A., *Surf. Sci.* **368**, 337 (1996).

140. Williams, C.T., Yang, Y., and Bain, C.D., *Catal. Lett.* **61**, 7 (1999).

141. Braun, R., Casson, B.D., Bain, C.D., van der Ham, E.W.M., Vrehen, Q.H.F., Eliel, E.R., Briggs, A.M., and Davies, P.B., *J. Chem. Phys.* **110**, 4634 (1999).

142. Lin, S., Oldfield, A., and Klenerman, D., *Surf. Sci.* **464**, 1 (2000).

143. Härle, H., Metka, U., Volpp, H.-R., and Wolfrum, J., *Phys. Chem. Chem. Phys.* **1**, 5059 (1999).

144. Buck, M., and Himmelhaus, M., *J. Vac. Sci. Technol. A* **19**, 2717 (2001).

145. Chen, Z., Shen, Y.-R., and Somorjai, G.A., *Ann. Rev. Phys. Chem.* **53**, 437 (2002).

146. Richter, L.T., Petrallimallow, T.P., and Stephenson, J.C., *Opt. Lett.* **23**, 1594 (1998).

147. Hess, C., Wolf, M., and Bonn, M., *Phys. Rev. Lett.* **85**, 4341 (2000).

148. Bonn, M., Hess, C., Funk, S., Miners, J., Persson, B.N.J., Wolf, M., and Ertl, G., *Phys. Rev. Lett.* **84**, 4653 (2000).

149. Hunt, J.H., Guyot-Sionnest, P., and Shen, Y.R., *Chem. Phys. Lett.* **133**, 189 (1987).

150. Galletto, P., Unterhalt, H., and Rupprechter, G., *Chem. Phys. Lett.* **367**, 785 (2003).

151. Rupprechter, G., Dellwig, T., Unterhalt, H., and Freund, H.-J., *J. Phys. Chem. B* **105**, 3797 (2001).

152. Unterhalt, H., Rupprechter, G., and Freund, H.-J., *J. Phys. Chem. B* **106**, 356 (2002).

153. Morkel, M., Unterhalt, H., Klüner, T., Rupprechter, G., and Freund, H.-J., *Surf. Sci.* **586**, 146 (2005).

154. Guyot-Sionnest, P., *Surf. Sci.* **585**, 1 (2005).

155. Lu, G.Q., Lagutchev, A., Dlott, D.D., and Wieckowski, A., *Surf. Sci.* **585**, 3 (2005).

156. Zhu, X.D., Suhr, H., and Shen, Y.R., *Phys. Rev. B* **35**, 3047 (1987).

157. Hess, C., Funk, S., Bonn, M., Denzler, D.N., Wolf, M., and Ertl, G., *Appl. Phys. A* **71**, 477 (2000).

158. van der Ham, E.W.M., Vrehen, Q.H.F., and Eliel, E.R., *Surf. Sci.* **368**, 96 (1996).

159. Ueba, H., *Prog. Surf. Sci.* **55**, 115 (1997).

160. Kung, K.Y., Chen, P., Wei, F., Rupprechter, G., Shen, Y.R., and Somorjai, G.A., *Rev. Sci. Instrum.* **72**, 1806 (2001).

161. Chabal, Y., *Surf. Sci. Rep.* **8**, 211 (1988).

162. Knözinger, H., and Huber, S., *J. Chem. Soc., Faraday Trans* **94**, 2047 (1998).

163. Hipps, K.W., and Crosby, G.A., *J. Phys. Chem.* **83**, 555 (1979).

164. Barner, B.J., Green, M.J., Saez, E.I., and Corn, R.M., *Anal. Chem.* **63** (1991).

165. Dunn, D.S., Golden, W.G., Severson, M.W., and Overend, J., *J. Phys. Chem.* **84**, 336 (1980).

166. Pfnür, H., Menzel, D., Hoffmann, F.M., Ortega, A., and Bradshaw, A.M., *Surf. Sci.* **93**, 431 (1980).

167. Golden, W.G., Saperstein, D.D., Severson, M.W., and Overend, J., *J. Phys. Chem.* **88**, 574 (1984).

168. Beitel, G.A., Laskov, A., Oosterbeek, H., and Kuipers, E.W., *J. Phys. Chem.* **100**, 12494 (1996).

169. Beitel, G.A., de Groot, C.P.M., Osterbeek, H., and Wilson, J.H., *J. Phys. Chem. B* **101**, 4035 (1997).

170. Ozensoy, E., Meier, D., and Goodman, D.W., *J. Phys. Chem. B.* **106**, 9367 (2002).

171. Rodríguez de la Fuente, O., Borasio, M., Galletto, P., Rupprechter, G., and Freund, H.-J., *Surf. Sci.* **566–568**, 740 (2004).

172. Hess, C., Ozensoy, E., and Goodman, D.W., *J. Phys. Chem. B* **107**, 2759 (2003).

173. Stacchiola, D., Thompson, A., Kaltchev, G., and Tysoe, W.T., *J. Vac. Sci. Technol. A* **20**, 2101 (2002).

174. Jugnet, Y., Cadete Santos Aires, F.J., Deranlot, C., Piccolo, L., and Bertolini, J.C., *Surf. Sci.* **521**, L639 (2002).

175. Ozensoy, E., and Goodman, D.W., *Phys. Chem. Chem. Phys.* **6**, 3765 (2004).

176. Andersen, M., Johansson, M., and Chorkendorff, I., *J. Phys. Chem. B* **109**, 10285 (2005).

177. Borasio, M., Rodríguez de la Fuente, O., Rupprechter, G., and Freund, H.-J., *J. Phys. Chem. B* **109**, 17791 (2005).

178. Niemantsverdriet, J.W., "Spectroscopy in Catalysis." VCH, Weinheim, 1993.

179. Broden, G., Pirug, G., and Bonzel, H., *Chem. Phys. Lett.* **51**, 250 (1977).

180. Broden, G., Rhodin, T.N., Bruckner, C.F., Benbow, R., and Hurych, Z., *Surf. Sci.* **59**, 593 (1976).

181. Held, G., Schuler, J., Sklarek, W., and Steinrück, H.-P., *Surf. Sci.* **398**, 154 (1998).

182. Surnev, S., Sock, M., Ramsey, M.G., Netzer, F.P., Wiklund, M., Borg, M., and Andersen, J.N., *Surf. Sci.* **470**, 171 (2000).

183. Kinne, M., Fuhrmann, T., Whelan, C.M., Zhu, J.F., Pantförder, J., Probst, M., Held, G., Denecke, R., and Steinrück, H.-P., *J. Chem. Phys.* **117**, 10852 (2002).

184. Joyner, R.W., and Roberts, M.W., *Chem. Phys. Lett.* **60**, 459 (1979).

185. Joyner, R.W., Roberts, M.W., and Yates, K., *Surf. Sci.* **87**, 501 (1979).

186. Au, C.T., Carley, A.F., and Roberts, M.W., *Int. Rev. Phys. Chem.* **5**, 57 (1986).

187. Boronin, A.I., Bukhtiyarov, V.I., Vishnevskii, A.L., Boreskov, G.K., and Savchenko, V.I., *Surf. Sci.* **201**, 195 (1988).

188. Ogletree, D., Bluhm, H., Lebedev, G., Fadley, C., Hussain, Z., and Salmeron, M., *Rev. Sci. Instrum.* **73**, 3872 (2002).

189. Bluhm, H., Hävecker, M., Kleimenov, E., Knop-Gericke, A., Liskowski, A., Schlögl, R., and Su, D.S., *Top. Catal.* **23**, 99 (2003).

190. Hävecker, M., Mayer, R.W., Knop-Gericke, A., Bluhm, H., Kleimenov, E., Liskowski, A., Su, D.S., Follath, R., Requejo, F.G., Ogletree, D.F., Salmeron, M., Lopez-Sanchez, J.A., Bartley, J.K., Hutchings, G.J., and Schlögl, R., *J. Phys. Chem. B* **107**, 4587 (2003).

191. Borgmann, D., Pantförder, J., Pöllmann, S., Denecke, R., and Steinrück, H.-P., Proceedings of the 103rd Bunsen Conference, 2004, Dresden, Germany, p. 80.

192. Pantförder, J., Pöllmann, S., Zhu, J.F., Borgmann, D., Denecke, R., and Steinrück, H.-P., *Rev. Sci. Instrum.* **76**, 014102 (2005).

193. Kaichev, V.V., Sorokin, A.M., Timoshin, A.I., and Vovk, E.I., *Instrum. Exp. Tech.* **45**, 50 (2002).

194. Bukhtiyarov, V.I., Kaichev, V.V., and Prosvirin, I.P., *Top. Catal.* **32**, 3 (2005).

195. Whelan, C.M., Neubauer, R., Borgmann, D., Denecke, R., and Steinrück, H.-P., *J. Chem. Phys.* **115**, 8133 (2001).

196. Somorjai, G.A., and Van Hove, M.A., *in* "Investigations of Surfaces and Interfaces—Part B" (B.W. Rossiter and R.C. Baetzold, Eds.), Wiley, New York, 1993.

197. Poppa, H., *Vacuum* **34**, 1081 (1984).

198. Poppa, H., *Catal. Rev.—Sci. Eng.* **35**, 359 (1993).

199. Gießel, T., Schaff, O., Hirschmugl, C.J., Fernandez, V., Schindler, K.M., Theobald, A., Bao, S., Lindsay, R., Berndt, W., Bradshaw, A.M., Baddeley, C., Lee, A.F., Lambert, R.M., and Woodruff, D.P., *Surf. Sci.* **406**, 90 (1998).

200. Woodruff, D.P., and Bradshaw, A.M., *Rep. Prog. Phys.* **57**, 1029 (1994).

201. Binnig, G., and Rohrer, H., *Rev. Mod. Phys.* **59**, 615 (1987).

202. Binnig, G., Quate, C.F., and Gerber, C., *Phys. Rev. Lett.* **56**, 930 (1986).

203. Mitsui, T., Rose, M.K., Fomin, E., Ogletree, D.F., and Salmeron, M., *Nature* **422**, 705 (2003).

204. Österlund, L., Rasmussen, P.B., Thostrup, P., Lægsgaard, E., Stensgaard, I., and Besenbacher, F., *Phys. Rev. Lett.* **86**, 460 (2001).

205. Besenbacher, F., *Rep. Prog. Phys.* **59**, 1737 (1996).

206. Hansen, K.H., Worren, T., Stempel, S., Lægsgaard, E., Bäumer, M., Freund, H.-J., Besenbacher, F., and Stensgaard, I., *Phys. Rev. Lett.* **83**, 4120 (1999).

207. Dulub, O., Hebenstreit, W., and Diebold, U., *Phys. Rev. Lett.* **84**, 3646 (2000).

208. Wahlström, E., Lopez, N., Schaub, R., Thostrup, P., Rønnau, A., Africh, C., Lægsgaard, E., Nørskov, J.K., and Besenbacher, F., *Phys. Rev. Lett.* **90**, 026101 (2003).

209. Hansen, K.H., Sljivancanin, Z., Lægsgaard, E., Besenbacher, F., and Stensgaard, I., *Surf. Sci.* **505**, 25 (2002).

210. Kolmakov, A., and Goodman, D.W., *Rev. Sci. Instrum.* **74**, 2444 (2003).

211. Datye, A.K., and Smith, D.J., *Catal. Rev.—Sci. Eng.* **34**, 129 (1992).

212. Wintterlin, J., *Adv. Catal.* **45**, 131 (2000).

213. Sachs, C., Hildebrand, M., Völkening, S., Wintterlin, J., and Ertl, G., *Science* **293**, 1635 (2001).

214. Schaub, R., Wahlström, E., Rønnau, A., Lægsgaard, E., Stensgaard, I., and Besenbacher, F., *Science* **299**, 377 (2003).

215. Kulawik, M., Nilius, N., Rust, H.-P., and Freund, H.-J., *Phys. Rev. Lett.* **91**, 256101 (2003).

216. McIntyre, B.J., Salmeron, M., and Somorjai, G.A., *J. Vac. Sci. Technol. A* **11**, 1964 (1993).

217. McIntyre, B.J., Salmeron, M.B., and Somorjai, G.A., *Rev. Sci. Instrum.* **64**, 687 (1993).

218. Jensen, J.A., Rider, K.B., Chen, Y., Salmeron, M., and Somorjai, G.A., *J. Vac. Sci. Technol. B* **17**, 1080 (1999).

219. Cernota, P., Rider, K., Yoon, H.A., Salmeron, M., and Somorjai, G.A., *Surf. Sci.* **445**, 249 (2000).

220. Lægsgaard, E., österlund, L., Thostrup, P., Rasmussen, P.B., Stensgaard, I., and Besenbacher, F., *Rev. Sci. Instrum.* **72**, 3537 (2001).

221. Hendriksen, B.L.M., and Frenken, J.W.M., *Phys. Rev. Lett.* **89**, 046101 (2002).

222. Thostrup, P., Kruse Vestergaard, E., An, T., Lægsgaard, E., and Besenbacher, F., *J. Chem. Phys.* **118**, 3724 (2003).

223. Ho, W., *J. Chem. Phys.* **117**, 11033 (2002).

224. Stipe, B.C., Rezaei, M.A., and Ho, W., *Science* **280**, 1732 (1998).
225. Nilius, N., Wallis, T.M., and Ho, W., *Science* **297**, 5588 (2002).
226. Datye, A.K., *J. Catal.* **216**, 144 (2003).
227. Henry, C.R., *Prog. Surf. Sci.* **80**, 92 (2005).
228. Schmidt, L.D., and Krause, K.R., *Catal. Today* **12**, 1035 (1992).
229. Burkhardt, J., and Schmidt, L.D., *J. Catal.* **116**, 240 (1989).
230. Giorgio, S., Henry, C.R., Chapon, C., and Roucau, C., *J. Catal.* **148**, 534 (1994).
231. José-Yacamán, M., Díaz, G., and Gómez, A., *Catal. Today* **23**, 161 (1995).
232. Jefferson, D.A., and Harris, P.J.F., *Nature* **185**, L459 (1987).
233. Jefferson, D.A., and Harris, P.J.F., *Nature* **332**, 617 (1988).
234. Harris, P.J.F., *J. Catal.* **97**, 527 (1986).
235. Bernal, S., Botana, F.J., Calvino, J.J., Lopez-Cartes, C., Perez-Omil, J.A., and Rodriguez-Izquierdo, J.M., *Ultramicroscopy* **72**, 135 (1998).
236. Bernal, S., Calvino, J.J., López-Cartes, C., Pintado, J.M., Pérez-Omil, J.A., Rodríguez-Izquierdo, J.M., Hayek, K., and Rupprechter, G., *Catal. Today* **52**, 29 (1999).
237. Sushumna, I., and Ruckenstein, E., *J. Catal.* **108**, 77 (1987).
238. Ramachandran, A.S., Anderson, S.L., and Datye, A.K., *Ultramicroscopy* **51**, 282 (1993).
239. Boyes, E., and Gai, P., *Ultramicroscopy* **67**, 219 (1997).
240. Gai, P., *Top. Catal.* **8**, 97 (1999).
241. Hansen, P., Wagner, J., Helveg, S., Rostrup-Nielsen, J., Clausen, B., and Topsøe, H., *Science* **295**, 2053 (2002).
242. Hansen, T., Wagner, J., Hansen, P., Dahl, S., Topsøe, H., and Jacobsen, C., *Science* **294**, 1508 (2001).
243. Thomas, J.M., and Gai, P.L., *Adv. Catal.* **48**, 171 (2004).
244. Wagner, J.B., Hansen, P.L., Molenbroek, A.M., Topsøe, H., Clausen, B.S., and Helveg, S., *J. Phys. Chem. B.* **107**, 7753 (2003).
245. Lopez-Cartes, C., Bernal, S., Calvino, J., Cauqui, M., Blanco, G., Perez-Omil, J., Pintado, J., Helveg, S., and Hansel, P., *Chem. Commun.* 644 (2003).
246. Giorgio, S., Joao, S.S., Nitsche, S., Chaudanson, D., Sitja, G., and Henry, C.R., *Ultramicroscopy* **106**, 503 (2006).
247. Penner, S., Wang, D., Su, D.S., Rupprechter, G., Podloucky, R., Schlögl, R., and Hayek, K., *Surf. Sci.* **532–535**, 276 (2003).
248. Wang, D., Penner, S., Su, D.S., Rupprechter, G., Hayek, K., and Schlögl, R., *J. Catal.* **219**, 434 (2003).
249. Chinchen, C., Denny, P.J., Jennings, J.R., Spencer, M.S., and Waugh, K.C., *Appl. Catal.* **36**, 1 (1988).
250. Schulz, H., *Appl. Catal. A: General* **186**, 3 (1999).
251. Gruber, H.L., *J. Phys. Chem.* **66**, 48 (1962).
252. Lundgren, E., Gustafson, J., Mikkelsen, A., Andersen, J.N., Stierle, A., Dosch, H., Todorova, M., Rogal, J., Reuter, K., and Scheffler, M., *Phys. Rev. Lett.* **92**, 046101 (2004).
253. Kaichev, V.V., Prosvirin, I.P., Bukhtiyarov, V.I., Unterhalt, H., Rupprechter, G., and Freund, H.-J., *J. Phys. Chem. B.* **107**, 3522 (2003).
254. Frank, M., and Bäumer, M., *Phys. Chem. Chem. Phys.* **2**, 3723 (2000).
255. Noordermeer, A., Kok, G.A., and Nieuwenhuys, B.E., *Surf. Sci.* **172**, 349 (1986).
256. Guo, X., and Yates, J.T., *J. Chem. Phys.* **90**, 6761 (1989).
257. Biberian, J.P., and Van Hove, M.A., *Surf. Sci.* **118**, 443 (1982).
258. Conrad, H., Ertl, G., and Küppers, J., *Surf. Sci.* **76**, 323 (1978).
259. Ohtani, H., Van Hove, M.A., and Somorjai, G.A., *Surf. Sci.* **187**, 372 (1987).
260. Tüshaus, M., Berndt, W., Conrad, H., Bradshaw, A.M., and Persson, B., *Appl. Phys. A* **51**, 91 (1990).
261. Bradshaw, A.M., and Hoffmann, F.M., *Surf. Sci.* **72**, 513 (1978).
262. Zasada, I., and Van Hove, M.A., *Surf. Sci. Lett.* **457**, L421 (2000).
263. Gelin, P., Siedle, A.R., and Yates, J.T., *J. Phys. Chem.* **88**, 2978 (1984).
264. Kuhn, W.K., Szanyi, J., and Goodman, D.W., *Surf. Sci. Lett.* **274**, L611 (1992).

265. Bourguignon, B., Carrez, S., Dragnea, B., and Dubost, H., *Surf. Sci.* **418**, 171 (1998).
266. Sautet, P., Rose, M.K., Dunphy, J.C., Behler, S., and Salmeron, M., *Surf. Sci.* **453**, 25 (2000).
267. Loffreda, D., Simon, D., and Sautet, P., *Surf. Sci.* **425**, 68 (1999).
268. Hammer, B., Morikawa, Y., and Nørskov, J.K., *Phys. Rev. Lett.* **76**, 2141 (1996).
269. Honkala, K., Pirila, P., and Laasonen, K., *Surf. Sci.* **489**, 72 (2001).
270. Hirschl, R., and Hafner, J., *Surf. Sci.* **498**, 37 (2002).
271. Klüner, T., Govind, N., Wang, Y.A., and Carter, E.A., *Phys. Rev. Lett.* **86**, 5954 (2001).
272. Klüner, T., Govind, N., Wang, Y.A., and Carter, E.A., *J. Chem. Phys.* **116**, 42 (2001).
273. Morkel, M., Rupprechter, G., and Freund, H.-J., *J. Chem. Phys.* **119**, 10853 (2003).
274. Kaichev, V.V., Morkel, M., Unterhalt, H., Prosvirin, I.P., Bukhtiyarov, V.I., Rupprechter, G., and Freund, H.-J., *Surf. Sci.* **566–568**, 1024 (2004).
275. Hollins, P., *Surf. Sci. Rep.* **16**, 51 (1992).
276. Eichler, A., *Surf. Sci.* **526**, 332 (2003).
277. Baldelli, S., Markovic, N., Ross, P., Shen, Y.R., and Somorjai, G.A., *J. Phys. Chem. B* **103**, 8920 (1999).
278. Backus, E.H.G., and Bonn, M., *Chem. Phys. Lett.* **412**, 152 (2005).
279. McCrea, K., Parker, J.S., Chen, P., and Somorjai, G.A., *Surf. Sci.* **494**, 238 (2001).
280. Szanyi, J., Kuhn, W.K., and Goodman, D.W., *J. Vac. Sci. Technol. A* **11**, 1969 (1993).
281. Behm, R.J., Christmann, K., and Ertl, G., *J. Chem. Phys.* **73**, 2984 (1980).
282. Evans, J., Hayden, B.E., and Lu, G., *Surf. Sci.* **360**, 61 (1996).
283. Raval, R., Haq, S., Harrison, M.A., Blyholder, G., and King, D.A., *Chem. Phys. Lett.* **167**, 391 (1990).
284. Cabilla, G.C., Bonivardi, A.L., and Baltanas, M.A., *Catal. Lett.* **55**, 147 (1998).
285. Wolter, K., Seiferth, O., Kuhlenbeck, H., Bäumer, M., and Freund, H.-J., *Surf. Sci.* **399**, 190 (1998).
286. Rainer, D.R., Wu, M.-C., Mahon, D.I., and Goodman, D.W., *J. Vac. Sci. Technol. A* **14**, 1184 (1996).
287. Brandt, R.K., Hughes, M.R., Bourget, L.P., Truszkowska, K., and Greenler, R.G., *Surf. Sci.* **286**, 15 (1993).
288. Wang, H., Tobin, R.G., Lambert, D.K., Fisher, G.B., and DiMaggio, C.L., *Surf. Sci.* **330**, 173 (1995).
289. Dellwig, T., Hartmann, J., Libuda, J., Meusel, I., Rupprechter, G., Unterhalt, H., and Freund, H.-J., *J. Mol. Catal. A* **162**, 51 (2000).
290. Libuda, J., Winkelmann, F., Bäumer, M., Freund, H.-J., Bertrams, T., Neddermeyer, H., and Müller, K., *Surf. Sci.* **318**, 61 (1994).
291. Libuda, J., Frank, M., Sandell, A., Andersson, S., Brühwiler, P.A., Bäumer, M., Martensson, N., and Freund, H.-J., *Surf. Sci.* **384**, 106 (1997).
292. Stierle, A., Renner, F., Streitel, R., Dosch, H., Drube, W., and Cowie, B.C., *Science* **303**, 1652 (2004).
293. Kresse, G., Schmid, M., Napetschnig, E., Shishkin, M., Köhler, L., and Varga, P., *Science* **308**, 1440 (2005).
294. Shaikhutdinov, S., Heemeier, M., Hoffmann, J., Meusel, I., Richter, B., Bäumer, M., Kuhlenbeck, H., Libuda, J., Freund, H.-J., Oldman, R., Jackson, S.D., Konvicka, C., Schmid, M., and Varga, P., *Surf. Sci.* **501**, 270 (2002).
295. Hayek, K., Kramer, R., and Paal, Z., *Appl. Catal. A* **162**, 1 (1997).
296. Unterhalt, H., Ph.D. thesis, Free University Berlin, 2002.
297. Rupprechter, G., Unterhalt, H., Borasio, M., Morkel, M., and Freund, H.-J., Annual Reports of the Max Planck Society (Jahrbuch), p. 193, 2005.
298. Knab, D., and Koenig, C., *J. Phys. Condens. Matter* **2**, 465 (1990).
299. Potterton, E.A., and Bain, C.D., *JElectroanal. Chem.* **409**, 109 (1996).
300. Humbert, C., Dreesen, L., Mani, A.A., Caudano, Y., Lemaire, J.-J., Thiery, P.A., and Peremans, A., *Surf. Sci.* **502–503**, 203 (2002).
301. Fano, U., *Phys. Rev.* **124**, 1866 (1961).
302. Fano, U., and Cooper, J.W., *Phys. Rev.* **137**, 1364 (1965).
303. Yudanov, I.V., Sahnoun, R., Neyman, K.M., Rösch, N., Hoffmann, J., Schauermann, S., Johánek, V., Unterhalt, H., Rupprechter, G., Libuda, L., and Freund, H.-J., *J. Phys. Chem. B* **107**, 255 (2003).

304. Risse, T., Carlsson, A., Bäumer, M., Klüner, T., and Freund, H.-J., *Surf. Sci.* **546**, L829 (2003).
305. Rainer, D.R., Xu, C., Holmblad, P.M., and Goodman, D.W., *J. Vac. Sci. Technol. A* **15**, 1653 (1997).
306. Ozensoy, E., Min, B.K., Santra, A.K., and Goodman, D., *J. Phys. Chem. B* **108**, 4351 (2004).
307. Borasio, M., Rupprechter, G., and Freund, H.-J., unpublished results.
308. Gotti, A., and Prins, R., *J. Catal.* **175**, 302 (1998).
309. Beck, W., Klapötke, T.M., Knizek, J., Nöth, H., and Schütt, T., *Eur. J. Inorg. Chem.* 523 (1999).
310. Conrad, H., Ertl, G., Koch, J., and Latta, E.E., *Surf. Sci.* **43**, 462 (1974).
311. Weissman, D.L., Shek, M.L., and Spicer, W.E., *Surf. Sci.* **92**, L59 (1980).
312. Stara, I., and Matolin, V., *Surf. Sci.* **313**, 99 (1994).
313. Kung, K.Y., Chen, P., Wei, F., Shen, Y.R., and Somorjai, G.A., *Surf. Sci. Lett.* **463**, L627 (2000).
314. Pery, T., Schweitzer, M.G., Volpp, H.-R., Wolfrum, J., Ciossu, L., Deutschmann, O., and Warnatz, J. Proceedings of the Combustion Institute, The Combustion Institute, 2002, p. 973.
315. Doering, D.L., Poppa, H., and Dickinson, J.T., *J. Catal.* **73**, 104 (1982).
316. Matolin, V., and Gillet, E., *Surf. Sci.* **238**, 75 (1990).
317. Matolin, V., Rebholz, M., and Kruse, N., *Surf. Sci.* **245**, 233 (1991).
318. Matolín, V., Stará, I., Tsud, N., and Johánek, V., *Prog. Surf. Sci.* **67**, 167 (2001).
319. Cordatos, H., Bunluesin, T., and Gorte, R.J., *Surf. Sci.* **323**, 219 (1995).
320. Schauermann, S., Hoffmann, J., Johánek, V., Hartmann, J., Libuda, J., and Freund, H.-J., *Catal. Lett.* **84**, 209 (2002).
321. Neurock, M., *Top. Catal.* **9**, 135 (1999).
322. Nørskov, J.K., Bligaard, T., Logadottir, A., Bahn, S., Hansen, L.B., Bollinger, M., Bengaard, H., Hammer, B., Sljivancanin, Z., Mavrikakis, M., Xu, Y., Dahl, S., and Jacobsen, C.J.H., *J. Catal.* **209**, 275 (2002).
323. Michaelides, A., Liu, Z.-P., Zhang, C.J., Alavi, A., King, D.A., and Hu, P., *J. Am. Chem. Soc.* **125**, 3704 (2003).
324. Rupprechter, G., Kaichev, V.V., Morkel, M., Unterhalt, H., and Bukhtiyarov, V.I., *Appl. Surf. Sci.* **235**, 26 (2004).
325. Denecke, R., Kinne, M., Whelan, C.M., and Steinrück, H.-P., *Surf. Rev. Lett.* **9**, 797 (2002).
326. Barber, M., Connor, J.A., Guest, M.F., Hall, M.B., Hillier, I.H., and Meredith, W.N.E., *Faraday Discuss. Chem. Soc.* **54**, 219 (1972).
327. Plummer, E.W., and Eberhardt, W., *Adv. Chem. Phys.* **49**, 533 (1982).
328. Föhlisch, A., Nyberg, M., Hasselström, J., Karis, O., Pettersson, L.G.M., and Nilsson, A., *Phys. Rev. Lett.* **85**, 3309 (2000).
329. deKoster, A., Jansen, A.P.J., and van Santen, R.A., *Faraday Discuss. Chem. Soc.* **87**, 263 (1989).
330. Moon, D.W., Cameron, S., Zaera, F., Eberhardt, W., Carr, R., Bernasek, S.L., Gland, J.L., and Dwyer, D.J., *Surf. Sci.* **180**, L123 (1987).
331. Shinn, N.D., and Madey, T.E., *J. Chem. Phys.* **83**, 5928 (1985).
332. Anderson, A.B., and Dowd, D.Q., *J. Phys. Chem.* **91**, 869 (1987).
333. Matolin, V., Gillet, E., and Kruse, N., *Surf. Sci.* **186**, L541 (1987).
334. Christmann, K., *Surf. Sci. Rep.* **9**, 1 (1988).
335. Christmann, K., *Prog. Surf. Sci.* **48**, 15 (1995).
336. White, J.M., and Akther, S., *CRC Crit. Rev. Solid State Mater. Sci.* **14**, 131 (1988).
337. Doyle, A., Shaikhutdinov, S., Jackson, S.D., and Freund, H.-J., *Angew. Chem. Int. Ed.* **42**, 5240 (2003).
338. Muschiol, U., Schmidt, P.K., and Christmann, K., *Surf. Sci.* **395**, 182 (1998).
339. Wilde, M., Matsumoto, M., Fukutani, K., and Aruga, T., *Surf. Sci.* **482**, 346 (2001).
340. Gdowski, G.E., Felter, T.E., and Stulen, R.H., *Surf. Sci.* **181**, L147 (1987).
341. Christmann, K., Chehab, F., Penka, V., and Ertl, G., *Surf. Sci.* **152/153**, 356 (1985).
342. Falconer, J.L., and Madix, R.J., *Surf. Sci.* **46**, 473 (1974).
343. Okuyama, H., Siga, W., Takagi, N., Nishijima, M., and Aruga, T., *Surf. Sci.* **401**, 344 (1998).
344. Behm, R.J., Penka, V., Cattania, M.-G., Christmann, K., and Ertl, G., *J. Chem. Phys.* **78**, 7486 (1983).
345. Farias, D., Schilbe, P., Patting, M., and Rieder, K.H., *J. Chem. Phys.* **110**, 559 (1999).

346. Twigg, M.V., "Catalyst Handbook." Wolfe Publishing Ltd, London, 1989.
347. Ackermann, M., Robach, O., Walker, C., Quiros, C., Isern, H., and Ferrer, S., *Surf. Sci.* **557**, 21 (2004).
348. Gusovius, A.F., Watling, T.C., and Prins, R., *Appl. Catal. A* **188**, 187 (1999).
349. Conrad, H., Ertl, G., and Latta, E.E., *J. Catal.* **35**, 363 (1974).
350. Kok, G.A., Noordermeer, A., and Nieuwenhuys, B.E., *Surf. Sci.* **135**, 65 (1983).
351. Conrad, H., Ertl, G., and Latta, E.E., *Surf. Sci.* **41**, 435 (1974).
352. Rieder, K.H., and Stocker, W., *Surf. Sci.* **148**, 139 (1984).
353. Wilke, S., Henning, D., Löber, R., Methfessel, M., and Scheffler, M., *Surf. Sci.* **307–309**, 76 (1994).
354. Eriksson, M., and Ekedahl, L.-G., *Appl. Surf. Sci.* **133**, 89 (1998).
355. Nyberg, C., and Westerlund, L., *Surf. Sci.* **256**, 9 (1991).
356. Johnson, A.D., Maynard, K.J., Daley, S.P., Yang, Q.Y., and Ceyer, S.T., *Phys. Rev. Lett.* **67**, 927 (1991).
357. Rupprechter, G., and Somorjai, G.A., *Catal. Lett.* **48**, 17 (1997).
358. Ceyer, S.T., *Acc. Chem. Res.* **34**, 737 (2001).
359. Mitsui, T., Rose, M.K., Fomin, E., Ogletree, D.F., and Salmeron, M., *Surf. Sci.* **511**, 259 (2002).
360. Mitsui, T., Rose, M.K., Fomin, E., Ogletree, D.F., and Salmeron, M., *Surf. Sci.* **540**, 5 (2003).
361. Silvestre-Albero, J., Rupprechter, G., and Freund, H.-J., *J. Catal.* **235**, 52 (2005).
362. Morkel, M., Ph.D. thesis, Free University Berlin, 2004.
363. Dong, W., and Hafner, J., *Phys. Rev. B* **56**, 15396 (1997).
364. Nyberg, C., Westerlund, L., Jönsson, L., and Andersson, S., *J. Electron. Spectr. Rel. Phenom.* **54/55**, 639 (1990).
365. Hoge, D., Tüshaus, M., and Bradshaw, A.M., *Surf. Sci.* **207**, L935 (1988).
366. Zenobi, R., Xu, J., and Yates, J.T., *Surf. Sci.* **276**, 241 (1992).
367. Andersson, S., *Solid State Commun.* **21**, 75 (1977).
368. Hicks, R.F., and Bell, A.T., *J. Catal.* **90**, 205 (1984).
369. Berlowitz, P.J., and Goodman, D.W., *J. Catal.* **108**, 364 (1987).
370. Ryndin, Y.A., Hicks, R.F., Bell, A.T., and Yermakov, Y.I., *J. Catal.* **70**, 287 (1981).
371. Vannice, M.A., *J. Catal.* **37**, 449 (1975).
372. Vannice, M.A., *Catal. Rev.—Sci. Eng.* **14**, 153 (1976).
373. Kim, Y., Peebles, H., and White, J.M., *Surf. Sci.* **114**, 363 (1982).
374. Yates, J.T., Williams, E., and Weinberg, W.H., *Surf. Sci.* **91**, 562 (1980).
375. Rebholz, M., Prins, R., and Kruse, N., *Surf. Sci. Lett.* **259**, L797 (1991).
376. Hindermann, J.P., Hutchings, G.J., and Kiennemann, A., *Catal. Rev.—Sci. Eng.* **35**, 1 (1993).
377. Rothaemel, M., Zanthoff, H.W., and Baerns, M., *Catal. Lett.* **28**, 321 (1994).
378. Mavrikakis, M., and Barteau, M.A., *J. Mol. Catal. A* **131**, 135 (1998).
379. Sellmer, C., Prins, R., and Kruse, N., *Catal. Lett.* **47**, 83 (1997).
380. Shen, W.-J., Okumura, M., Matsumura, Y., and Haruta, M., *Appl. Catal. A: General* **213**, 225 (2001).
381. Rieck, J.S., and Bell, A.T., *J. Catal.* **99**, 278 (1986).
382. Chen, B., and Falconer, J.L., *J. Catal.* **134**, 737 (1992).
383. Steininger, H., Lehwald, S., and Ibach, H., *Surf. Sci.* **117**, 342 (1982).
384. Ertl, G., Neumann, M., and Streit, K.M., *Surf. Sci.* **64**, 393 (1977).
385. Avery, N.R., *J. Chem. Phys.* **74**, 4202 (1981).
386. Longwitz, S., Schnadt, J., Kruse Vestergaard, E., Vang, R.T., Lægsgaard, E., Stensgaard, I., Brune, H., and Besenbacher, F., *J. Phys. Chem. B* **108**, 14497 (2004).
387. Sheppard, N., and Nguyen, T.T., *Adv. IR Raman Spectrosc.* **5**, 67 (1978).
388. Olsen, C.W., and Masel, R.I., *Surf. Sci.* **201**, 444 (1988).
389. Hayden, B.E., and Bradshaw, A.M., *Surf. Sci.* **125**, 787 (1983).
390. Persson, B.N.J., Tüshaus, M., and Bradshaw, A.M., *J. Chem. Phys.* **92**, 5034 (1990).
391. Su, X., Cremer, P.S., Shen, Y.R., and Somorjai, G.A., *Phys. Rev. Lett.* **77**, 3858 (1996).
392. Pedersen, M.O., Bocquet, M.-L., Sautet, P., Laegsgaard, E., Stensgaard, I., and Besenbacher, F., *Chem. Phys. Lett.* **299**, 403 (1999).
393. Kruse Vestergaard, E., Thostrup, P., An, T., Hammer, B., Lægsgaard, E., and Besenbacher, F., *Phys. Rev. Lett.* **88**, 259601 (2002).

394. Biberian, J.P., and Van Hove, M.A., *Surf. Sci.* **138**, 361 (1984).
395. Jensen, J.A., Rider, K.B., Salmeron, M., and Somorjai, G.A., *Phys. Rev. Lett.* **80**, 1228 (1998).
396. Somorjai, G.A., Su, X., McCrea, K.R., and Rider, K.B., *Top. Catal.* **8**, 23 (2000).
397. Heiz, U., Sherwood, R., Cox, D.M., Kaldor, A., and Yates, J.T., *J. Phys. Chem.* **99**, 8730 (1995).
398. Rupprechter, G., Eppler, A.S., and Somorjai, G.A., *in* "Electron Microscopy 1998" (H.A.C. Benavides and M. Jose-Yacaman, Eds.), Institute of Physics Publishing, Bristol, p. 369, 1998.
399. Avoyan, A., Rupprechter, G., Eppler, A.S., and Somorjai, G.A., *Top. Catal.* **10**, 107 (2000).
400. Somorjai, G.A., Hwang, K., and Parker, J., *Top. Catal.* **26**, 87 (2003).
401. McCrea, K., Parker, J.S., and Somorjai, G.A., *J. Phys. Chem. B* **106**, 10854 (2002).
402. McCrea, K.R., Parker, J.S., and Somorjai, G.A., *in* Surface Chemistry and Catalysis (A.F. Carley, P.R. Davis, G.J. Hutchings, and M.S. Spencer, Eds.), Springer, p. 55. 2002.
403. Zhdanov, V.P., and Kasemo, B., *Surf. Sci. Rep.* **29**, 31 (1997).
404. Hayek, K., Goller, H., Penner, S., Rupprechter, G., and Zimmermann, C., *Catal. Lett.* **92**, 1 (2004).
405. Gierer, M., Barbieri, A., Van Hove, M.A., and Somorjai, G.A., *Appl. Surf. Sci.* **391**, 176 (1997).
406. Beutler, A., Lundgren, E., Nyholm, R., Andersen, J.N., Setlik, B., and Heskett, D., *Surf. Sci.* **371**, 381 (1997).
407. Starke, U., Van Hove, M.A., and Somorjai, G.A., *Prog. Surf. Sci.* **46**, 305 (1994).
408. Peden, C.H.F., Goodman, D.W., Blair, D.S., Berlowitz, P.J., Fisher, G.B., and Oh, S., *J. Phys. Chem.* **92**, 1563 (1988).
409. Deutschmann, O., Behrendt, F., and Warnatz, J., *Catal. Today* **46**, 155 (1998).
410. Haruta, M., *Catal. Today* **26**, 153 (1997).
411. Valden, M., Lai, X., and Goodman, D.W., *Science* **281**, 1647 (1998).
412. Chen, M.S., and Goodman, D.W., *Science* **306**, 252 (2004).
413. Lemire, C., Meyer, R., Shaikhutdinov, S.K., and Freund, H.-J., *Angew. Chem. Int. Ed.* **43**, 118 (2004).
414. Meyer, R., Lemire, C., Shaikhutdinov, S.K., and Freund, H.-J., *Gold Bull.* **37**, 72 (2004).
415. Piccolo, L., Loffreda, D., Cadete Santos Aires, F.J., Deranlot, C., Jugnet, Y., Sautet, P., and Bertolini, J.C., *Surf. Sci.* **566–568**, 995 (2004).
416. Miragliotta, J., Rabinowitz, P., Cameron, S.D., and Hall, R.B., *Appl. Phys. A* **51**, 221 (1990).
417. Bandara, A., Kubota, J., Onda, K., Wada, A., Kano, S.S., Domen, K., and Hirose, C., *Surf. Sci.* **427–428**, 331 (1999).
418. Westerberg, S., Wang, C., Chou, K., and Somorjai, G.A., *J. Phys. Chem. B* **108**, 6374 (2004).
419. Bandara, A., Kubota, J., Onda, K., Wada, A., Kano, S.S., Domen, K., and Hirose, C., *J. Phys. Chem. B* **102**, 5951 (1998).
420. Bandara, A., Kubota, J., Onda, K., Wada, A., Domen, K., and Hirose, C., *Appl. Phys. B* **68**, 573 (1999).
421. Hess, C., Bonn, M., Funk, S., and Wolf, M., *Chem. Phys. Lett.* **325**, 139 (2000).
422. Funk, S., Bonn, M., Denzler, D.N., Hess, C., Wolf, M., and Ertl, G., *J. Chem. Phys.* **112**, 9888 (2000).
423. Arnolds, H., Symonds, J.P.R., Zhang, V.L., and King, D.A., *Rev. Sci. Instrum.* **74**, 3943 (2003).
424. Roke, S., Kleyn, A.W., and Bonn, M., *Chem. Phys. Lett.* **370**, 227 (2003).
425. Symonds, J.P.R., Arnolds, H., Zhang, V.L., Fukutani, K., and King, D.A., *J. Chem. Phys.* **120**, 7158 (2004).
426. Zhang, V.L., Arnolds, H., and King, D.A., *Surf. Sci.* **587**, 102 (2005).
427. Bandara, A., Kano, S., Onda, K., Katano, S., Kubota, J., Domen, K., Hirose, C., and Wada, A., *Bull. Chem. Soc. Jpn.* **75**, 1125 (2002).
428. Roeterdink, W.G., Berg, O., and Bonn, M., *J. Chem. Phys.* **121**, 10174 (2004).
429. Roeterdink, W.G., Aarts, J.F.M., Kleyn, A.W., and Bonn, M., *J. Phys. Chem. B* **108**, 14491 (2004).
430. Cremer, P.S., Su, X., Somorjai, G.A., and Shen, Y.R., *J. Mol. Catal. A* **131**, 225 (1998).
431. Chen, Z., Gracias, D.H., and Somorjai, G.A., *Appl. Phys. B* **68**, 549 (1999).
432. Volpp, H.-R., and Wolfrum, J., *in* "Applied Combustion Diagnostics" (K. Kohse-Höinghaus and J.B. Jeffries, Eds.), Taylor & Francis, New York, 2001.
433. Esch, F., Greber, T., Kennou, S., Siokou, A., Ladas, S., and Imbihl, R., *Catal. Lett.* **38**, 165 (1996).
434. Horiuti, I., and Polanyi, M., *Trans. Faraday Soc.* **30**, 1164 (1934).

435. Kesmodel, L.L., and Gates, J.A., *Surf. Sci.* **111**, L747 (1981).
436. Gates, J.A., and Kesmodel, L.L., *Surf. Sci.* **124**, 68 (1983).
437. Gates, J.A., and Kesmodel, L.L., *Surf. Sci.* **124**, 68 (1983).
438. Lloyd, D.R., and Netzer, F.P., *Surf. Sci.* **129**, 1249 (1983).
439. Stuve, E.M., and Madix, R.J., *J. Phys. Chem.* **89**, 105 (1985).
440. Camplin, J., Eve, J., and McCash, E., *Surf. Rev. Lett.* **4**, 1371 (1997).
441. Sandell, A., Beutler, A., Jaworowski, A., Wiklund, M., Heister, K., Nyholm, R., and Andersen, J.N., *Surf. Sci.* **415**, 411 (1998).
442. Ogasawara, H., Ichihara, S., Okuyama, H., Domen, K., and Kawai, M., *J. Electron Spectrosc. Relat. Phenom.* **114**, 339 (2001).
443. Sekitani, T., Takaoka, T., Fujisawa, M., and Nishijima, M., *J. Phys. Chem.* **96**, 8462 (1992).
444. Stacchiola, D., Azad, S., Burkholder, L., and Tysoe, W.T., *J. Phys. Chem. B* **105**, 11233 (2001).
445. Sock, M., Eichler, A., Surnev, S., Andersen, J.N., Klötzer, B., Hayek, K., Ramsey, M.G., and Netzer, F.P., *Surf. Sci.* **545**, 122 (2003).
446. Neurock, M., and van Santen, R.A., *J. Phys. Chem. B* **104**, 11127 (2000).
447. Ge, Q., and Neurock, M., *Chem. Phys. Lett.* **358**, 377 (2002).
448. Cremer, P.S., Stanners, C., Niemantsverdriet, J.W., Shen, Y.R., and Somorjai, G.A., *Surf. Sci.* **328**, 111 (1995).
449. Kaltchev, M., Thompson, A.W., and Tysoe, W.T., *Surf. Sci.* **391**, 145 (1997).
450. Stacchiola, D., Kaltchev, G., Wu, G., and Tysoe, W.T., *Surf. Sci.* **470**, L32 (2000).
451. Stacchiola, D., Burkholder, L., and Tysoe, W.T., *Surf. Sci.* **511**, 215 (2002).
452. Borasio, M., Rodríguez de la Fuente, O., Rupprechter, G., and Freund, H.-J., 2007, in preparation.
453. Borasio, M., Ph.D. thesis, Free University Berlin, 2006.
454. Stacchiola, D., and Tysoe, W.T., *Surf. Sci.* **540**, L600 (2003).
455. Doyle, A., Shaikhutdinov, S., and Freund, H.-J., *J. Catal.* **223**, 444 (2004).
456. Frank, M., Bäumer, M., Kühnemuth, R., and Freund, H.-J., *J. Vac. Sci. Technol. A* **19**, 1497 (2001).
457. Rupprechter, G., and Somorjai, G.A., *Catal. Lett.* **48**, 17 (1997).
458. Beebe, T., and Yates, J.T., *J. Am. Chem. Soc.* **108**, 663 (1986).
459. Davis, R.J., and Boudart, M., *Catal. Sci. Technol.* **1**, 129 (1991).
460. Chen, P., Kung, K., Shen, Y., and Somorjai, G.A., *Surf. Sci.* **494**, 289 (2001).
461. Cremer, P.S., Su, X., Shen, Y.R., and Somorjai, G.A., *J. Phys. Chem.* **100**, 16302 (1996).
462. Yang, M., and Somorjai, G.A., *J. Am. Chem. Soc.* **126**, 7698 (2004).
463. Yang, M., Chou, K.C., and Somorjai, G.A., *J. Phys. Chem. B* **107**, 5267 (2003).
464. Yang, M., and Somorjai, G.A., *J. Phys. Chem. B* **108**, 4405 (2004).
465. Stöhr, J., Sette, F., and Johnson, A.L., *Phys. Rev. Lett.* **53**, 1684 (1984).
466. Cassuto, A., Kiss, J., and White, J.M., *Surf. Sci.* **255**, 289 (1991).
467. Döll, R., Gerken, C.A., Van Hove, M.A., and Somorjai, G.A., *Surf. Sci.* **374**, 151 (1997).
468. Ibach, H., *Surf. Sci.* **117**, 685 (1982).
469. Ibach, H., and Mills, D.L., "Electron Energy Loss Spectrscopy and Surface Vibration." Academic Press, New York, 1982.
470. Mohsin, S., Trenary, M., and Robota, H., *J. Phys. Chem.* **92**, 5229 (1988).
471. Rekoske, J.E., Cortright, R.D., Goddard, S.A., Sharma, S.B., and Dumesic, J.A., *J. Phys. Chem.* **96**, 1880 (1992).
472. Cremer, P.S., and Somorjai, G.A., *J. Chem. Soc. Farady Trans.* **91**, 3671 (1995).
473. Cremer, P.S., Su, X., Shen, Y.R., and Somorjai, G.A., *J. Am. Chem. Soc.* **118**, 2942 (1996).
474. Cremer, P.S., Su, X., Shen, Y.R., and Somorjai, G.A., *Catal. Lett.* **40**, 143 (1996).
475. Cremer, P.S., Su, X., Shen, Y.R., and Somorjai, G.A., *J. Chem. Soc. Faraday Trans.* **92**, 4717 (1996).
476. Ohtani, T., Kubota, J., Kondo, J.N., Hirose, C., and Domen, K., *Surf. Sci.* **415**, L983 (2001).
477. Tang, D.C., Hwang, K.S., Salmeron, M., and Somorjai, G.A., *J. Phys. Chem. B* **108**, 13300 (2004).
478. Lüth, H., Rubloff, G.W., and Grobmann, W.D., *Surf. Sci.* **63**, 325 (1977).
479. Christmann, K., and Demuth, J.E., *J. Chem. Phys.* **76**, 6308 (1982).
480. Solymosi, F., Berkó, A., and Tóth, Z., *Surf. Sci.* **285**, 197 (1993).

481. Bhattacharya, A.K., Chesters, M.A., Pemble, M.E., and Sheppard, N., *Surf. Sci.* **206**, L845 (1988).
482. Hartmann, N., Esch, F., and Imbihl, R., *Surf. Sci.* **297**, 175 (1993).
483. Gates, J.A., and Kesmodel, L.L., *J. Catal.* **83**, 437 (1983).
484. Guo, X., Hanley, L., and Yates, J.T., *J. Am. Chem. Soc.* **111**, 3155 (1989).
485. Davis, J.L., and Barteau, M.A., *Surf. Sci.* **187**, 387 (1987).
486. Davis, J.L., and Barteau, M.A., *Surf. Sci.* **235**, 235 (1990).
487. Francis, S.M., Corneille, J., Goodman, D.W., and Bowker, M., *Surf. Sci.* **364**, 30 (1996).
488. Levis, R.J., Zhicheng, J., and Winograd, N., *J. Am. Chem. Soc.* **111**, 4605 (1989).
489. Chen, J.-J., Jiang, Z.-C., Zhou, Y., Chakraborty, B.R., and Winograd, N., *Surf. Sci.* **328**, 248 (1995).
490. Rebholz, M., Matolin, V., Prins, R., and Kruse, N., *Surf. Sci.* **251–252**, 1117 (1991).
491. Kruse, N., Rebholz, M., Matolin, V., Chuah, G.K., and Block, J.H., *Surf. Sci.* **238**, L457 (1990).
492. Rebholz, M., and Kruse, N., *J. Chem. Phys.* **95**, 7745 (1991).
493. Schennach, R., Eichler, A., and Rendulic, K.D., *J. Phys. Chem. B* **107**, 2552 (2003).
494. Zhang, C.J., and Hu, P., *J. Chem. Phys.* **115**, 7182 (2001).
495. Wickham, D.T., Logsdon, B.W., Cowley, S.W., and Butler, C.D., *J. Catal.* **128**, 198 (1991).
496. Matsumura, Y., Okumura, M., Usami, Y., Kagawa, K., Yamashita, H., Anpo, M., and Haruta, M., *Catal. Lett.* **44**, 189 (1997).
497. Usami, Y., Kagawa, K., Kawazoe, M., Matsumura, Y., Sakurai, H., and Haruta, M., *Appl. Catal. A: General* **171**, 123 (1998).
498. Shiozaki, R., Hayakawa, T., Liu, Y.Y., Ishii, T., Kumagai, M., Hamakawa, S., Suzuki, K., Itoh, T., Shishido, T., and Takehira, K., *Catal. Lett.* **58**, 131 (1999).
499. Levis, R.J., Zhicheng, J., and Winograd, N., *J. Am. Chem. Soc.* **110**, 4431 (1988).
500. Rodriguez, N.M., Anderson, P.E., Wootsch, A., Wild, U., Schlögl, R., and Paal, Z., *J. Catal.* **197**, 365 (2001).
501. Paul, J.-F., and Sautet, P., *J. Phys. Chem. B* **102**, 1578 (1998).
502. Zhang, C.J., and Hu, P., *J. Chem. Phys.* **116**, 322 (2002).
503. Yudanov, I.V., Neyman, K.M., and Rösch, N., *Phys. Chem. Chem. Phys.* **6**, 116 (2004).
504. Borasio, M., Morkel, M., Rupprechter, G., and Freund, H.-J., 2007, in preparation.
505. Schauermann, S., Hoffmann, J., Johánek, V., Hartmann, J., Libuda, J., and Freund, H.-J., *Angew. Chem. Int. Ed.* **41**, 2532 (2002).
506. Barros, R.B., Garcia, A.R., and Ihlarco, L.M., *J. Phys. Chem. B* **105**, 11186 (2001).
507. Mitchell, W.J., Xie, J., Jachimowski, T.A., and Weinberg, W.H., *J. Am. Chem. Soc.* **117**, 2606 (1995).
508. Endo, M., Matsumoto, T., Kubota, J., Domen, K., and Hirose, C., *J. Phys. Chem. B* **105**, 1573 (2001).
509. Libuda, J., and Freund, H.-J., *J. Phys. Chem. B* **106**, 4901 (2002).
510. Davis, J.L., and Barteau, M.A., *J. Am. Chem. Soc.* **111**, 1782 (1989).
511. Desai, S.K., Neurock, M., and Kourtakis, K., *J. Phys. Chem. B* **106**, 2559 (2002).
512. Reuter, K., and Scheffler, M., *Phys. Rev. B* **65**, 035 406 (2001).
513. Kim, S.H., and Wintterlin, J., *J. Phys. Chem. B* **108**, 14565 (2004).
514. Demoulin, O., Rupprechter, G., Seunier, I., Clef, B.L., Navez, M., and Ruiz, P., *J. Phys. Chem. B* **109**, 20454 (2005).
515. Schalow, T., Laurin, M., Brandt, B., Schauermann, S., Guimond, S., Kuhlenbeck, H., Starr, D.E., Shaikhutdinov, S.K., Libuda, J., and Freund, H.-J., *Angew. Chem. Int. Ed.* **44**, 2 (2005).
516. Datye, A.K., Bravo, J., Nelson, T.R., Atanasova, P., Lyubovsky, M., and Pfefferle, L., *Appl. Catal. A: General* **198**, 179 (2000).
517. Hansen, W., Bertolo, M., and Jacobi, K., *Surf. Sci.* **253**, 1 (1991).
518. Höbel, F., Ph.D., Technical University Berlin, 2007, in preparation.
519. Weiss, W., and Schlögl, R., *Top. Catal.* **13**, 75 (2000).
520. Shaikhutdinov, S., Meyer, R., Lahav, D., Bäumer, M., Klüner, T., and Freund, H.-J., *Phys. Rev. Lett.* **91**, 076102 (2003).
521. Meyer, R., Bäumer, M., Shaikhutdinov, S.K., and Freund, H.-J., *Surf. Sci. Lett.* **546**, L813 (2003).

522. Lemire, C., Meyer, R., Heinrich, V.E., Shaikhutdinov, S., and Freund, H.-J., *Surf. Sci.* **572**, 103 (2004).
523. Höbel, F., Bandara, A., Rupprechter, G., and Freund, H.-J., *Surf. Sci.* **600**, 963 (2006).
524. Mendes, F.M.T., Perez, C.A.C., Noronha, F.B., and Schmal, M., *Catal. Today* **101**, 45 (2005).
525. Starr, D.E., Mendes, F.M.T., Middeke, J., Blum, R.-P., Niehus, H., Lahav, D., Guimond, S., Uhl, A., Klüner, T., Schmal, M., Kuhlenbeck, H., Shaikhutdinov, S., and Freund, H.-J., *Surf. Sci.* **599**, 14 (2005).
526. Middeke, J., Blum, R.-P., Hafemeister, M., and Niehus, H., *Surf. Sci.* **587**, 219 (2005).
527. Dry, M.E., *Catal. Today* **71**, 227 (2002).
528. Silvestre-Albero, J., Rupprechter, G., and Freund, H.-J., *Chem. Commun.*, 80 (2006).
529. Silvestre-Albero, J., Rupprechter, G., and Freund, H.-J., *J. Catal.* **240**, 58 (2006).
530. Arnold, H., Döbert, F., and Gaube, J., *in* "Handbook of Heterogeneous Catalysis" (G. Ertl, H. Knözinger and J. Weitkamp, Eds.), Wiley, Weinheim, p. 2144–2165, 1997.
531. Hammerschaimb, H.U., and Spinner, J.B., U.S. Patent 4774375 (1988).
532. Furlong, B., Hightower, J., Chan, T., Sarkany, A., and Guczi, L., *Appl. Catal. A: General* **117**, 41 (1994).
533. Bertolini, J.C., Delichere, P., Khanra, B., Massardier, J., Noupa, C., and Tardy, B., *Catal. Lett.* **6**, 215 (1990).
534. Bond, G.C., Webb, G., Wells, P.B., and Winterbottom, J.M., *J. Chem. Soc. (Resumed)*, 3218 (1965).
535. Boitiaux, J.P., Cosyns, J., and Vasudevan, S., *Appl. Catal.* **6**, 41 (1983).
536. Tardy, B., Noupa, C., Leclercq, C., Bertolini, J.C., Hoareau, A., Treilleux, M., Faure, J.P., and Nihoul, G., *J. Catal.* **129**, 1 (1991).
537. Molnár, A., Sárkány, A., and Varga, M., *J. Mol. Catal. A: Chemical* **173**, 185 (2001).
538. Doyle, A., Shaikhutdinov, S., and Freund, H.-J., *Angew. Chem. Int. Ed.* **44**, 629 (2005).
539. Mittendorfer, F., Thomazeau, C., Raybaud, P., and Toulhoat, H., *J. Phys. Chem. B* **107**, 12287 (2003).
540. Sautet, P., and Paul, J., *Catal. Lett.* **9**, 245 (1991).